

Development of NIR Detectors and Science Requirments for SNAP

by

Matthew G. Brown

A dissertation submitted in partial fulfillment
of the requirements for the degree of
Doctor of Philosophy
(Physics)
in The University of Michigan
2007

Doctoral Committee:

Professor Gregory Tarlé, Chair
Professor Katherine Freese
Associate Professor David W. Gerdes
Associate Professor Timothy A. McKay
Assistant Professor Rebecca A. Bernstein

Copyright © Matthew G. Brown 2007
All Rights Reserved

ABSTRACT

Development of NIR Detectors and Science Requirments for SNAP

by

Matthew G. Brown

Chair: Gregory Tarlé

The SuperNova Acceleration Probe (SNAP) is an optical and near infrared space telescope designed to study the properties of dark energy with multiple techniques. One of SNAP's primary science goals is to constrain the dark energy equation of state using observations of thousands of type Ia supernovae from a redshift of 0.1–1.7. The highest redshift supernovae provide the most leverage on cosmology measurements since dark energy models, especially those with a time dependent equation of state, begin to diverge at redshifts greater than 1. For objects beyond a redshift of 1, the restframe optical light is shifted to the near infrared (NIR). The SNAP focal plane uses 36 visible CCD detectors and 36 hybridized HgCdTe detectors to achieve accurate measurements of both nearby and high redshift objects over a large field of view. The SNAP NIR detector development effort has succeeded in producing low noise, high quantum efficiency HgCdTe detectors. This work focuses on the characterization and simulation of NIR detectors properties, and the ability of SNAP to constrain the nature of dark energy. Simulations show that recently achieved increases in quantum efficiency lead to the largest gains in accuracy for supernova photometry. The best R&D detectors are approaching the performance of ideal (no noise, QE = 100%) NIR detectors for supernovae observations. Simulated uncertainties for type Ia supernovae are combined with results from cosmic microwave background observations and the SNAP weak lensing survey to constrain the dark energy equation of state. Supernovae alone cannot constrain the nature of dark energy with high accuracy. Independent measurements that have different systematic uncertainties and are sensitive to different combinations of cosmological parameters are needed to achieve the desired precision. With the currently achieved detector technology, the SNAP supernova and weak lensing surveys will constrain $\sigma_{w_0} = 0.04$ and $\sigma_{w_a} = 0.14$.

To Linda

ACKNOWLEDGMENTS

My five and a half years in graduate school include some of the most fun and fulfilling times in my life. I have had the opportunity to grow and learn with the help and encouragement of many people.

I would like to thank my family, for putting me in a position to succeed from the start of my childhood. The time my parents spent with me throughout my childhood and their value for education are two of the greatest gifts a son can have. My grandparents provided love and support, especially through Grandma's care packages and my grandfather's encouragement and words of wisdom. My brother Jeff is a great role model who I have looked up to for as long as I can remember. And thank you to my wife Linda, for being brave enough to marry a physicist. She is a wonderful, loving person who deserves more thanks than I can give her.

I would also like to thank everyone who has helped me during my time at Michigan. My adviser, Greg Tarlé, envisioned a great research project, taught me the skills I needed to complete my Ph.D., and provided many funny anecdotes along the way. Mike Schubnell spent many hours helping me understand laboratory measurements and provided advice when I was faced with difficult problems. I want to thank Andy Tomasch, Chris Bebek, the Michigan SNAP and DES groups, and my committee members for sharing their knowledge with me and making my time here fun and productive.

Thanks to everyone who has helped along the way: family, friends, roommates, coworkers, and professors. I hope I can provide the same guidance and support you have given me to future generations.

PREFACE

This thesis represents an overview of infrared detector testing and science simulations completed during the last five years at the University of Michigan. My adviser has asked me to provide a summary of the work the I completed during this period.

My primary laboratory responsibility was characterizing near infrared detectors for the SNAP project. The detector data presented in Ch. 5 was all acquired and analyzed at the University of Michigan, except where noted in the text. I wrote and debugged all of the waveform code for the Raytheon 1k and 2k SB-301 FPAs. Mike Schubnell and I developed the waveform code for the Rockwell H1RG and H2RG FPAs with some help from Bob Leach. Both waveform codes have been distributed by Bob Leach and used at various labs to readout NIR FPAs.

All detectors require mechanical and electrical interfaces to mount inside of dewars and connect to readout electronics. The mechanical connections include copper plates to mount the detectors inside the dewars, dark enclosures for low background testing, and LED mounts to provide illumination inside the dewar at 140 K. I worked with Mike Schubnell, Andy Tomasch, and Curtis Weaverdyck to draw up the interface plates and enclosures, and have them fabricated in our machine shop. Electrically, I defined the connections and made the readout cables for all of the Raytheon detectors, including fabrication of a printed circuit board with Jon Ameal to accommodate 1k devices mounted to lead-less chip carriers. I tested the cables and measured the noise contribution from the cables and readout electronics before including a detector in the system. Mike Schubnell and I worked together on a similar procedure for the Rockwell electrical connections.

A large effort went into development of data acquisition software over the last few years as well. Early in the SNAP program we used Voodoo, a Java based GUI

distributed by Bob Leach, for data acquisition. Voodoo was difficult to maintain and modify, so we began to develop our own custom data acquisition software at Michigan. The first attempt was a LabView based code written by Mike Borysow (now at University of Texas). This code worked, but was also difficult to modify and maintain. Eventually the data acquisition was written in python, and extended to include scripting capability. I defined and debugged the scripting language, with Mike Borysow primarily responsible for the programming and code development. I have written a number of automated test scripts for multiplexer gain, conversion gain, read noise, dark current, and quantum efficiency tests. I have also added automated temperature control with the help of two undergraduate students, Dylan Moreland and Mike Anderson.

The analysis code for all detector tests was developed by myself and Mike Schubnell. We both wrote a set of IDL scripts to analyze dark current, read noise, and gain data, then I wrote all of the scripts in python and integrated them with a MySQL database and CGI web interface to automatically post and display results at <http://gargamel.physics.lsa.umich.edu>. The database records were originally defined by Mike Borysow and Anna Paulson. Anna also wrote the initial CGI python scripts to search the results database and display plots on the web. I now update and maintain all of this code.

Two projects that I spent considerable time on are the conversion gain/inter pixel coupling and the pixel self heating. I did all of the data acquisition, analysis, and presentation for both of these projects.

Mike Borysow and Nate Barron did an excellent job developing the Spot-o-Matic hardware and software. They made all of the initial Spot-o-Matic measurements on the Raytheon InGaAs detector and Rockwell H2RG #40. Since they both left Michigan, I have made the remainder of the Spot-o-Matic measurements along with Curtis Weaverdyck. I updated all of the analysis code for Spot-o-Matic data and wrote the text for a paper on the Spot-o-Matic. I also worked on software to extract the diffusion and capacitive coupling from spot scan data by fitting the measured response to a convolution of models for each component of the pixel response. Ken

Beyerlein used this code to fit data for 3 different detectors. He and I also worked on simulations of undersampled photometry using the measured pixel responses, which appears in the Spot-o-Matic paper.

The simulation results in Ch. 4 use the SNAPsim package developed by the SNAP simulation group. I modified and debugged the exposure time calculations and detector code, and wrote classes to produce the data in Ch. 4. I also used SNAPsim to do the cosmology calculations for the cosmology fits in Ch. 3 and 6. I checked all SNAPsim distance modulus calculations against a python class that I wrote to perform similar calculations (during this process I discovered a bug in the SNAPsim code that incorrectly calculated all distances for non-flat cosmologies). I wrote both the Bayesian and χ^2 fitting code used to make the plots in Ch. 3. The maximum likelihood fitting is included in SNAPsim, I only made minor modifications to this code and used it to check my work.

The results in Ch. 6 use data from SNAPsim and the Dark Energy Task Force (DETF). I generated all the the SNAPsim supernovae data and performed the fits with both my code and the SNAPsim maximum likelihood fitting code. The supernova Fisher matrices I derived are based the covariance matrices from χ^2 fits. The SNAPsim code to directly calculate derivatives of the distance modulus was not working when I attempted to calculate the Fisher matrices directly via that method. I checked all of my supernova Fisher matrices against the DETF Fisher matrices provided by Gary Bernstein. I used the DETF Fisher matrices for microwave background, weak lensing, and baryon oscillation data to produce the joint constraints in Ch. 6.

I have had a lot of help producing the results in this thesis. The detector test results are the product of 4 years of hard work by everyone involved with developing the infrared detector testing facilities at Michigan. The simulation and science requirements rely on code developed by many different people within the SNAP collaboration. I want to thank everyone whose work has helped me over the years.

CONTENTS

| | |
|--|-----------|
| DEDICATION | ii |
| ACKNOWLEDGMENTS | iii |
| PREFACE | iv |
| LIST OF FIGURES | xi |
| LIST OF TABLES | xv |
| CHAPTER | |
| 1 Introduction | 1 |
| 1.1 A Brief History | 2 |
| 1.2 The SuperNova Acceleration Probe | 3 |
| 1.3 Understanding Dark Energy with SNAP Near Infrared Observations | 6 |
| 2 Cosmology Overview | 10 |
| 2.1 Introduction | 10 |
| 2.2 Fundamental Concepts | 10 |
| 2.3 General Relativity and the Robertson-Walker Metric | 15 |
| 2.3.1 Einstein Field Equations | 15 |
| 2.3.2 Robertson-Walker Metric | 16 |
| 2.3.3 Stress Energy and Equation of State | 18 |
| 2.3.4 Friedmann Equation | 18 |
| 2.3.5 Redshift | 20 |
| 2.3.6 Accelerated Expansion | 21 |
| 2.3.7 Curvature | 22 |
| 2.4 Cosmological Parameters | 24 |
| 2.4.1 Dark Energy Equation of State | 26 |

| | | |
|----------|--|-----------|
| 2.5 | Dark Energy Models | 28 |
| 2.5.1 | Constant w | 30 |
| 2.5.2 | Scalar Field | 30 |
| 2.5.3 | Chaplygin Gas | 32 |
| 2.5.4 | Modified Friedmann Equations | 33 |
| 2.6 | Cosmological Probes | 35 |
| 2.6.1 | Type Ia supernovae - Direct Distance Measurements . . . | 36 |
| 2.6.2 | Weak Lensing | 37 |
| 2.6.3 | Baryon Acoustic Oscillation and Cluster Abundances . . | 39 |
| 2.7 | The Magnitude System | 41 |
| 2.8 | Further Reading | 42 |
| 3 | Cosmology with Standard Candles | 44 |
| 3.1 | Luminosity Distance | 45 |
| 3.1.1 | Derivation | 45 |
| 3.2 | Distance Modulus | 48 |
| 3.2.1 | Λ CDM Cosmologies | 50 |
| 3.2.2 | Time Varying $w(z)$ Cosmologies | 52 |
| 3.3 | Type Ia Supernovae as Standard Candles | 53 |
| 3.3.1 | Brightness Indicators | 55 |
| 3.3.2 | Extracting the Distance Modulus | 56 |
| 3.4 | Cosmological Constraints from Type Ia Supernovae - Methods . . | 59 |
| 3.4.1 | χ^2 Tests | 59 |
| 3.4.2 | Maximum Likelihood Fits | 60 |
| 3.4.3 | Bayesian Estimation | 61 |
| 3.4.4 | Fisher Matrix | 63 |
| 3.5 | Cosmological Constraints from Existing Type Ia Supernova Data | 64 |
| 3.5.1 | Λ CDM Cosmologies | 65 |
| 3.5.2 | Constant w Fits | 69 |
| 3.5.3 | w_0 and w_a fits | 71 |
| 3.6 | Conclusions | 73 |

| | | |
|----------|--|-----|
| 4 | Science Driven Detector Requirements | 76 |
| 4.1 | SNAP Science Requirements | 77 |
| 4.1.1 | Requirements on w_0 and w_a | 80 |
| 4.2 | Simulation Overview | 80 |
| 4.3 | Source Parameterization | 82 |
| 4.3.1 | Lightcurve Templates | 82 |
| 4.3.2 | Flux Variance and Zodiacal Light | 85 |
| 4.3.3 | Simulated Lightcurves | 87 |
| 4.4 | NIR Detector Parameterization | 89 |
| 4.4.1 | Lightcurve Signal to Noise | 89 |
| 4.4.2 | Detector Read Noise and Dark Current Trade Studies | 90 |
| 4.4.3 | Quantum Efficiency vs. Total Noise Trade Studies | 93 |
| 4.5 | Establishing Draft level Detector Requirements | 95 |
| 4.6 | Conclusions | 98 |
| 5 | Development of SNAP NIR Detectors | 99 |
| 5.1 | Hybridized NIR Focal Plane Arrays | 99 |
| 5.1.1 | HgCdTe vs. InGaAs | 103 |
| 5.2 | Summary of NIR Detector Development (2004 – 2006) | 103 |
| 5.2.1 | Requirements and Test Procedures | 110 |
| 5.2.2 | Additional Development | 111 |
| 5.3 | NIR Test Procedures and Results | 112 |
| 5.3.1 | Multiplexer Gain | 113 |
| 5.3.2 | Conversion Gain | 115 |
| 5.3.3 | Dark Current | 117 |
| 5.3.4 | Pixel Self Heating (aka. Reset Anomaly) | 121 |
| 5.3.5 | Read Noise | 123 |
| 5.3.6 | Quantum Efficiency | 128 |
| 5.3.7 | Intra-pixel Variation | 133 |
| 5.3.8 | Well Depth | 134 |
| 5.3.9 | Persistence | 135 |

| | | |
|----------|---|------------|
| 5.3.10 | Cosmic Rays and Luminescence | 137 |
| 5.3.11 | Other effects | 138 |
| 5.4 | Detector Wrap Up | 139 |
| 5.5 | Correlated Noise and Gain in Unfilled and Epoxy Under-filled Hybridized HgCdTe Detectors | 140 |
| 5.5.1 | Autocorrelation Procedure | 142 |
| 5.5.2 | Autocorrelation Results | 143 |
| 5.5.3 | Inter-pixel Capacitance Summary | 147 |
| 5.6 | Spot-o-Matic Intra-pixel Response Measurements | 148 |
| 5.6.1 | Overview of Technique | 149 |
| 5.6.2 | Characterizing Beam Spots | 150 |
| 5.6.3 | Pixel Response Measurements | 151 |
| 5.6.4 | Results and Analysis | 153 |
| 5.6.5 | A sensor with anomalous substructure - FPA #40 | 159 |
| 5.6.6 | Photometry Simulations | 161 |
| 5.6.7 | Summary of Results | 162 |
| 6 | Simulated Constraints on Dark Energy | 165 |
| 6.1 | Dark Energy constraints with Supernovae | 166 |
| 6.1.1 | w_0 and w_a Constraints I | 169 |
| 6.1.2 | w_0 and w_a Constraints II | 173 |
| 6.2 | Constraining Cosmology with Multiple Techniques | 176 |
| 6.2.1 | Supernovae and Weak Lensing | 178 |
| 6.2.2 | Supernovae and Baryon Acoustic Oscillations | 180 |
| 6.2.3 | All Techniques | 181 |
| 6.3 | Conclusions | 183 |
| | BIBLIOGRAPHY | 186 |

LIST OF FIGURES

Figure

| | | |
|-----|--|----|
| 1.1 | A cutaway of the SNAP telescope (left) with a close-up view of the focal plane (right). | 5 |
| 1.2 | Simulated SNAP supernova data, plotted as the difference between the data and the concordance cosmological model. | 7 |
| 2.1 | Scale factor vs. time in a flat (solid), closed (dashed) and open (dot dash) matter dominated universe with $H_0 = 70 \text{ km s}^{-1} \text{ Mpc}^{-1}$ | 23 |
| 2.2 | Apparent magnitude of a standard candle for many different dark energy models. | 29 |
| 3.1 | Distance modulus, $\mu(z)$, for various Λ CDM cosmologies with different matter and dark energy density (Ω_M, Ω_Λ). | 50 |
| 3.2 | Magnitude difference for type Ia supernova for a number of proposed dark energy models minus the concordance Λ CDM cosmology ($\Omega_M = 0.26, \Omega_\Lambda = 0.74$). | 53 |
| 3.3 | Probability density function for Ω_M from a fit to the gold sample data. | 66 |
| 3.4 | Bayesian estimation of the probability density function for Ω_M and Ω_Λ using the gold sample data from Riess et al. [2004]. | 67 |
| 3.5 | 68.3%, 95.4%, and 99.7% confidence intervals for Ω_M and Ω_Λ from fits to the gold sample data. | 68 |
| 3.6 | 68.3%, 95.4%, and 99.7% confidence interval for Ω_M and w_0 using Bayesian (top panel) and maximum likelihood (bottom panel) fits to the gold sample. | 70 |

| | | |
|-----|---|-----|
| 3.7 | 68.3%, 95.4%, and 99.7% confidence interval for w_0 and w_a from fits to the gold sample supernova data. | 72 |
| 4.1 | Simulated spectrum of a type Ia supernova at peak brightness in the restframe and at $z = 1.7$ | 83 |
| 4.2 | Zodiacal flux at the north ecliptic pole from Aldering [2001] | 86 |
| 4.3 | A $z = 1.7$ type Ia supernova lightcurve observed every 4 days through the nine SNAP filters. | 88 |
| 4.4 | Signal to Noise vs. epoch in SNAP filter 8, the reddest SNAP filters, assuming a total detector noise of $10e^-$ per 300s exposure. The detection threshold for type Ia supernovae is $S/N > 3$ | 90 |
| 4.5 | Contours of constant parameter error for the distance modulus, μ , for type Ia supernova at $z = 1.7$. The top plot assumes QE= 60%, bottom: QE= 95%. | 91 |
| 4.6 | Lightcurve parameter and μ errors for a $z = 1.7$ type Ia supernova assuming noiseless NIR detectors. | 93 |
| 4.7 | Distance modulus uncertainty contours for total NIR detector noise up to $20e^-$ | 94 |
| 4.8 | The redshift distribution of type Ia supernovae in one 16 month SNAP deep survey. | 96 |
| 5.1 | The readout unit cell of a multiplexed FPA. | 100 |
| 5.2 | Cold stage assembly with FPA mounted | 102 |
| 5.3 | Sample data for a multiplexer gain measurement. | 114 |
| 5.4 | Sample dark current histogram for a Rockwell HAWAII-2RG FPA. | 118 |
| 5.5 | Mean dark current as a function of temperature. | 120 |
| 5.6 | The impact of pixel self heating on the detector output for Fowler sampled data with a 300s exposure delay. | 122 |
| 5.7 | Fowler sampled noise data for two of the lowest noise detectors produced for SNAP. | 125 |
| 5.8 | Fowler-1 and Fowler-16 noise histograms for H2RG #103. | 126 |

| | | |
|------|---|-----|
| 5.9 | Schematic diagram of the optical components of the quantum efficiency setup. | 129 |
| 5.10 | Quantum efficiency for RSC lot 1 FPA #40 and the more recent FPA # 102. | 130 |
| 5.11 | QE for RVS 1k \times 1k HgCdTe FPA #598141 after 3 different processing steps. | 131 |
| 5.12 | QE of an RVS InGaAs detector as a function of detector temperature. | 132 |
| 5.13 | Sample well depth histogram for a RVS 1k device. | 134 |
| 5.14 | Persistence data for H2RG #103. | 136 |
| 5.15 | example | 137 |
| 5.16 | Conversion gain data for a H2RG 1.7 μ m cutoff HgCdTe. | 144 |
| 5.17 | Schematic diagram of the optical components of the Spot-O-Matic. | 149 |
| 5.18 | Schematic Diagram of the Foucault knife-edge scanning procedure. | 150 |
| 5.19 | One-dimensional scan of an arbitrary single pixel at a wavelength of 1050 nm. | 151 |
| 5.20 | Two-dimensional scan of an arbitrary single pixel at a wavelength of 1050 nm. | 152 |
| 5.21 | One-dimensional scan for 1050 nm light over 5 adjacent pixels located along the y -direction. | 155 |
| 5.22 | Convolution of one-dimensional pixel scan data. | 156 |
| 5.23 | A boxcar response convolved with the best fit diffusion and capacitive coupling. | 158 |
| 5.24 | Two-dimensional scan for 1050 nm light, summed over an array of 8 \times 8 adjacent pixels. | 159 |
| 5.25 | One-dimensional scan over four adjacent pixels located along the y -direction. | 160 |
| 5.26 | Two-dimensional scan of an arbitrary single pixel at a wavelength of 1300 nm. | 161 |
| 5.27 | Two-dimensional scan summed over an array of 6 \times 6 adjacent pixels. | 162 |
| 5.28 | Fractional photometric error vs. sampling frequency. | 163 |

| | | |
|-----|---|-----|
| 6.1 | Distance modulus error vs. redshift for a SNAP supernova survey with 0, 1, 2, and all 3 NIR filters included. | 167 |
| 6.2 | 68.3% and 95.4% confidence contours for w_0 and w_a for a systematic uncertainty limited supernova survey. | 170 |
| 6.3 | 68.3% and 95.4% confidence contours for w_0 and w_a when adding and subtracting a redshift dependent systematic error of $\sigma_{\text{sys}} = 0.02(1 + z)/2.7$ | 172 |
| 6.4 | Simulated distance modulus data for 2000 type Ia supernova using the SNAPsim framework. | 173 |
| 6.5 | 68.3% and 95.4% confidence contours for w_0 and w_a from simulated SNAP supernova data. | 175 |
| 6.6 | 68.3% and 95.4% confidence contours in the w_0, w_a plane from SNAP supernova data plus WMAP CMB data and a 1000 deg ² space based weak lensing survey. | 179 |
| 6.7 | 68.3% and 95.4% confidence contours in the w_0, w_a plane from SNAP supernova data plus WMAP CMB data and a baryon acoustic oscillation survey of 10 ⁸ galaxies. | 181 |
| 6.8 | 68.3% and 95.4% confidence contours in the w_0, w_a plane from SNAP supernova data plus WMAP CMB data, a 1000 deg ² space based weak lensing survey, and a baryon acoustic oscillation survey of 10 ⁸ galaxies. | 182 |

LIST OF TABLES

Table

| | | |
|-----|---|-----|
| 2.1 | Table of cosmological parameters with best fit values. | 25 |
| 3.1 | Best fit cosmology parameters using the gold sample supernova. | 74 |
| 4.1 | Draft Level 1 Science Requirements. | 78 |
| 4.2 | SNAP NIR detector specifications at the start of the infrared research and development program in 2001. | 79 |
| 4.3 | Zodiacal flux at the detector surface. | 87 |
| 5.1 | NIR devices tested during SNAP R&D program. | 104 |
| 5.2 | Rockwell H2RG autocorrelation results. | 143 |
| 5.3 | Autocorrelation for and unfilled Raytheon HgCdTe FPA. | 145 |
| 5.4 | Autocorrelation for an epoxy backfilled Raytheon HgCdTe FPA. | 146 |
| 5.5 | Five 1.7 μm HgCdTe FPAs that have been tested using the Spot-o-Matic. | 154 |
| 6.1 | Uncertainty on the dark energy equation of state for various combina- tion of future dark energy measurements. | 184 |

CHAPTER 1

Introduction

The recent discovery that the expansion of the universe is accelerating has started a revolution in the field of cosmology. The thing causing the acceleration is called dark energy, but little is known about its nature. Dark energy must have negative pressure; the simplest example is vacuum energy, which has constant density as space expands. Discovering the nature of dark energy is one of the most fundamental problems in physics today, and measuring its properties requires new instruments able to make precision observations of distant objects. The SuperNova Acceleration Probe (SNAP) is one instrument that combines state of the art instrumentation with a dedicated space based mission to explore dark energy. SNAP will probe dark energy with a variety of techniques, including type Ia supernovae, weak lensing, and baryon acoustic oscillations. The combination of precision observations with complementary techniques yields tight constraints on dark energy models and will advance understanding of the fundamental physics of dark energy.

Many major advances in cosmology and astrophysics have followed advances in instrumentation. Telescopes expand the light collection and resolution of the human eye. Photographic plates allowed longer exposures to integrate light from faint objects, then Charge Coupled Devices (CCDs) helped start a digital age for astronomy while providing further increases in sensitivity. Increases in computing power and the development of algorithms to analyze large datasets enable large surveys with terabytes of data to be quickly processed. Modern instruments use hybridized arrays to extend high resolution imaging beyond the optical bandpass into the near infrared. All of these developments have led to increased precision and a better understanding of the universe.

1.1 A Brief History

When astronomers began observing the sky they had no idea that some of the light they were seeing was billions of years old, emitted from objects billions of light-years away. Early astronomers believed all objects were located on celestial spheres, with the earth or the sun at the center of the universe. Aristotle and Ptolemy argued for the earth centered system, with the sun, moon, and planets traveling in circular epicycles. Many years later, Copernicus argued for a heliocentric theory, with the sun at the center. Neither model could correctly calculate the motion of the planets across the sky. The data needed to understand the structure of the solar system was not available until late in the 16th century, when astronomers like Tycho Brahe set out to catalog the sky with careful, systematic observations. Existing instruments only had an accuracy of about one degree, so Brahe designed new instruments that could measure positions to within half an arc-minute (1/120 degree). In 1596, Johannes Kepler used these measurements to calculate the planetary orbits and shattered the celestial spheres with his First Law of planetary motion: the orbits of the planets are ellipses, with the sun at one focus of the ellipse.

Understanding continued to grow with the development of the telescope. Galileo was the first to use the telescope for astronomy, observing Jupiter and its moons. With the telescope it became possible to resolve the planets and calculate their size. Understanding the size of the solar system was one step towards understanding the scale of the universe. When nebulae were discovered, some believed they were much more distant than the resolved stars. The nebulae were diffuse clouds of unresolved light. In the 1920s, better instruments were built and it became apparent that some of the nebulae were in fact distant galaxies similar to the Milky Way. The discovery of many diverse galaxies scattered throughout the universe and estimates of the distance and age of these objects lead to two important facts: the universe is big and old.

In addition to being big and old, the universe appears approximately the same in all directions. The number of galaxies, their brightness, and distribution is roughly constant in every direction. The observation that the universe is both homogeneous

and isotropic helped advance theoretical understanding of the universe and is still one of the critical axioms of modern cosmology. The second theoretical advancement came from General Relativity. Einstein was able to understand gravity in terms of the curvature of space and time. Solutions to the Einstein equation led to a dynamic universe, so Einstein used a left over integration constant, called the cosmological constant, to balance the attractive matter and leave the universe static. Many scientists believed the universe was static until 1929, when Edwin Hubble made the first direct measurement of the expansion of the universe. Hubble's observations of 24 extra-galactic nebulae from the 2m telescope at Mt. Wilson started a revolution in the understanding of cosmology. Big Bang Nucleosynthesis and the cosmic microwave background are two pieces of the Hot Big Bang model that rely on an expanding universe.

Over the last few decades the field of cosmology has evolved into a precision science, with a small number of parameters describing the large-scale features of the observable universe. The current generation of experiments can measure most of the parameters to an accuracy of about 10%. The next generation of instruments will push these constraints down to the 2% level, where control of systematic uncertainties drives the experimental procedure. Currently only cosmic microwave background (CMB) experiments, such as the Wilkinson Microwave Anisotropy Probe (WMAP), have achieved this level of accuracy. Improvements in technology lead to more precise measurements and better control of systematic errors. Next generation instruments like SNAP will take advantage of the latest technology to achieve measurements with unprecedented depth and precision, further improving our knowledge of dark energy and cosmology.

1.2 The SuperNova Acceleration Probe

SNAP is a dedicated space-based mission designed to study the properties of dark energy. The SNAP telescope has diffraction limited f/10.8 optics with a 2 meter aperture and a three mirror anastigmatic design, which allows for a long focal length in a compact package. The focal plane consists of 36 $3.5\text{k} \times 3.5\text{k}$ high resistivity thick

CCDs, manufactured at Lawrence Berkeley National Laboratory (LBNL), and $36\ 2k \times 2k$ near infrared (NIR) focal plane arrays (FPAs), likely using HgCdTe technology. Two vendors, Rockwell Scientific and Raytheon Vision Systems, are competing to produce high quantum efficiency, low noise HgCdTe detectors. The thick CCDs have excellent red response, with high quantum efficiency up to 1000 nm. This overlaps the NIR bandpass, which extends from 800 – 1700 nm, allowing the two detector technologies to be cross calibrated. The detectors are covered by 9 different fixed filters, 6 in the visible and 3 in the NIR. The filter spacing and width is log scaled to maintain roughly constant signal to noise (S/N) in all the filters. SNAP also utilizes a high throughput, low resolution ($R \sim 70$), visible and NIR spectrograph covering the same wavelength range. A conceptual drawing of the telescope and focal plane are shown in Fig. 1.1.

The SNAP focal plane will be one of the largest ever in space. The field of view is almost 0.7 square degrees, and the focal plane has more than 440 million visible and 150 million infrared pixels. The field of view is over 600 times larger than the Hubble Space Telescope’s (HST) Wide Field Camera (WFC). To achieve such a large field, the telescope is under sampled, with a pixel scale of only 0.1 arcsec in the visible and 0.17 arcsec in the NIR. The point spread function (PSF) is under sampled by about a factor of three at 1000 nm; uniform intra-pixel response is required to meet the photometry specifications. Intra-pixel response testing that is able to measure the uniformity within a pixel at the 1% level has been developed for SNAP NIR FPAs. The intra-pixel uniformity requirement has been met by both HgCdTe vendors.

There are four SNAP reference surveys designed to probe dark energy with a number of different techniques. There are two supernova surveys, near the north and south ecliptic poles, which each cover about 7.5 square degrees in 15 to 18 months. The supernova surveys observe each field in all 9 filters on a four day cadence for the duration of the survey. The depth for each pointing is 27.7 AB mag per filter, with a final co-added depth of about 30.3 mag. The two surveys will discover and follow-up more than 2000 type Ia supernovae from a redshift of 0.1 – 1.7. Multi-color imaging and spectroscopy near peak brightness provide uniform observations

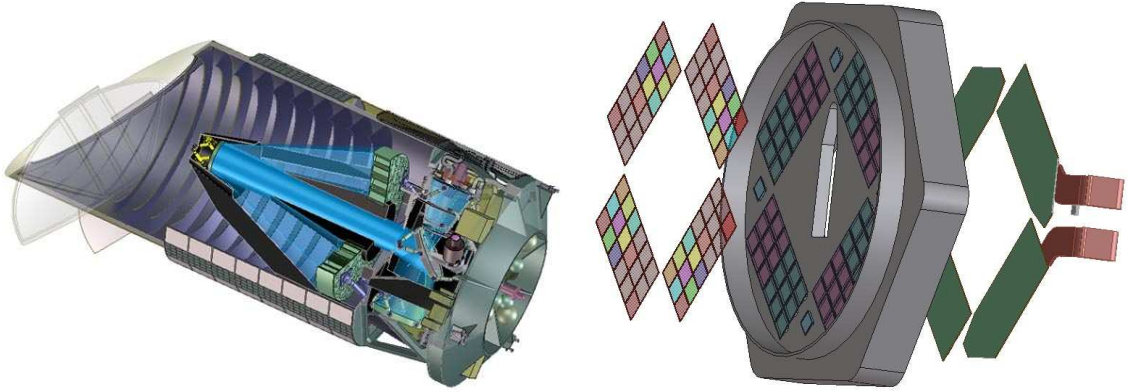


Figure 1.1. A cutaway of the SNAP telescope (left) with a close-up view of the focal plane (right). The focal plane consists of 36 visible CCD detectors and 36 NIR HgCdTe detectors with fixed filters above each detector

for each supernova and limit systematic uncertainties. The resulting Hubble diagram for type Ia supernovae is used to constrain the dark energy density and equation of state. Figure 1.2 gives a preview of simulated SNAP data with the expected errors for the SNAP supernova surveys, assuming the standard cosmological model ($\Omega_M = 0.26, \Omega_\Lambda = 0.74, w = -1$) and $\Delta z = 0.1$ redshift bins. The data are shown as a difference from the standard cosmology model and assume a systematic error limit of $0.02(1+z)/2.7$ magnitudes per redshift bin.

One goal for the SNAP supernova observations is to reduce the systematic uncertainties with precision observations of the entire supernova lightcurve. Systematic errors can arise from the astrophysical nature of the supernova events and the supernova's host galaxy. These include: redshift dependent evolution, K-correction, Milky Way and host galaxy dust extinction, Malmquist bias, gravitational lensing, and non-type Ia contamination. Reducing these sources of systematic error requires detailed understanding of the supernovae and their environment, which is achieved through careful instrument and mission design, e.g. by obtaining a spectrum of every supernova at the same epoch to search for homogeneous sub-classes of type Ia events or by observing in regions of the sky with low galactic (Milky Way) extinction.

The other main source of systematic uncertainty comes from the calibration of the instrument. Uncorrelated calibration errors between the filters can result from

incomplete knowledge of the calibration lamp spectrum and lead to magnitude offsets between filters. The detectors can also contribute to the calibration uncertainty. Biases in the observed flux of bright and dim sources (known as flux-dependent non-linearity in NIR detectors) or a systematic increase in the measured signal of pixels which experienced a high flux in a previous measurement (persistence) are two examples of detector induced systematic errors. The systematic error budget for SNAP is currently being developed, and detector tests are ongoing to ensure that these effects will not bias any of the dark energy results.

In addition to the deep survey, there are two wide-field surveys to complement the supernova program with weak lensing, galaxy cluster, and baryon acoustic oscillation data. The baseline wide-field survey covers 300 – 1000 square degrees with a limiting magnitude of 27.7 (AB) per filter. The panoramic survey images 7000 – 10000 square degrees, with shorter exposures and a limiting depth of 26.7 AB magnitudes. Both surveys observe the entire field in all 9 filters, providing high signal to noise multi-color photometry and photometric redshift estimates. Simulations of these data are not incorporated into the NIR requirements at this time, however the data from these surveys, in particular weak lensing measurements in the wide survey, are essential for constraining the dark energy equation of state.

1.3 Understanding Dark Energy with SNAP Near Infrared Observations

Measuring the impact of dark energy on the expansion of the universe requires accurate observations over a wide range of redshifts. For type Ia supernovae, the highest redshift supernovae provide the most leverage to distinguish dark energy models, as illustrated by Fig. 1.2. One important goal is to determine if dark energy is consistent with a cosmological constant. To measure the properties of dark energy, it is parameterized in terms of an equation of state that can approximate many of the models shown in Fig. 1.2. Measuring a statistically significant deviation from the cosmological constant equation of state, or any time variation in the dark energy

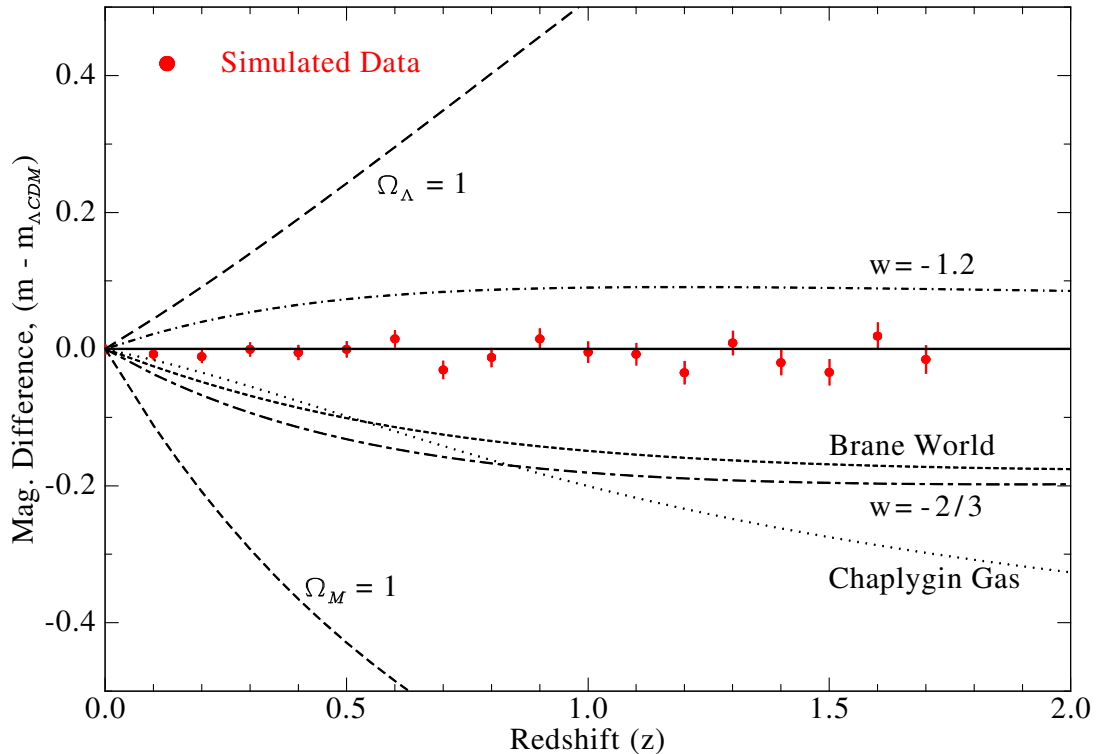


Figure 1.2. Simulated SNAP supernovae data, plotted as the difference between the data and the concordance cosmological model ($\Omega_M = 0.26, \Omega_\Lambda = 0.74$). The data assume a systematic error limit of $0.02(1+z)/2.7$ magnitudes, in $\Delta z = 0.1$ redshift bins. A number of different dark energy models are shown for reference. All models assume a flat universe with $\Omega_{tot} = 1$.

density, would represent a significant breakthrough.

Weak lensing, cluster abundances, and baryon acoustic oscillation measurements provide additional dark energy constraints that can break parameter degeneracies. In addition, CMB measurements from the WMAP satellite [Spergel et al., 2003, 2006] and future missions such as Planck [<http://www.rssd.esa.int/Planck/>] provide prior constraints on the total density and dark energy parameters that complement the supernova results. Simulated supernova data are used along with anticipated constraints from future experiments and SNAP weak lensing data to project constraints on the dark energy equation of state. The projected constraints represent a significant improvement over constraints from existing datasets, and the use of multiple techniques breaks parameter degeneracies and ameliorates concerns about systematic errors dominating a single measurement.

Precision observations of high redshift type Ia supernovae require high quality NIR detectors. Simulations of the most distant type Ia supernovae help to define the detector noise and quantum efficiency requirements. The simulations are also used to highlight the importance of NIR observations for constraining the dark energy equation of state. Simulations of a supernova survey cutting off at $z = 1$ and SNAP-like surveys with limited or no NIR observations demonstrate that dark energy constraints are considerably weaker without NIR data for high redshift supernovae.

The SNAP NIR detector development program has led to a number of improvements in detector performance. Test results for engineering-grade devices from both vendors are presented. The development of readout and testing procedures is covered, including detector effects that were discovered and characterized in laboratory testing during the SNAP R&D program. The infrared program has been an overwhelming success for the SNAP project, realizing large gains in both quantum efficiency and read noise for HgCdTe detectors. High quantum efficiency results in the largest gains in accuracy for measurements of the apparent magnitude for type Ia supernovae. The apparent magnitude is reconstructed from multi-band lightcurve fits, and high quantum efficiency provides better signal to noise (S/N) near the peak of the lightcurves where observations are limited by photon shot (Poisson) noise.

This thesis is focused on optimizing the SNAP NIR detector performance to constrain the dark energy equation of state as well as possible. First, I present an overview of cosmology, which introduces some basic concepts from General Relativity. The following chapter discusses extracting cosmology parameters from type Ia supernova data, concentrating on the dark energy equation of state. Results using existing supernova data show the current constraints and begin to demonstrate the importance of high redshift supernovae and space based NIR observations. The development of the SNAP NIR detector requirements is discussed in Chapter 4. Simulations of the detector performance are used to refine the initial detector specifications into science driven requirements. The next chapter covers the detector development, including performance improvements and the development of testing software and procedures for SNAP NIR detectors. The detector results are used to simulate data for the

baseline SNAP supernova survey and predict constraints on the distance modulus for individual supernovae. The simulated supernova data are fit to a variety of dark energy models to estimate constraints on the dark energy equation of state. Prior constraints from future surveys and data from complementary techniques employed by SNAP are added to the simulated supernova data. Finally, conclusions are drawn about the ability of SNAP to constrain dark energy and the importance of the SNAP NIR detectors for achieving those constraints.

CHAPTER 2

Cosmology Overview

2.1 Introduction

The field of cosmology attempts to answer some of the most fundamental questions about the history and fate of the universe: How old is the universe? Will it last forever or come to an end? How big is the universe? Is it infinite or finite in extent?

Answering these questions requires a mathematical model to describe the universe, a description of its energy content and an understanding of the forces that govern the evolution of space and time. The current cosmological model contains all the necessary components: the Robertson-Walker metric describes the space; the energy components are assumed to be perfect fluids characterized by an equation of state; and General Relativity describes the dynamics of the universe. Observations of the cosmic microwave background, large scale structure, and type Ia supernovae provide independent probes of the underlying cosmology of the universe. Results from these and other emerging techniques have converged on a widely accepted cosmological model known as the ‘concordance’ cosmology.

2.2 Fundamental Concepts

Modern cosmology is based on a small number of theoretical concepts that are well supported by observation. The field began in the early 1900s with Einstein’s theory of General Relativity. Over the next few decades, observations by Hubble and theoretical work by Friedmann, Robertson, and Walker laid the foundations of modern cosmology. More recently, observations of large scale structure, the cosmic microwave background (CMB) and type Ia supernovae have increased our knowledge of the en-

ergy constituents in the universe. Some of the fundamental concepts in modern cosmology are:

1. The universe is homogeneous and isotropic.
2. The universe is expanding.
3. The universe was hot and dense in the past.
4. A period of rapid expansion (inflation) occurred very early in the universe's history.
5. Big Bang Nucleosynthesis produced light elements in the early universe.
6. Most of the matter in the universe is non-baryonic dark matter.
7. Galaxies and clusters of galaxies evolved from small density perturbations imprinted in the CMB.
8. The expansion of the universe is accelerating.

The assumption that the universe is homogeneous and isotropic is based on simple observational evidence. In every direction, there is approximately the same distribution of galaxies, and on large enough scales (> 1000 Mpc), the total mass in a co-moving volume appears constant. Observations of the cosmic microwave background in the 1990s quantified the homogeneity and isotropy in terms of the temperature fluctuations in the CMB photons [Gorski et al., 1996]. In any given direction the temperature is the same to one part in 10^5 , after correcting for the motion of the Earth through the inertial rest frame. The temperature fluctuations result from density perturbations in the early universe. The matter in the universe formed structures based on these small density fluctuations; however, the total matter distribution remains approximately homogeneous on large scales.

The expansion of the universe was first observed by Hubble [1929]. Prior to Hubble's measurement, Einstein had proposed a static universe, with a cosmological constant, or vacuum energy, to balance the attractive matter in the Einstein equation.

A static universe would likely have an infinite lifetime, existing in the same static equilibrium for all time. However, the equilibrium created by adding the cosmological constant is unstable, and Hubble's observations showed that the universe is in fact expanding.

The expansion of the universe implies that at some point in the past the universe was smaller, and thus hotter and denser than it is today. This model is now known as the Hot Big Bang [Gamow, 1946]. In the early universe, the temperature and density are high and the hydrogen is ionized. In the resulting plasma, the photons couple to the baryons via Thompson scattering with the free electrons. Density perturbations in the baryons result in temperature fluctuations in the photons. As the universe expands and cools, the electrons become bound in hydrogen atoms and the Thompson cross-section drops by many orders of magnitude. This transition is known as recombination, and occurs at the surface of last scattering; after the formation of neutral hydrogen the photons free stream through the universe. The photons redshift as the universe continues to expand leading to a modern background of microwave radiation, the CMB. The discovery of the CMB by Penzias and Wilson [1965] confirmed the existence of a hot, dense phase in the early universe.

Inflation in the early universe was proposed as a mechanism to explain the flat geometry of the universe, the lack of magnetic monopoles, and the horizon problem¹ [Guth, 1981]. In the inflationary model, the universe undergoes a period of rapid expansion very early in its history. Inflation expands the universe by more than 60 e foldings (e^{60}) in about 10^{-30} seconds. Quantum fluctuations are expanded to a macroscopic size, seeding the observed temperature fluctuations in the CMB and providing the initial density perturbations needed for structure formation. The expansion smooths any curvature in the early universe and results in a spatially flat geometry, a prediction confirmed by recent CMB measurements.

Big Bang Nucleosynthesis describes the production of light elements (deuterium, helium, lithium) in the early universe [Gamow, 1946, Alpher et al., 1948]. Early theories predicted that all elements were produced in stellar interiors or supernovae

¹The horizon problem asks why regions of the sky which are acausal appear the same.

explosions [Hoyle et al., 1956, Burbidge et al., 1957]. These theories cannot predict the light element abundances, underestimating the fraction of both helium and deuterium. Helium accounts for nearly 25% of the observed baryonic matter density [Tytler et al., 2000, Burles et al., 2001], and deuterium is relatively abundant despite being destroyed in stellar interactions. Big Bang Nucleosynthesis predicts that these elements are produced in a non-equilibrium process, when the universe is about 3 minutes old and the temperature is near 10^9 K. At this point colliding protons and neutrons become bound in deuterium, which can combine with a neutron to form tritium, a proton to form helium 3, or another deuterium to form Helium 4. A small amount of lithium 7 is also produced. The relative abundance of these elements depends strongly on the baryon density in the early universe. The measured abundances of all the light elements require a present day baryon density of about 4% of the critical density. This is in excellent agreement with recent measurements of the baryon density from the CMB power spectrum [Spergel et al., 2003, 2006]. The success of Big Bang Nucleosynthesis is further evidence for a hot dense phase in the early universe.

The matter content of the universe consists of two components, ‘ordinary’ baryonic matter, and a non-baryonic component called dark matter. The baryonic matter only accounts for a small percentage of the total energy density in the universe, about 4%. Approximately 22% of the total energy density is contained in dark matter, which is ‘observable’ through its gravitational interaction, via velocity dispersion in clusters [Zwicky, 1933], galactic rotation curves, or gravitational lensing measurements. The leading candidate for dark matter is a WIMP (weakly interacting massive particle, see [Eidelman et al., 2004] and references therein), possibly the lightest supersymmetric partner.

Because it dominates the mass density, dark matter plays an important role in the formation of large scale structure (see e.g. Padmanabhan [1993]). Soon after inflation, the dark matter begins to gravitationally collapse in over-dense regions of the universe. During this time the baryonic matter is ionized and coupled to the photons, and radiation pressure in the photon-baryon fluid prevents gravitational

collapse of the baryons. This gives the dark matter a ‘head start’ on the baryons, so that dark matter structures are already beginning to form when the baryons decouple from the photons at the surface of last scattering, about 10^4 years after the Big Bang. The baryons then fall into the potential wells created by the dark matter and form planets, stars, galaxies, and clusters. In a matter dominated universe, structure formation continues far into the future as clusters form super-clusters and progressively larger structures, but in the presence of a cosmological constant the accelerated expansion freezes out structure formation on the largest scales.

The most recent addition to the standard model of cosmology is the observation of accelerated expansion. In a spatially flat universe with only matter and radiation, the expansion will slow over time. Observations of type Ia supernovae by two groups show that the expansion is accelerating [Perlmutter et al., 1999, Riess et al., 1998]. This discovery, along with indications of spatial flatness and low ($\sim 26\%$) matter density, has led to the introduction of dark energy into the standard cosmological model. Dark energy must have a negative pressure to resist the attractive matter and cause the expansion to accelerate. There are many models for dark energy; the simplest is the cosmological constant or vacuum energy, proposed by Einstein. Measurements of large scale structure and the CMB agree with the type Ia supernovae results, which show that the dark energy density is about 74% of the total energy density in the universe today.

These 8 fundamental concepts are united in a model known as the concordance cosmology. In this model the universe begins with a hot big bang and an inflationary period of rapid expansion. Small perturbations in the initial density field that give rise to structure formation are imprinted as temperature fluctuations in the CMB. The universe is expanding, and recently the expansion is accelerating due to dark energy. The universe appears spatially flat, consistent with predictions from inflation, with about 74% dark energy and 26% matter, assuming the dark energy is a cosmological constant. Most of the matter is non-baryonic dark matter, only observable through its gravitational interactions. The concordance cosmology is well supported by current observations; future instruments with high precision are needed to look for deviations

from this model.

This list of fundamental concepts in cosmology is not exhaustive; it covers the topics necessary to understand the cosmology measurements presented in this work. Other events in the early universe, such as Baryogenesis [Sakharov, 1967], play an important role in producing the observable matter in the universe, but are not covered here. The references in Sec. 2.8 offer a more complete overview of cosmology and astrophysics.

2.3 General Relativity and the Roberson-Walker Metric

The theory of General Relativity was proposed by Einstein [1916]. General Relativity is a deep subject that is difficult to summarize in a few pages. The concepts needed for cosmology calculations using the Friedmann equation are covered here; the references at the end of this chapter provide a more in depth treatment. The general principle of relativity assumes that the laws of physics must be the same for all observers, both accelerating and at rest. The theory characterizes the gravitational force in terms of the curvature of space-time. All forms of stress-energy in the universe, including matter and radiation, lead to space-time curvature. The attraction of massive objects due to the gravitational force in Newtonian mechanics is replaced by inertial motion in a curved background. Particles travel on time-like or null geodesics in the curved spacetime. The curvature introduced by different forms of stress-energy is described by the Einstein Field Equations.

2.3.1 Einstein Field Equations

The dynamics of the universe are governed by the solutions of the Einstein Field Equations,

$$R_{\mu\nu} - \frac{1}{2}\mathcal{R}g_{\mu\nu} \equiv G_{\mu\nu} = 8\pi GT_{\mu\nu} + \Lambda g_{\mu\nu}, \quad (2.1)$$

where $G_{\mu\nu}$ is the Einstein tensor, $T_{\mu\nu}$ is the stress-energy tensor for all energy densities (matter, radiation, etc.), Λ is the cosmological constant, and $g_{\mu\nu}$ is the metric tensor. The speed of light, $c = 1$, for the remainder of this discussion. In these units the speed of light serves as a conversion factor between distance and time. The Ricci

tensor, $R_{\mu\nu}$, and the Ricci scalar, \mathcal{R} , are defined in terms of derivatives of the metric tensor, with

$$\begin{aligned}\mathcal{R} &\equiv g^{\mu\nu}R_{\mu\nu}, \\ R_{\mu\nu} &\equiv R_{\mu\alpha\nu}^{\alpha}, \\ R_{\nu\alpha\beta}^{\mu} &= \partial_{\alpha}\Gamma_{\nu\beta}^{\mu} - \partial_{\beta}\Gamma_{\nu\alpha}^{\mu} + \Gamma_{\sigma\alpha}^{\mu}\Gamma_{\nu\beta}^{\sigma} - \Gamma_{\sigma\beta}^{\mu}\Gamma_{\nu\alpha}^{\sigma}, \\ \Gamma_{\alpha\beta}^{\mu} &= \frac{1}{2}g^{\mu\sigma}(\partial_{\beta}g_{\sigma\alpha} + \partial_{\alpha}g_{\sigma\beta} - \partial_{\sigma}g_{\alpha\beta}),\end{aligned}$$

following the metric sign convention from Kolb and Turner [1990], $(+, -, -, -)$. The repeated indices are summed over, and the derivatives are taken over the four space-time coordinates.

The Einstein Field Equations are second order nonlinear partial differential equations; exact solutions do not exist for most cases. However, solutions can be derived after applying the principles of Sec. 2.2. For a homogeneous and isotropic universe with 4 space-time dimensions and a perfect fluid approximation for the stress-energy tensor, the solutions to Eq. (2.1) are known as the Friedmann equations (Sec. 2.3.4). The homogeneous and isotropic Robertson-Walker metric and the form of the stress-energy tensor are discussed below.

2.3.2 Robertson-Walker Metric

The Robertson-Walker metric provides a mathematical description of the universe in terms of four space-time coordinates. The metric allows calculations of distances and trajectories in the universe and describes the structure of space-time at every point in the space. Assuming a homogeneous and isotropic space simplifies the metric to be the same at each point, but allows variations in time. The Robertson-Walker metric is an approximation that is valid on large scales (> 1000 Mpc) where the matter in the universe is approximately homogeneous; the Earth and the Milky Way are overdense regions on a scale where the universe is obviously not homogeneous and this metric does not apply.

The Robertson-Walker metric is the simplest metric with three spatial and one

time dimension that is homogeneous and isotropic. The scale factor, $a(t)$, sets the length scale in the universe and is independent of position. $a(t)$ can evolve with time, but the evolution is uniform throughout the universe. The Robertson-Walker metric is given as

$$ds^2 = dt^2 - a^2(t) \left[\frac{dr^2}{1 - kr^2} + r^2 d\theta^2 + r^2 \sin^2 \theta d\phi^2 \right], \quad (2.2)$$

or in tensor notation

$$ds^2 = dt^2 - a(t)^2 dx^i dx^j \delta_{ij}, \quad (2.3)$$

where $a(t)$ is the cosmic scale factor and has units of length, and k determines the curvature of the space with $k = 0, 1, -1$ for flat, closed, and open geometries respectively. The coordinates r, θ, ϕ and t are co-moving coordinates chosen so that objects at rest in the co-moving frame remain at rest. The expansion and universal dynamics are determined by $a(t)$. The coordinate distance, defined as the instantaneous distance between 2 space-time points at time t , is $a(t)r$. This differs from the proper distance (following the definition from Kolb and Turner [1990])² between two co-moving points

$$d_{proper} = a(t) \int_0^{r_1} \frac{dr}{\sqrt{1 - kr^2}}, \quad (2.4)$$

which requires an integral over the co-moving coordinate r . The co-moving distance is Equation (2.4) divided by the scale factor. The co-moving distance is related to the scale factor by the geodesic equation, $ds^2 = 0$. Light traverses the universe on null geodesics with $ds^2 = 0$. Geodesics are lines of constant θ and ϕ and isotropy implies that we can set $d\theta = d\phi = 0$. Thus, for the Robertson-Walker metric

$$\frac{dt}{a(t)} = \frac{dr}{\sqrt{1 - kr^2}}. \quad (2.5)$$

Equation (2.5) defines the relationship between the distance, scale factor, and time in the Robertson-Walker metric. Cosmological measurements using the luminosity

²Weinberg [1972] defines proper distance without the factor of $a(t)$ in front of the integral. Kolb and Turner [1990] call that quantity the co-moving distance.

or angular diameter distance fit data to the solutions of (2.5). The solutions depend on the evolution of the scale factor, $a(t)$, which in turn depends on the total energy content of the universe, defined by the stress-energy tensor.

2.3.3 Stress Energy and Equation of State

The stress-energy tensor, sometimes called the energy-momentum tensor, describes the energy content of the universe. For a homogeneous and isotropic universe the tensor takes the perfect fluid form,

$$T^{\mu\nu} = (\rho + p)U^\mu U^\nu + p g^{\mu\nu}, \quad (2.6)$$

where U^μ is the velocity 4-vector and the metric signature is again $(+, -, -, -)$. The T^{00} component is the energy density and the pressure terms represent the momentum flux density. In simpler notation, the stress-energy tensor is just the diagonal tensor $T_{\mu\nu} = \text{diag}(\rho, -p, -p, -p)$ (recall that $c = 1$, energy and pressure units are equivalent).

2.3.4 Friedmann Equation

Following the development of General Relativity work began on finding solutions to the Einstein Field Equations to model the universe. Einstein, de Sitter, Lemaître, and Friedmann were all working on this difficult problem. Einstein and de Sitter explored static solutions to the field equations, while Friedmann [1922] derived a set of dynamic equations that describe an expanding universe. Lemaître [1927, 1931] independently derived the same solutions and expanded on Friedmann's work. The two independent Friedmann equations are

$$\frac{\dot{a}^2}{a^2} + \frac{k}{a^2} - \frac{\Lambda}{3} = \frac{8\pi G}{3} \rho \quad (2.7)$$

and

$$2\frac{\ddot{a}}{a} + \frac{\dot{a}^2}{a^2} + \frac{k}{a^2} = -8\pi G p. \quad (2.8)$$

The second equation is sometimes referred to as the acceleration equation. The Hubble parameter³, defined as $H(a) \equiv \dot{a}/a$, is often used in Eq. (2.7). The present day value of $H(a)$ is known as the Hubble constant, H_0 . The Hubble parameter contains all the information about the expansion of the universe; it depends on both the energy content and underlying metric. Changes to the Friedmann equation arise in higher dimensional theories and non-homogeneous cosmological models that change the expression for $H(a)$. These modifications to the Hubble parameter are discussed in Sec. 2.5, along with various dark energy models that modify the expansion.

An expression for the energy density is derived by differentiating Eq. (2.7) and eliminating \ddot{a} ,

$$\dot{\rho} = -3\frac{\dot{a}}{a}(\rho + p). \quad (2.9)$$

This is a statement of conservation of energy. The same expression can be derived from the First Law of Thermodynamics, $dE + pdV = d(\rho a^3) + p d(a^3) = 0$. Equation (2.9) also helps define the equation of state,

$$w \equiv \frac{p}{\rho}, \quad (2.10)$$

where all three quantities can vary with the scale factor, $a(t)$. For a constant w the solution to Eq. (2.9) is

$$\rho \propto a^{-3(1+w)}, \quad (2.11)$$

the evolution of the energy density as the universe expands. Ordinary matter is pressureless, with $w = 0$ and $\rho \propto a^{-3}$, radiation has $w = 1/3$ and $\rho \propto a^{-4}$, and a cosmological constant has $w = -1$, with $\rho \propto \text{constant}$. Other equations of state are possible, and many dark energy models include equations of state that vary with scale factor (and time). Different parameterizations of w and dark energy models are discussed in Sec. 2.4.1.

The density terms in the Friedmann equations are a sum over all the energy

³ $H(a)$ is sometimes referred to as the Hubble ‘constant.’ This work refers to H_0 as the Hubble constant, and calls $H(a)$ the Hubble parameter, since it can vary with time.

densities in the universe, and the total energy density determines the curvature. The critical density is defined such that the curvature, $k = 0$ in Eq. (2.7),

$$\rho_c = \frac{3H^2}{8\pi G}. \quad (2.12)$$

The symbol Ω is used to express the density in critical units, with $\Omega \equiv \rho/\rho_c$. For a universe with matter and a cosmological constant, the Friedmann equation can be expressed as

$$H(a)^2 = H_0^2 \left(\Omega_{M,0} a^{-3} + \Omega_{\Lambda,0} + \frac{k}{H_0^2 a^2} \right), \quad (2.13)$$

where the subscript 0 represents the present day value. The subscript will be dropped for the remainder of this discussion, and all Ω 's are assumed to be the present value unless otherwise stated. Evaluating this expression at the present epoch ($H(a) = H_0$ and $a(t_0) = 1$) defines the curvature density,

$$\Omega_k \equiv \frac{k}{H_0^2 a^2} = 1 - \Omega_M - \Omega_\Lambda, \quad (2.14)$$

in a universe dominated by matter and vacuum energy. The curvature is zero when the total density is one. More general forms for the dark energy are represented by replacing Ω_Λ with Ω_X and including the variation of the dark energy density with scale factor from Eq. (2.9).

2.3.5 Redshift

Redshift is defined by the total expansion from time t to t_1 . A photon with wavelength λ at time t will have wavelength λ_1 at some later time t_1 such that

$$\frac{\lambda_1}{\lambda} = \frac{a(t_1)}{a(t)} \equiv (1 + z). \quad (2.15)$$

By convention the present day scale factor $a(t_1) = 1$ and $a(t) = (1 + z)^{-1}$.

The meaning of the redshift can be tricky to interpret. Many people describe redshift as a Doppler shift of light due to the recession velocity of galaxies. This view is incorrect; the redshift is due to the expansion of space, not physical motion of the

galaxies. In the Doppler view, the maximum recession velocity is the speed of light, which is also incorrect. In General Relativity space can expand faster than the speed of light! In fact, in the standard cosmological model, galaxies at $z > 1.5$ are now receding faster than the speed of light [Lineweaver and Davis, 2005]. These galaxies are still observable because the light arriving today was emitted billions of years ago, when these galaxies were much closer and receding more slowly. If the expansion continues to accelerate, the light emitted by an object at $z > 1.5$ right now will never reach the earth, and a traveler or message from the earth can never reach this galaxy, even traveling at the speed of light.

It is important to keep these concepts in mind when thinking about redshift. Galaxies are approximately at rest in the universe⁴; the space between the galaxies is expanding. There is a small peculiar velocity for galaxies due to gravitational interactions that can be up to a few 1000 km/s in large clusters of galaxies. The measured redshift is a combination of the redshift due to expansion and the Doppler shift from the peculiar velocity through space. This accounts for the blueshift of light from Andromeda, which has a peculiar velocity pointed towards the Milky Way. The key point to keep in mind is that the cosmological redshift is due to the expansion of space, not the physical velocity of the galaxies through space.

2.3.6 Accelerated Expansion

The Friedmann equations provide the condition for accelerated expansion. Taking the difference of Equations (2.7) and (2.8) gives an expression for $\ddot{a}(t)$ in terms of the energy density and pressure,

$$\frac{\ddot{a}}{a} = -\frac{4\pi G}{3}(\rho + 3p). \quad (2.16)$$

The condition for acceleration is $p < -1/3\rho$, or in terms of the equation of state, $w < -1/3$. The well known constituents of the universe such as matter and radiation have $w = 0$ and $+1/3$ respectively, and cannot cause accelerated expansion. A new

⁴The CMB defines the universal restframe.

energy component must exist with $w < -1/3$ to account for the recently observed acceleration. This component is called dark energy.

In most dark energy models the energy density of the dark energy has only recently become comparable to the matter density. In these models the expansion of the universe only begins to accelerate when dark energy dominates the total energy density. At some point in the past, the universe was matter dominated, and the expansion was decelerating. Assuming a flat, Λ CDM cosmology, the condition for accelerated expansion is

$$\frac{\ddot{a}}{a} > -\frac{H_0^2}{2}(\Omega_M(1+z)^3 + \Omega_\Lambda - 3\Omega_\Lambda). \quad (2.17)$$

The transition between accelerated and decelerated expansion occurs at a redshift

$$z_t = 1 - \left(\frac{2\Omega_\Lambda}{\Omega_M}\right)^{1/3}. \quad (2.18)$$

For redshifts less than z_t the expansion is accelerating, but for z greater than z_t the universe is decelerating, and for $z \gg z_t$ the universe is matter dominated and the dark energy component can be ignored. For the concordance cosmology with $\Omega_M = 0.26$ and $\Omega_\Lambda = 0.74$, the transition redshift is $z_t = 0.78$. In this model, the transition to accelerated expansion occurs approximately 6.7 billion years ago, when the universe is about half its current age.

2.3.7 Curvature

The curvature of the universe plays a significant role in determining the ultimate fate of the cosmos. Curvature is related to the total energy density. The critical density, ρ_c , is defined such that when $\Omega_{total} \equiv \rho_{total}/\rho_c = 1$ the curvature is zero ($k = 0$ in Equation (2.2)), and the geometry of the universe is spatially flat (i.e. Euclidian). If the universe is over dense, $\Omega_{total} > 1$, the geometry is closed, analogous to the surface of a sphere in two dimensions. An open universe has negative curvature and is under dense, $\Omega_{total} < 1$; the geometry is similar to a saddle in two dimensions. In a matter dominated universe with no dark energy, the curvature determines the fate.

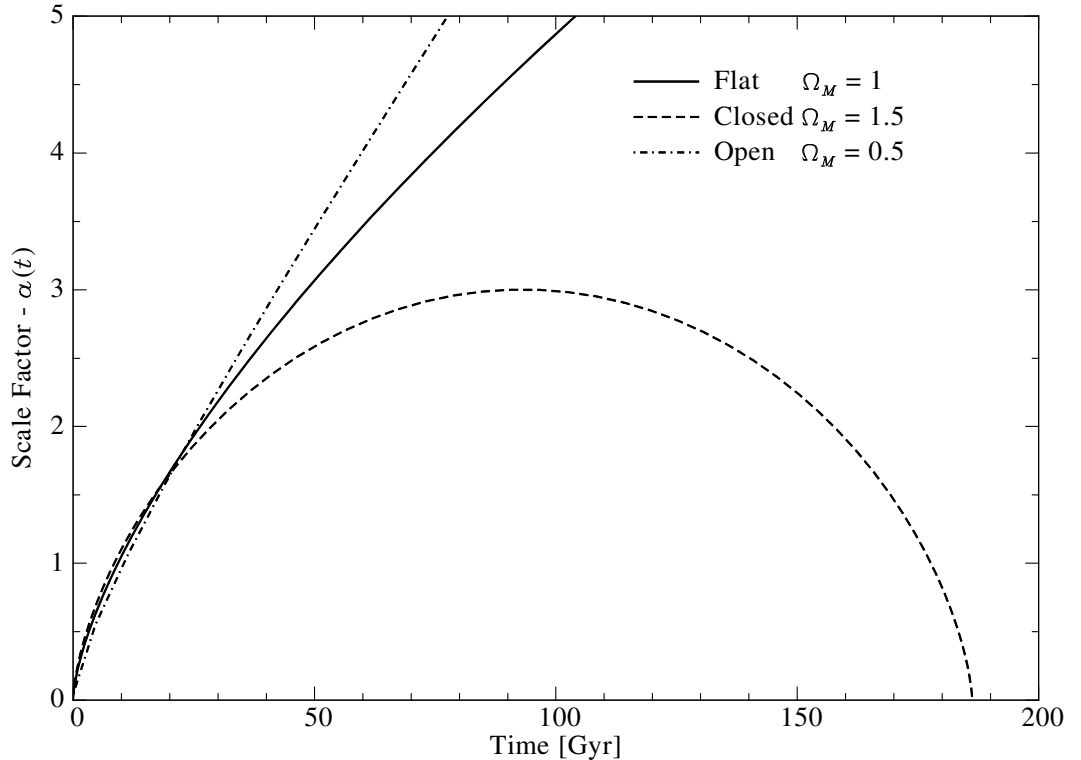


Figure 2.1. Scale factor vs. time in a flat (solid), closed (dashed) and open (dot dash) matter dominated universe with $H_0 = 70 \text{ km s}^{-1} \text{ Mpc}^{-1}$.

A closed universe will eventually re-collapse, an open universe expands forever, and a flat universe will coast asymptotically to rest. Figure 2.1 illustrates these three scenarios for the matter dominated case.

The presence of dark energy complicates the fate of the universe. For the cosmological constant model of dark energy, a closed universe can expand forever if the dark energy density is high enough. The negative pressure from the dark energy causes the expansion to accelerate at late times despite the positive spatial curvature. Some theories even allow a negative dark energy density. In these models a flat or open universe can re-collapse because the negative dark energy density is attractive, applying positive pressure and halting the expansion. Models with a negative dark energy density are strongly disfavored by all modern observations and are not considered in this work.

Current observational evidence favors a spatially flat universe. The CMB data

using the location of the first acoustic peak is the best direct measurement of the curvature, and results in a total density of $\Omega_{tot} = 1.02 \pm 0.02$ [Spergel et al., 2003]. This measurement is based on only the first year WMAP data. The analysis of the 3 year WMAP data [Spergel et al., 2006] assumes a spatially flat universe. Inflation predicts a flat universe; the CMB observations support this prediction.

2.4 Cosmological Parameters

The understanding of cosmology has progressed to the point where the large scale features of the universe can be described by a model cosmology with a relatively small number of parameters. A subset of these parameters which describe the energy content of the universe is listed in Table 2.1. H_0 measures the present day expansion rate and is related to the age of the universe. n_s is the scalar index describing the primordial density fluctuations that lead to anisotropy in the CMB. The next 3 parameters describe the matter, baryonic matter, and dark energy densities in critical units; the best fit values in the table all assume a spatially flat universe with $\Omega_{tot} = 1$; Ω_M and Ω_X are not independent. Note that the value of Ω_b depends on the Hubble constant. The final 2 parameters describe the dark energy equation of state, parameterized in terms of a time independent part, w_0 and a first order time dependence, w_a . There are a number of other common parameters that describe the universe. Some, such as the age, can be derived from the parameters in Table 2.1, while others, e.g. σ_8 (the RMS matter fluctuations in an 8 Mpc comoving volume), provide details about structure formation or astrophysical processes that are impacted by cosmology.

Five of the parameters in Table 2.1 can be constrained using measurements of type Ia supernovae; $H_0, \Omega_M, \Omega_X, w_0, w_a$. The other two parameters are included because of their relation to inflation and Big Bang Nucleosynthesis, two very important processes in the early universe. Many inflation models predict n_s slightly less than one. The current 3σ deviation from a flat, $n_s = 1$, primordial spectrum supports these inflationary models. The baryon density determines the light elements abundances from Big Bang Nucleosynthesis. The CMB observations give $\Omega_b \approx 0.044$, in excel-

| Symbol | WMAP - Λ CDM | WMAP - Constant w |
|--|---|---|
| $H_0 = 100 h \text{ km s}^{-1} \text{ Mpc}^{-1}$ | $73.5 \pm 3.2 \text{ km s}^{-1} \text{ Mpc}^{-1}$ | $66.1_{-8.8}^{+8.2} \text{ km s}^{-1} \text{ Mpc}^{-1}$ |
| n_s | 0.951 ± 0.016 | $0.946_{-0.17}^{+0.016}$ |
| Ω_M | 0.237 ± 0.034 | $0.306_{-0.081}^{+0.089}$ |
| $\Omega_b h^2$ | $0.02230_{-0.00073}^{+0.00075}$ | $0.02213_{-0.00072}^{+0.00073}$ |
| Ω_X | 0.763 ± 0.034 | $0.694_{-0.089}^{+0.081}$ |
| w_0 | -1 (fixed) | $-0.81_{-0.20}^{+0.22}$ |
| w_a | 0 (fixed) | 0 (fixed) |

Table 2.1. Table of cosmological parameters with best fit values. The final 2 columns contain the best fit values from WMAP year 3 data for a cosmological constant model of the dark energy (Λ CDM) and a constant equation of state model. All the data assume a flat universe, results from <http://www.rssd.esa.int/Planck/> and Spergel et al. [2006].

lent agreement with the value inferred from independent measurements of primordial deuterium, He^3 , He^4 , and Li^7 abundances.

The best fit values for six of the cosmology parameters are also shown in Table 2.1. Constraints for a cosmological constant or Λ CDM universe favor a low mass density compared to independent type Ia supernova results (Riess et al. [2004] report $\Omega_M = 0.29_{-0.03}^{+0.05}$ with $H_0 = 65 \text{ km s}^{-1} \text{ Mpc}^{-1}$). When w_0 is allowed to vary, the dark energy density can change with time, and the best fit value of Ω_M increases and its uncertainty more than doubles. Both of these fits assume a constant dark energy equation of state, $w_a = 0$. Allowing this parameter to vary increases the uncertainties on the density parameters. Many of the parameter constraints from cosmology measurements depend very strongly on the assumed model cosmology. Assuming a spatially flat Λ CDM universe allows the matter and dark energy densities to be tightly constrained. Some authors use these constraints as priors when fitting type Ia supernova data, even when changing the model to include constant values of w_0 other than -1 and non-zero values of w_a . Clearly the constraints on the matter and dark energy density change substantially when the model cosmology is not a cosmological constant. With that in mind, there is still a significant advantage to combining CMB data with type Ia supernovae and other cosmology probes, if the constraints are properly applied. For example, type Ia supernovae and WMAP year three data taken together give $\Omega_M = 0.273 \pm 0.027$ and $w_0 = -0.942 \pm 0.074$ for a

spatially flat constant w cosmology [Spergel et al., 2006]. Best fit parameter values and uncertainties for a number of cosmology models and different combinations of cosmology probes are available at <http://www.rssd.esa.int/Planck/>.

2.4.1 Dark Energy Equation of State

Understanding dark energy is one of the primary goals in cosmology today. A large number of experiments currently proposed are targeting dark energy through a variety of techniques, discussed in Sec. 2.6. There are an even larger number of dark energy models proposed to explain the cosmic acceleration. The models include: the cosmological constant; other constant equations of state, sometimes called quiescence; quintessence, a self interacting scalar field with a minimal coupling to gravity; Chaplygin gas, which acts like pressureless dust at early times and a cosmological constant at late times; and modifications to the Friedmann equation, common in brane world models, modified Newtonian dynamics and other higher dimensional theories. So far, none of the models is clearly preferred over the others, with the possible exception of the cosmological constant. To circumvent this problem, it is easiest to parameterize the dark energy in a general way that can approximate a large number of the models.

Dark energy is parameterized in terms of its equation of state, $w \equiv p/\rho$, the ratio of the pressure and energy density. The dark energy density varies with redshift according to the solution of Eq. (2.9). For an arbitrary equation of state, $w(z)$, the dark energy density is

$$\rho_{DE} = \rho_{DE,0} \exp \left[\int_0^z -3(1+w(z)) \frac{dz}{(1+z)} \right]. \quad (2.19)$$

The simplest parameterization assumes w is constant in time, and the density scales as $\rho \propto (1+z)^{-3(1+w)}$. There are two common parameterizations that introduce a first order time variation into the equation of state. Cooray and Huterer [1999] propose a linear variation with redshift,

$$w(z) = w_0 + w'z, \quad (2.20)$$

where $w' \equiv dw/dz(z = 0)$ is the time variation at the present epoch. The major shortcoming of this model for the equation of state is that the asymptotic behavior at high z gives unrealistic values for w . This parameterization of w cannot be used with CMB data, which extends to redshifts greater than 1000. An alternative parameterization which asymptotes to a constant w at high redshift is

$$w(a) = w_0 + w_a(1 - a) = w_0 + w_a \frac{z}{1 + z} \quad (2.21)$$

[Chevallier and Polarski, 2001, Linder, 2003]. This model easily accommodates high redshift and CMB data, and approximates slow roll (variations of order of the Hubble time) scalar field dark energy better than the linear parameterization. w_a can be defined as $w_a = -2 dw/d\ln a|_{z=1}$, since the dark energy begins to become important near this time. In this case, w_0 is the present day value of the equation of state. Other definitions of w_0 and w_a are discussed in Linder [2004]. The dark energy density in the w_a parameterization is

$$\rho_{DE} = \rho_{DE,0} (1 + z)^{-3(1+w_0+w_a)} e^{-3w_a z/(1+z)}. \quad (2.22)$$

This parameterization is often used in the literature and is the default parameterization in the SNAP simulation. This is also the parameterization used for fitting the dark energy equation of state in this work.

There are a number of different techniques to extract information about dark energy. Alternative equation of state parameterizations include work by Corasaniti and Copeland [2002] and a statefinder diagnostic from Alam et al. [2003]. In addition, Wang et al. [2004] explore the possibility of directly measuring the dark energy density, $\rho_X(z)$. Wang and Tegmark [2005] expand on this work and discuss methods to maximize information in the case of time varying dark energy. All of these independent analysis techniques can be applied to SNAP data to increase our understanding of dark energy.

2.5 Dark Energy Models

Current dark energy models, including the cosmological constant, suffer from two main problems. The first is the order of magnitude of the dark energy density. Calculating the value of a cosmological constant in quantum field theory, with the Planck mass ($M_p = \sqrt{\hbar c/G}$) and Planck length ($L_p = \sqrt{G\hbar/c^3}$) as the fundamental scales, yields an energy density that is about 120 orders of magnitude larger than the presently observed value [Weinberg, 1989]. The second issue deals with present day ratio of the dark energy and matter densities. For an unknown reason, $\rho_X/\rho_M \sim 1$ today, yet for most of the past $\rho_M \gg \rho_X$, and far in the future the dark energy density will be much greater than the matter density. This has been called the Nancy Kerrigan problem: “Why me? Why now? Why? Why? Why?” [Turner, 2001]. Sometimes the anthropic principle is invoked to resolve this issue. We observe the universe when the dark energy and matter densities are approximately equal because this time in the universe produces conditions favorable for human observers. Or, in a multi-verse view, there are many universes with various values of the cosmological constant and we happen to live in one with a value that allows for the formation of stars, planets, and people. This answer is not satisfactory for most scientists, so alternate models that can ‘naturally’ explain this coincidence are being explored.

Dark energy models can be grouped into a few categories. Some of the most popular models currently discussed in the literature are: constant w (including the cosmological constant), scalar fields, Chaplygin gas, and modified Friedmann equations. The apparent magnitude of a type Ia supernova is shown for a few of the proposed dark energy models in Fig. 2.2. For constant w or scalar field dark energy, the parameterized equation of state is useful to distinguish the models. If there is no time variation and $w = -1$, then the cosmological constant is clearly favored. If some time variation in $w(z)$ is observed, then solutions for the scalar field models become attractive. The equation of state, $w(z)$, does not uniquely determine the scalar field potential, but it is a useful design parameter when planning a dark energy mission.

Modifications to the Friedmann equation are more complicated. In this case, the

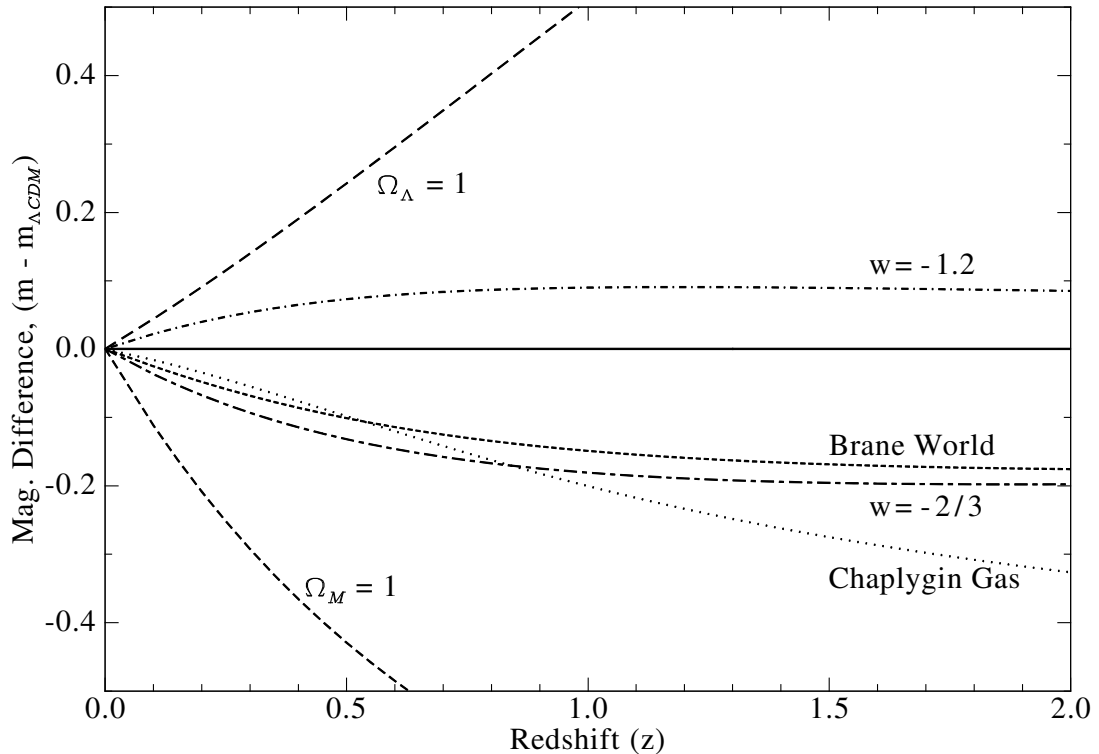


Figure 2.2. Apparent magnitude of a standard candle for many different dark energy models. All models assume a flat universe with $\Omega_{tot} = 1$ and data are plotted as the difference between each model and the concordance Λ CDM cosmology ($\Omega_M = 0.26, \Omega_\Lambda = 0.76$).

model used to calculate the luminosity distance is incorrect and the parameterized dark energy equation of state is being incorrectly interpreted. Constraints on the parameterized equation of state are used later in this work to demonstrate the accuracy achievable with the SNAP satellite. The equation of state is used during mission planning and will not necessarily be used in the final analysis of SNAP data. Theoretical advancements in the years before SNAP data are available could lead to changes in the current view of dark energy or new analysis procedures. Right now, w_0 and w_a are useful for their ability to approximate many of the models discussed below and to characterize time variation in the dark energy density or the equation of state itself.

2.5.1 Constant w

Dark energy models with a constant equation of state can either be a cosmological constant or some other form of energy with a fixed ratio of pressure to density. The theoretical effort dealing with the cosmological constant is focused on correctly calculating its value based on quantum gravity or some other fundamental physics theory. A great deal of work has gone into this problem with limited success thus far (see Padmanabhan [2006] and references therein for a review). For a proposal such as SNAP, the challenge is not to understand why the cosmological constant takes its present day value, but to determine if it is in fact constant. A measurable deviation from $w_0 = -1$ or $w_a = 0$ would be a sign of new physics beyond a cosmological constant, however it does not rule out the presence of vacuum energy in the universe. It is still possible to have a small cosmological constant component plus some scalar field or other dark energy giving an effective equation of state not equal to -1 [Linder, 2004].

Other constant w models include a network on non-interacting cosmic strings, with $w = -1/3$ or domain walls, with $w = -2/3$ (In general, networks of topological defects have $w = -N/3$ [Turner, 2001]). In constant w models, the Hubble parameter for a spatially flat universe is

$$H(z) = H_0 \left[\Omega_M(1+z)^3 + \Omega_X(1+z)^{3(1+w)} \right]^{1/2} \quad (2.23)$$

Cosmic strings do not produce accelerated expansion, inconsistent with current observations. Models with colliding domain walls produce acceleration with a measurable deviation from the cosmological constant model. A constant equation of state can also be produced using a properly tuned scalar field potential [Ureña-López and Matos, 2000].

2.5.2 Scalar Field

Scalar field models of dark energy generally invoke a time varying vacuum energy in an attempt to naturally explain the present value of ρ_X . They assume that a scalar

field ϕ and some potential $V(\phi)$ can explain the accelerated expansion of the universe. The Lagrangian for quintessence [Peebles and Ratra, 1988, Steinhardt et al., 1999] dark energy models is defined as

$$\frac{1}{2}\partial_a\phi\partial^a\phi - V(\phi), \quad (2.24)$$

and the dark energy equation of state is

$$w_\phi \equiv \frac{p_\phi}{\rho_\phi} = \frac{\frac{1}{2}\dot{\phi}^2 - V(\phi)}{\frac{1}{2}\dot{\phi}^2 + V(\phi)}. \quad (2.25)$$

Assuming the total density is one, the Hubble parameter evolves as

$$H(z) = \sqrt{\frac{8\pi G}{3}} \left[\rho_{M,0}(1+z)^3 + \frac{1}{2}\dot{\phi}^2 + V(\phi) \right]^{1/2}. \quad (2.26)$$

A number of different quintessence potentials have been proposed. One class of potentials involves pure exponential potentials of the form $V(\phi) \propto e^\phi$ [Ferreira and Joyce, 1998, Barreiro et al., 2000]. In these models the energy density of the scalar field mimics the dominant energy density component in an effort to explain the similarity between the matter and dark energy densities. The disadvantage of these models is that nucleosynthesis requires $\Omega_\phi < 0.2$ [Ferreira and Joyce, 1998], inconsistent with current measurements. Another set of potentials in which the matter and dark energy densities are nearly equal are known as tracker solutions [Steinhardt et al., 1999, Zlatev et al., 1999]. Unlike the pure exponential potentials, the late time behavior is very insensitive to the initial conditions. One example of this type of tracker solution is a power law potential, $V(\phi) = \phi^{-\alpha}$ [Steinhardt et al., 1999, Peebles and Ratra, 1988]. These potentials require less fine tuning to reproduce the measured densities; however, the predicted equation of state is not in agreement with current data.

Scalar field dark energy models are not considered in detail in this work. One reason for this is that the quintessence Lagrangian is not the only allowable Lagrangian

for a scalar field dark energy. A tachyon potential of the form

$$L_{tach} = -V(\phi)\sqrt{1 - \partial_a\phi\partial^a\phi} \quad (2.27)$$

is one other possibility that arises in some string theories [Sen, 2002]. This adds some complexity to the scalar field models. The Lagrangian must be known before the equation of state and thus the evolution of the Hubble parameter can be derived. In fact, if $H(z)$ and $\rho(z)$ for the non-dark energy components are known, exact solutions for the scalar field, ϕ , and the potential, $V(\phi)$ can be derived for both Lagrangians [Padmanabhan, 2006]; the solution for the potential is not unique. This makes designing a mission to measure scalar field dark energy very difficult. The important observable for determining if a scalar field dark energy is possible is time evolution of the dark energy density, which is well measured by the equation of state and the parameters w_0 and w_a .

2.5.3 Chaplygin Gas

Chaplygin gas is a form of dark energy which appears like ordinary matter at high redshift and a cosmological constant at late times [Kamenshchik et al., 2001, Bilić et al., 2002]. This model tries to explain the transition from an apparently matter dominated to cosmological constant dominated universe with a single energy component. The Chaplygin gas equation of state has $p_c = -A/\rho_c$; the energy density is given as

$$\rho_c = \sqrt{A + B(1+z)^6}. \quad (2.28)$$

At high redshift the second term dominates and the Chaplygin gas density behaves like matter, but at late times the first term dominates and the energy density is constant. The two Chaplygin gas parameters, A and B , can be defined in terms of a single parameter, κ , which is the ratio of the cold dark matter and Chaplygin gas energy densities at the start of the matter dominated phase in the universe. For a

spatially flat universe, the evolution of the Hubble parameter is

$$H(z) = H_0 \left[\Omega_M(1+z)^3 + \frac{\Omega_M}{\kappa} \sqrt{\kappa^2 \left(\frac{1-\Omega_M}{\Omega_M} \right)^2 - 1 + (1+z)^6} \right]^{1/2}. \quad (2.29)$$

Commonly used values of κ in the literature are $\kappa = 1 - 2$ [Alam et al., 2003].

The Chaplygin gas equation of state is motivated by string theory. In some parameterizations, a d -brane configuration leads to an equation of state with $p = -A/\rho$ [Colistete et al., 2002]. Despite its convenient feature of combining the dark energy and dark matter into a single fluid, Chaplygin gas is not well supported as a dark energy theory because it alters structure formation in ways that appear inconsistent with existing data [Sandvik et al., 2004].

2.5.4 Modified Friedmann Equations

Another possible explanation for the observed expansion of the universe is that the model, in this case the Friedmann equation, is incorrect. Milgrom [1983] proposed a modification to Newtonian dynamics on large scales, now known as MOND. Relativistic MOND theories now exist which modify gravity and thus General Relativity on large scales. Many authors claim that MOND is inconsistent with existing observations, most recently citing data from the bullet cluster as an example [Clowe et al., 2006]. MOND supporters answer the criticisms [Angus et al., 2006], but the validity of MOND theories remains widely questioned.

Modifications to the Friedmann Equation also arise from higher dimensional theories (more than the nominal 3 space + 1 time). Chung and Freese [2000] showed that the expansion can be modified to include terms that scale as the density to powers other than one. One possibility is Cardassian expansion [Freese and Lewis, 2002], where

$$H(z) = A\rho + B\rho^n \quad (2.30)$$

and there is no cosmological constant or dark energy. If $n < 2/3$ the ordinary matter will cause the expansion to accelerate at late times when the ρ^n term dominates the

expansion. This is only one possibility for Cardassian expansion. In general, the correction to the Friedmann equation can be an arbitrary function of the density.

A subclass of higher dimensional theories, known as brane world cosmology models, posit that the negative pressure we call dark energy is due to extra spatial dimensions [Sahni and Shtanov, 2003, Deffayet et al., 2002]. The 4-dimensional universe we observe is embedded in a higher dimensional bulk where only gravity can propagate. Some brane world models can be approximated by a time varying equation of state. Linder [2004] show that the brane world model considered in their work could be reproduced with a magnitude error of less than 0.01 for $z < 2$ using an effective equation of state with $w_0 = -0.78$ and $w_a = 0.32$. This model has a similar expansion history to the cosmological constant, despite very different physics. This model is revisited in Ch. 6 when assessing uncertainties on the dark energy equation of state for SNAP.

Another possibility which does not include any dark energy was recently proposed by Kolb et al. [2005b,a]. In this model the inhomogeneities in the matter distribution modify the expansion. The Friedmann equations assume a uniform matter distribution; accounting for the inhomogeneities could explain the observed behavior in the universe. This is a controversial idea, and counter arguments have been proposed in which inhomogeneity does not cause accelerated expansion [Hirata and Seljak, 2005].

Modified Friedmann equation models are attractive because they attempt to explain the expansion without the addition of a new energy component or a yet to be defined scalar field. Unfortunately, these models are difficult to account for in the mission planning stage. The mission goal must be to measure the expansion history as accurately as possible. A recent statement from the Dark Energy Task Force (DETF)⁵ supports this goal [Albrecht et al., 2006]:

“Whether general relativity is incorrect or the Universe is filled with an unanticipated form of energy, exploration of the acceleration of the Universe’s expansion will profoundly change our understanding of the composition and nature of the Universe.”

⁵The DETF was formed by NASA, NSF, and DOE to assess the current and future prospects for constraining the nature of dark energy.

With this in mind it is clear that the w_0, w_a parameterization of dark energy is suitable during the design phase as it describes how the expansion evolves and can be used to determine the transition between accelerated and decelerated expansion. The wealth of data that result from a mission like SNAP can then be used to fit any dark energy model or modification to General Relativity; the current stage is focused on ensuring that the data are of the highest possible fidelity.

2.6 Cosmological Probes

The dynamics of the universe on large scales depends on the total energy content and the interactions among the energy components. In the standard cosmological model, the Friedmann equation gives the expansion rate (Hubble parameter) as a function of redshift,

$$H(z) = \sqrt{\frac{8\pi G}{3}} \left[\sum_i \rho_i + \frac{k}{a^2} \right]^{1/2}, \quad (2.31)$$

where the sum over the density components includes matter, radiation, dark energy, etc. As discussed above, the Friedmann equation may be modified due to changes in gravity on large scales or the presence of large extra dimensions, which can add additional terms to $H(z)$. Measurements of $H(z)$ provide direct information about the energy content in the universe and allow constraints to be placed on the cosmological parameters from Sec. 2.4. Understanding cosmology begins with understanding the evolution of the Hubble parameter by measuring $H(z)$.

The cosmological ‘observables’ used to constrain $H(z)$ are: the age of the universe, distance measurements (angular diameter or luminosity distance), and the linear growth factor. The age of the universe at redshift z is given as

$$t(z) = \int_z^\infty \frac{dz'}{(1+z')H(z')}. \quad (2.32)$$

The Hubble parameter enters the age expression in a similar fashion to the angular diameter and luminosity distances. Unfortunately, direct measurements of the age as a function of redshift are extremely difficult and cannot compete with the accuracy

of the two distance measurements. There are no major projects planned to constrain cosmology using age measurements.

The measurements used to constrain the distance and linear growth factor utilize type Ia supernovae, weak lensing, baryon acoustic oscillations, and cluster abundances. Each of these methods for determining $H(z)$ depends on different combinations of the distance and/or growth factor, and has different systematic uncertainties associated with it. The SNAP deep and wide surveys are optimized for type Ia supernovae and weak lensing, respectively. These two probes provide complementary constraints on the dark energy parameters and represent the best method to attack the dark energy problem at this time. Future missions will use all four techniques to constrain the energy content of the universe and determine the nature of dark energy.

2.6.1 Type Ia supernovae - Direct Distance Measurements

The angular diameter and luminosity distance depend on the comoving distance, $d(z)$, which requires an integral of $H(z)^{-1}$. In a flat universe

$$d(z) \propto \int_0^z \frac{dz'}{H(z')}; \quad (2.33)$$

the angular diameter distance is $d_A = d(z)/(1+z)$ and the luminosity distance is $d_L = d(z)(1+z)$. In curved space, the expression in Eq. (2.33) has an additional *sin* or *sinh* term depending on the sign of the curvature (see Sec. 3.1.1 for details).

Measuring the luminosity distance requires very bright ‘standard candles,’ objects with well known absolute brightness. Type Ia supernovae are the leading candidate for a standard candle to probe cosmology due to their uniformity and brightness. One advantage of type Ia supernovae is that the observables, flux and redshift, are straightforward to measure. A number of empirically derived relationships between peak brightness and color, lightcurve width, and spectral features provide strong evidence for the effectiveness of type Ia supernovae as a standardizable candle. The main disadvantage is the rarity of type Ia events. Large portions of the sky must be monitored over the course of many months, and follow up spectroscopy needs to be

quickly scheduled to observe the spectrum near peak brightness. Further details on deriving cosmological constraints from type Ia supernova data are discussed in Ch. 3.

The other three probes are also sensitive to the distance measurements, through the angular diameter distance or the co-moving volume element. None of these methods is as well tested as type Ia supernovae, however the large datasets available from wide field lensing or galaxy surveys could result in these methods providing comparable constraints to type Ia supernovae in the near future.

2.6.2 Weak Lensing

Photons from distance sources are deflected by inhomogeneities in the mass distribution along the line of sight; this effect is known as gravitational lensing [Einstein, 1936]. The consequence of gravitational lensing is that the light from distance galaxies is (de)magnified and distorted as it propagates through the universe. Lensing is classified as strong or weak. Strong lensing occurs when a background galaxy is near a very dense object, e.g. a massive cluster, and the light travels on multiple paths to the observer. Strong lensing produces multiple images of a galaxy, and can stretch the galaxy images into arcs around the lens. Strong lensing is rare; more often, galaxy shapes undergo a small distortion (of order 1% [Refregier, 2003]), due to weak gravitational lensing. Measurements of the weak lensing distortion provide detailed information about the mass distribution and the power spectrum of density perturbations, which depend on the underlying cosmology and energy components in the universe.

Distortions of galaxy shapes are characterized by a shear, γ , and a convergence, κ . The shear measures the anisotropic changes in the galaxy shape, and the convergence describes dilation and contraction. These parameters define a shear matrix, given as

$$\Psi_{ij} \equiv \frac{\partial(\delta\theta_i)}{\partial\theta_j} \equiv \begin{pmatrix} \kappa + \gamma_1 & \gamma_2 \\ \gamma_2 & \kappa - \gamma_1 \end{pmatrix}, \quad (2.34)$$

where $\partial(\delta\theta_i)$ is the angular offset of an object at position θ [Schneider et al., 1992, Jain et al., 2000]. Ψ_{ij} is the distortion, which can be measured if the intrinsic galaxy shape

is known. Unlensed galaxies are expected to have random shapes and orientations on the sky. By averaging over measurements of many galaxies and cross-correlating on large scales, the small shear signal can be detected. Galaxy shapes are measured by an ellipticity, ϵ_{obs} , derived from the moments of the surface brightness [Kaiser et al., 1995], or more recently using shapelet decomposition [Bernstein and Jarvis, 2002, Refregier and Bacon, 2003]. Accurate shape measurements are essential for detecting the shear signal in weak lensing surveys.

Weak lensing measurements provide a map of the matter distribution by measuring the redshifts and shapes of a large number of background galaxies (see Hoekstra et al. [2002], Refregier [2003] and references therein). The measurements assume that there is no preferential alignment of the galaxies and require multi-color wide-field imaging to collect a large sample of galaxies and calculate photometric redshifts. Weak lensing data are used to measure the power spectrum of density perturbations, which depends on the linear growth factor, $D_1(z)$. The linear growth factor is the solution to the differential equation

$$\ddot{D}_1 + 2H(z)\dot{D}_1 - \frac{3}{2}\Omega_M H_0^2(1+z)^3 D_1 = 0 \quad (2.35)$$

[Padmanabhan, 1993]. The growth factor depends on the matter and dark energy content in the universe through its dependence on $H(z)$. Measurements of $D_1(z)$ have a much different dependence on the Hubble parameter compared to distance measurements, which provides complementary constraints that can break parameter degeneracies.

Lensing data are used to probe cosmology in a number of ways. In cosmic shear measurements, dark matter is responsible for the observed lensing signal. Shear measurements provide information about the dark matter power spectrum and the growth factor, $D_1(z)$. The skewness from lensing measurements probes small scales (< 10 arc-min) where the power spectrum is highly non-linear [Hui, 1999]. A new technique, known as cross correlation cosmography [Bernstein and Jain, 2004], provides a purely geometrical measure of angular diameter distance, which complements

the power spectrum data.

Weak lensing measurements require very accurate shape measurements over large regions of the sky. A number of systematic effects can lead to a false detection of a cosmic shear signal. Most of the uncertainty comes from variations in the point spread function (PSF) due to changing atmospheric conditions (seeing), thermal instability of the telescope assembly, or charge transfer efficiency degradation in CCDs. For every exposure the PSF must be calibrated and deconvolved from the image at each point in the focal plane. Ground based instruments attempt to control the PSF stability using adaptive optics systems to account for variations in the atmosphere. One of the main advantages of a space based platform such as SNAP is the stability of the PSF. Catastrophic failures and systematic bias in photometric redshift estimation are another source of systematic uncertainty. The SNAP NIR bandpasses provide information for photometric redshift calibration that can greatly reduce the number of catastrophic failures and bias. Refregier et al. [2004] estimate the cosmological constraints using simulated weak lensing data for the SNAP wide survey. After accounting for all systematic errors they find an uncertainty of 1.5% for Ω_M and 12% for w_0 , comparable to the SNAP supernova constraints and orthogonal in the Ω_M, w_0 plane. These constraints are consistent with the findings of the DETF [Albrecht et al., 2006].

2.6.3 Baryon Acoustic Oscillation and Cluster Abundances

Two new techniques with the potential to improve cosmological constraints are baryon acoustic oscillations and galaxy cluster abundances. The presence of baryons creates oscillations in the matter power spectrum. These oscillations have recently been observed in large galaxy redshift surveys [Eisenstein et al., 2005, Cole et al., 2005]. Baryon oscillation surveys measure both the Hubble parameter and angular diameter distance using the length scale of the oscillations as a standard ruler. The physical scale of the oscillations depends on the matter and baryon densities, which are available from CMB measurements. The observed scale of these oscillations depends on the dark energy and matter content in the universe through the angular diameter

distance.

Baryon acoustic oscillation measurements are just beginning to be used for cosmology and face many challenges. In addition to the strong dependence on the CMB measurements of the matter and baryon density, there are a number of systematic effects due to nonlinear coupling of Fourier modes and nonlinear growth, bias, and redshift distortions that can obscure the baryon oscillation signal. Seo and Eisenstein [2005] address some of the systematic uncertainties for future redshift surveys.

Measurements of galaxy clusters attempt to measure the cluster mass function $dN(M)/dV/dz$. The mass function depends on both the linear growth factor, $D_1(z)$, and the comoving volume, $dV \propto d(z)^2/H(z)$. At high redshift, the change in the volume is small and the cluster measurements are most sensitive to the growth factor. At later times, the growth of structure slows and the volume increases quickly, providing a more geometric measurement using clustering data. Bahcall et al. [2003] use the cluster mass function from the Sloan Digital Sky survey to constrain $\Omega_M = 0.19^{+0.08}_{-0.07}$, using only 300 optically selected clusters. New optical cluster searches have now produced catalogs with more than 10^4 cluster up to $z = 0.3$ [Koester et al., 2006]; cosmology constraints using this new dataset are now in progress [Roza et al., 2006].

The main challenge for determining the cluster mass function is calibrating the cluster mass against the observable cluster properties. For optical clusters, the mass can be inferred from the cluster luminosity within a fixed radius and cross-checked using the velocity dispersion of the cluster members. Cosmology constraints are derived by comparing the measured data to large cosmology simulations or theoretical/semi-analytic Press-Schechter predictions [Press and Schechter, 1974] (only valid in the linear regime). Cluster searches in the X-ray and radio can also be used to measure the mass function. Measurements of X-ray detected clusters attempt to relate the virial mass to the temperature. Radio clusters are detected by the Sunyaev-Zeldovich effect. In clusters of galaxies, free electrons in the hot inter-cluster medium up scatter approximately 1% of the CMB photons via inverse Compton scattering. This creates a small deficit of low energy CMB photons that is observable with radio telescopes. The advantage of Sunyaev-Zeldovich cluster detection is that the effect is nearly in-

dependent of redshift, which should lead to a much more complete sample of galaxy clusters. Optical and X-ray cluster surveys are limited to only the brightest clusters at high redshift; careful modeling of the selection function is needed to understand the cosmological implications from the observed clusters. A Sunyaev-Zeldovich signal has been observed for known clusters, but no new clusters have been found with this technique to date.

A number of experiments have been proposed to measure $H(z)$ using different combinations of type Ia supernovae, weak lensing, baryon acoustic oscillations and galaxy clusters. There are a few ongoing projects, such as the Sloan Digital Sky Survey, WMAP and various type Ia supernovae searches, which provide the current constraints that favor the ‘concordance’ cosmology. These projects will not lead to significant increases in our knowledge of cosmology, but help to increase understanding of systematic uncertainties and refine measurement techniques for future experiments. Midterm experiments (stage III in the language of the DETF, expected to provide a factor of 3 improvement in the joint constraint on w_0 and w_a) will provide some additional cosmological constraints, but their main power will be in expanding datasets and refining analysis techniques in preparation for next generation cosmology probes, such as SNAP. These next generation experiments (DETF stage IV, expected to provide a factor of 10 improvement in the joint constraint on w_0 and w_a) will use new technologies, and in some cases space based platforms, to increase both the precision and quantity of data for type Ia supernovae, weak lensing, cluster counts, and baryon acoustic oscillations. Combining measurements from two or more of these techniques, in particular type Ia supernovae and weak lensing, leads to much tighter cosmological constraints than any one measurement (see Sec. 6.2). In addition, using both a distance and growth of structure measurement helps guard against systematic errors that may not be apparent when using a single technique.

2.7 The Magnitude System

The brightness of astronomical objects is typically measured in magnitudes instead of flux units. The magnitude scale is a logarithmic brightness scale introduced by

Pogson [1857]. The logarithmic response is similar to the response of the human eye, the first photon detector used for astronomy. Pogson established the scale of the magnitude system by defining a 1st magnitude star as 100 times brighter than a 6th magnitude star, so that the magnitude is given as

$$m_x = -2.5 \log_{10} \frac{F_x}{F_{\text{vega},x}} = -2.5 \log_{10} F_x + C \quad (2.36)$$

where x is the bandpass. The Vega magnitude is constant in each bandpass, and represents the zero-point for the magnitude system. Aller et al. [1982] gives the value of C for most common magnitude systems.

A convenient feature of the magnitude system is that for small magnitude errors ($\sim < 0.1$), the magnitude error is roughly equal to the percent error on the flux. A magnitude error of $\Delta m = 0.01$ corresponds to a 1% uncertainty on the flux.

The bandpass for astronomical measurements are often based on the Johnson-Cousins UBVRI system introduced by Johnson and Morgan [1953], then extended by Cousins [1974a,b]. Many modern instruments use colored glass filters defined by Bessell [1990], which approximate the Johnson-Cousins passbands. Most type Ia supernova measurements are based on the restframe B and V band luminosity, which is well studied for nearby type Ias. High redshift supernovae are observed through longer wavelength filters then K-corrected [Humason et al., 1956, Oke and Sandage, 1968] to estimate the B or V band magnitudes.

2.8 Further Reading

There are a number of textbooks that offer a more in depth treatment of General Relativity, cosmology and astrophysics. A few helpful resources are:

General Relativity

- Schutz [1985], *A first course in general relativity*
- Weinberg [1972], *Gravitation and Cosmology: Principles and Applications of the General Theory of Relativity*

Cosmology

- Ryden [2003], *Introduction to cosmology*
- Kolb and Turner [1990], *The Early Universe*
- Peebles [1993], *Principles of physical cosmology*
- Peacock [1999], *Cosmological Physics*

Astrophysics/Large scale structure

- Peebles [1980], *The large-scale structure of the universe*
- Padmanabhan [1993], *Structure Formation in the Universe*
- Clayton [1983], *Principles of Stellar Evolution and Nucleosynthesis*

CHAPTER 3

Cosmology with Standard Candles

Edwin Hubble first observed the expansion of the universe in 1929 [Hubble, 1929]. He used measurements of the flux from variable stars like Cepheid variables and novae to estimate the distance to 24 extra-galactic nebulae. The redshift of spectral lines for these objects measures an apparent recession velocity. Hubble found a linear relation between velocity and distance in the local universe known as Hubble's law, $v = H_0 d$. The present day Hubble constant, H_0 , is an important cosmological parameter; it determines both the distance scale and age of the universe. Hubble's initial estimate of H_0 was plagued by systematic uncertainties in the distance measurement, but his methodology for measuring expansion is still used today.

Freedman et al. [2001] have constrained H_0 to $72 \pm 8 \text{ km s}^{-1} \text{ Mpc}^{-1}$ (including systematic errors) using Cepheid variables to calibrate the absolute luminosity of a number of other independent distance indicators, e.g. type Ia supernovae, the Tully-Fisher relation, and type II supernovae. Measurements of H_0 by Freedman et al. focus on the nearby universe, covering distances from 60 – 400 Mpc, where the linear Hubble law holds. Cosmology measurements of the matter and dark energy density require observations over much larger distances. For distances greater than about 400 Mpc, the linear approximation of the distance-redshift relation no longer holds, and distances are calculated in the framework of General Relativity.

Measuring the absolute distance to astronomical objects is a difficult task. The Hubble Key Project was a multi-year project designed to measure H_0 with a systematic uncertainty of 10% [Freedman et al., 2001]. Understanding the systematic errors in the absolute distance calibration is one of the biggest challenges. Fortunately, many cosmology measurements only require relative distance measurements. When

observing type Ia supernovae, different values of H_0 add a constant offset to the absolute magnitude. H_0 is treated as a nuisance parameter that is marginalized over to yield constraints on the dark energy density and equation of state¹. The ability to constrain cosmology with relative distance measurements independent of H_0 is one of the strengths of the standard candle method.

3.1 Luminosity Distance

Standard candles are objects of known absolute brightness. The observed flux from one of these objects is a straightforward measure of the distance to the object, or the look-back time to the epoch when the light was emitted. The observed flux is defined as

$$F = \frac{L}{4\pi d_L^2}, \quad (3.1)$$

which introduces the luminosity distance, d_L . L is the absolute source luminosity (restframe energy per unit time) and F is the observed flux. The luminosity distance depends on the scale factor, the comoving distance to the source, and the redshift, with

$$d_L^2 = a^2(t_0) r_1^2(t_1) (1+z)^2 \quad (3.2)$$

for a detector at comoving coordinate $(r, t) = (0, t_0)$. The $a(t_0) r_1$ term represents the proper distance to the source. The 2 factors of $(1+z)$ come from time dilation and redshift of the source photons. The incident energy from the source is redshifted by $(1+z)$ and the arrival time of the photons at the detector is delayed by $(1+z)$ compared to their restframe emission. The solution for $r_1(t_1)$ depends on the energy content and the geometry of the universe.

3.1.1 Derivation

A derivation of the luminosity distance for the Robertson-Walker metric with arbitrary curvature is given below. The energy density of the universe in this example is

¹Marginalization integrates over all possible values of a parameter to produce constraints on the remaining parameters independent of the nuisance parameter.

dominated by matter and dark energy, however the general form used for the dark energy density can be generalized to represent radiation or any other energy component. Radiation can be neglected from the present day back to $z \sim 1000$, when the radiation density becomes comparable to the matter density. The dark energy equation of state is defined as $w(z) = w_0 + w_a z/(1+z)$ [Chevallier and Polarski, 2001, Linder, 2003]. Specific solutions for a cosmological constant, $w = -1$, or constant w ($w_a = 0$), simplify the final expression for $d_L(z)$ given in Equation (3.7).

The luminosity distance depends on the co-moving distance between the observer, at $r = 0, t = 0$, and the source at position (r_1, t_1) . The geodesic equation, Eq. (2.5), relates the co-moving distance to the scale factor and time. Integrating the right hand side of (2.5) for flat, closed, and open geometries gives

$$\int_0^{r_1} \frac{dr}{\sqrt{1 - kr^2}} = \begin{cases} r_1 & \text{if } k = 0, \\ \frac{1}{\sqrt{k}} \sin^{-1} r_1 \sqrt{k} & \text{if } k > 0, \\ \frac{1}{\sqrt{-k}} \sinh^{-1} r_1 \sqrt{-k} & \text{if } k < 0. \end{cases} \quad (3.3)$$

Solving for the comoving distance,

$$r_1(z) = \frac{1}{\sqrt{|k|}} \times \mathcal{S} \left\{ \sqrt{|k|} \int_0^{t_1} \frac{dt}{a(t)} \right\} = \frac{1}{H_0 \sqrt{|\Omega_k|}} \times \mathcal{S} \left\{ H_0 \sqrt{|\Omega_k|} \int_0^z \frac{dz}{H(z)} \right\}, \quad (3.4)$$

where k is the curvature from Eq. (2.7) ($k = \Omega_k H_0^2$ from the definition of the curvature density²). \mathcal{S} depends on the curvature, with $\mathcal{S}(x) =: x$ for a flat geometry, $\sin(x)$ for closed geometries, and $\sinh(x)$ for open geometries. In a flat geometry, the two factors of $\sqrt{|\Omega_k|}$ cancel to avoid dividing by zero.

The solution for $H(z)$ requires an understanding of the interactions of the fundamental energy fields from General Relativity, which is contained in the Friedmann equation,

$$H^2 \equiv \frac{\dot{a}^2}{a^2} = \frac{8\pi G}{3} \sum \rho_i - \frac{k}{a^2}. \quad (3.5)$$

²Perlmutter et al. [1997] use κ to denote Ω_k . This should not be confused with k in expression (3.4), which is the curvature from the Friedmann equation.

The different energy components are represented by ρ_i , and include matter and dark energy for this example. The cosmological constant is equivalent to a constant energy density, so the Λ term in Equation (2.7) can be replaced by an equivalent energy density, ρ_Λ . The matter density is proportional to $a(t)^{-3}$ and the dark energy density scales as

$$\begin{aligned}\rho_X &= \rho_{X,0} e(z; w_0, w_a) \\ e(z; w_0, w_a) &= \exp \left[3 \int_0^z \frac{(1 + w(z))}{1 + z} dz \right] \\ w(z) &= w_0 + w_a \frac{z}{1 + z},\end{aligned}$$

where the subscript 0 represents the present day value, and X is used to denote arbitrary dark energy (when specifically referring the the cosmological constant model for dark energy Ω_X is replaced by Ω_Λ). The present day value of the critical density is $\rho_c = \frac{3H_0^2}{8\pi G}$. Rewriting the energy densities in terms in critical units, symbolized by Ω_i , the Friedmann equation becomes

$$H(z)^2 = H_0^2 \left[\Omega_m(1+z)^3 + \Omega_X e(z; w_0, w_a) - \Omega_k(1+z)^2 \right], \quad (3.6)$$

using the scale factor-redshift relation, $a(t) = (1+z)^{-1}$. All Ω 's represent the present day value; the subscript 0 is dropped for the remainder of the discussion. The curvature density, $\Omega_k = \frac{k}{H_0^2} \equiv 1 - \Omega_m - \Omega_X$, is zero for a flat universe.

Pulling everything together, the luminosity distance is

$$\begin{aligned}d_L(z; \Omega_m, \Omega_{de}, H_0, w_0, w_a) &= \frac{c(1+z)}{\sqrt{\Omega_k} H_0} \times \\ &\mathcal{S} \left\{ \sqrt{\Omega_k} \int_0^z \frac{dz}{[\Omega_m(1+z)^3 + \Omega_k(1+z)^2 + \Omega_X e(z; w_0, w_a)]^{1/2}} \right\}.\end{aligned} \quad (3.7)$$

Equation (3.7) is the key expression for constraining cosmology parameters with standard candles in a standard Friedmann-Robertson-Walker cosmology. For type Ia supernovae, the luminosity distance predicts the observed flux for an object with

known absolute luminosity at redshift z . This expression is used to fit the cosmology parameters H_0 , Ω_m , Ω_X , w_0 , w_a , or some subset of these parameters, depending on prior constraints. The arbitrary dark energy equation of state with a time dependent term can approximate many dark energy models. Solutions for the luminosity distance in higher dimensional theories with modified Friedmann equations are derived by following the same procedure, with the appropriate expression for $H(z)$ (see Sec. 2.5).

Extending Eq. (3.7) to include additional energy density terms, e.g. radiation, is trivial. Radiation has an equation of state $w = 1/3$; the density scales as a^{-4} . Replacing Ω_X with Ω_R and solving for $e(z; w_0, w') = (1+z)^4$ gives the solution for a universe dominated by matter plus radiation with arbitrary curvature.

3.2 Distance Modulus

The observed flux is related to the absolute luminosity by the inverse square law and the luminosity distance, as given by Eq. (3.1). The flux and luminosity depend on the bandpass or filter the object is measured through, and the spectrum of the supernova. For historical reasons, astronomers measure brightness in magnitudes rather than flux units (see Sec. 2.7). For type Ia supernovae, the absolute magnitude, M_x , is defined as the magnitude of an object observed at a distance of 10 pc in filter x ,

$$M_x = -2.5 \log_{10} F_x(10\text{pc}) + C. \quad (3.8)$$

The constant C is defined by the flux of a standard source, such as the star Vega. This makes magnitude estimates relative measurements, which are easier to calibrate than absolute flux measurements. The magnitude difference of two objects is given as,

$$m_1 - m_2 = -2.5 \log_{10} F_1 + C + 2.5 \log_{10} F_2 - C = 2.5 \log_{10} \left(\frac{F_2}{F_1} \right), \quad (3.9)$$

and the constant C cancels. The magnitude difference is the relative difference in flux for the two objects under consideration. For type Ia supernovae, the luminosity is (approximately) fixed and $F \propto d_L^{-2}$. The difference between the apparent and the absolute magnitude is

$$m_x - M_x \equiv \mu_x = 2.5 \log_{10} \left(\frac{d_L}{10\text{pc}} \right)^2, \quad (3.10)$$

which introduces the distance modulus, μ . The distance modulus and the redshift are the two observables for standard candles. Type Ia supernovae have an intrinsic B band luminosity of $M_B = -19.46$ (note that this depends on the value of H_0), which is used to calculate the distance modulus along with the apparent magnitude. Expressing the luminosity distance in Mpc and multiplying d_L by the Hubble constant, Equation (3.10) becomes

$$\mu_x = 5 \log_{10}(H_0 d_L) + 25 - 5 \log_{10} H_0. \quad (3.11)$$

The 25 comes from a factor of $-5 \log_{10}(10^{-5} \text{ Mpc})$, the distance where the absolute magnitude is defined. $H_0 d_L$ is often called the ‘Hubble constant free luminosity distance,’ and given the symbol D_L . It is convenient to separate out the Hubble constant when fitting supernova data since it is a nuisance parameter that only shifts the absolute value of $\mu(z)$ without affecting the overall shape. Perlmutter et al. [1999] combine the H_0 term with the other constant terms and define $\mathcal{M} \equiv M_x + 25 - 5 \log_{10} H_0$; then the apparent magnitude is

$$m_x = \mathcal{M} + 5 \log_{10}(D_L(z; \Omega_M, \Omega_X, w_0, w_a)). \quad (3.12)$$

This combines the absolute magnitude and the Hubble constant into a single nuisance parameter that is marginalized over to yield confidence intervals on the other cosmological parameters independent of the absolute distance scale and supernova luminosity.

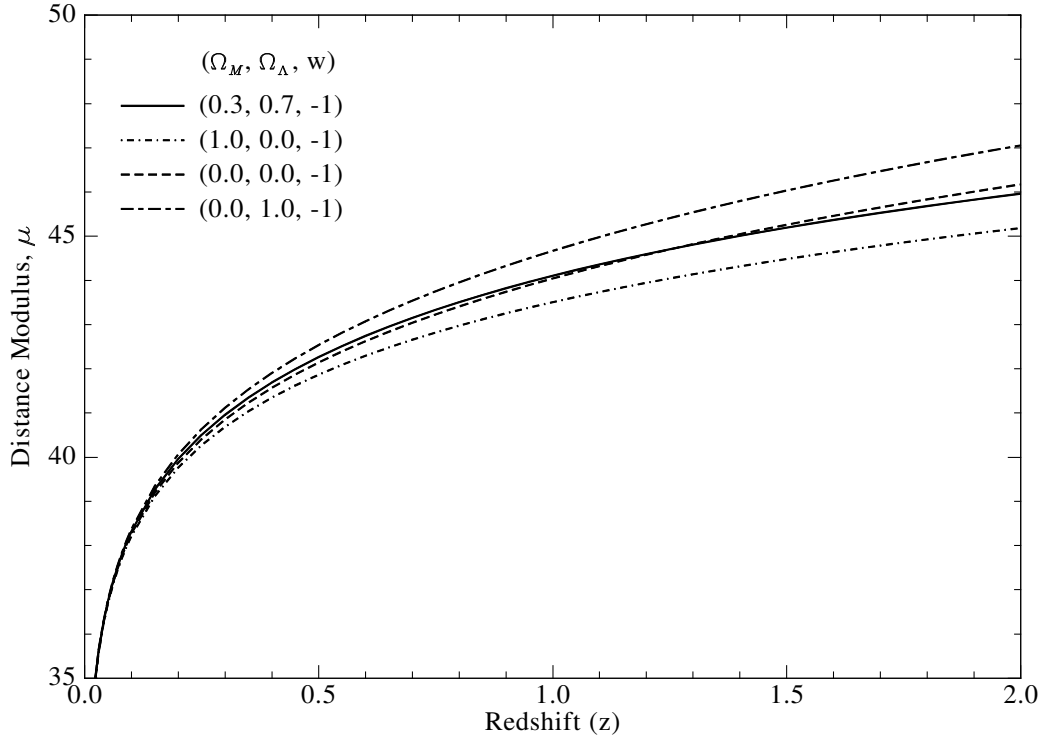


Figure 3.1. Distance modulus, $\mu(z)$, for various Λ CDM cosmologies with different matter and dark energy densities (Ω_M, Ω_Λ). Solid line: concordance cosmology (0.26, 0.74), dot dash: Matter dominated (1.0, 0,0), dash: Open-empty (0.0,0,0), dash long dash: Lambda dominated (0.0, 1.0).

3.2.1 Λ CDM Cosmologies

The distance modulus depends on the cosmological parameters related to the matter and dark energy density as well as the redshift. The dependence of the distance modulus on the energy content is derived by integrating Equation (3.7) for a range of different redshifts. Figure 3.1 shows the distance modulus as a function of redshift for 4 different Λ CDM cosmologies with $H_0 = 70 \text{ km s}^{-1} \text{ Mpc}^{-1}$. Changing H_0 is equivalent to a change in the intrinsic magnitude of the standard candle, it only affects the absolute distance calibration and shifts the curve by a constant offset. As long as a sample of low z (< 0.1) supernovae are available to ‘anchor’ the Hubble diagram, knowledge of H_0 and the absolute luminosity are not necessary. The present day energy densities and the dark energy equation of state change the shape and slope of the curve as a function of redshift. Luminosity distance measurements with standard candles are designed to constrain these parameters.

The four models presented in Fig. 3.1 result in very different expansion histories and can already be distinguished with existing type Ia supernova data. Cosmological constraints using type Ia supernova data are discussed in Sec. 3.4. The importance of high redshift observations is beginning to show in this figure. All these very different cosmologies give similar results at low redshift, but diverge as z increases.

For the concordance cosmology model ($\Omega_M = 0.26, \Omega_\Lambda = 0.74, w = -1$), supernovae initially appear dimmer than they would in a matter dominated or open, empty universe. This is due to the accelerated expansion caused by the dark energy. Objects at the same redshift appear fainter in a universe with dark energy than they do when only matter is present. The interesting feature of the flat, cosmological constant models is that as long as $\Omega_M > 0$, then at some time in the past the universe was matter (or radiation) dominated and the expansion was decelerating. This is apparent in the figure where the distance modulus for the concordance model crosses the open, empty universe curve at a redshift of ~ 1.2 . By this point, the universe is already in a matter dominated decelerating state. From Sec. 2.3.6, the transition from acceleration to deceleration for a flat Λ CDM universe occurs at

$$z_t = 1 - \left(\frac{2\Omega_\Lambda}{\Omega_M} \right)^{1/3}, \quad (3.13)$$

with $z_t = 0.78$ for the concordance cosmology model.

The matter dominated (top) and Lambda dominated (bottom) curves in Fig. 3.1 represent the extremes for the luminosity distance in flat, Λ CDM cosmologies (ignoring models with negative cosmological constant, which are physically allowable but strongly disfavored by current observations). These cosmologies deviate from the concordance model by up to 1 magnitude over the redshift range shown. The magnitude scale is logarithmic, and the flux difference for $\Delta m = 1$ is

$$F_1 = F_2 10^{-0.4\Delta m} = 0.398 F_2. \quad (3.14)$$

A dimming by 1 magnitude is equivalent to a reduction in flux by more than 60%.

Even small magnitude differences are easily observable. For $\Delta m < 0.1$ the magnitude difference is approximately the percent error in flux. The difference between the concordance model and the open, empty universe is ~ 0.1 mag for $z < 1.5$. The intrinsic dispersion of type Ia supernovae after stretch correction is $0.12 - 0.15$ magnitude; these two models can easily be distinguished with a fairly small (~ 100) sample of supernovae as long as the systematic photometry errors are $< 10\%$. The Λ CDM cosmologies in Fig. 3.1 are easy to differentiate with existing ground based observational techniques. The much more difficult task of constraining the nature of dark energy requires measurements of the equation of state, $w(z)$, and its time evolution. This requires a large sample of type Ia supernovae and careful control of systematic uncertainties, since deviations in μ for different dark energy models are much smaller and more difficult to measure. The necessary redshift range and photometric accuracy can be achieved with a space based visible and NIR instrument, such as SNAP.

3.2.2 Time Varying $w(z)$ Cosmologies

A number of different dark energy models are discussed in Sec. 2.5. Many of these models can be approximated using the parameterized dark energy equation of state, $w(z) = w_0 + w_a z/(1+z)$. Figure 3.2 shows some of the dark energy models and their magnitude difference compared to the standard concordance cosmology. Many of the models in the literature predict brighter standard candles at high redshift (lower magnitude), such as Chaplygin gas with $\kappa = 1$, a brane world model with a time varying equation of state (this model is approximated by $w_0 = -0.78, w_a = 0.32$), and the $w = -2/3$ model inspired by colliding domain walls. These three models illustrate the importance of high redshift observations. Below $z = 1$, the Chaplygin gas model crosses both the brane world and domain wall models. The Chaplygin gas model does not deviate from either of these models by more than 5% until $z > 1$.

The only models that predict dimmer supernova than the concordance cosmology either have higher dark energy density, as in the top long dashed curve, or an equation of state less than -1. A larger dark energy density is unlikely based on experimental grounds, and theory favors $w > -1$. An observation of a number of type Ia super-

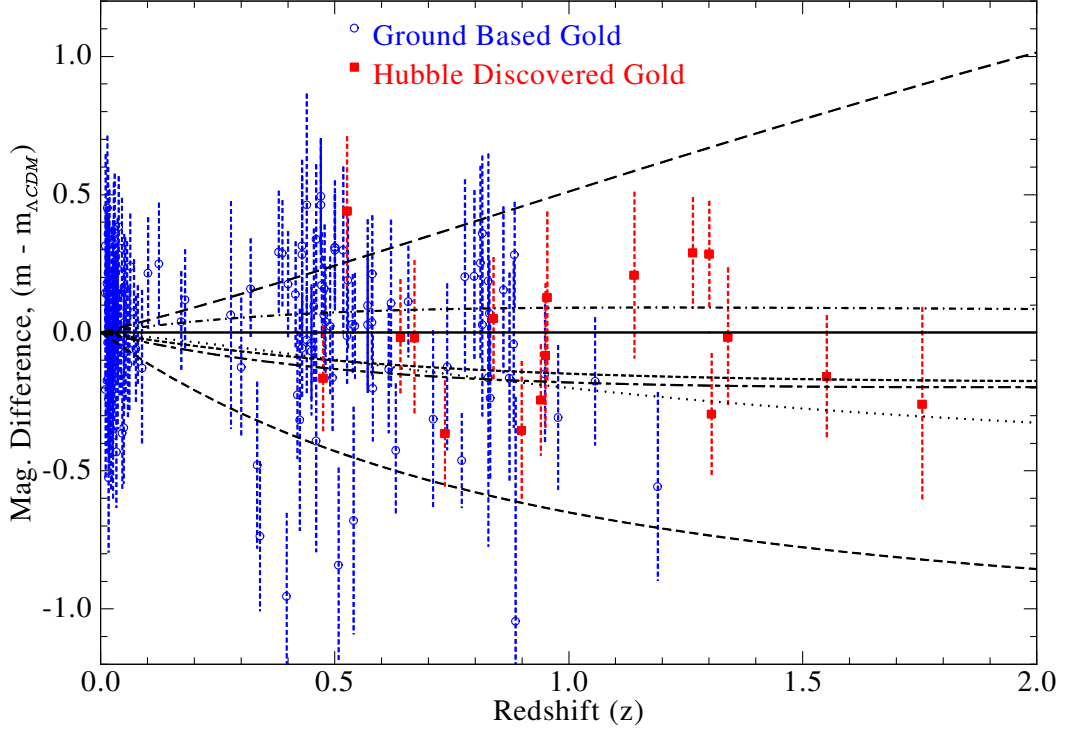


Figure 3.2. Magnitude difference for type Ia supernova for a number of proposed dark energy models minus the concordance Λ CDM cosmology ($\Omega_M = 0.26, \Omega_\Lambda = 0.76$). All models assume a flat universe with $\Omega_{tot} = 1$. The Riess et al. [2004] gold sample data is shown as open blue circles for ground discovered supernovae and closed red squares for HST discovered supernovae.

novae that are much dimmer than the cosmological constant model may indicate the presence of some previously unknown dust component which systematically dims the distant supernovae. Near infrared observations can constrain dust extinction for all known dust models, which preferentially scatter the shorter wavelengths. Only a new form of ‘grey’ dust, which scatters uniformly at all wavelengths, could also impact the near infrared, and these models are already strongly disfavored by supernovae observations [Riess et al., 2004].

3.3 Type Ia Supernovae as Standard Candles

Constraining cosmology with distance measurements requires a standard candle that is both extremely bright and uniform. Type Ia supernovae are some of the brightest known objects in the universe, often brighter than their host galaxy at peak intensity. These supernovae are transient events that brighten over the course of about 10

restframe days, then slowly decline. Type Ia supernovae are luminous enough to be observed more than 100 days after peak brightness in nearby galaxies. They are thought to be thermonuclear detonations of carbon/oxygen white dwarfs [Woosley and Weaver, 1986]. Other supernovae types (II, Ib, and Ic) are the result of core collapse of massive ($> 8 M_{\odot}$) stars. These events have a wide range of explosion energies and can result in neutron star or black hole remnants. Type Ia supernovae are a much more homogeneous class of supernovae because the thermonuclear detonation of the white dwarf progenitor occurs at nearly the same mass for all events and the entire star is burned; there is no remnant from a type Ia explosion.

Theoretical understanding of type Ia supernovae is not complete. The prominent theory maintains that a carbon/oxygen white dwarf accretes matter from a companion star until it nears the Chandrasekhar mass, approximately $1.4 M_{\odot}$. This is the maximum mass that a star can support with electron degeneracy pressure. Before reaching this limit, the pressure and temperature within the white dwarf are high enough to ignite fusion reactions, converting rest mass into energy and resulting in a runaway detonation. The specifics of the detonation are not well understood. Hydrodynamic simulations are used to predict observable features from the detonations, however the simulations are unable to reproduce the variety of type Ia events observed thus far. The theory does predict that type Ia events should be very uniform, since all the explosions occur at nearly the same mass. This claim is supported by measurements of nearby type Ia events. Hamuy et al. [1995] measure a B and V band magnitude dispersion of $0.3-0.5$ mag from luminous type Ia events; Perlmutter et al. [1997] measure a dispersion $\sigma_B = 0.26$ for a subset of nearby supernovae discovered within 5 days of maximum brightness or sooner. The restframe B and V bands are used to normalize type Ia events because the flux is a maximum in these filters.

The peak brightness for type Ia explosions is correlated to other supernova properties, including the lightcurve width, color, and spectral features. The correlations with brightness discovered so far are based on empirical evidence from supernova observations. Theory and hydrodynamical simulations have difficulty predicting the colors and spectral features. The width, color, and spectral indicators can all be used

to normalize the peak brightness from many type Ia events. This ‘corrects’ under or over-luminous events to a ‘standard’ type Ia absolute magnitude. The corrected sample has a lower dispersion in apparent magnitude. The evidence for the correlations and methods to improve the estimates of the peak brightness are discussed below.

3.3.1 Brightness Indicators

Wilson [1939] recognized the potential of type Ia supernovae to constrain cosmology soon after their discovery. Only a small number of supernovae were discovered and followed up until the 80s and early 90s, when systematic supernova searches with digital processing of CCD images began. These programs have discovered hundreds of type Ia supernovae and obtained multi-color photometry and spectroscopy at various stages of the lightcurve. These newly available data have confirmed predictions about the uniformity of type Ia supernovae and led to the discovery of a number of features that correlate with the peak brightness. The uncertainties quoted below for different supernova normalization methods vary widely depending on the sample of supernovae they are applied to. As the methods have evolved, the supernova sample and the variety of type Ia supernova events has increased. The published uncertainties for the newer methods are often higher than the initial width-luminosity corrections because they are applied to a much broader sample of type Ia supernovae, while the earlier methods were only tested on small, uniform samples.

One of the first features that was exploited to normalize type Ia events is the width-luminosity relationship. Phillips [1993] and Hamuy et al. [1995, 1996b] found that the restframe B band magnitude was correlated with the decline rate and width of the supernova lightcurve. The brighter events have wide, slowly declining lightcurves, and the dim supernovae have narrow, fast lightcurves. Hamuy et al. [1995] also found that the more luminous supernovae occur in galaxies with young stellar populations. This hints at correlations between progenitor age and/or metallicity and peak brightness. Phillips et al. [1999] use a normalization of the B band luminosity based on the change in magnitude in the first 15 days after maximum light, known as Δm_{15} . This correction reduces the dispersion to $\sigma_B = 0.11$ and $\sigma_V = 0.09$ mag when applied

to a sample of nearby ($0.01 < z < 0.1$) Calan/Tololo supernovae [Hamuy et al., 1996a] with low host galaxy extinction. An alternative to Δm_{15} , called the stretch correction, is used in Perlmutter et al. [1997].

The peak luminosity of a type Ia supernovae is also correlated with the restframe $B - V$ and $V - I$ colors [Riess et al., 1995, 1996, Phillips et al., 1999]. One difficulty with using this correlation is measuring the host galaxy dust extinction, which can only be estimated using these same colors. It turns out that the restframe colors are only correlated to the luminosity near peak brightness; late time colors (30 days $< t < 60$ days) appear to be independent of the luminosity [Lira, 1995]. The late time color can be used to estimate the extinction, then combined with color information near peak brightness to normalize the supernova luminosities. Methods that use both color and the width-luminosity relation to fit multi-band lightcurves reduce the B and V band dispersions as low as $\sigma_B, \sigma_V \sim 0.11 - 0.12$.

The width-luminosity and color corrections to the supernova peak brightness both come from broadband observations of supernova lightcurves. The spectra of type Ia events provide even more information with the potential to reduce the dispersion. Nugent et al. [1995] measured correlations between line strengths and luminosity in supernova spectra, while Mazzali et al. [1998] used the velocity of the ejected matter, which provides information about the energetics of the supernova explosion. Both of these methods show promise, but are not yet in use due to the limited spectral information available for type Ia supernovae. Programs like the Nearby Supernova Factory [Aldering et al., 2002] are working to obtain a large sample of spectra at various epochs for nearby supernovae; the SNAP satellite will measure spectra of over 2000 type Ia supernovae near peak brightness. These datasets will increase understanding of type Ia supernova phenomenology and could reveal additional luminosity indicators in type Ia supernova spectra.

3.3.2 Extracting the Distance Modulus

Cosmology constraints from type Ia supernovae require accurate knowledge of the redshift and distance modulus. The redshift is determined from spectroscopic mea-

measurements of the supernova and its host galaxy; the distance modulus is derived from multi-color lightcurve information. The colors provide information about the peak brightness as well as estimates of the host galaxy dust extinction for the bluer filters. For high redshift events, K-corrections [Kim et al., 1996] are also needed to connect the observed bandpasses to the restframe B or V band magnitudes.

Early techniques used to normalize type Ia events utilize a small subset of supernovae to empirically fit a relationship between the luminosity and lightcurve width. Color information is used to estimate extinction, then the extinction corrected magnitudes are used to define the width-luminosity relationship. Two common methods are stretch and Δm_{15} . The stretch [Perlmutter et al., 1997] method fits the observed lightcurves to templates that are broadened or narrowed by the stretch factor, s . The Δm_{15} method, which only considers the drop in B band luminosity [Phillips et al., 1999], has been extended to include V and I band observations and renamed dm_{15} [Germany, 2001]. Both of these methods reduce the B band dispersion to $\sigma_B = 0.11 - 0.17$ mag.

More sophisticated techniques that incorporate the late time lightcurve data as well as additional color information are now in development. The MLCS [Riess et al., 1996] and MLCS2k2 [Jha, 2002] methods use the U band to improve extinction measurements and reduce the dispersion to $\sigma_B, \sigma_V \sim 0.12$. The authors claim that coverage of a supernova in 4 to 5 bandpasses extending to 100 days after maximum is ideal for fitting the distance modulus; however, the fits presented in Tonry et al. [2003] only use B and V band lightcurves up to 40 days after maximum due to the limited supernovae datasets. This stresses the need for larger datasets with multi-color observations, beginning with the rise of the supernova lightcurve and extending many days past peak brightness.

Tonry et al. [2003] also present the Bayesian Adaptive Template Method (BATM), which compares observed lightcurves to redshifted and extinguished lightcurves of 20 well sampled nearby supernovae. This method does not optimize for the observed correlations with peak brightness and also avoids K-corrections. The scatter in peak magnitude is higher than the other methods, $\sigma = 0.18 - 0.22$, but the systematic

errors could be lower than MLCS. A third method, known as CMAGIC [Wang et al., 2003, Conley et al., 2006], uses the supernova colors after the optical maximum to reduce the dispersion to $\sigma < 0.11$ mag for supernovae with $B - V < 0.2$ mag at maximum brightness.

All of the distance modulus estimates suffer from a lack of uniform, high quality observations of type Ia lightcurves and spectra. The ground based dataset is limited by systematic calibration errors and the number of observations of each supernova's lightcurve. Precision measurements with supernovae require a set of observations with an instrument designed to control systematic errors. Space based instruments offer the best control of systematic uncertainties, and SNAP is an ideal instrument for discovering and following up a large number of supernovae.

The B and V band dispersions depend on the sample of supernovae to which each method is applied. The above methods are tested against a small set of nearby supernovae with little or no host galaxy dust extinction. Most of the results in the literature thus far only deal with supernovae at redshift less than 0.1. To increase the statistical power of supernovae for cosmology measurements, these methods are applied to larger and higher redshift datasets, which introduces K-corrections and complicates extinction estimates. Infrared observations become increasingly important as the restframe optical light is redshifted into the NIR. A set of NIR filters are needed to provide uniform observations of the restframe supernova colors at all redshifts.

The MLCS, BATM, and CMAGIC methods require multi-color observations over the entire supernova lightcurve to extract the host galaxy extinction and distance modulus. It now appears that the corrected distance modulus will have a dispersion of $0.10 - 0.15$ mag once high quality datasets become available. This is at the level where a relatively small number of supernovae (~ 50 per redshift bin) will reduce the statistical uncertainty to < 0.02 mag. At this point, systematic uncertainty from the distance modulus fitting techniques or shifts in supernova brightness due to metallicity or progenitor age become the dominant source of error. Missions that limit the systematic errors with a uniform set of well sampled lightcurves and spectra will

have the most success constraining the nature of dark energy with type Ia supernovae.

3.4 Cosmological Constraints from Type Ia Supernovae - Methods

The distance modulus depends on the matter and dark energy content of the universe as well as the dark energy equation of state. Observations of standard candles provide an apparent magnitude and redshift which are used to derive constraints on $\Omega_M, \Omega_X, w_0, w_a$. For type Ia supernovae, the apparent magnitude and redshift are derived from multi-band lightcurve data and spectra of the supernova and its host galaxy. A variety of fitting techniques can be used to extract uncertainties on cosmology parameters given these data. The basic principle of all the fitting techniques is to determine the most probable values of the model parameters, $\Omega_M, \Omega_X, w_0, w_a$, given a set of observations, (μ_i, z_i) , with errors $\sigma_{\mu,i}$. Errors in the redshift due to the peculiar velocity of the galaxies relative to the Hubble flow are included in the magnitude error, $\sigma_{\mu,i}$.

The most common fitting techniques are maximum likelihood and Bayesian parameter estimation. Maximum likelihood fits attempt to find the most likely values for the model parameters, while Bayesian estimation derives the probability density function for the fit parameters. The two methods attempt to answer different questions, which naturally leads to slightly different results. Estimates of parameter constraints and techniques to add prior knowledge about the fitting parameters also differ. Results for both methods are presented in a comparative manner. Two additional methods that provide quick estimates of goodness of fit and parameter uncertainties are χ^2 minimization and Fisher matrix calculations.

3.4.1 χ^2 Tests

For a given set of supernova observations, (μ_i, z_i) , the χ^2 statistic provides a simple test of different dark energy models. Assuming a set of uncorrelated supernova

observations with Gaussian errors in μ , χ^2 is defined as

$$\chi^2 \equiv \sum_{i=1}^N \frac{(\mu_i - \mu(z_i; H_0, \Omega_M, \Omega_X, w_0, w_a))^2}{\sigma_{\mu,i}^2}. \quad (3.15)$$

If the observed values, μ_i , agree exactly with the model values then $\chi^2 = 0$. The statistical nature of the flux measurements used to derive the distance modulus make this outcome extremely unlikely. On average each μ_i should deviate from the model value by $\sigma_{\mu,i}$, such that the expectation value for χ^2 is

$$\langle \chi^2 \rangle = \nu = n - n_c, \quad (3.16)$$

where ν is the number of degrees of freedom, defined as the number of data points, n , minus the number of constraints or fit parameters, n_c . The χ^2 per degree of freedom, defined as $\chi_\nu^2 \equiv \chi^2/\nu$, is often used as a goodness of fit measure with an expectation value $\langle \chi_\nu^2 \rangle = 1$. When using a χ^2 test, the probability is expressed as the probability of obtaining a value of χ^2 greater than the measured value. Tabulated values of the integrated χ_ν^2 distribution are available in Bevington and Robinson [2003]. High values of χ_ν^2 have low probability and typically result from an incorrect data model or mis-estimation of the uncertainties, $\sigma_{\mu,i}$. When $\chi_\nu^2 \sim 1$ approximately half of the observations will be above and half below this χ_ν^2 value, indicating good agreement between the data and the model.

3.4.2 Maximum Likelihood Fits

Calculating the value of χ^2 for a specific model is a useful way to test dark energy models; fitting data requires finding the model parameters that minimize the value of χ^2 for the data, (μ_i, z_i) . For Gaussian measurement errors, $\sigma_{\mu,i}$, the minimum value of χ^2 is the maximum of the likelihood function,

$$\mathcal{L} = \frac{1}{2\pi\sigma_i} \exp \left[-\frac{(\mu_i - \mu_{\text{model}}(z_i; \theta))^2}{2\sigma_i^2} \right]. \quad (3.17)$$

The minimum χ^2 corresponds to the most likely value for the model parameters. Efficient minimization routines such as Minuit [<http://cminuit.sourceforge.net/>] can be used to quickly find the best fit parameter values and their covariance. Estimates of the parameter uncertainties from the covariance matrix provide confidence intervals on the fit parameters. These estimates assume the fit parameters and measurement uncertainties are normally distributed; this assumption is not always true, especially at high confidence levels where parameter distributions can have large tails. However, the speed of the minimization routines compared to a full Bayesian probability calculation make this method effective for quickly estimating parameter uncertainties.

When prior knowledge about the fit parameters is available, it can be incorporated into the likelihood function. Many authors utilize constraints on the matter density from CMB or cluster abundances, e.g. $\Omega_M = 0.237 \pm 0.034$, the WMAP constraint for a flat Λ CDM cosmology. Prior constraints modify the likelihood function in Eq. (3.17). In this case, the maximum likelihood is not the minimum χ^2 , but the same routines can be used to efficiently maximize the likelihood function. Likelihood fits for existing type Ia supernova data are shown in Sec. 3.5.

3.4.3 Bayesian Estimation

The probability of obtaining a set of observations, (μ_i, z_i) , for a given cosmology is defined as

$$p(\mu_i, z_i | H_0, \Omega_M, \Omega_X, w_0, w_a). \quad (3.18)$$

The Bayesian approach attempts to answer the opposite question: given a set of observations, what is the probability that the universe is defined by the cosmology parameters $(H_0, \Omega_M, \Omega_X, w_0, w_a)$? Bayes's theorem provides the answer:

$$p(H_0, \Omega_M, \Omega_X, w_0, w_a | \mu_i, z_i) = \frac{p(\mu_i, z_i | H_0, \Omega_M, \Omega_X, w_0, w_a) p(H_0, \Omega_M, \Omega_X, w_0, w_a)}{p(\mu_i, z_i)}. \quad (3.19)$$

Bayes's postulate then states that the prior probabilities, $p(H_0, \Omega_M, \Omega_X, w_0, w_a)$ and $p(\mu_i, z_i)$, can be assumed to be constant with all values having an equal probability [Lupton, 1993]. If prior knowledge of the fitting parameters is available, it can easily

be included to improve the constraints on the remaining fit parameters.

The probability density function for the distance moduli is approximately Gaussian for type Ia supernovae (strong gravitational lensing is one example of an effect that can lead to non-Gaussianity). In this case

$$p(\mu_i, z_i | H_0, \Omega_M, \Omega_X, w_0, w_a) = \prod_i \frac{1}{\sqrt{2\pi\sigma_i^2}} \exp \left[-\frac{(\mu_i - \mu(z_i; H_0, \Omega_M, \Omega_X, w_0, w_a))^2}{2\sigma_{\mu,i}^2} \right]. \quad (3.20)$$

The product of the exponentials is the sum of the arguments which makes the term in brackets equal to $-\chi^2/2$ from Eq. (3.15). Plugging this result into Eq. (3.19) and assuming the prior probability on the distance moduli is constant yields

$$p(H_0, \Omega_M, \Omega_X, w_0, w_a | \mu_i, z_i) \propto \exp(-\chi^2/2) p(H_0, \Omega_M, \Omega_X, w_0, w_a). \quad (3.21)$$

The probability density can be normalized to one by integrating this expression over the allowed values of $H_0, \Omega_M, \Omega_X, w_0$, and w_a . $p(H_0, \Omega_M, \Omega_X, w_0, w_a)$ is assumed to be constant (a flat prior) if no additional information about these parameters is available.

The Bayesian method allows direct calculation of the probability of a set of cosmology parameters and easy addition of prior knowledge about the model parameters. The probability density function for the fit parameters is often called the conditional or posterior probability. The likely range for the parameters is referred to as the credibility interval, instead of the usual confidence interval specified for other fitting techniques.

Bayesian estimation eliminates the assumption that the distributions for the model parameters are symmetric and Gaussian. Error estimation from the covariance matrix, derived by minimization routines or the Fisher Matrix method discussed below, uses this assumption to specify confidence intervals. The Bayesian method also allows multi-dimensional fits to be reduced to one or two dimensions by marginalizing over the additional parameters. For example, assuming a flat universe ($\Omega_X = 1 - \Omega_M$) with a constant dark energy equation of state ($w_a = 0$), the joint probability of Ω_M

and w_0 is

$$p(\Omega_M, w_0 | \mu_i, z_i) = \int_{-\infty}^{\infty} p(H_0, \Omega_M, w_0 | \mu_i, z_i) dH_0. \quad (3.22)$$

The drawback of Bayesian estimation is the large number of calculations required. A typical calculation of the posterior probability uses of order 1000 calculations per parameter on a large and finely spaced grid. For large parameter spaces, a faster method of estimating the parameter uncertainties is often desirable.

3.4.4 Fisher Matrix

The Fisher information matrix provides a quick and efficient method of estimating parameter errors given a dataset with Gaussian uncertainties, σ_i . Calculations of the Fisher matrix only require knowledge of the measurement errors and the derivative of the model with respect to the model parameters. The Fisher matrix cannot be used to fit data, it is only a tool to estimate errors at specific points in the parameter space.

The Fisher information matrix is defined as

$$F_{ij} = -\frac{\partial \ln \mathcal{L}(\mathbf{x}; \theta)}{\partial \theta_i \partial \theta_j}, \quad (3.23)$$

where \mathbf{x} is the measured data and θ_i is the i^{th} fit parameter. The likelihood is defined in Eq. (3.17). Assuming Gaussian distributions for the model parameters, θ_i , the Fisher matrix is the inverse of the covariance matrix,

$$\langle \partial p_j \partial p_k \rangle = (F^{-1})_{jk}. \quad (3.24)$$

This result can be derived by expanding the probability density function about the true value of the model parameters. The Fisher matrix is an exact solution when the true model parameters are known and both the measured data and the model parameters follow Gaussian distributions. When working with real data, the true model parameters are not known; estimates must be used based on the measured data. In this case the Fisher information matrix gives the most optimistic error

estimates for the model parameters.

For type Ia supernovae, the measured data are the distance modulus and redshift, $\mu(z)$, and the parameters are $\theta = H_0, \Omega_M, \Omega_X, w_0, w_a$. Evaluating the derivatives of the likelihood function gives

$$F_{ij} = \sum_k \frac{\partial \mu_k}{\partial \theta_i} \frac{\partial \mu_k}{\partial \theta_j} \frac{1}{\sigma_k^2}, \quad (3.25)$$

where the sum runs over the measured distance moduli, and the derivatives are evaluated at redshift z_k . The Fisher matrix can be calculated from the measurement errors and the derivative of the fit model at each measurement. It is most useful when comparing constraints on different dark energy models with simulated supernova data. Error contours for various w_0, w_a combinations only require evaluating the derivative of the distance modulus.

The Fisher matrix is also used to combine information from multiple experiments, e.g. type Ia supernovae and weak lensing. The joint confidence interval from these two techniques is obtained by simply adding the two Fisher matrices and inverting to derive the covariance matrix. Prior constraints on the fit parameters (assuming they are Gaussian) are included by adding a matrix that is zero everywhere except in the diagonal component of the constrained parameter. Setting this element to $1/\sigma^2$ is equivalent to a Gaussian prior, with width σ , on the fit parameter. Combined constraints from type Ia supernovae, weak lensing, and baryon acoustic oscillations are presented in Sec. 6.2.

3.5 Cosmological Constraints from Existing Type Ia Supernova Data

Currently there are hundreds of type Ia supernovae that have been discovered and followed up with sufficient photometry and spectroscopy to determine the extinction corrected distance modulus. Unfortunately, there is not yet a consensus on the best luminosity indicators or the proper lightcurve fitting procedures to extract the distance modulus. Each group with a supernova program uses their own techniques,

which leads to offsets in the apparent magnitude. In one large sample of type Ia supernovae, Tonry et al. [2003] present results for 230 supernovae with distances and host extinctions. They correct for offsets in the magnitude zero-point from the MLCS, Δm_{15} , BATM, and stretch lightcurve fitting methods. This provides an estimate of the distance to each supernova, but can introduce systematic errors from the combination of different methods.

In an effort to normalize type Ia supernovae analysis, Riess et al. [2004] compiled a data set using published photometry and spectroscopy of 186 supernovae. Most of the data³ were refit with the MLCS2k2 [Jha, 2002], then separated into a ‘gold’ and ‘silver’ sample. The gold sample contains 157 supernovae that are clearly identified as type Ia, have enough photometry to effectively sample the lightcurve (beginning no more than 10 days after maximum light), and have less than 1 magnitude of dust extinction. The remaining 29 supernovae are classified as silver. 17 of the gold sample supernovae (and 2 silver) were discovered with the Hubble Space Telescope, most at redshifts greater than 0.8. These high redshift supernovae are only 10% of the total sample, yet they improve the constraints on the dark energy equation of state parameters, w_0 and w_a , by a factor of 1.9. Higher redshifts, accessible with space based survey telescopes, are one of the keys to understanding the nature of dark energy with type Ia supernovae.

I have refit the gold sample data using the fitting techniques discussed in Sec. 3.4. The results below are consistent with Riess et al. [2004] after accounting for differences in assumptions about H_0 and the mass density, Ω_M .

3.5.1 Λ CDM Cosmologies

Measurements of type Ia supernovae depend on five of the cosmology parameters: $H_0, \Omega_M, \Omega_X, w_0$, and w_a . Assuming a Λ CDM cosmology reduces the number of parameters from 5 to 3. Constraining the universe to be spatially flat, $\Omega_{tot} = 1$, leaves only 2 free parameters, H_0 and Ω_M . The dark energy equation of state is

³A small number of high redshift supernovae do not have published photometry. The published magnitude for these objects is zero-point corrected to the MLCS2k2 method.

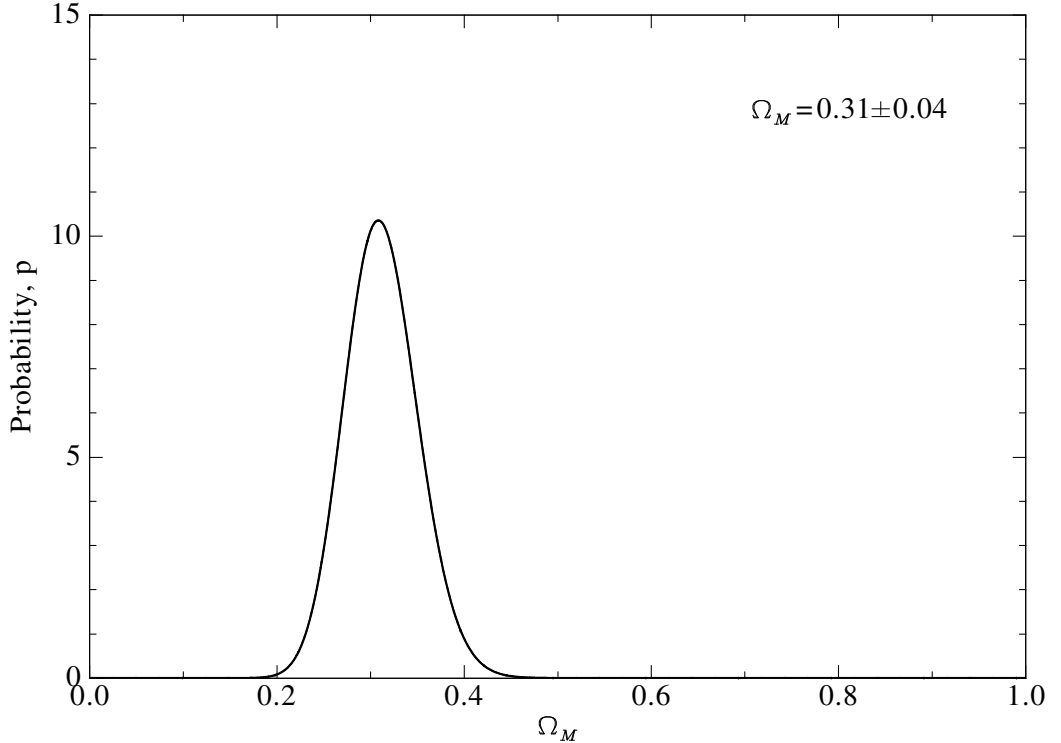


Figure 3.3. Probability density function for Ω_M from a fit to the gold sample data. The p.d.f. is normalized so that $\int_0^\infty p(\Omega_M; \mu_i) = 1$.

fixed at $w_0 = -1$, $w_a = 0$, and $\Omega_\Lambda = 1 - \Omega_M$ due to the flatness requirement. Minimizing χ^2 yields $H_0 = 64.32 \pm 0.76 \text{ km s}^{-1} \text{ Mpc}^{-1}$ (statistical only) and $\Omega_M = 0.309 \pm 0.038$, assuming a Gaussian distribution for the fit parameters. The best-fit value for H_0 ignores systematic uncertainties in the calibration of the type Ia supernova absolute luminosity. Type Ia supernovae cannot be used to constrain H_0 unless the absolute luminosity is known independent of H_0 . A more realistic constraint on Ω_M is obtained using Bayesian estimation and marginalizing over H_0 . The resulting probability density function for Ω_M is shown in Fig. 3.3. All of the fits in this section marginalize over H_0 or assume it is fixed at $65 \text{ km s}^{-1} \text{ Mpc}^{-1}$ (following Riess et al. [2004]). Fixing H_0 leads to slightly smaller error contours for the dark energy parameters.

Removing the flatness requirement from the cosmological model yields the joint probability of Ω_M and Ω_Λ (after marginalizing over H_0). The 2-d probability density function from a Bayesian estimator is shown in Fig. 3.4. Contours of constant

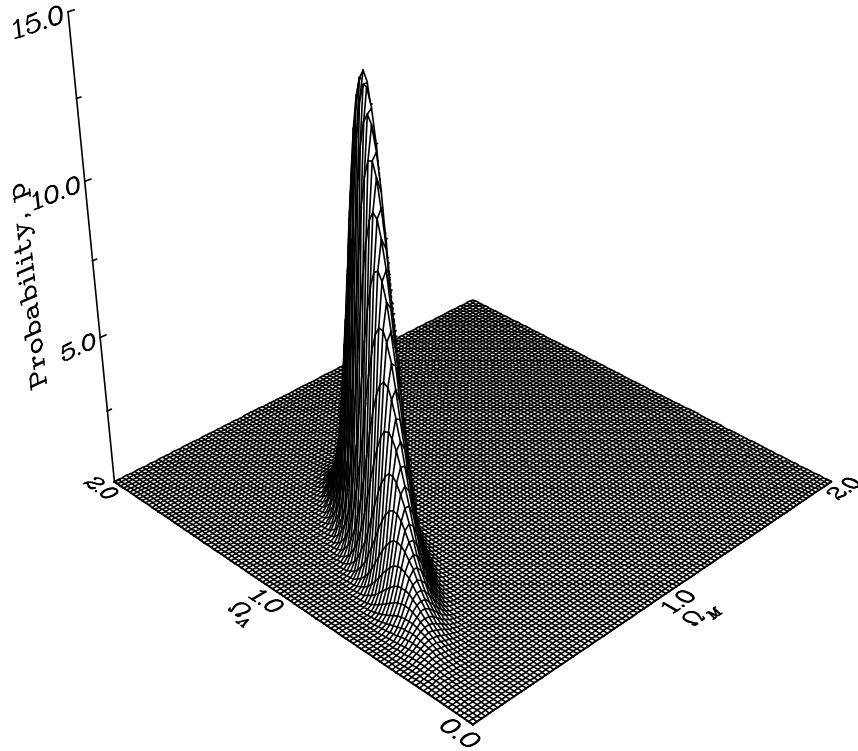


Figure 3.4. Bayesian estimation of the probability density function for Ω_M and Ω_Λ using the gold sample data from Riess et al. [2004]. H_0 acts as a nuisance parameters that is marginalized over and the p.d.f. is normalized so that $\int_0^\infty \int_{-\infty}^\infty p(\Omega_M, \Omega_\Lambda; \mu_i) d\Omega_\Lambda d\Omega_M = 1$.

probability containing 68.3%, 95.4% and 99.7% of the probability are projected in the $\Omega_M - \Omega_\Lambda$ plane in Fig. 3.5. Overplotted in this figure are the confidence intervals from a maximum likelihood estimator (when no priors are assumed this is equivalent to χ^2 minimization). These ellipses are symmetric due to the assumption of a Gaussian parameter distribution. The intervals from the Bayesian estimate give a slightly asymmetric error ellipse, tending towards a lower total density. The Bayesian calculation provides more accurate parameter constraints at the cost of additional computation. The χ^2 minimization finds the best fit parameters and their covariance in less than 1 minute, while the Bayesian calculation can take many hours depending on the range and step size for the parameter space explored.

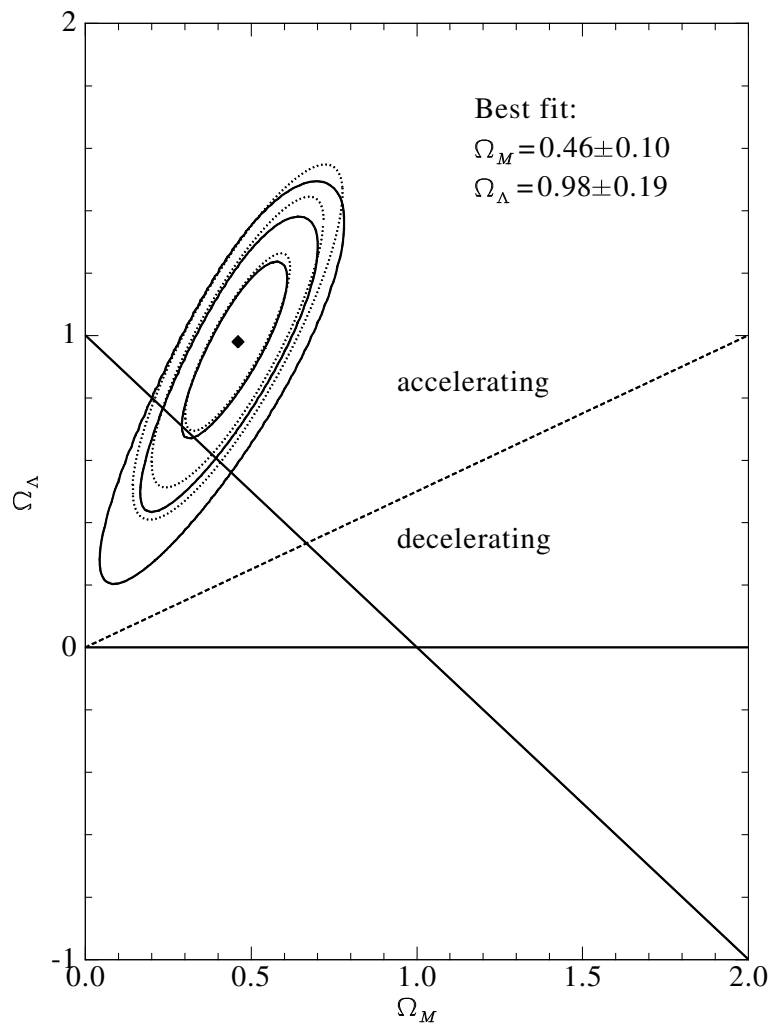


Figure 3.5. 68.3%, 95.4%, and 99.7% confidence intervals for Ω_M and Ω_Λ from fits to the gold sample data. The solid contours are from a Bayesian parameter estimation; the dotted contours use a maximum likelihood analysis.

The data in Fig. 3.5 show strong evidence for a non-zero dark energy density, $\Omega_\Lambda > 0$, at more than 99.99% confidence. A flat universe falls within the edge of the 68.3% interval for the Bayesian estimate, but just beyond this contour for the likelihood fit. The best fit parameter values are $\Omega_M = 0.46$ and $\Omega_\Lambda = 0.98$ (assuming the dark energy is a cosmological constant) in both cases.

3.5.2 Constant w Fits

Extending the cosmology model to include more general dark energy models with a constant equation of state increases the number of fit parameters to 3 (assuming a spatially flat universe). For a constant equation of state, $w_a = 0$, the best fit cosmology parameters are $\Omega_M = 0.49 \pm 0.066$ and $w_0 = -2.4 \pm 1.2^4$, inconsistent with the concordance cosmology. When the 17 high redshift supernovae discovered with *HST* are excluded, the best fit values are $\Omega_M = 0.539 \pm 0.045$ and $w_0 = 3.8 \pm 2.3$. The best fit values demonstrate the degeneracy between the dark energy equation of state and the matter density in direct distance measurements. The increased expansion caused by a more negative equation of state is compensated for by a higher matter (and lower dark energy) density. This is one of the challenges in direct distance measurements.

Constraints from type Ia supernova data are much more powerful when prior knowledge about the matter density is known from some other source. WMAP combined with galaxy data from 2dF galaxy redshift survey [Colless, 1999] measure $\Omega_M \sim 0.26 \pm 0.03$, for a constant w cosmology [<http://map.gsfc.nasa.gov/>]. Applying a Gaussian constraint on Ω_M to the above data reduces the error on w_0 by a factor of 10 and brings the best fit values of Ω_M and w_0 into agreement with the concordance cosmology model, $\Omega_M = 0.27 \pm 0.03$ and $w_0 = -0.935 \pm 0.126$. Figure 3.6 shows 68.3%, 95.4%, and 99.7% confidence contours in the Ω_M, w_0 plane for Bayesian and maximum likelihood parameter estimates both with and without the prior constraint on the matter density. In each case, the 68.3% confidence contour for the supernova data alone does not overlap the 68.3% contour that includes the Ω_M prior.

⁴All errors quoted in the text are 1σ Gaussian errors from a maximum likelihood fit to the data.

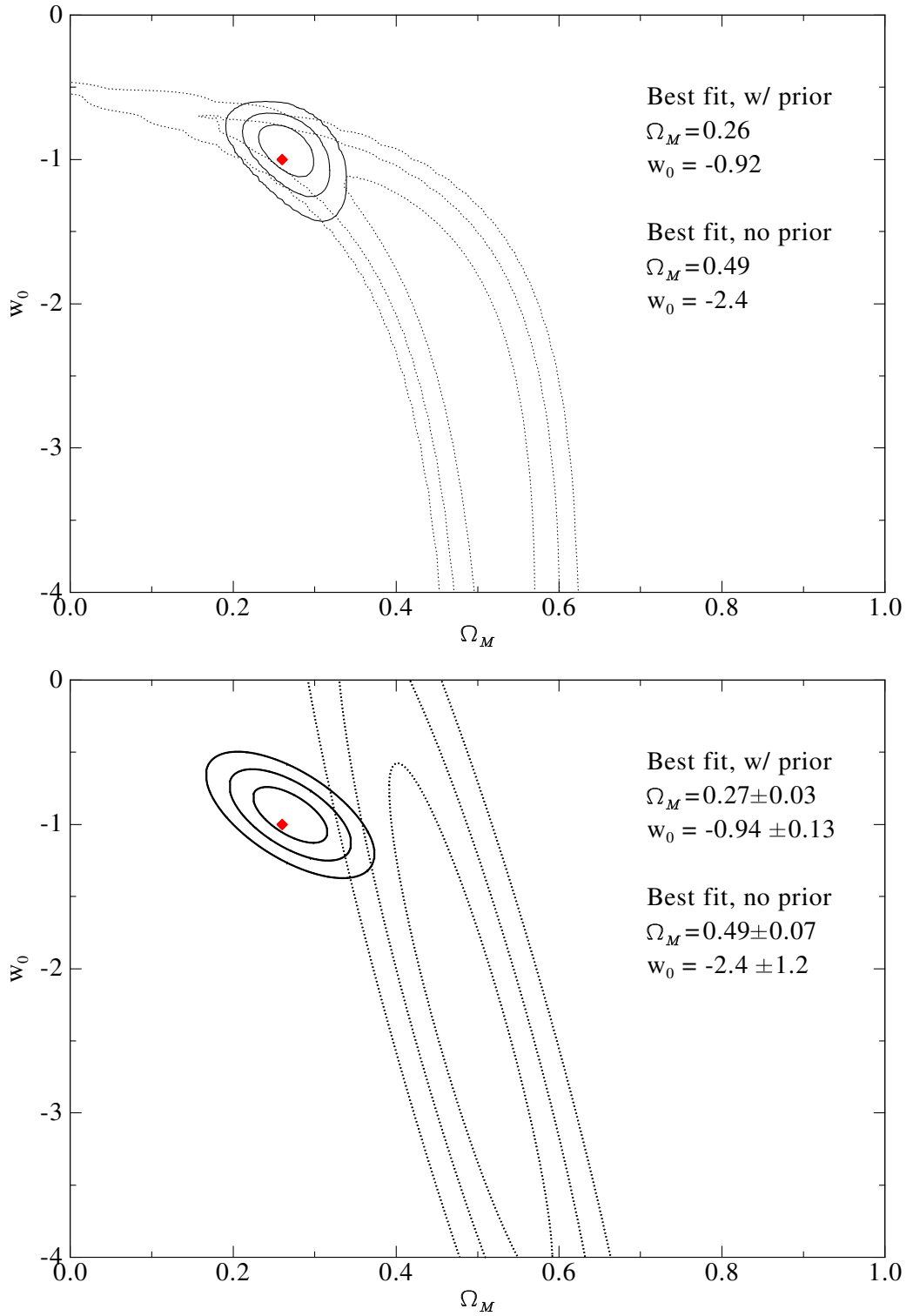


Figure 3.6. 68.3%, 95.4%, and 99.7% confidence interval for Ω_M and w_0 using Bayesian (top panel) and maximum likelihood (bottom panel) fits to the gold sample. The red point is the concordance value of (Ω_M, w_0) . Solid curves include a prior of $\Omega_M = 0.26 \pm 0.03$; dotted curves assume no priors.

The Bayesian and maximum likelihood fits give very different results for this particular example. The symmetric likelihood contours include $w_0 = 0$ within the 95.4% contour. This is equivalent to a flat, matter dominated universe; all values of Ω_M are equally likely when $w_0 = 0$ for a spatially flat universe. The contours from the likelihood fit are inconsistent with this fact. The Gaussian assumption in the likelihood fit is not a good approximation in this example. The Bayesian contours predict that the probability for a matter dominated, $w_0 = 0$, is much less than 0.01%. The asymmetric Bayesian contours provide a much more realistic estimate of the parameter distributions for Ω_M and w_0 .

There are two important points to take from these data. One is the dependence of the fit results on the assumed cosmology model. All the results assume spatial flatness, which constrains the matter and dark energy densities and reduces the number of fit parameters. The second is the impact of the prior constraint on Ω_M . Constraining Ω_M greatly increases the precision of the w_0 estimate, and different priors will give different best fit values of w_0 ; the prior used above is not the only published constraint on the matter density. Other choices include WMAP alone, $\Omega_M = 0.306^{+0.089}_{-0.081}$, or WMAP plus SDSS, $\Omega_M = 0.366^{+0.065}_{-0.068}$. Both of these priors lead to $w < -1$ and a higher matter density. The dependence of the type Ia supernovae results on the assumed prior must be considered when interpreting constraints on dark energy.

3.5.3 w_0 and w_a fits

The most general form of dark energy considered here includes some time variation, w_a , in the equation of state. The universe is still assumed to be spatially flat, leaving 4 parameters in the model used to calculate the distance modulus. The Bayesian parameter estimates also assume H_0 is fixed⁵ at $65\text{km s}^{-1}\text{Mpc}^{-1}$ and marginalize over Ω_M . When no prior constraints are applied to the matter density, a maximum likelihood fit to the gold sample supernovae yields $\Omega_M = 0.446 \pm 0.129$, $w_0 = -2.34 \pm 1.02$ and $w_a = 3.73 \pm 4.17$. The current set of supernova data cannot begin to rule

⁵This has little impact on the constraints on w_0 and w_a but leads to a factor of 100 – 1000 improvement in the speed of the fit.

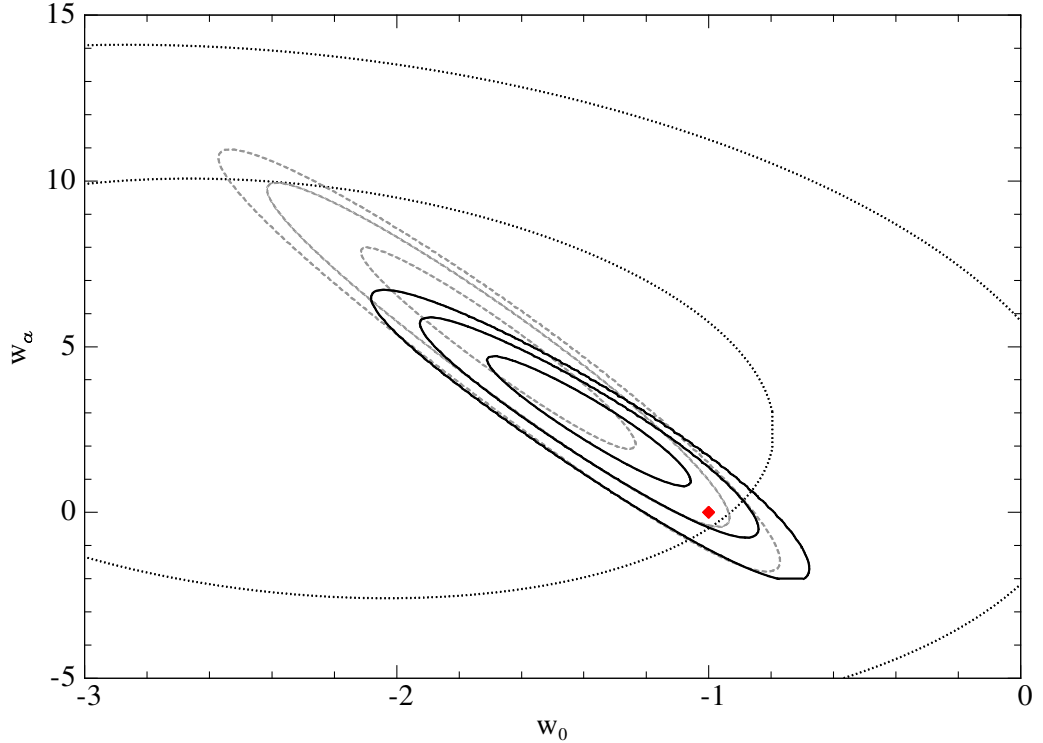


Figure 3.7. 68.3%, 95.4%, and 99.7% confidence interval for w_0 and w_a from fits to the gold sample supernova data. The dotted contours assume no priors; solid black contours constrain $\Omega_M = 0.26 \pm 0.03$ using the full gold sample; and the dashed gray contours constrain $\Omega_M = 0.26 \pm 0.03$ but exclude the 17 *HST* discovered supernovae from the gold sample. The concordance value for w_0 and w_a is shown in red.

out any of the dark energy models discussed in Sec. 2.5. If a Gaussian prior is applied to the matter density, $\Omega_M = 0.26 \pm 0.03$, the best fit changes to $w_0 = -1.38 \pm 0.24$ and $w_a = 2.8 \pm 1.49$. The concordance cosmology with a cosmological constant dark energy lies just within the 95.4% confidence interval in Fig. 3.7.

Figure 3.7 shows the two dimensional confidence contours in the w_0, w_a plane. The dotted contour shows the results of a likelihood fit with no prior constraints; the 68.3% contour does not even fit within the parameter space shown. The solid black and dashed grey contours include a prior of $\Omega_M = 0.26 \pm 0.03$. This is the same prior as above, but now the cosmology model has changed; the prior is only used to point out the improvement in accuracy on w_0 and w_a that comes with a tight constraint on Ω_M . The solid contours includes all 157 supernovae in the gold sample. The dashed grey contours only use 140 of these supernovae that were discovered by ground based

telescopes; the area of these contours is 1.9 times larger than the solid contours, and the best fit parameter values shift to $w_0 = -1.68$ and $w_a = 5.1$. The 6 highest redshift supernovae were all discovered with HST. A space platform provides excellent seeing and low background needed to detect faint, high redshift supernovae.

3.6 Conclusions

Type Ia supernovae are now widely used as standard candles to constrain cosmology parameters. The current dataset of type Ia supernovae contains a few hundred objects with varying degrees of photometric and spectroscopic coverage. Despite this fact, a subset of the well observed supernovae with low host galaxy extinction can already be used to detect a non-zero dark energy density at $> 99.99\%$ confidence, assuming a cosmological constant and arbitrary curvature. Including the assumption that the universe is spatially flat improves this constraint.

For more general dark energy models, including constant and time varying equations of state, two important factors lead to large improvements in the parameter estimation: high redshift supernovae and knowledge of the mass density. Removing the 17 *HST* discovered supernovae from the gold sample increases the uncertainty on the dark energy equation of state by a factor of almost 2. 10 of these 17 supernovae are at $z > 0.8$. Only 3 type Ia supernovae have been discovered above this redshift from the ground. Space based observations also provide access to the NIR, which is obscured by the sky brightness and variable absorption features in the atmosphere for ground based instruments. The zodiacal background in space is up to 500 times dimmer than the night sky between $1 - 1.7 \mu\text{m}$. A space telescope with NIR instrumentation can discover and observe the restframe optical lightcurves of thousands of high redshift type Ia supernovae. The NIR provides uniform measurements of the restframe *B* band lightcurves at high redshift and limits systematic uncertainties by improving color and extinction measurements at all redshifts.

A tight constraint on the mass density, Ω_M , can lead to a factor of 10 improvement in the uncertainty on w_0 , the time independent equation of state parameter. Current datasets are too limited to clearly define the ‘correct’ Ω_M prior, yet a prior is

| Model | Prior | Ω_M | w_0 | w_a |
|--------------------------|----------------------------|---------------------|------------------|-----------------|
| Flat Λ CDM | None | 0.309 ± 0.038 | - | - |
| Curved Λ CDM | None | $0.459 \pm 0.104^*$ | - | - |
| Flat, const w | None | 0.492 ± 0.066 | -2.40 ± 1.20 | - |
| Flat, const w^\dagger | None | 0.539 ± 0.045 | -3.81 ± 2.27 | - |
| Flat, const w | $\Omega_M = 0.26 \pm 0.03$ | 0.270 ± 0.030 | -0.94 ± 0.13 | - |
| Flat, w_0, w_a | None | 0.446 ± 0.129 | -2.34 ± 1.02 | 3.37 ± 4.17 |
| Flat, w_0, w_a | $\Omega_M = 0.26 \pm 0.03$ | 0.261 ± 0.030 | -1.45 ± 0.24 | 3.09 ± 1.49 |
| Flat, w_0, w_a^\dagger | $\Omega_M = 0.26 \pm 0.03$ | 0.260 ± 0.030 | -1.93 ± 0.43 | 6.29 ± 2.49 |

Table 3.1. Best fit cosmology parameters using the gold sample supernova. In the noted rows the 17 *HST* discovered supernovae are excluded from the sample.

* $\Omega_X = 0.978 \pm 0.188$

† Excludes 17 *HST* discovered supernovae.

almost always used when fitting type Ia supernovae. Prior knowledge of Ω_M is needed for precision dark energy measurements with future supernova surveys, and will be available as CMB, weak lensing, baryon acoustic oscillation and cluster abundance data improve. More sophisticated fitting methods which simultaneously fit type Ia supernova and weak lensing data are particularly useful for eliminating assumptions about prior distributions and correctly combining datasets. Combining the Fisher matrices for simulated datasets from future missions accomplishes this goal with a limited number of assumptions, see Sec. 6.2. For current datasets, the impact of the assumed priors should be carefully examined when considering constraints on dark energy. Table 3.1 summarizes the best fit parameter values for different cosmology models, with and without imposing a prior on Ω_M .

Published constraints on the dark energy equation of state with type Ia supernovae all rely on some assumption about the matter density. Proponents of a cosmological constant may favor a lower mass density since this leads to $w \sim -1$. Those who propose scalar field or brane world models may choose a different prior that leads to better agreement with their model. The current state of understanding does not allow strict limits to be placed on any of the dark energy parameters using type Ia supernova data alone. All the fits shown make a number of assumptions, both in the model (flatness and a Robertson-Walker metric), and the choice of prior constraints.

The focus of this section is to outline the fitting techniques and demonstrate the improvements in type Ia constraints when including high redshift supernovae and combining the data constraints from independent measurements.

CHAPTER 4

Science Driven Detector Requirements

The first 3 chapters of this thesis focus on a general discussion of dark energy, cosmology, and type Ia supernovae. They include an overview of the dynamics of the universe and the energy components that affect the expansion rate. Chapter 3 includes details about measuring the expansion history of the universe with type Ia supernovae and using these data to constrain the dark energy density and equation of state. The uncertainties on the dark energy parameters using the current supernovae dataset are dominated by the intrinsic dispersion in type Ia events. For these observations, instrumental noise and efficiency are not yet the limiting factor.

The next two chapters are focused on the NIR detector development for SNAP. One of the current SNAP science goals is to measure 2000 type Ia supernova from $0.1 < z < 1.7$ with a statistical accuracy of better than 2%. The uncertainty is limited by observing the restframe optical emission of all supernovae through 9 filters covering the visible and NIR spectrum. Beyond $z = 1$, the restframe B and V band emission is observed in the infrared. At the start of the SNAP project, available NIR detectors did not meet the noise, quantum efficiency, or size requirements for achieving the science goals. An infrared R&D program began in 2001, with the goal of producing large format ($2k \times 2k$), $1.7 \mu\text{m}$ cutoff detectors that could meet the science requirements.

The infrared R&D program has two parts. One part is the development of hybridized $1.7 \mu\text{m}$ HgCdTe and InGaAs detectors with Rockwell Scientific and Raytheon Vision Systems. The detectors undergo detailed characterization in SNAP NIR detector testing labs. Test results are shared with the vendors to improve understanding of device physics and detector performance. This is one of the most successful pro-

grams within SNAP. The collaborative effort between the testing labs and vendors has resulted in $2k \times 2k$ detectors with nearly 100% internal quantum efficiency and improved read noise.

The second part of the R&D program is deriving science driven requirements on detector performance. Detector requirements on noise and quantum efficiency flow down from high level science goals and mission level requirements on the lifetime and operating temperature. Trade studies during the design phase for SNAP were used to define the initial NIR detector specifications. The process of turning these specifications into science driven requirements involves detailed testing of NIR detectors and simulations of the detector performance.

4.1 SNAP Science Requirements

Work to define high level science requirements for SNAP is in progress. The existing requirements outlined in 00028-MW02 rev. C, *SNAP Mission Definition and Requirements Document* are given in Table 4.1. In addition to the requirements in Table 4.1, new requirements were included in the SNAP ROSES proposal for NASA. The high level science objectives are to “measure w , $w(z)$ and Ω_{DE} , with complementary measurements”, with “accuracy to distinguish time-varying models” or a “new law of gravity.” These high level requirements lead to requirements on the number and redshift distribution of type Ia supernovae, as well as accuracy requirements on the peak brightness and color. SNAP is designed to limit systematic uncertainties and reduce measurement errors below the systematic limit. The limiting systematic error and the statistical requirements for high redshift type Ia supernovae are not yet known. As a result, many of the sub-systems, such as the NIR detectors, are unable to define science driven performance requirements. In place of requirements, a set of draft level specifications for the NIR system provide a guide for the detector development. The specifications will be rewritten in terms of performance requirements once a flow down from dark energy constraints to supernova observables is in place.

Some draft level 2 requirements for the SNAP instrument have been derived from trade studies. Examples of level 2 requirements are the instrument’s field of view

| Number | Requirement |
|--------|---|
| 1.1 | Obtain over 2000 classified Type Ia supernovae for analysis in the redshift range $0.1 < z < 1.7$ |
| 1.2 | Derive supernova color and relative peak luminosity on average to 2% (statistical) |
| 1.3 | Obtain supernova spectrographic observations near peak intensity with a resolution R 100 over 0.35 to 1.7 microns wavelength. |
| 1.4 | Perform deep multi-color photometric and weak lensing surveys with field sizes of approximately 15 and 300 square degrees |

Table 4.1. Draft Level 1 Science Requirements.

and signal to noise limits at various points on the supernova lightcurve. The existing level 1 and 2 requirements place requirements on the detector size, wavelength range, and pixel pitch. Observing 2000 type Ia supernovae up to $z = 1.7$ within a 16 month deep supernova survey requires 36 visible detectors and 36 $2k \times 2k$ NIR detectors with a pixel scale of approximately 0.17 arcsec and sensitivity to at least $1.7 \mu\text{m}$. The performance specifications for the NIR detectors are more difficult to define based on the current draft requirements.

The initial NIR performance specifications are based on spreadsheet calculations of signal to noise at peak brightness of the supernova lightcurve. The QE specification is based on the best QE achieved in NIR detectors at the time, and the read noise and dark current are chosen to limit the detector noise contribution to less than half of the noise due to zodiacal light for each 300s exposure. The draft specifications from 00028-MW02 rev. C are shown in Table 4.2.

At the start of the R & D program, the largest $1.7 \mu\text{m}$ FPAs produced for science observations were $1k \times 1k$, and the read noise and quantum efficiency did not meet the SNAP specifications. Only one vendor, Rockwell Scientific, and one detector material, HgCdTe, were under consideration. To mediate risk and help drive performance improvements through competition, a second vendor, Raytheon Vision Systems, was funded to produce $1.7 \mu\text{m}$ HgCdTe FPAs, and InGaAs arrays were grown by Sensor's Unlimited and hybridized to both Rockwell and Raytheon multiplexers. The competition helped bring about large gains in detector performance, using both internally

| Parameter | Draft Specification |
|-----------------------------|---|
| Field-of-view | Approximately 0.34 square degrees |
| Plate Scale | 0.17 arcsec/pixel |
| Wavelength coverage | 900nm - 1700nm (1500nm required) |
| Detector Type | HgCdTe Hawaii-2RG (1.7 μm cut-off) |
| Detector Architecture | 36 HgCdTe 2k \times 2k Arrays with 18 μm pixels |
| Detector Array Temperature | 140 K |
| Detector Quantum Efficiency | > 60% average |
| Read Noise | 5 e^- (multiple samples) (8 e^- required) |
| Exposure Time | 300 sec (typical single exposures) |
| Dark Current | 0.02 $e^-/\text{s}/\text{pix}$ (0.2 $e^-/\text{s}/\text{pix}$ required) |
| Readout Time | 30 sec |
| Exposure control | Electronic |
| Filters | 3 bands |

Table 4.2. SNAP NIR detector specifications at the start of the infrared R&D program in 2001.

and SNAP funded development runs. As the detector development proceeded, work began on simulations of the performance requirements.

The goal of the SNAP NIR detector program is to produce detectors that achieve the SNAP science goals for constraining dark energy. Part of the NIR R&D effort is to refine the specifications in Table 4.2 into science driven detector requirements. The current work uses the statistical uncertainty limit (level 1 science requirement 1.2) on type Ia supernova peak magnitude as a measure of detector performance. The simulations presented develop the machinery to estimate the uncertainty in supernova peak brightness measurements as a function of the NIR detector noise and quantum efficiency. Spreadsheet signal to noise calculations are replaced with a Java based simulation package that can simulate lightcurves for supernovae in all 9 SNAP filters. The package includes distance modulus and cosmology fitting to extract errors on the individual supernova observations as well as the dark energy parameters. The expected performance of the NIR system for different combinations of detector read noise, dark current, and quantum efficiency is presented below.

4.1.1 Requirements on w_0 and w_a

The draft requirements do not include any statement about constraints on the dark energy equation of state. There are a range of supernova surveys that meet the first two requirements, but lead to very different constraints on dark energy. Work is ongoing to redefine the requirements in Table 4.1 to satisfy a requirement on the measurement uncertainty for the equation of state parameters w_0 and w_a . A reasonable assumption for constraints on the equation of state comes from the Dark Energy Task Force (DETF), which calls for a factor of ten improvement on the combination of w_0 and w_a compared to projected constraints from current and ongoing experiments. To achieve a factor of ten improvement on the equation of state, SNAP must constrain $\sigma_{w_0} < 0.04$ and $\sigma_{w_a} < 0.12$. Meeting this goal requires a high redshift supernova survey combined with constraints from weak lensing, baryon oscillation and/or CMB data. Constraints on w_0 and w_a for future surveys are presented in Ch. 6.

4.2 Simulation Overview

Simulations of type Ia supernova observations for different combinations of NIR detector read noise, dark current, and quantum efficiency are used to define the detector performance requirements. Detailed simulations are presented for supernovae at a redshift of 1.7, the cutoff for the SNAP supernova program. SNAP will observe supernovae beyond $z = 1.7$, but with limited spectrographic information. The simulations show that increased quantum efficiency provides the largest gains in accuracy for supernovae measurements. The impact of improved quantum efficiency is magnified for variable objects like supernovae, which are observed a number of times during the course of their lightcurves. The brightest points are often photon noise dominated and are weighted most heavily in lightcurve fits. HgCdTe detectors have now achieved internal quantum efficiencies near 100%, and improvements in read noise over the past few years have led to detectors that exceed the performance required by the initial detector specifications.

The simulations use a Java based software package called SNAPsim [Kuznetsova

et al., 2005]. The code simulates observations of various astronomical objects with a user defined telescope, instrument, and observing strategy. Optional weather and seeing constraints can be added for ground based observations. For variable objects like type Ia supernovae, a template lightcurve is fit to the observations in each filter. Multi-color lightcurves are used to derive a distance modulus and dust extinction for each object. Simulations of type Ia supernovae at $z = 1.7$ are used to study the impact of detector performance on distance modulus measurements.

Detector properties measured in laboratory experiments are used as inputs to the simulations. The NIR detector requirements are based on simulations of supernova only; the role of the NIR detectors in weak lensing shape measurements is not yet defined. The NIR observations are used to measure photometric redshifts for weak lensing, which requires high S/N, similar to the supernova observations. The dominant noise source for the supernova observations is the zodiacal background flux. For the detectors to meet the requirements for Ia supernova photometry, the total detector noise must be much less than the noise due to zodiacal photons in a 300 s exposure. This constraint ensures that all NIR observations with an exposure time greater than 300 s will be zodiacal background, not detector noise, dominated. The shortest exposure time in the four baseline SNAP surveys is 300 s. Using the supernova observations to define the NIR detector requirements ensures that measurements of all objects in the four survey fields will be zodiacal light limited.

The detector properties are parameterized within the simulation. All of the pixels have the same read noise, dark current, and quantum efficiency. Realistic distributions of the NIR detector noise and quantum efficiency are not included in the simulation and are difficult to predict based on laboratory measurements. All of the detectors tested for SNAP are engineering grade developmental detectors. The median or modal performance of the pixels meets the science requirements, however 1 – 10% of the pixels lie in the tail of the pixel distribution, more than 4σ from the mean (σ is defined as the RMS deviation). Science grade detectors should have a much narrower pixel distribution, but the degree of improvement between science and engineering grade detectors will not be known for some time. One of the challenges

facing the NIR program is developing a requirement on the pixel noise and quantum efficiency distributions.

The simulations use the baseline observing sequence for SNAP; each field is imaged in all 9 filters on a 4 day cadence. Each observation consists of four, 300 s dithered exposures for a total integration time of 1200 s. The NIR filters cover twice as much area in the focal plane, and get two such observations at each pointing. The supernovae are assumed to be point sources with approximately diffraction limited point spread functions at all wavelengths.

4.3 Source Parameterization

The simulation procedure begins with a list of targets, a model for the backgrounds and cosmology, and a sequence of observations for each target. The targets are represented by a redshift and a time dependent spectrum. Observations of the target objects are ‘realized’ and saved for future processing. The targets are type Ia supernovae, observed every 4 days in each of the 9 SNAP filters. The simulated supernovae have no dust extinction, intrinsic magnitude dispersion, or other potential sources of systematic error, although code to implement these effects is available in simulation package. Each event is identical except for its redshift and statistical fluctuations. This decouples any systematic errors from the statistical uncertainties introduced by the detector performance.

4.3.1 Lightcurve Templates

Supernova lightcurves are simulated using restframe templates for a type Ia supernovae in units of $\text{ergs}/\text{cm}^2/\text{s}/\text{\AA}$ as a function of epoch (from -20 to +70 days from peak) and wavelength [Nugent et al., 2002]. For epochs greater than 70 restframe days the template is extrapolated using a wavelength dependent decay time that varies from 27 – 65 days. The template spectra at peak brightness are shown in Fig. 4.1 in both the supernova restframe and at a redshift of 1.7.

The templates are normalized to the Vega magnitude system, where the magnitude of Vega at 10 parsecs is 0 in all bandpasses. The type Ia absolute magnitude is -19.46

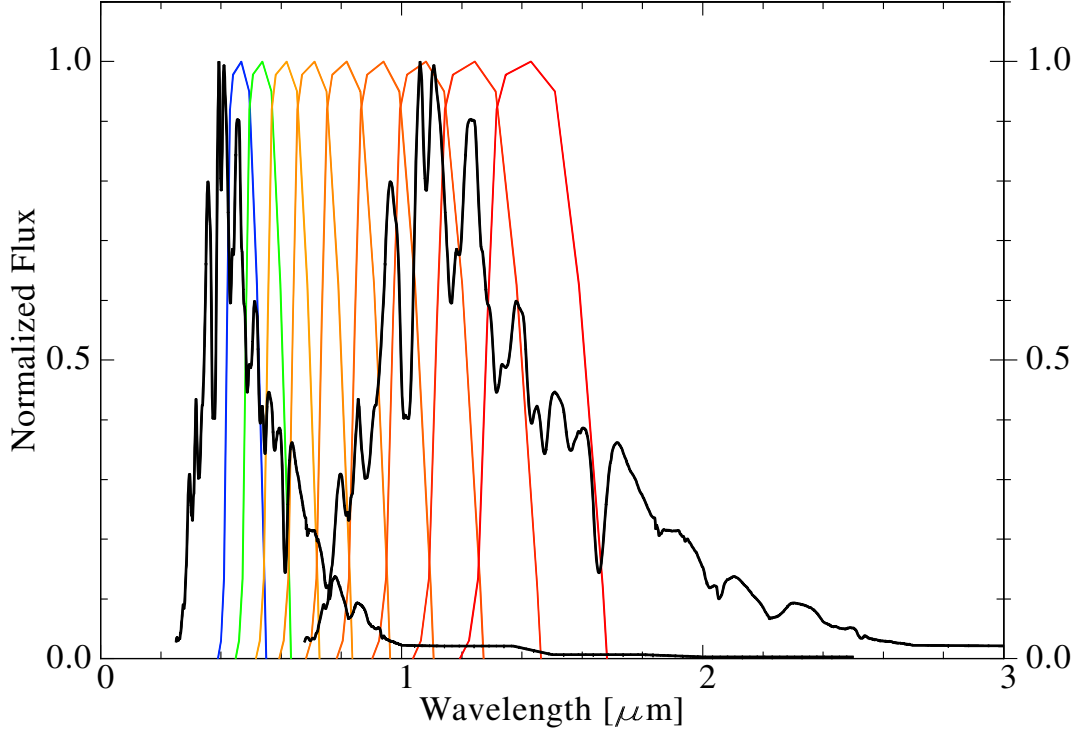


Figure 4.1. Simulated spectrum of a type Ia supernova at peak brightness in the restframe and at $z = 1.7$. The 9 SNAP filter bandpasses are shown for reference.

for a Hubble constant, $H_0 = 60 \text{ km s}^{-1} \text{ Mpc}^{-1}$. The Hubble constant sets the overall scale and does not affect any of the results presented below. The absolute source luminosity for each point (epoch, λ) in the template is

$$L(\lambda) = F_{src}(\lambda) 4\pi (10pc)^2 \left(\frac{h_0}{0.6}\right)^2 10^{-(19.46/2.5)} \lambda d(\ln \lambda) \quad (4.1)$$

in $\text{erg/s}/\ln(\lambda)$. F_{src} is the normalized flux from the templates. The templates assume $h_0 = 0.6$, ($H_0 \equiv h_0 100 \text{ km s}^{-1} \text{ Mpc}^{-1}$); the factor of $h_0/0.6$ corrects the distances for the ‘true’ value of h_0 in the simulation. The final factor of $\lambda d(\ln \lambda)$ converts from per λ to per $\ln \lambda$ which preserves the integrated flux when redshifting the source without having to re-normalize. In these units the template is redshifted by simple z scaling, $\lambda = \lambda_{restframe}(1+z)$. The effect of time dilation and stretch is to rescale the time so that $t = t_{template}(1+z)s$. The simulations below assume $s = 1$ for all supernovae.

After generating and redshifting the spectrum, propagation effects including host galaxy dust, Milky Way dust, atmospheric transmission (for ground based observatories), telescope transmission, filter transmission and detector quantum efficiency are applied (in the simulations presented the host galaxy and Milky Way dust extinction are set to zero). The final step is to calculate the source distance based on the input cosmology. The detector noise, dark current, and quantum efficiency simulations assume a flat, Λ CDM cosmology with $\Omega_\Lambda = 0.7$, $\Omega_M = 0.3$, and $w = -1$ ¹. The purpose of these simulations is to derive the statistical uncertainty on the distance modulus, thus the assumed cosmology does not greatly impact the results. The distance modulus depends on the co-moving distance to each supernova. For a flat, Λ CDM cosmology the co-moving distance is given as

$$r(z) = \frac{c}{H_0} \int_0^z \frac{dz}{\sqrt{\Omega_M (1+z)^3 + 1 - \Omega_M}}. \quad (4.2)$$

The observed flux for a source with luminosity L is

$$F_{obs} = \frac{L}{4\pi r(z)^2 (1+z)^2}, \quad (4.3)$$

where $r(z)(1+z)$ is the luminosity distance, $d_L(z)$. The two factors of $(1+z)$ account for the energy redshift and time dilation. The distance modulus, μ , is proportional to the logarithm of the flux, or in terms of the luminosity distance,

$$\mu(z) \equiv m - M \propto -2.5 \log_{10} F_{obs} \propto 5 \log_{10} d_L(z; H_0, \Omega_M, \Omega_\Lambda, w_0, w'). \quad (4.4)$$

The source flux is measured by the the mean number of photon counts at the detector,

$$COUNTS = A_{tel} t \int_{\lambda_{min}}^{\lambda_{max}} F_{obs}(\lambda) \left(\frac{\lambda}{hc} \right) T(\lambda) d\lambda, \quad (4.5)$$

where A_{tel} is the telescope collecting area, t is the exposure time, and $T(\lambda)$ contains all

¹The simulations were carried out prior to the release of the WMAP year 3 data [Spergel et al., 2006], when the concordance value for the mass density was $\Omega_M \sim 0.3$.

the transmission effects due to dust, atmosphere, filters, optics, and detector quantum efficiency. The factor of λ/hc converts from energy units to photons. Calibration information translates the counts into an apparent magnitude in each filter. The variance for each measurement is the mean signal plus sky background and detector noise contributions.

4.3.2 Flux Variance and Zodiacal Light

The redshifted templates and the cosmology from Sec. 4.3.1 are used to determine the photon counts recorded by the detectors at each epoch through each filter. The flux variance is calculated based on the source flux, the background zodiacal light flux, and the detector noise and quantum efficiency. The flux variance is given as

$$\sigma^2 = COUNTS + F_{zodi} A_{tel} A_{PSF} QE N_{exp} t + (RN^2 + DC t) N_{exp} N_{pix}, \quad (4.6)$$

where F_{zodi} is the zodiacal flux in $\gamma/m^2/arcsec^2/s$ and A_{PSF} is the area of the point spread function. The PSF is diffraction limited in the NIR, so A_{PSF} grows as λ^2 and the integrated zodiacal light increases for the redder filters despite a declining zodiacal spectrum beyond $0.61 \mu m$. The exposure time, t , is 300 s for the SNAP supernova survey, with $N_{exp} = 4$ exposures per pointing for the visible filters and $N_{exp} = 8$ for the larger NIR filters (the default parameters for the SNAP deep survey, see Sec. 1.2). Equation (4.6) assumes the dark current is Poisson distributed and that the detector's conversion gain ($e^-/COUNT$) is one.

The dominant noise source should be the shot noise on the source flux and zodiacal background light, not the detector read noise and dark current contributions. The zodiacal background, shown in Fig. 4.2, is due to sunlight scattered off dust grains. SNAP chooses to survey near the north and south ecliptic poles where the zodiacal background is minimized. Aldering [2001] studied the observed background in the SNAP north field and found a broken log-linear relation provides the best fit to the

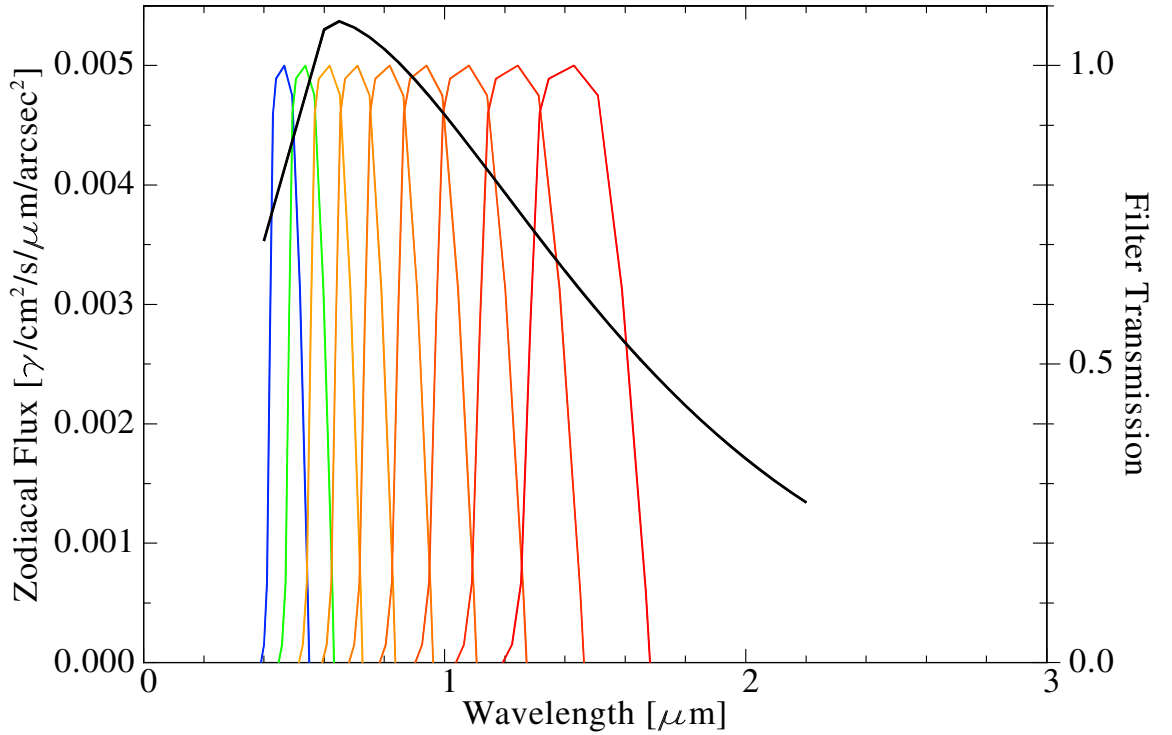


Figure 4.2. Zodiacal flux at the north ecliptic pole from Aldering [2001]. The 9 SNAP filter bandpasses are over-plotted for reference.

zodiacal spectrum;

$$\begin{aligned}
 f(\lambda) &= 10^{-17.755} && \text{for } 0.40 < \lambda < 0.61, && (4.7) \\
 f(\lambda) &= 10^{-17.755-0.730(\lambda-0.61\mu\text{m})} && \text{for } 0.61 < \lambda < 2.20,
 \end{aligned}$$

where f is in units of $\text{erg cm}^{-2} \text{s}^{-1} \text{\AA}^{-1} \text{arcsec}^{-2}$. This is the zodiacal spectrum used in SNAPsim. The spectrum is convolved with the telescope transmission and the filter response functions (see Fig. 4.2) then integrated over the filter bandpass to calculate the photon flux at the detector surface, shown in Table 4.3. The filters are logarithmically spaced with $\lambda = \lambda_0 * 1.15^n$ for the n^{th} SNAP filter². The CCD

²The filter spacing, like many of the telescope parameters, is not yet finalized. Recent work on filter design indicates that a spacing of 1.16^n may be optimal. Changes of this nature have a minimal effect on the results presented here, and in many cases improve measurement uncertainties by optimizing the observing efficiency.

| SNAP Filter | Central λ [nm] | Zodiacal Flux [$\frac{\gamma}{\text{srs}}$] | PSF Area [sr] | Zodiacal Rate [$\frac{\gamma}{\text{s}}$] | N_{pix} |
|-------------|---------------------------|--|------------------------|--|-----------|
| 0 | 461.5 | 4.326×10^{11} | 8.36×10^{-13} | 0.362 | 3.62 |
| 1 | 530.8 | 5.927×10^{11} | 9.16×10^{-13} | 0.543 | 3.96 |
| 2 | 610.4 | 7.593×10^{11} | 1.02×10^{-12} | 0.776 | 4.42 |
| 3 | 701.9 | 8.853×10^{11} | 1.16×10^{-12} | 1.027 | 5.02 |
| 4 | 807.2 | 9.837×10^{11} | 1.35×10^{-12} | 1.328 | 5.84 |
| 5 | 928.3 | 8.306×10^{11} | 1.59×10^{-12} | 1.320 | 6.88 |
| 6 | 1067.5 | 1.112×10^{12} | 2.25×10^{-12} | 2.502 | 3.31 |
| 7 | 1227.7 | 1.118×10^{12} | 2.68×10^{-12} | 2.996 | 3.95 |
| 8 | 1411.8 | 1.080×10^{12} | 3.25×10^{-12} | 3.506 | 4.78 |

Table 4.3. Zodiacal flux at the detector surface (equivalent to 100% detector QE). The zodiacal rate is per aperture for a point source through each SNAP filter.

pixels have a $10.5 \mu\text{m}$ pitch, and the larger HgCdTe pixels have a $18 \mu\text{m}$ pitch. For a focal length of 21.84 m this gives a pixel area of 2.31×10^{-13} sr in the visible and 6.79×10^{-13} sr in the infrared, or a pixel scale of 0.1 arcsec and 0.17 arcsec, respectively. The PSF area assumes a diffraction limited spot with radius $\theta_r = 1.22\lambda/D$ plus charge diffusion, aberrations, and attitude control jitter. The number of pixels for the aperture calculation is given in the last column of Table 4.3. The zodiacal light is an irreducible background that limits the photometric precision and establishes a scale for detector noise; the detector specifications require a total detector noise less than half the zodiacal background for a 300 s exposure.

4.3.3 Simulated Lightcurves

Simulated lightcurves for a $z = 1.7$ supernova and the default SNAPsim detector parameters (QE $\sim 60\%$, RN = $6 e^-$, and DC = $0.1 e^-/\text{pixel/s}$) are shown in Fig. 4.3. Figure 4.3 illustrates the importance of NIR observations for high redshift supernovae. The final 3 filters capture most of the photons from this distant source. There is little or no restframe ultra-violet emission redshifted to the optical.

The simulated lightcurves in Fig. 4.3 are fit to templates with 3 independent parameters, flux at maximum (F_{max}), stretch (s), and time of peak brightness (T_0). The lightcurve fits are used as input to the distance modulus (μ) fitter. The individual lightcurve fits do not account for host galaxy or Milky Way dust extinction,

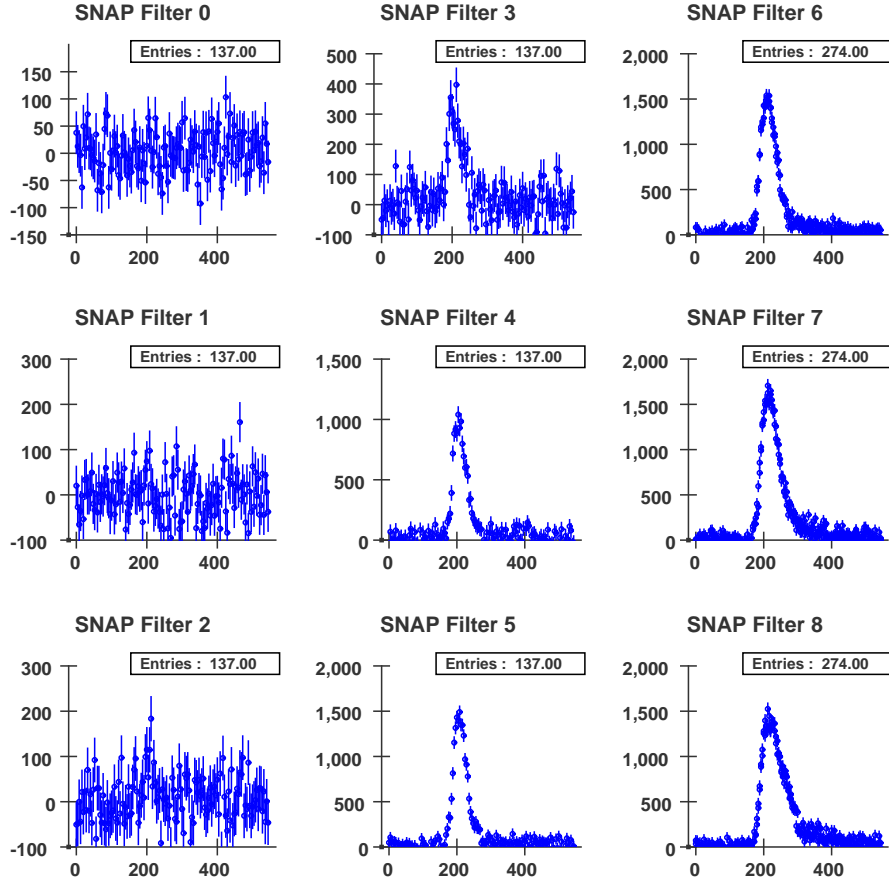


Figure 4.3. A simulated $z = 1.7$ type Ia supernova lightcurve, observed every 4 days through the nine SNAP filters. The X axis is in days and the Y axis is the observed photon count per observation. ‘Entries’ specifies the total number of observations for each filter. The larger NIR filters have twice the number of observations, and the NIR detectors are assumed to have $QE = 60\%$, $RN = 6 e^-$, and $DC = 0.1 e^-/pix/s$.

so the dust parameters are fit along with μ . SNAPsim fits the Cardelli, Clayton and Mathis[Cardelli et al., 1989] dust parameters A_V and R_V directly from the multicolor lightcurves, which can lead to slightly larger uncertainties in the distance modulus compared to traditional techniques. The supernova stretch is also refit using the multi-color data. Stretch and dust are the two parameters that can introduce the largest errors on μ ; other parameters have a lesser effect and are not considered at this time.

4.4 NIR Detector Parameterization

NIR detectors are parameterized in terms of their quantum efficiency, read noise and dark current. Early in the simulation process it became apparent that the read noise and dark current could be combined into a single total detector noise parameter. Simulations exploring the read noise and dark current parameter space are discussed in Sec. 4.4.2. The rest of the results presented assume zero dark current and replace the read noise with the total noise. Total noise is easy to measure in laboratory experiments for different Fowler and up the ramp sampling modes (these modes are defined in Sec. 5.3.5), and limits the parameter space of the simulations. Also, using a measurement of the total noise eliminates the assumption that the dark current is Poisson distributed. The read noise and dark current specifications are now consolidated into a single total noise requirement. This is made possible by the fixed photometric exposure time of 300s for all SNAP surveys.

4.4.1 Lightcurve Signal to Noise

As a supernova lightcurve brightens and fades, the S/N varies in each filter. Changes in quantum efficiency impact the S/N for each observation on the supernova’s lightcurve. In the case of photon or background (zodiacal) limited seeing, the first two terms in Eq. 4.6 dominate, and the noise scales as \sqrt{QE} . Since the signal scales directly with QE, $S/N \propto \sqrt{QE}$ for photon limited observations. At peak brightness, the observations are in this photon dominated regime. S/N for a $z = 1.7$ supernova in the last NIR filter is plotted for selected QEs in Fig. 4.4. The signal does not include any fluctuations due to shot noise on the source photons or detector noise. The noise calculation assumes a total detector noise of $10 e^-$, higher than the initial specification of $5 e^-$, but typical of values measured in the detectors from the second SNAP development run.

The S/N vs. epoch plots in Fig. 4.4 are useful for determining the time when a supernova can be identified. The detection threshold for early identification of supernovae candidates is a $S/N > 3$ on the rising edge of the lightcurve. As the QE improves from 60% to 95% each supernova is detected a few observations earlier,

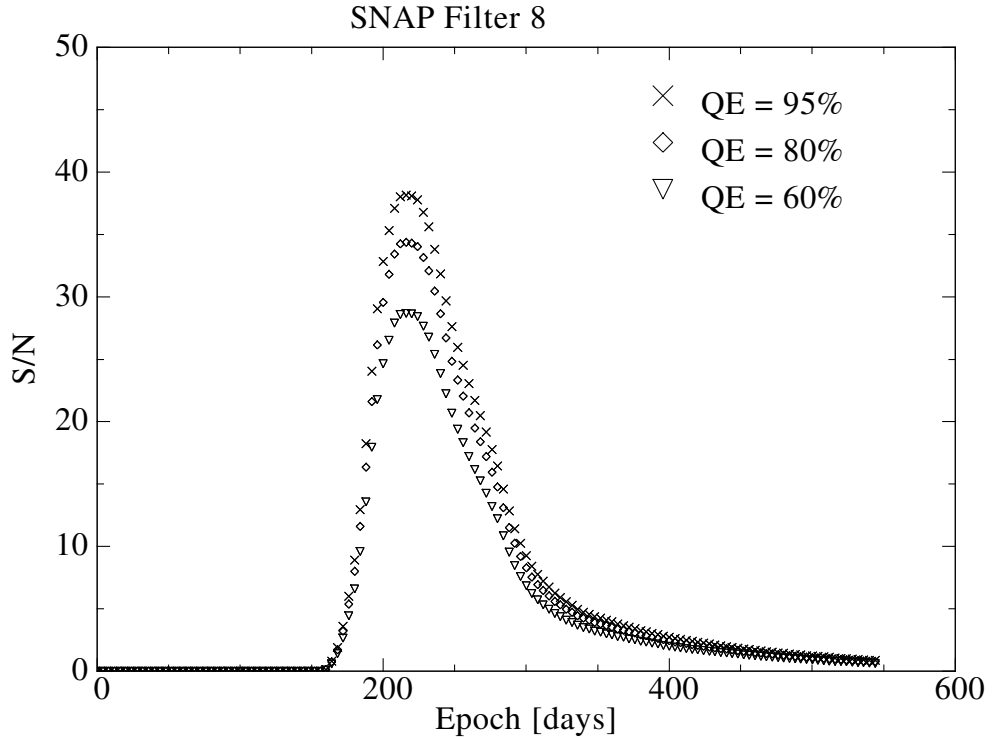


Figure 4.4. Signal to Noise vs. epoch in SNAP filter 8, the reddest SNAP filters, assuming a total detector noise of $10e^-$ per 300s exposure. The detection threshold for type Ia supernovae is $S/N > 3$.

leaving additional time to schedule spectroscopic followup.

4.4.2 Detector Read Noise and Dark Current Trade Studies

The uncertainty on distance modulus estimates depends on the NIR detector read noise and dark current. The effects of read noise and dark current are simulated for two different detector quantum efficiencies: 60% and 95%. The simulations in Sec. 4.4.3 address the effect of quantum efficiency in more detail. 60% is the best quantum efficiency achieved at the start of the SNAP HgCdTe development and 95% is the maximum quantum efficiency for HgCdTe detectors that have an anti-reflective coating. Without an anti-reflective coating the high index of refraction of the CdTe substrate (or the passivation layer in substrate removed detectors) reflects about 20% of the light; the coating reduces the reflection to 5%. The simulations assume constant efficiency across the entire detector bandpass from $0.9 - 1.7 \mu\text{m}$.

Contours of fixed error on the distance modulus are plotted as a function of read

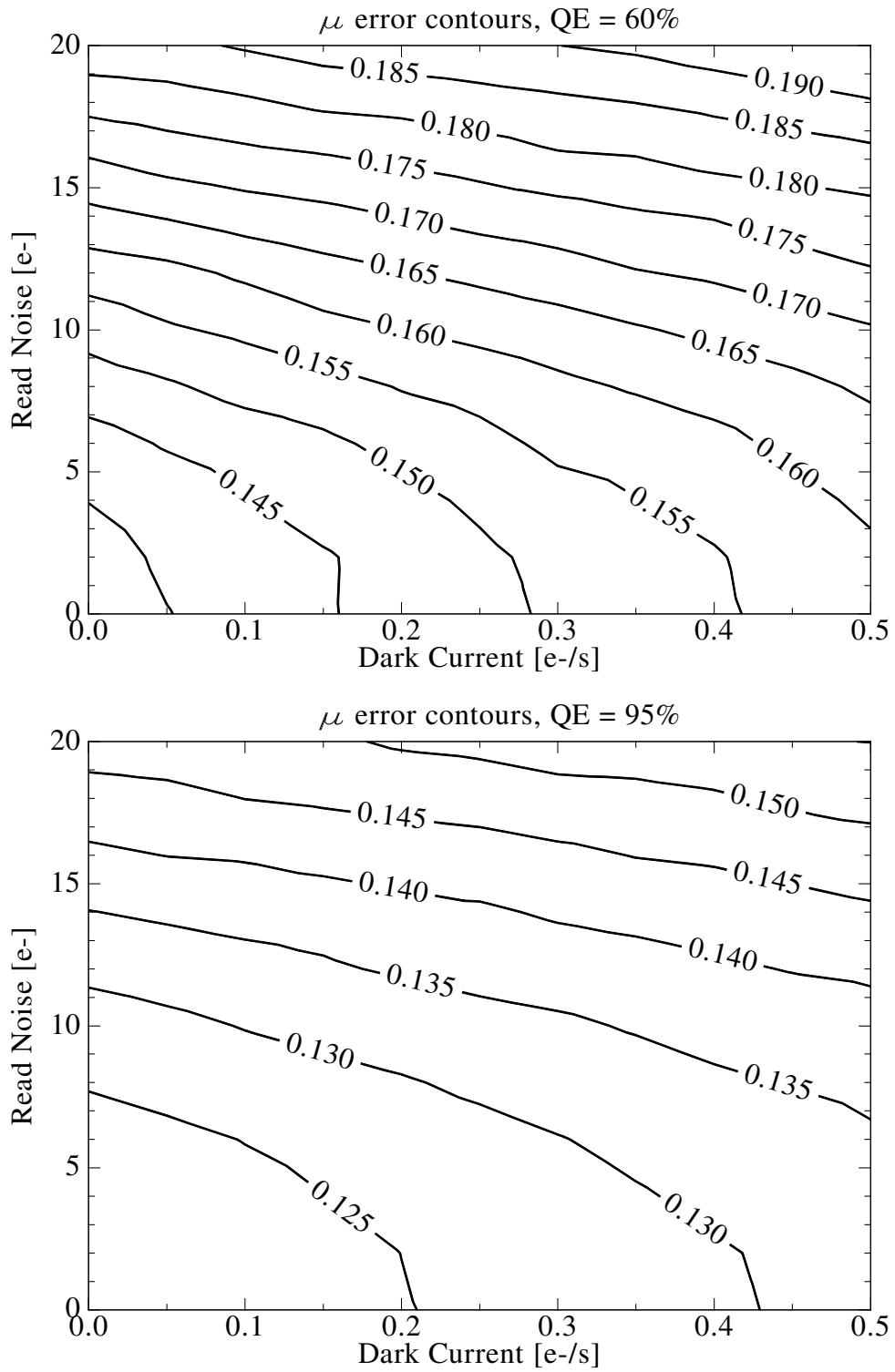


Figure 4.5. Contours of constant parameter error for the distance modulus, μ , for type Ia supernova at $z = 1.7$. The top plot assumes QE=60%, bottom: QE=95%.

noise and dark current in Fig. 4.5. Results are shown for a type Ia supernova at a redshift of 1.7. For a fixed quantum efficiency, contours of constant error follow contours of constant total noise, as expected. The distance modulus is proportional to the logarithm of the peak flux; for small σ_μ , the percent error is approximately σ_μ . All calculations of the μ error use the same visible lightcurves, which are only realized once to save time and ensure that only variations due to the NIR detector performance are studied. For stability, the fit errors are calculated from the average of 4 realizations of each NIR lightcurve.

Figure 4.5 clearly shows that read noise dominates the detector noise contribution for the parameter space studied. The relatively short 300 s exposure time lessens the impact of the dark current relative to the RN^2 term in Eq. (4.6). For example, assuming a read noise of $8 e^-$ and a dark current of $0.1 e^-/\text{s}/\text{pixel}$ the total variance due to detector noise for a 4 pixel aperture and four 300 s exposures in filter 8 is $1504 e^-$. If three 400 s exposures are used the variance drops to $1248 e^-$, while two 600 s exposures lowers it to $992 e^-$. Fewer, longer exposures are obviously favored for detectors that are read noise dominated. However, the shorter exposure time allows more dithers for better reconstruction of diffraction limited seeing (which is most important for gravitational weak lensing measurements) and better cosmic ray rejection, particularly for the visible CCD detectors which do not offer non-destructive readout. The information lost due to cosmic rays and fewer dithers may outweigh the gains from improved detector noise in the NIR.

The importance of high quantum efficiency is also illustrated in Fig. 4.5. If the quantum efficiency is only 60%, the total detector noise must be kept below $5 e^-$ for each 300 s exposure to achieve a μ error of 0.14 mag, while the same accuracy can be achieved with more than $15 e^-$ noise and substantial dark current with high quantum efficiency detectors. For the μ errors to be in the same range as the stretch corrected intrinsic dispersion of 0.10 – 0.15 mag, high quantum efficiency is essential. This goal can only be achieved with longer exposures or a larger telescope aperture when the quantum efficiency is 60%.

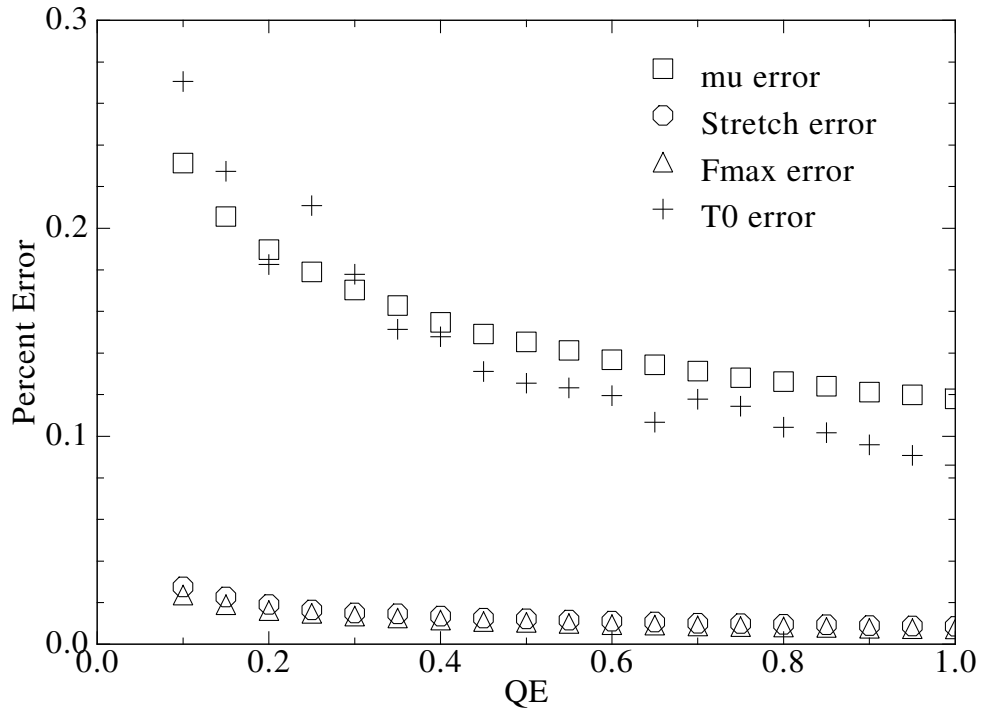


Figure 4.6. Lightcurve parameter and μ errors for a $z = 1.7$ type Ia supernova assuming noiseless NIR detectors.

4.4.3 Quantum Efficiency vs. Total Noise Trade Studies

The previous simulations focused on regions of the detector parameter space that represented the performance measured in the first SNAP detector development run. The second detector development run (including some internally funded FPAs) showed great improvements in quantum efficiency and a modest reduction in noise. Raytheon SB-301 #598141 has 80% QE from $0.9 - 1.7 \mu\text{m}$ with no anti-reflective coating. Without a coating the reflection at the detector surface is 20%; the internal QE of this device is near 100%. This FPA also has a low Fowler-1 read noise of $16 e^-$, but high dark current at 140 K prevented effective noise reduction at higher Fowler numbers. Rockwell Scientific H2RG #102 also showed high QE and improved noise. This detector has an anti-reflective coating applied, and the QE is over 90% from $0.9 - 1.7 \mu\text{m}$. The single read noise is slightly higher than RVS #598141, but this device has very low dark current, and Fowler-16 sampling at 140 K reduces the total noise to less than $10 e^-$ in a 300 s exposure.

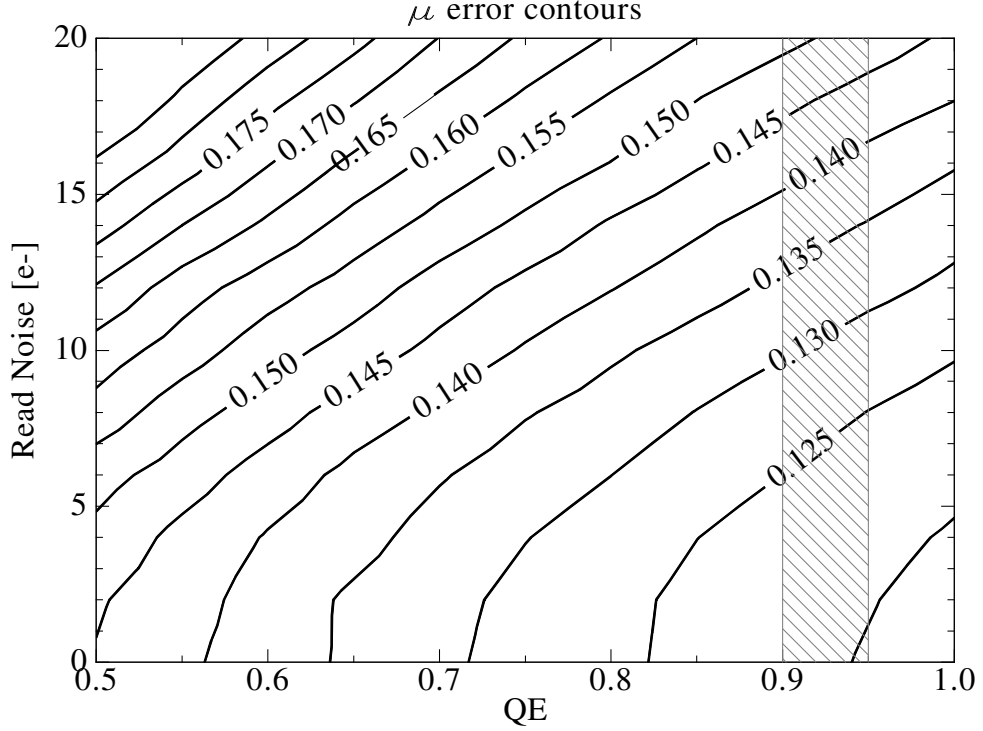


Figure 4.7. Distance modulus uncertainty contours for total NIR detector noise up to $20e^-$. The expected QE for SNAP science grade devices is shown in the shaded region.

The quantum efficiency studies explore the QE vs. total detector noise phase space. The simulations are similar to the read noise vs. dark current simulations above, again assuming a type Ia supernova at $z = 1.7$. The simulated data include a single realization of each lightcurve in the 6 visible filters, followed by 4 realizations of each lightcurve in the NIR filters for each QE and RN pair. The μ errors are derived from a combination of all the lightcurve fits; the lightcurve parameter errors in Fig. 4.6 are presented for SNAP filter 8, the reddest NIR filter.

The parameter errors vs. QE are shown in Fig. 4.6 for a noiseless detector. These curves represent the best performance possible for the default SNAP observation strategy of four 300 s exposures in each filter every four days (eight exposures for the larger NIR filters). The percent error on the lightcurve parameters F_{max} and s are small and are not greatly impacted by the overall NIR QE. However, the combination of the multiple lightcurve fits produces a distance modulus error that is more sensitive to the NIR QE.

A more detailed view of the μ error is shown in Fig. 4.7. The contours in the total noise vs. QE plane show that improved quantum efficiency is the most important factor in achieving precision observations of distant supernovae. By improving the QE from 60 to 80% the tolerance on the read noise to achieve $\sigma_\mu = 0.14$ mag increases by more than a factor of two. The best engineering grade detectors delivered thus far have a median total noise of $10 e^-$ per 300 s Fowler-16 exposure and $\text{QE} > 90\%$. The statistical uncertainty on the distance modulus is only 0.13 mag for these parameters. A perfect detector with 100% internal quantum efficiency and no noise results in an uncertainty of 0.12 mag. The best R&D detectors deliver an uncertainty for each supernova within 1% of the best possible performance for the baseline observing program. When averaging observations of 100 supernovae the accuracy of the best R&D detectors is within 0.1% of a perfect NIR detector. The only way to improve the uncertainty in μ is to modify the observing cadence, aperture area, or exposure time. With $\text{QE} > 90\%$ and $\text{RN} < 10 e^-$ observations are zodiacal light limited (the detector noise is less than 20% of the total noise due to the zodiacal background plus read noise and dark current). Reproducing the high quantum efficiency from the second lot of SNAP HgCdTe detectors while continuing to reduce the noise and improve the pixel distributions is now the goal of the SNAP detector development effort.

4.5 Establishing Draft level Detector Requirements

The distance modulus errors derived from simulations of type Ia supernovae as a function of detector noise and quantum efficiency provide the information necessary to derive the detector level requirements. As an example, consider draft level requirement 1.2, which states that the statistical uncertainty for type Ia supernovae must be less than 2%. This is not the final requirement for supernova photometry, but it is useful to outline the process used to define the NIR detector requirements.

The statistical uncertainty depends on the number of supernovae observed and the bin size. The default distribution for a 16 month survey with 2000 type Ia supernovae followed spectroscopically is shown in Fig. 4.8. The redshift distribution of the the SNAP supernova survey is constrained by the number of supernovae discovered at

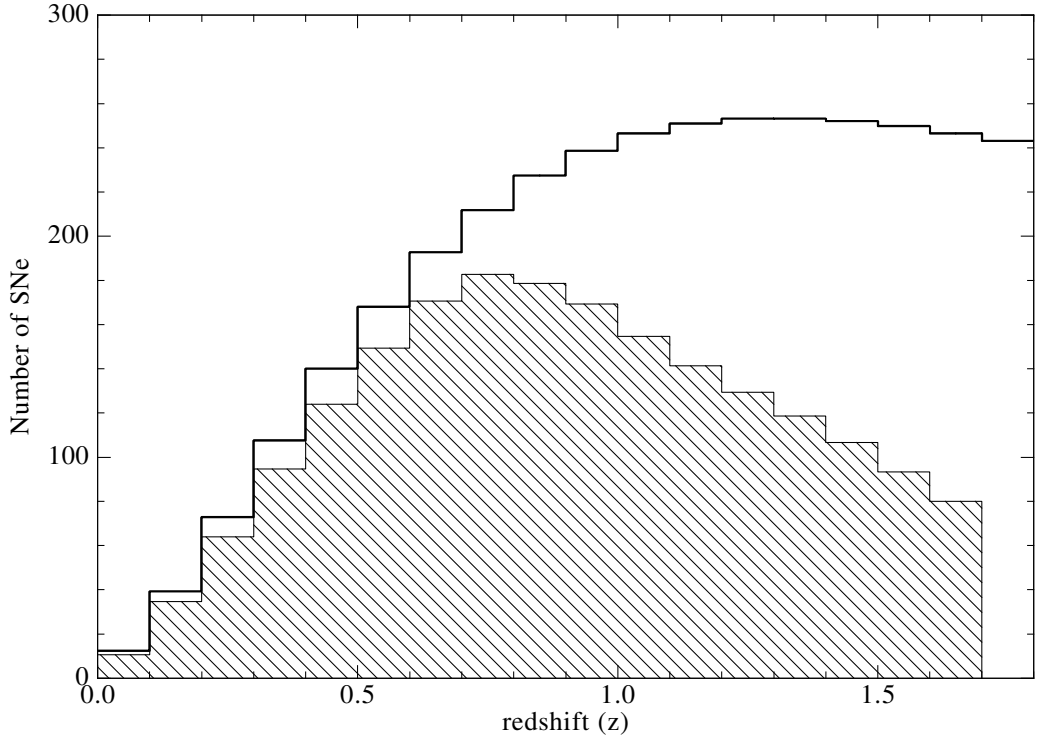


Figure 4.8. The redshift distribution of type Ia supernovae in one 16 month SNAP deep survey. The solid line shows the number of events discovered in each redshift bin. The shaded region includes all events with spectroscopic follow-up near peak brightness.

each redshift and the spectroscopic follow-up time. A type Ia supernova at $z = 1.7$ requires approximately 8 hours of spectroscopic follow up, and the time scales as $(1 + z)^6$ for $z > 1$. A large number of supernovae will be discovered at $z > 1$, but only selected events are scheduled for spectroscopic follow up. Studies to optimize the redshift distribution to constrain w_a show that a larger number of high redshift events is preferred [Miquel, 2005]. Work of this nature will lead to more rigorously defined high level science requirements. The current example assumes the default redshift distribution, which includes approximately 80 supernovae at $z = 1.7$.

The statistical accuracy in each redshift bin depends on both the measurement uncertainty due to detector noise and the supernova intrinsic dispersion. The intrinsic B band dispersion of type Ia supernovae is $0.3 - 0.5$ mag [Hamuy et al., 1995] prior to any lightcurve width or color correction. Empirically derived relationships between the peak B band magnitude and lightcurve width/color reduce the dispersion to

0.1 – 0.17 mag after standardizing nearby supernovae. Many of the normalization methods achieve errors of 0.09 – 0.12 mag when using a subsample of ‘well observed’ supernovae, with multiple colors and epochs beginning near peak brightness [Riess et al., 1996, Perlmutter et al., 1997, Phillips et al., 1999]. No supernova to date has been observed with the level of photometric coverage that every one of the more than 2000 supernova in the SNAP deep field will receive. A dispersion of 0.12 mag for the corrected distance modulus is chosen as a conservative estimate for type Ia supernovae in the SNAP deep survey.

To satisfy draft level requirement 1.2, the statistical uncertainty on the supernova peak magnitude measurements must obey

$$\sqrt{\frac{\sigma_{stat}^2 + \sigma_{intrinsic}^2}{N_{SNe}}} \leq 0.02, \quad (4.8)$$

where N_{SNe} is the number of supernovae in the redshift bin (recall that for small magnitude errors, the magnitude error is equal to the percent error). At $z = 1.7$, there are 80 supernovae with $\sigma_{intrinsic} = 0.12$ mag. This sets a requirement on the statistical uncertainty: $\sigma_{stat} < 0.133$. The contours in Fig. 4.7 define a portion of the detector noise and quantum efficiency parameter space that meets this goal. The statistical uncertainty is $\sigma_{stat} = 0.13$ for infrared detectors with QE = 90% from 900 – 1700 nm and a total noise of $10e^-$ per 300s exposure. Raytheon SB-301 # 141 can meet the noise requirement if cooled to 100 K to reduce the dark current, and the quantum efficiency can be achieved by adding an anti-reflective coating. The latest lot of Rockwell HgCdTe detectors (H2RG #102 and #103) meets both of the requirements at 140 K, the SNAP operating temperature.

The process for determining detector requirements from high level requirements on the accuracy of type Ia supernova peak magnitude measurements is now in place. For the current level 1 science requirements in controlled document 00028-MW02 rev. C, *SNAP Mission Definition and Requirements Document*, the requirements on the NIR detector performance are quantum efficiency over 90% and a total noise, including read noise and shot noise due to dark current in 300s, less than $10e^-$.

This is a very strict requirement, however it is subject to change. The final SNAP requirements will be based on constraints on the dark energy parameters, w_0 and w_a . A small change in the accuracy requirements for the last redshift bin ($z = 1.7$) could lead to less stringent NIR detector requirements, with a minimal impact on the dark energy constraints. In addition, the requirements on the supernova peak magnitude will likely be based on the systematic, not statistical, uncertainty limits for type Ia supernovae. It is very difficult to quantify the impact of detector noise and quantum efficiency on systematic errors, so the statistical error is used as a guide.

4.6 Conclusions

The current generation of NIR detectors deliver an uncertainty on the supernovae distance modulus within 1% of an ideal detector for simulated observations of type Ia supernova at $z = 1.7$, and at lower redshifts the accuracy improves. The current status of the high level science requirements does not allow final science driven requirements to be placed on the NIR detectors, however the current best performance of $10 e^-$ total noise in 300 s and $QE > 90\%$ is far above the initial specifications ($RN = 5 e^-$, $DC < 0.2 e^- /s/pixel$, and $QE > 60\%$). The total noise budget is dominated by the zodiacal background light, not the detector read noise and dark current. The main challenge facing the detector development is to improve the uniformity of the pixel distributions while maintaining high quantum efficiency and low total noise. The next step for the NIR program is to establish requirements for the shape of the pixel noise and quantum efficiency distributions and derive the final detector requirements once high level goals for constraining dark energy are available.

The machinery to estimate constraints on w_0 and w_a from supernova data is already in place. The key to understanding the nature of dark energy is to combine the supernova data with complementary data from weak lensing, baryon oscillations or CMB measurements (i.e. Planck). The combination of multiple techniques can break parameter degeneracies and improve dark energy constraints. Ch. 6 presents estimated constraints on w_0 and w_a for different combinations of cosmology measurements.

CHAPTER 5

Development of SNAP NIR Detectors

This chapter focuses on NIR detector development and laboratory measurements of detector properties. Measurements of read noise, dark current and quantum efficiency are covered, as well as secondary effects such as intra-pixel variation and persistence. Much of the R&D effort has focused on developing techniques to accurately characterize the detectors, so that the results can be used in simulations of detector performance. Common measurement techniques for noise, dark current, and conversion gain have been refined as understanding of the detector physics has improved. The new techniques are presented with sample data from a number of HgCdTe and InGaAs detectors.

5.1 Hybridized NIR Focal Plane Arrays

The SNAP focal plane consists of 36 hybridized NIR focal plane arrays with $1.7\ \mu\text{m}$ HgCdTe bump bonded to a complementary metal-oxide semiconductor (CMOS) multiplexer. The accumulation of photo-generated e^- hole pairs on isolated photodiodes causes a drop in reverse bias which is sensed by a MOSFET source follower. The multiplexer is an array of discrete reset and readout transistors, and can be read non-destructively. A sample unit cell is shown in Fig. 5.1. These devices differ from the visible CCD detectors, which read all of the pixels through one of four output transistors. A CCD physically moves charge from each pixel to the output transistor, clearing the integrated charge with each read; the source follower in the NIR unit cell preserves the integrated charge until it is reset.

The major difference between hybridized FPAs and CCDs is the readout. A CCD

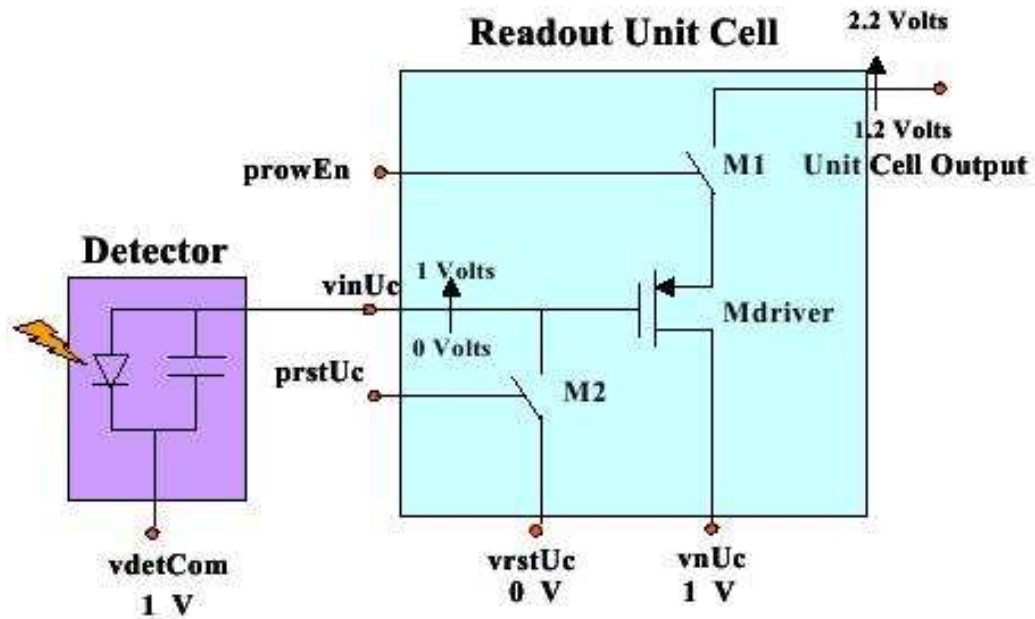


Figure 5.1. The readout unit cell of a multiplexed FPA. The purple box labeled ‘Detector’ is the HgCdTe diode, which is bump bonded to the CMOS unit cell. Each pixel has 3 transistors: the output source follower (Mdriver), the row enable transistor (M1), and the reset transistor (M2). This figure is reproduced with permission from the Raytheon Readout Model # SB-301 User’s Guide and Operating Manual.

is readout by first resetting the gate of the output transistor and reading the level to establish a zero-point, then transferring the next pixel’s charge to the gate of the output transistor and recording the new level. The difference between the two levels is the signal; this readout mode is known as Correlated Double Sampling (CDS). CDS reads eliminate kTC noise [Johnson, 1928] associated with resetting the output transistor and result in a fast, low noise readout. The noise bandwidth is limited by reading the signal level a few micro-seconds after resetting the output transistor.

Multiplexed FPAs operate by addressing and reading out each pixel individually. The charge resides on the gate of the pixel’s output transistor, and is read non-destructively. This leads to a variety of readout modes that can be used to reduce noise and reject cosmic ray hits. Two common readout modes in multiplexed detectors are Fowler and up the ramp sampling. A Fowler-N exposure reads the entire array N times, exposes the array to light for some time (300 s for SNAP), then reads the array N more times. The groups of N reads before and after the exposure are averaged to

reduce the noise. The difference of the two groups of reads is the signal. This eliminates kTC noise in the same way a CDS read does for CCD detectors, however the two samples are acquired seconds apart (as opposed to μs for a CCD), and long timescale drifts do not correlate between the two reads. Fowler sampling reduces the read noise by \sqrt{N} for an ideal white noise spectrum. Most pixels have some low frequency noise component, generically called $1/f$ noise, which establishes a noise floor above the ideal $1/\sqrt{N}$ limit.

Fowler sampling is effective for reducing the read noise, but it does not provide any information during charge integration. Up the ramp sampling is a mode which reads the device continually as it integrates charge; e.g. the detector is read once every 10 s during the course of a 300 s exposure. If a cosmic ray deposits charge in a pixel this will be apparent as a discontinuity in the slope. Up the ramp sampling can reject cosmic ray events, and in some cases recover the flux from slope measurements before and after the cosmic ray. This mode also reduces the noise, but not as effectively as Fowler sampling. The main disadvantage of up the ramp sampling is the large volume of data that must be stored or processed during the exposure. A single 2k x 2k detector sampled 30 times during an exposure will output 240 MB of data. The 36 SNAP NIR detectors would produce over 2 TB of data every day in this mode.

The SNAP NIR detectors will employ Fowler sampling to reduce the read noise while the shutter is closed. Between each 300 s exposure, the shutter is closed for 30 s to accommodate the CCD readout. The HgCdTe detectors readout in 1 – 2 seconds (depending on the number of outputs), allowing time for up to 15 Fowler reads while the shutter is closed. Fowler data is averaged in memory so that only a single frame is saved for each exposure, limiting processing and storage requirements. For the current read noise performance, Fowler sampling is an effective readout mode. However, the read mode may change if read noise improves or if pixel self heating dictates a constant cadence readout (see Sec. 5.3.4 for details).

Two companies produce a majority of the large format near infrared devices for the astronomical community: Rockwell Scientific offers HgCdTe sensors hybridized onto the HAWAII family of multiplexers, and Raytheon Vision Systems (RVS) produces

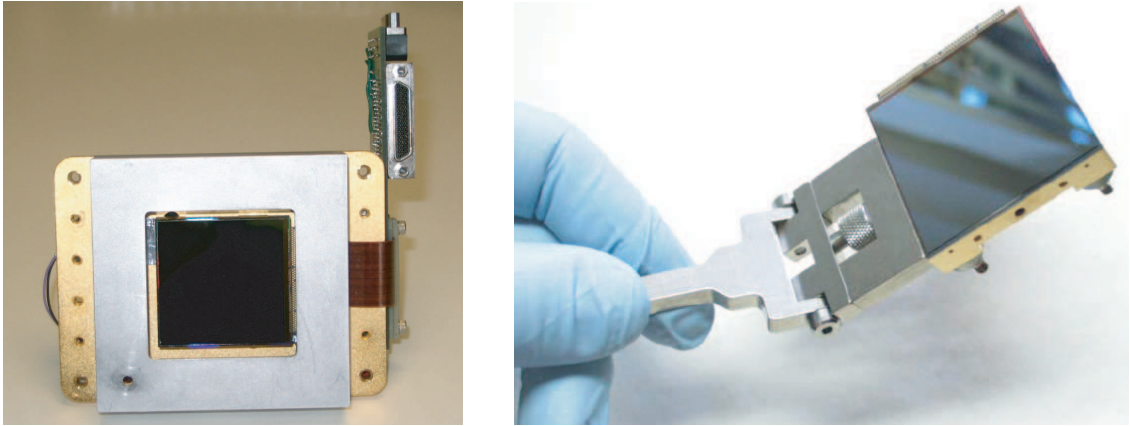


Figure 5.2. Left: Cold stage assembly with FPA mounted. A cover can be attached to shield the detector from thermal radiation. Right: Rockwell’s $2k \times 2k$ detector hybridized onto the HAWAII-2RG multiplexer and mounted onto a molybdenum carrier.

$1.7 \mu\text{m}$ cutoff $2k \times 2k$ FPAs based on the SB301 multiplexer. Both Rockwell and RVS were contracted by the SNAP R&D program to develop detectors that comply with the SNAP science specifications using HgCdTe technology .

Rockwell Scientific is recognized as a leading manufacturer of large format HgCdTe infrared FPAs, and boasts a long history of developing devices for the astronomical community. The SNAP project selected the largest available Rockwell infrared device, a $2k \times 2k$ HgCdTe detector array produced in MBE technology, mated to the HAWAII-2RG CMOS multiplexer. The HAWAII-2RG (H2RG) multiplexer was developed for the JWST [<http://www.jwst.nasa.gov/>] project and is a good match for SNAP. The multiplexer has an $18 \mu\text{m}$ pixel pitch and incorporates multiple output modes (1, 4 or 32 channels), operational modes and data rates. Pixel clocking rates of up to 200 kHz are supported¹.

Raytheon Vision Systems developed a $2.5 \mu\text{m}$ cut-off $2k \times 2k$ device for the VISTA project and, based on this FPA, developed a short wave ($1.7 \mu\text{m}$) version for SNAP. The SB301 multiplexer uses a $20 \mu\text{m}$ pixel pitch and a simplified read-out control which only requires two user provided clocks. It offers 4 and 16-channel read-out

¹The lowest read noise is achieved in the slow clocking mode which nominally supports data rates up to 100 kHz. No performance degradation was observed when overclocking at 200 kHz. The multiplexer also supports a fast clocking mode of up to 5 MHz, but at higher read-out noise levels [Rockwell, 2004].

modes at pixel rates up to 200 kHz.

Both RSC and RVS devices have been successfully used by ground-based telescopes, and our R&D efforts indicate that both companies are nearing the SNAP science driven performance specifications using $1.7\ \mu\text{m}$ HgCdTe.

5.1.1 HgCdTe vs. InGaAs

Two detector technologies were considered for the SNAP NIR detectors: HgCdTe and InGaAs. The bandgap in HgCdTe changes as the ratio of the Hg and Cd are varied. HgCdTe is commonly used in $1.7\ \mu\text{m}$, $2.5\ \mu\text{m}$ and $5.0\ \mu\text{m}$ cutoff near and mid infrared detectors. Improvements in the processing of the longer cutoff materials are often useful at $1.7\ \mu\text{m}$ as well; parallel development of HgCdTe for many diverse applications has resulted in a mature technology. InGaAs was considered during the R&D period as an alternate technology, but suffered from a lack of development time and money. InGaAs has a cutoff wavelength of $1.7\ \mu\text{m}$ at room temperature, however the band gap is temperature dependent and the cutoff shifts to $1.57\ \mu\text{m}$ at 140 K. If the same resources that have been put into developing large format HgCdTe detectors over the last 10 years had instead gone to InGaAs, this technology may have been chosen. However, due to the large amount of parallel development and the maturity of processing techniques, HgCdTe proved to be the best material for SNAP. The discussion below focuses on HgCdTe results and technical challenges.

5.2 Summary of NIR Detector Development (2004 – 2006)

In order to perform all of the tasks required for the characterization and testing of HgCdTe and InGaAs near infrared FPAs, the SNAP project assembled a near infrared team and initiated R&D efforts at several institutions: the California Institute of Technology (Caltech), the University of Michigan (UM), Jet Propulsion Laboratory (JPL), and Indiana University (IU). In addition, some device characterization and evaluation were contracted with the Independent Detector Testing Laboratory (IDTL) operated by the Space Telescope Science Institute (STScI) and the Detector Characterization Laboratory (DCL) at NASA's Goddard Space Flight Center.

| Device | ID | Format | Received | Comment |
|---------------------------|--------|---------|-------------|-----------------|
| RVS Virgo HgCdTe 75616981 | | 1k × 1k | Feb. 2004 | |
| RVS-SU Virgo InGaAs | R301IG | 1k × 1k | April 2004 | |
| RVS Virgo HgCdTe 598140 | RHG140 | 1k × 1k | April 2005 | |
| RVS Virgo HgCdTe 598141 | RHG141 | 1k × 1k | April 2005 | |
| RVS Virgo HgCdTe 598141 | R141AB | 1k × 1k | Nov. 2005 | epoxy backfill |
| RVS Virgo HgCdTe 598141 | R141SR | 1k × 1k | March 2006 | 10 μm substrate |
| RVS Virgo HgCdTe 595640 | RHG640 | 1k × 1k | April 2005 | |
| RVS Virgo HgCdTe 09A | R2K09A | 2k × 2k | July 2005 | lot 2a |
| RVS Virgo HgCdTe 13A | RHG13A | 2k × 2k | July 2006 | lot 3 |
| RVS Virgo HgCdTe 18A | | 2k × 2k | July 2006 | lot 3 |
| RSC HgCdTe H2RG 32-040 | H32040 | 2k × 2k | Spring 2004 | lot 1 |
| RSC HgCdTe H2RG 32-038 | | 2k × 2k | Spring 2004 | lot 1 |
| RSC HgCdTe H2RG 32-039 | | 2k × 2k | Spring 2004 | lot 1 |
| RSC HgCdTe H1RG-25 | H2BAND | 1k × 1k | Spring 2005 | banded array |
| RSC-SU InGaAs H1RG-105 | | 1k × 1k | Spring 2005 | |
| RSC HgCdTe H2RG-102 | H2-102 | 2k × 2k | July 2005 | |
| RSC HgCdTe H2RG-103 | H2-103 | 2k × 2k | July 2005 | |

Table 5.1. NIR devices tested during SNAP R&D program.

Spring 2004

By early 2004, the NIR team was assembled and detector evaluation facilities were in place. The read-out and control electronics were tested throughout 2003 using bare multiplexers. A detector procurement and development program for 1.7 μm HgCdTe FPAs began with the two competing vendors, Rockwell Scientific (RSC) and Raytheon Vision Systems (RVS). Both vendors delivered 1.7 μm detectors developed specifically for SNAP. RSC fabricated two lots of HgCdTe detectors for SNAP (lot #1 and lot #2). The lot #1 fabrication was based on the Hubble Space Telescope's Wide Field Camera 3 (WFC3) development of 1k × 1k HgCdTe. The WFC3 baseline process was extended to a 2k × 2k format with an emphasis on reducing the read noise while maintaining good QE; the WFC3 detectors with the best read noise characteristic showed degraded quantum efficiency (< 30%). This was one concern targeted in the RSC SNAP program. Experimental variations in the HgCdTe growth

and passivation processes for lot #2 were unsuccessful, and did not produce useful devices. The devices delivered to the SNAP project by RSC were 32-038, 32-039, and 32-040. Following discussions with RSC, part of the focus for the next RSC HgCdTe lot (lot #3) shifted to improving the QE, in particular eliminating the low wavelength droop, using substrate removal. This was promising as it had been successful with 2.5 μm devices.

RVS was building on their experience with the VIRGO SB-301 multiplexer and 2.5 μm HgCdTe FPAs ($2\text{k} \times 2\text{k}$) that were developed for the VISTA program [McMurtry et al., 2005]. Dark current appeared to be a potential problem early in the RVS development, but trends towards lower dark current in VISTA detectors helped build confidence in RVS. The first 1.7 μm HgCdTe FPA (75616981) was hybridized by RVS and delivered to UM in February of 2004. This device had an unacceptably large dark current ($> 10^6 \text{ e}^-/\text{pixel}/\text{s}$ at 90 K) that prevented any read noise or quantum efficiency characterization. It became clear that the next RVS HgCdTe lot would require a credible plan to reduce the dark current. In place of the HgCdTe detector, RVS loaned a $1\text{k} \times 1\text{k}$ InGaAs detector (ID R301IG) to UM for testing in May 2004.

As soon as the first devices were delivered, an active program of device characterization began. In addition to the characterization of HgCdTe detectors, alternative sensor technology (InGaAs) was under investigation. Also at this time, optical test setups were implemented at UM and STScI. Both laboratories demonstrated calibrated flat-field illumination for measuring QE as a function of wavelength, and UM developed a NIR pinhole projection system to measure intra-pixel response with micron sized spots of light (see Sec. 5.6).

Fall 2004

The first lots of FPAs from RVS and RSC (RVS-SU InGaAs and HgCdTe 32-038, 32-039, and 32-040 from RSC) were able to meet several of the SNAP specifications (such as QE and dark current). Intra-pixel variations were studied for the RVS InGaAs detector with promising results. The read noise specifications, however, remained a challenge. Contracts for the production of a second round of detectors were in place

with both vendors for delivery in the Spring of 2005. RVS was able to demonstrate dark current improvements in Vista 2.5 μm HgCdTe development, and expected the same progress with the 1.7 μm HgCdTe. The new RSC lot was optimized for substrate removal and RSC continued to work on reducing the read noise.

Spring 2005

In the spring of 2005 preliminary test results for the second batch of 1.7 μm HgCdTe devices (RSC lot #3, RVS lot #2) were available. Combined with the results from the first batch of detectors, nearly all of the SNAP specifications (QE, dark current, intra-pixel variation) were met, although not all in a single device. Low read noise was achieved, but not at the SNAP operating temperature of 140 K. RVS HgCdTe #598141 has less than $5 e^-$ (Fowler-16) for a minimum exposure time readout at 90 K. For a 300 s delay between the Fowler pairs, the noise was $7.7 e^-$ (Fowler-16), again at 90 K. Measurements were made at 90 K due to high dark current at 140 K ($\sim 4 e^-/\text{pixel}/\text{s}$, a major improvement over lot #1, but still above the SNAP specification), which dominates the $1/\sqrt{N}$ behavior for Fowler-N sampling. The Fowler-1 read noise in this device is the best achieved to date, $15.9 e^-$ at 140 K and $15.0 e^-$ at 90 K. We believed that the Fowler-16 noise performance at 140 K would be similar to the 90 K results, if the dark current could be reduced.

RVS lot #2 produced four $1\text{k} \times 1\text{k}$ HgCdTe FPAs with a cutoff wavelength of $\sim 1.8 \mu\text{m}$. Three of these detectors tested at UM show flat, 80% QE across the entire NIR bandpass (0.9 – 1.7 μm). The high index of refraction of the CdZnTe substrate reflects about 20% of the light at the detector surface (these devices do not have an anti-reflective coating), which means that the internal QE is near 100%. This is one of the major advancements in the NIR program.

The lot #3 devices from RSC were 1.7 μm $1\text{k} \times 1\text{k}$ HgCdTe banded arrays. Banded arrays have variations in the implant size and geometry within the HgCdTe diode aimed at reducing read noise. These RSC devices did show improved read noise, but at the expense of QE. Prior to substrate removal the QE was only $\sim 28\%$, and removing the substrate did not improve the QE as RSC had expected. An

additional problem was that many of the RSC detectors exhibit a drop in QE at short wavelengths ($< 1.2 \mu\text{m}$). The QE performance became a concern for the RSC HgCdTe at this point in the R&D program.

RSC also delivered their first InGaAs device to JPL in 2005. This detector uses Sensors Unlimited $1.7 \mu\text{m}$ (room temperature cutoff) InGaAs bump bonded to a H1RG multiplexer. The JPL results show that the InGaAs detector technology meets the SNAP dark current requirements ($< 0.2 e^-/\text{pixel/s}$ at 140 K) and the read noise is comparable to the RSC HgCdTe. Both of the InGaAs devices tested have high QE (80%), but the long wavelength cutoff is $1.57 \mu\text{m}$ at 140 K. Increasing the cutoff involves developing a new growth recipe and would increase the dark current and total noise in 300 s.

Following the second development run the two vendors were faced with different challenges: RVS needed to reduce the dark current at 140 K and RSC needed to work on reducing the read noise and simultaneously improving the QE to match the RVS performance. RVS achieved a huge improvement between lots #1 and #2, and was proceeding with an internally funded $2\text{k} \times 2\text{k}$ development to lower the dark current. RSC took a step back following the failed lot #2 in the first development run and the low QE in the lot #3 banded arrays. At this point, RVS appeared to have an edge in performance (we believed it would be easier for RVS to lower dark current than for RSC to improve QE), but had yet to explore substrate removal or anti-reflective (AR) coating. RSC already used both of these techniques to help improve QE.

Summer 2005

The detector development continued in the summer of 2005 with the delivery of internally funded parts from both vendors. RVS delivered HgCdTe #09A, a $2\text{k} \times 2\text{k}$ FPA that has the lowest dark current of any RVS detector produced for SNAP, $0.18 e^-/\text{pixel/s}$ at 140 K. The dark current is still above the bulk g-r limit for $1.7 \mu\text{m}$ HgCdTe, but is more than a factor of 10 lower than any other RVS FPA. With the improved dark current, the Fowler-16 read noise at 130 K is only $7.2 e^-$ for a 300 s exposure. The QE in this detector is 70% above $1.2 \mu\text{m}$, but declines to 50% at $0.9 \mu\text{m}$.

Despite the small drop off in QE, this device represented another advancement for RVS.

Rockwell delivered detectors #102 and #103 in July of 2005, the two best FPAs produced during the R&D program. Both detectors are substrate removed and have an anti-reflective coating, and the QE is over 90% from 0.9 – 1.7 μm . The response even extends into the visible; the QE at 0.45 μm is $\sim 40\%$. The noise in both detectors is near the best for the RSC SNAP program. The Fowler-1 noise is $25 e^-$, and the Fowler-16 noise is $8.5 e^-$ for a 300 s exposure at 140 K. These detectors are near the ideal performance for supernova photometry in the SNAP deep survey. The new challenge is to improve the pixel distributions for read noise and QE. The numbers quoted above are the median performance, which ignores tails in the pixel noise and QE distributions that impact the overall detector performance. If the best pixel performance could be reproduced in all 4 million pixels, these detectors would qualify as SNAP science grade FPAs.

During the first two years of the NIR program, the SNAP NIR team and the detector vendors developed an understanding of the physics underlying many of the detector performance issues. The SNAP NIR team and the vendors were optimistic that SNAP science grade NIR detectors would be produced in the next development run. Both vendors had realized major improvements with the internally funded devices. Contracts for new developmental lots were put in place with RVS (lot #3) and RSC (lot #4). The contract with RVS focused on reducing dark current to bulk levels, in part by using a new 1.7 μm HgCdTe LPE melt to replace the earlier 1.8 μm material. The contract with RSC targeted the reduction of read noise while maintaining the high QE from #102 and #103. Both vendors expected to produce SNAP science grade $2k \times 2k$ FPAs.

Fall 2005

In the fall of 2005, new development lots were being grown by RVS and RSC and the best 1.7 μm HgCdTe detectors were undergoing extensive testing. The best RVS and RSC detector performance results were comparable (after cooling the RVS detectors

to eliminate the dark current), but RVS lagged in two important areas, substrate removal and anti-reflective coating. For space applications, the CdZnTe substrate above the HgCdTe diode must be removed to prevent proton-induced photoluminescence [Kavadias et al., 1994]. Substrate removal has the potential to damage the device and degrade performance. RVS also need to develop an AR coating to boost QE to 95%; this process can degrade performance if applied incorrectly. Part of the new RVS contract involved substrate removal and AR coating with the low noise FPA #141. The first step in substrate removal is to backfill the bump bond region between the HgCdTe diode and the multiplexer with epoxy. After adding the epoxy, this device was returned for UM for re-characterization. The performance was very stable after this step. The only major change was the inter-pixel capacitance, which was expected when adding epoxy. The gain changed slightly, however the measured QE agreed with the unbackfilled result within 1%. The QE of this device was stable and repeatable within 1% over the course of 6 months and a major processing step. The inter-pixel capacitance measurements before and after backfill helped illustrate asymmetric coupling in the multiplexer. The next step was to thin the substrate, using diamond turning, to a thickness of $\sim 10 \mu\text{m}$. This was also successful and no changes in performance were apparent. The final step of chemically removing the remaining substrate then passivating and AR coating has not been completed for RVS detectors at this time.

2006

In 2006, RVS lot #3 and RSC lot #4 detectors were delivered with disappointing results. The RVS detectors (#13A and #18A) do not show any improvements in dark current and the read noise has increased to over $50 e^-$ (Fowler-1, 300s exposure). RVS is working to understand the cause of the degraded performance before beginning further development for SNAP. The RSC lot #4 devices do not reproduce the high quantum efficiency from FPAs #102 and #103, however RSC has offered an explanation for the reduced QE. The new devices have a different doping (doping type 1) than #103 and 5 other high QE devices (doping type 2) from the WFC3

development. The correlation between the doping and high QE was not known until after the SNAP layers were grown. FPA #102 has doping type 1, but it appears to be an anomaly; unfortunately, the new lot was based on the #102 recipe before test results for the WFC3 devices with doping 2 were available. The data presented by RSC convinced the SNAP NIR team that the loss of QE is well understood within RSC, and a new development run has been funded. This lot is split, with 4 layers grown using the H2RG #103 process (which meets the SNAP NIR requirements) and 8 layers incorporating new noise reduction processes with doping type 2 (expected to exceed NIR requirements). This lot will test two important aspects of the detector program at RSC: the ability to reproduce results from an established process, and RSC's understanding of noise sources within $1.7\ \mu\text{m}$ FPAs. This lot began in August of 2006; hybridized FPAs will be delivered before Christmas.

5.2.1 Requirements and Test Procedures

In addition to testing NIR detectors, simulations of the detector performance were underway to establish science driven requirements for the NIR detectors. The initial NIR specifications were based on spreadsheet signal to noise calculations and did not flow down from the high level science requirements for type Ia supernovae. The simulation results and the improved quantum efficiency led to new draft level specifications for the NIR detectors, based on supernova photometry. Read noise and dark current are combined into a single total noise requirement: total noise less than $10\ e^-$ in a 300 s exposure. The readout mode is not specified by the requirement, but must be consistent with the shutter closed time of 30 s. The maximum Fowler number that could be accommodated in this time is 15. The revised quantum efficiency specification is $\text{QE} > 90\%$, after application of an anti-reflective coating. The simulations in Ch. 4 demonstrate that improvements in quantum efficiency in the NIR lead to the largest gains in photometric accuracy for type Ia supernovae.

Another goal of the R&D program is to establish measurement and data analysis techniques that will be used to qualify science grade detectors. Many of the standard measurement and analysis techniques for quantities like read noise, dark current, and

conversion gain have been refined during this program. Accurate conversion gain measurements are essential for converting measured detector quantities such as read noise, dark current, and quantum efficiency into meaningful units. Gain measurements had systematically overestimated conversion gain by up to $\sim 20\%$ because inter-pixel capacitance was not taken into account (Moore et al. [2003b], Sec. 5.5). RSC devices with epoxy underfill show large inter-pixel coupling effects ($\sim 20\%$), while negligible inter-pixel coupling effects are observed in devices without underfill. A new analysis procedure that accounts for correlated noise due to inter-pixel capacitance and methods to mask hot pixels and cosmic rays is now implemented as part of the gain measurement. For dark current measurements, a negative signal is observed in short exposure time ramps after the device is idle. This effect, formerly called ‘reset anomaly,’ is now understood in terms of local heating within the pixels, and can be eliminated with constant cadence clocking. Discrepancies between ‘spatial’ and ‘temporal’ noise estimates were resolved at Caltech. After careful study of inter-pixel variation in spatial noise estimates and reference pixel corrections for temporal noise measurements, results for the two measurement agree, and in many cases the noise is lower than initially thought. The spatial noise techniques developed at Caltech have been implemented at UM and JPL.

5.2.2 Additional Development

The section above is focused on the standard detector tests: read noise, dark current, and quantum efficiency. There are many other aspects to NIR detectors that must be considered during the R&D phase. One important issue is intra-pixel sensitivity variations, which can lead to photometry errors for undersampled imagers such as SNAP. An infrared pinhole projection system, the Spot-o-Matic, was developed at the University of Michigan to project μm -size spots of light onto NIR detectors. Early tests of an RVS InGaAs detector demonstrated that a simple sum over pixels resulted in $< 1.5\%$ variation in response. This is an important result for the NIR system, as it means that dithering is not necessary for precision photometry (dithering is still needed to properly sample the PSF for shape measurements in both the visible and

NIR).

The lot #2 RVS HgCdTe detector #598141 also has uniform intra-pixel response. This is not surprising as the internal QE of this device is near 100%; all of the charge is collected within this device. One of the big surprises in the R&D program came from RSC HgCdTe Lot #1 device 32-040, which exhibits a periodic intra-pixel structure. The summed response varies by $\sim 20\%$ (RMS) for a 4×4 region of pixels. RSC declares this device an anomaly and cannot explain the structure. The intra-pixel response in later RSC devices is correlated with the QE. RSC HgCdTe Lot 3 #25, a banded array, shows large random variations in the intra-pixel response, and the summed response varies by $\sim 11\%$ (recall that this device has $\text{QE} < 30\%$). Bands with smaller implant dimensions show larger variations and greater diffusion as expected. A major improvement was realized in RSC #102, which has close to 100% internal QE and an RMS deviation in the summed response of only 1.6%, consistent with the RVS results for high QE detectors. The Spot-o-Matic and intra-pixel response results are revisited in Sec. 5.6.

5.3 NIR Test Procedures and Results

The NIR detector testing program has two components. First, the SNAP NIR testing facilities perform detailed studies of the NIR detector performance to gain understanding of the detector properties. The results of these studies are shared with the detector vendors, Rockwell Scientific and Raytheon Vision Systems, as part of a collaborative effort to improve the detector performance. The second part of the testing program is to define the procedures to measure and qualify detectors as science grade for SNAP. New test and analysis procedures have been developed for the conversion gain, read noise, dark current in the presence of pixel self heating (aka ‘reset anomaly’), and intra-pixel sensitivity variations. A calibrated flat-field illumination system has also been built (thanks to collaborators at Indiana University) to measure absolute quantum efficiency within $\pm 5\%$. Some of the tests involve building new hardware, while others redefine data acquisition and analysis techniques to more accurately estimate device characteristics, e.g. the read noise.

The laboratory infrastructure, including cryogenics, dark enclosures, LED illumination systems and readout electronics are covered in the appendix. The readout electronics consist of Astro-cam components described in Leach and Low [2000]. Up to 32 channels of parallel readout are available from four ARC-46, 8 channel infrared video processor boards combined with a revision 3B infrared clock driver board and 250 MHz timing and PCI cards. Custom data capture and analysis code were developed in the python programming language to acquire and process detector data. Documentation of the data capture and analysis, along with all of the results presented below are available for download from <http://gargamel.physics.lsa.umich.edu>. Documentation of the website layout and CGI content are available at the same site. A substantial effort went into defining test procedures and developing automated data acquisition and analysis scripts. All of the data and results are recorded in a database, and the results are automatically posted to the web. The web interface allows collaborators and vendors to view all the test data acquired at the University of Michigan.

A summary of test procedures and sample data for the standard SNAP FPA tests are presented below. First, the multiplexer gain and conversion gain are presented. These tests provide the absolute calibration of the detector output voltage in e^- . Next, dark signals, such as read noise, dark current, and pixel self heating, are discussed. Optical sensitivity tests of quantum efficiency and intra-pixel variation follow. Finally, potential systematic errors from persistence, cosmic ray events, and non-linearity are addressed. Work on these systematic effects is ongoing; the standard noise and sensitivity tests are now defined and implemented in the testing laboratories as a result of the R&D program.

5.3.1 Multiplexer Gain

The multiplexer gain is defined as the change in output voltage as a function of the detector biases. The gain is measured by varying the reset bias (v_{reset}), then recording the detector's output voltage. Typical values of the multiplexer gain are 0.90 – 0.96 (gain is measured in Volts/Volt, and is unitless). This test is also used to

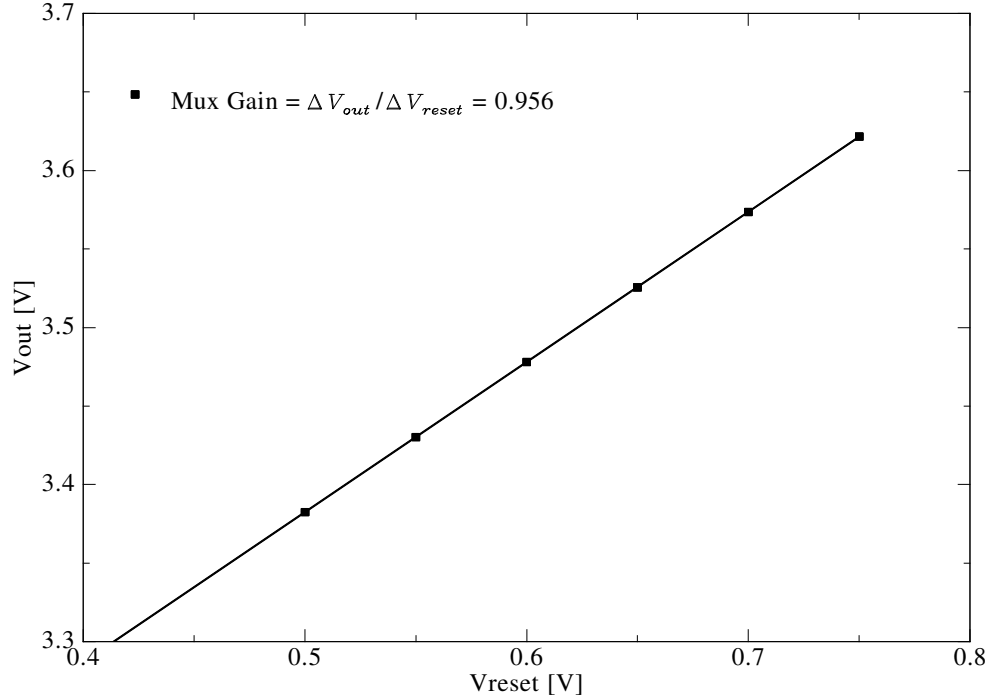


Figure 5.3. Sample data for a multiplexer gain measurement. These data taken with detector ID R141SR, channel 2, acquired 03/07/2006 (series 4).

measure the sensitivity of the output voltage to other detector biases. The noise at the detector output is most sensitive to the biases with high gain. These results are used to optimize the biasing of the detector to reduce the read noise [Smith et al., 2005].

The first step in the multiplexer gain measurement is to characterize the readout electronics without a detector in the system. The conversion factor for the ARC-46 is $5.25 \mu\text{V}/\text{ADU}^2$ ($\text{ADU} \equiv$ Analog to Digital Unit, the least significant bit of the digitizing ADC (Analog to Digital converter)). This calibration allows the detector output, measured in ADU , to be converted to Volts. A sample gain measurement is shown in Fig. 5.3. The digitized output level changes by 1 ADU for every $5.49 \mu\text{V}$ increase in V_{reset} ; the multiplexer gain for this channel is 0.956.

A gain for the reset bias greater than 0.9 indicates that the device is properly biased. Low gains are recorded when the bias voltages are outside of their optimal

²This number depends on the integration time and the bias settings for the ARC-46 video boards. All results presented use the default settings and an integration time of $3 \mu\text{s}$

range and the output source follower is not drawing adequate current. The multiplexer gain also tests the linearity of the output. Non-linear response at the output is a sign that the bias levels are incorrect. The final function of the multiplexer gain measurement is to provide an absolute calibration of $\mu V/ADU$ at the pixel source follower, which is used to calculate the pixel nodal capacitance from the conversion gain (this is not actually a gain; see Sec. 5.3.2).

5.3.2 Conversion Gain

Conversion gain is an important but poorly named quantity, as it is actually the factor used to convert from ADU measured by the readout electronics to e^- collected at the detector node. The conversion gain is not a real gain. To add to the confusion, some authors refer to the conversion gain as simply the ‘gain.’ In this work, gain, g , is defined in units of ADU/e^- or $\mu V/e^-$ and conversion gain, which is sometimes called inverse gain, is given the symbol g_c and has units of e^-/ADU . The gain also measures the pixel capacitance, which defines the well depth and sensitivity to noise on the bias voltages.

The conversion gain provides the absolute calibration for read noise, dark current, and quantum efficiency measurements. Errors in the conversion gain lead to errors on all other measured quantities. Conversion gain is measured using the photon transfer method [Mortara and Fowler, 1981, Janesick et al., 1985], which compares the mean signal to the variance under flat-field illumination. For a Poisson process, the mean and variance must be equal; the conversion gain is the factor that multiplies the pixel distribution (in ADU) to make this condition true. The mean of the pixel distribution is easy to estimate, but the variance can be difficult to measure, due to the presence of correlated noise. One method to estimate the variance is on a pixel by pixel basis, by taking a large number of exposures ($> 10^4$ for an error less than 1%) and calculating the standard deviation for each pixel; this method is known as temporal sampling. Temporal sampling takes many hours and requires a stable illumination source. The alternative is spatial sampling, which calculates the variance from the difference of two frames. Spatial sampling assumes all the pixels are identical; differencing two

frames corrects pixel to pixel variations, and this assumption is valid. The biggest issue when using a spatial statistic is the impact of correlations in the pixel outputs on the variance estimate.

Moore et al. [2003b] found that inter-pixel capacitance shares charge between neighboring pixels and leads to an underestimation of the variance (overestimation of the conversion gain) when using a standard variance estimator. A new variance estimator, which accounts for nearest neighbor correlations, is given as

$$v_i = \sigma_i^2 = \frac{1}{2N} \left(\sum_{k,l} D_i^2[k, l] + \sum_{k,l} D_i[k, l]D_i[k + 1, l] + \sum_{k,l} D_i[k, l]D_i[k, l + 1] + \sum_{k,l} D_i[k, l]D_i[k - 1, l] + \sum_{k,l} D_i[k, l]D_i[k, l - 1] \right),$$

where N is the total number of pixels and $D_i[k, l]$ is the signal measured in pixel k, l in the Fowler-1 difference frame, D_i . Using this technique to estimate the variance, the gain is $4.97 \mu V/e^-$ (32.2 fF) for Rockwell H2RG detectors and $2.13 \mu V/e^-$ (75.1 fF) for Raytheon SB-301 detectors³. The Raytheon FPA capacitance is more than double that of the Rockwell detectors, which leads to higher well depth and a lower capacitive coupling strength, but increased noise sensitivity.

Extensive studies of inter-pixel capacitance and its impact on the measured conversion gain were carried out at the University of Michigan [Brown et al., 2006a]. A summary of the test results is given in Sec. 5.5. The source of the inter-pixel coupling is studied for both RSC and Raytheon detectors, and the impact of epoxy underfill in the region between the HgCdTe diode and the multiplexer is explored. This work found that approximately half of the coupling occurs in the multiplexer, and it can be asymmetric depending on the multiplexer geometry. This component is minimized with careful multiplexer design. The remaining coupling occurs between the depletion regions of neighboring pixels, and appears to be unavoidable in all arrays studied.

³These are typical values. Variations of order 10% are common as doping and/or the implant area changes.

5.3.3 Dark Current

Accurate knowledge of the conversion gain is needed to calibrate measurements of detector noise sources, such as dark current and read noise. Dark current is defined as the accumulation of charge generated by thermal excitation in the bulk material rather than incident photons, and thus depends sensitively on the temperature. For $1.7\ \mu\text{m}$ HgCdTe, the bulk limited DC should be $\sim 0.01\ \text{e}^-/\text{pixel}/\text{s}$ at 140K. The initial SNAP specification was $\text{DC} < 0.2\ \text{e}^-/\text{pixel}/\text{s}$ at 140 K. This constraint is driven by the background zodiacal light level, which is approximately $0.7 * QE\ \text{e}^-/\text{pixel}/\text{s}$ for all 3 NIR filters. The total signal due to dark current must be well below the zodiacal light in each 300 s exposure to ensure that the dark current does not make a significant contribution to the total noise budget.

The dark current sets a noise floor for the total detector noise in 300 s. Read noise, addressed in Sec. 5.3.5, is random in nature and can be reduced with multiple sampling techniques, such as Fowler sampling; shot noise on the dark current is not reduced by reading the detector output multiple times. For $\text{DC} = 0.2\ \text{e}^-/\text{pixel}/\text{s}$, the shot noise on the accumulated charge in 300 s is almost $8\ \text{e}^-$. If the dark current is reduced to $0.02\ \text{e}^-/\text{pixel}/\text{s}$, then it contributes less than $2\ \text{e}^-$ to the total detector noise in 300 s. Although the new requirements do not include an explicit dark current requirement, the dark current must be below $0.2\ \text{e}^-/\text{pixel}/\text{s}$ to achieve low total detector noise for SNAP.

Measurements of the dark current require a photon free environment and an understanding of bias and temperature drifts that cause changes in the output signal. Temperature sensitivity and pixel self heating are covered in Sec. 5.3.4. To prevent contamination of the measurement, dark current measurements are performed with the FPA inside a light-tight enclosure mounted to the cold stage at a temperature of 140 K (blackbody radiation below $1.7\ \mu\text{m}$ is many orders of magnitude less than the dark current at 140 K). The dark current measurements are always performed after the sensor is powered on continuously for many hours and thermal equilibrium is established. A sample dark current histogram is shown in Fig. 5.4.

Measurements of the dark current are subject to contamination due to read glow,

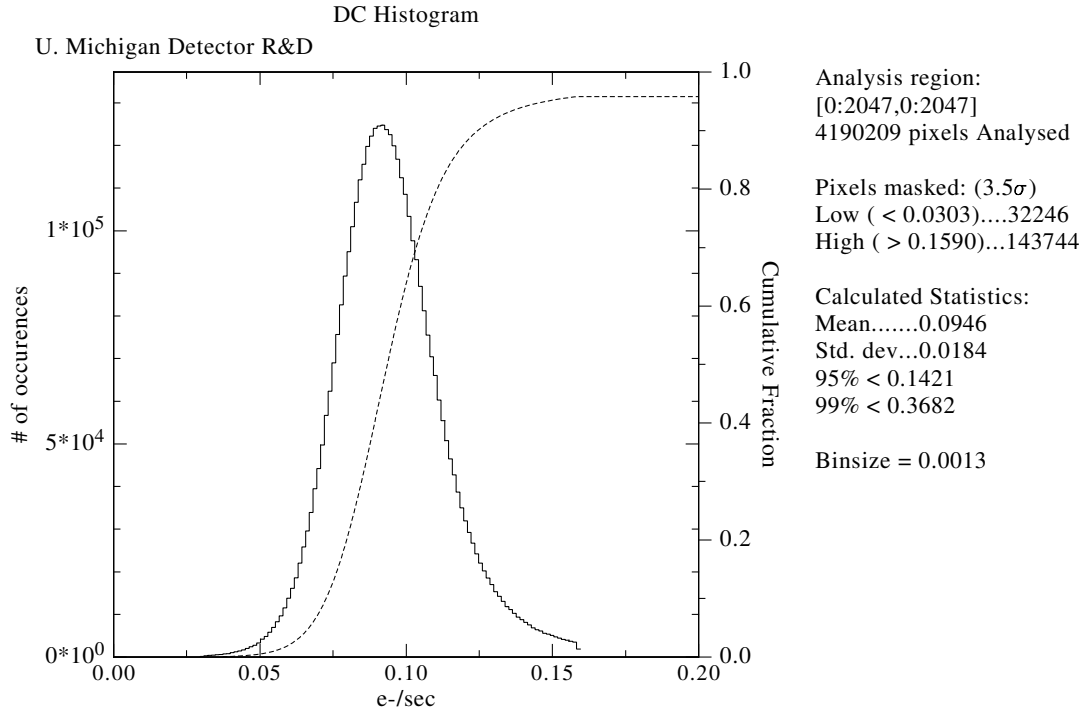


Figure 5.4. Sample dark current histogram for a Rockwell HAWAII-2RG FPA.

a small amount of charge injected into each pixel when the detector is read out. When a pixel is addressed and read out, current flows through the source follower FET in the multiplexer, which can stimulate the emission of infrared photons. This appears as an increased dark current when a fast readout cadence is employed. Rockwell H2RG multiplexers do not exhibit any measurable read glow (consistent with zero within the accuracy of the dark current measurements) [Smith et al., 2006]. For RVS $1.7 \mu\text{m}$ HgCdTe detectors, read glow has not been measured due to the high dark current at 140 K. The glow is expected to be temperature dependent, and the large dark current at 140 K masks any potential glow in the multiplexer at this temperature. Smith et al. [2004] measure a read glow of $0.04 \pm 0.01 e^-$ per read in a $2.5 \mu\text{m}$ HgCdTe RVS VIRGO detector at 77 K.

The read glow and dark current contribute to the total detector noise. The common assumption is that the noise is Poisson distributed and scales as the square root of the signal, however measurements by Figer et al. [2003] indicate that this may not

be true. Defining the detector requirements in terms of total noise in 300 s, instead of having separate read noise and dark current requirements, ameliorates any potential problems that this may cause. Once the readout mode for the NIR detectors is defined for SNAP, total noise measurements that include dark current and read glow will be used to qualify science grade detectors. This is one example of the evolution of requirements and measurement techniques during the R&D program leading to more reliable detector characterization.

Temperature Dependence

The dark current varies with detector temperature. The bulk dark current scales as

$$DC \propto kT^{3/2} \exp\left(\frac{E_g}{2kT}\right), \quad (5.1)$$

[Janesick, 2001] where k is the Boltzmann constant, T is the detector temperature, and the bandgap energy, $E_g = 0.73$ eV for $1.7 \mu\text{m}$ cutoff HgCdTe. In InGaAs the bandgap is temperature dependent, with

$$E_g(T) = E_g(0) - \frac{\alpha T^2}{T + \beta}, \quad (5.2)$$

where $E_g(0) = 0.814$ eV, $\alpha = 4 \times 10^{-4}$ eV/K, and $\beta = 182$ K [Geddo et al., 1994]. A general rule of thumb is that the dark current changes by a factor of 7 – 10 for every 10 degree change in temperature near 140 K. The normalization depends on the impedance of the detector material (which depends on the pixel area and the thickness of the diode). Figure 5.5 shows the dark current as a function of temperature. The dark current in the device shown is nearly bulk limited and follows the theory down to approximately 135 K. At this point, leakage currents, which are not temperature dependent [McLean, 1997], become the dominant source of dark current.

Rockwell Status

RSC has achieved the DC specification in all the FPAs produced for SNAP. RSC H2RG-32-039 has a median dark current of only 0.01 e⁻/pixel/s at 140K, the theoretical limit. The dark current observed in the banded arrays (lot #3) is more than

H2RG-103 Dark current

1.7 μ m cutoff, substrate removed, no detectable mux glow

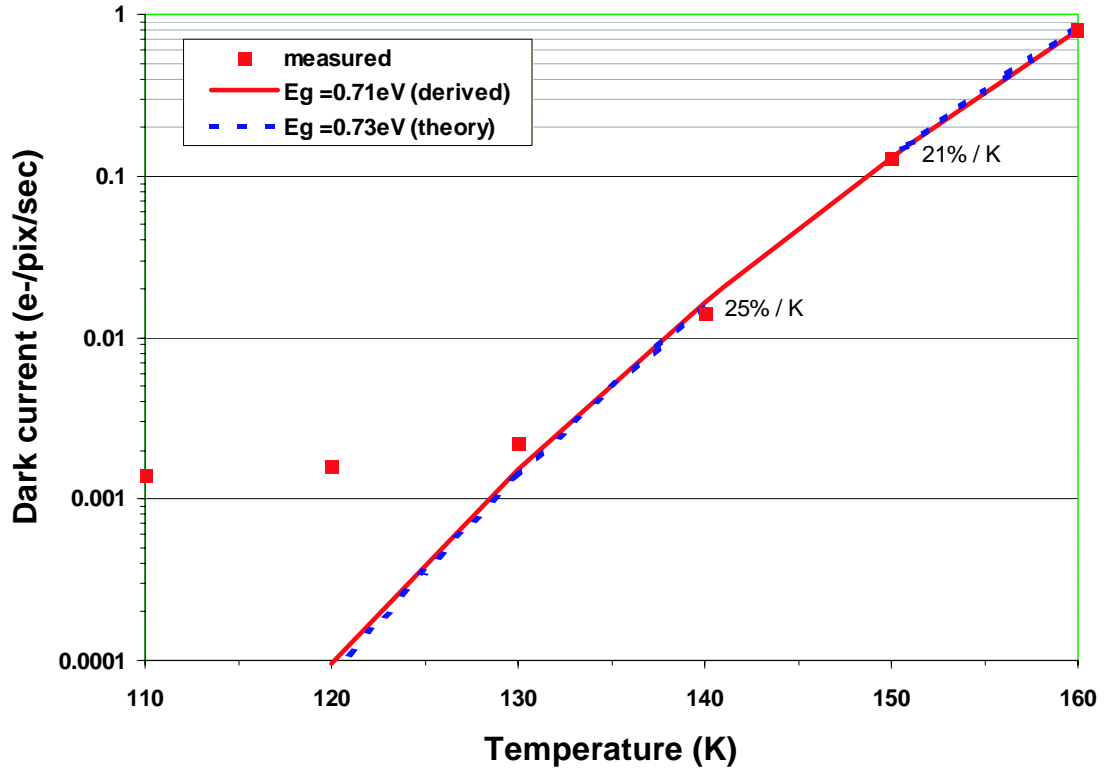


Figure 5.5. Mean dark current as a function of temperature. The dark current scales according to the theoretical curve down to 135 K then approaches a 0.014e-/s floor. The scaling implies a bandgap, which is very close to hc/λ_{cutoff} . Data provided by R. Smith.

an order of magnitude higher. H2RG-103, a more recent device, is typical of the RSC 1.7 μ m cut-off HgCdTe performance, which reliably achieves DC < 0.05 e⁻/pixel/s at the 140K. At this level, the impact on the total noise per 300s exposure is minor. Longer integration times (up to 1 hour) are used for the spectrograph, which can be cooled to lower temperatures with a separate radiator. Figure 5.5 shows that the dark current floor for H2RG-103 is reached at 120 K. The spectrograph detector will operate at or below 120 K, to reduce the dark current to levels where the shot noise is negligible. The dark current of Rockwell devices continues to be studied, in particular the uniformity and correlation with high read-out noise. Smith et al. [2006] found that high dark current pixels accounted for approximately half of all high noise pixels in H2RG-103. The median performance of the Rockwell FPAs meets the SNAP

requirements for total noise; the remaining challenge is to improve the dark current distribution and limit the number of high dark current pixels.

Raytheon Status

Dark currents for initial RVS devices exceed the SNAP specification by a factor of 10 or more, however, this does not seem to be coupled to other performance parameters. RVS's first attempt at a $1.7\ \mu\text{m}$ HgCdTe device (lot 1) had such a high DC ($> 10^7\ \text{e}^-/\text{pixel}/\text{s}$ at 140K) that it was unusable. RVS lot 2 #7598141 reduced the dark current to $20\ \text{e}^-/\text{pixel}/\text{s}$ at 140K and $< 0.1\ \text{e}^-/\text{pixel}/\text{s}$ at 90K, however, the temperature dependence shows that it is not bulk g-r limited. This indicates substantial surface contributions to the dark current. Although this is an improvement by six orders of magnitude, it still does not meet SNAP specifications. RVS did manage to produce one low dark current device, #09A. Improved surface passivation in this device resulted in a median dark current of $0.18\ \text{e}^-/\text{pixel}/\text{s}$ at 140 K. Unfortunately, RVS was unable to reproduce this performance in the latest developmental detectors, and the dark current remains a major challenge for the RVS HgCdTe program.

5.3.4 Pixel Self Heating (aka. Reset Anomaly)

The dark current measurement procedure is straightforward, however the small magnitude of the dark signal is easily contaminated by temperature and bias drifts. The detector's output voltage is a sensitive function of temperature (100 to $1000\ \text{e}^-/\text{K}$ for the detectors tested, see results at <http://gargamel.physics.lsa.umich.edu>). Drifts in the detector output are observed as a result of global heating of the entire detector package as well as local heating within detector pixels. The drifts due to global temperature changes can be controlled with the excellent thermal stability of the SNAP focal plane. Local heating and cooling are impacted by the readout cadence, and may place restrictions on the NIR readout mode.

Local heating within the pixels is observed as a negative signal in short exposure time dark current ramps following a reset, and was initially called 'reset anomaly.' A large positive signal was observed in the HST NICMOS detectors [Boker et al., 2000],

but at the time, the NICMOS science team was unable to explain the observed signal. During the SNAP R&D program, ‘reset anomaly’ was studied in detail for an InGaAs detector. The results indicate that the anomaly is due to local (at the pixel cell level) temperature changes that occur when the clocking cadence is interrupted [Brown, 2005]. When a pixel is read out, current flows through the pixel source follower FET and power is dissipated in the pixel. Slowing the readout cadence leads to cooling of the output FET and a positive voltage change on the output. Increasing the readout cadence leads to local heating within the pixel, which appears as a negative signal at the pixel output. As can be seen in Fig. 5.6, continuously clocking and reading the detector eliminates this effect.

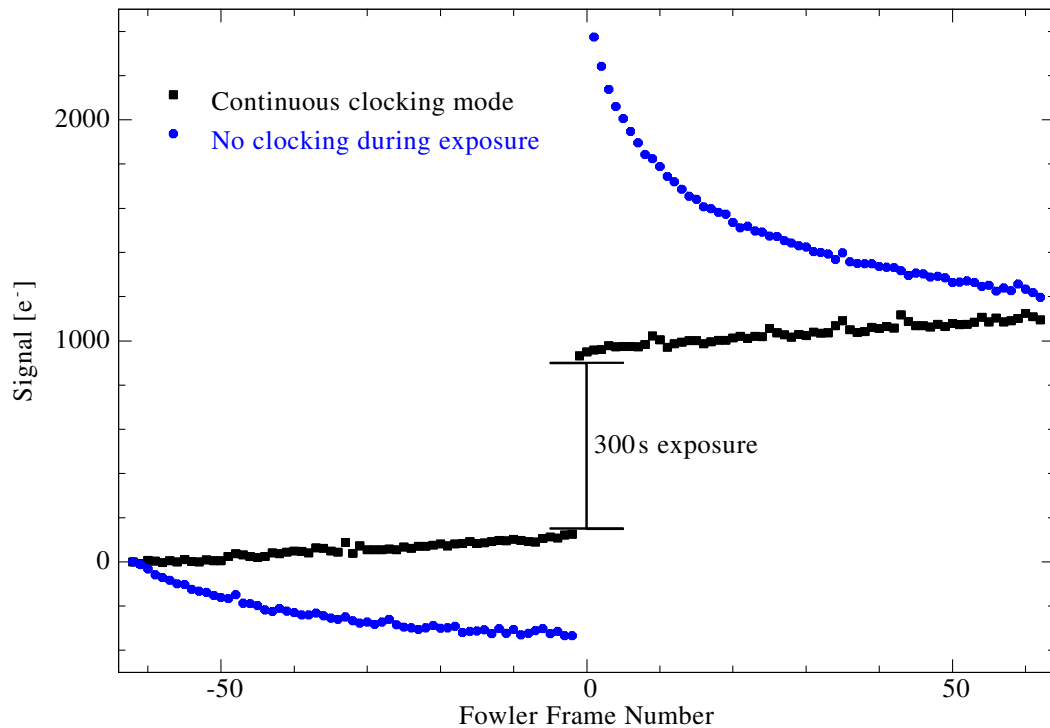


Figure 5.6. The impact of pixel self heating on the detector output for Fowler sampled data with a 300 s exposure delay. The filled squares show data with the device in continuous clocking mode. The measured signal agrees with the expectation from dark current measurements. The filled circles show the data when the device sits idle before and during the exposure (frame number 0 is a 300 s delay). Following the exposure, the signal increases above the dark current expectation then is negative due to local heating: ‘reset anomaly’ without a reset.

Figure 5.6 shows data for the RVS InGaAs detector (ID R301IG) using two different Fowler-64 exposure procedures. In the first test (filled circles), the device sits

idle before and during the 300s exposure. After the exposure, the measured signal begins far above the expectation for dark current only, as a result of cooling of the pixel FETs during the idle period. Once the readout begins, local heating causes the signal to decrease until it returns to the dark current floor. This is an example of ‘reset anomaly’ without a reset, which demonstrates that the observed change in signal is independent of resetting the detector and depends strongly on the readout cadence. The filled squares in Fig. 5.6 show the same test with continuous clocking both before and during the exposure. This eliminates the self heating effects and produces the expected result. The same temperature effect is also observed, although not as strong, in RSC and RVS HgCdTe devices. Continuous cadence clocking and reading eliminates this anomaly in all detectors studied for SNAP. Temperature drifts due to local heating lead to systematic offsets in the pixel output level and add noise to Fowler sampled data. A readout strategy that takes these effects into account while minimizing other noise sources and maximizing observing efficiency needs to be defined for the SNAP science grade FPAs.

5.3.5 Read Noise

The combination of the integrated dark current and the read noise in each exposure determine the total detector noise for each SNAP FPA. Read noise is the uncertainty in the measured charge accumulated in a single pixel caused by random fluctuations in the output voltage. Contributions to read noise include shot noise in FETs, Johnson noise [Johnson, 1928, Nyquist, 1928], $1/f$ noise, shot noise on the dark current, and drifts in the bias voltages. Read noise can originate in the readout electronics, the multiplexer, and the detector material. External noise sources are minimized by shielding, stabilizing bias voltages and temperatures, and/or bandwidth-limiting the output. Random noise sources in the detector average out through repeated sampling of the detector. Shot noise due to dark current and $1/f$ noise are not reduced by multiple sampling; these two effects establish a minimum noise floor for each detector.

The read noise depends on the exposure time, the sampling method, and the statistic chosen to define the noise. The two common methods of estimating the

noise are spatial and temporal averaging. Spatial noise is a measure of the pixel to pixel variance in a single dark frame. This method assumes that pixel to pixel noise variations are small. Cosmic rays and hot pixels must be accounted for when estimating the spatial noise. A Gaussian fit to the difference of two Fowler-1 frames provides a robust estimate of spatial noise in the presence of outliers (the noise is the standard deviation of the pixel distribution divided by $\sqrt{2}$ using this method). Spatial noise provides high statistical accuracy due to the large number of pixels available in the FPAs tested.

Temporal noise is defined as the fluctuations in a given pixel when an exposure is repeated. This is the noise source of interest for astronomical observations. Temporal noise estimates require a large number of measurements (> 100 frames), and are subject to electronic and thermal drifts. Any shifts in the DC output of the FPA appear as excess noise for all the pixels. Both vendors provide reference pixels near the edge of the detector that are designed to track DC shifts in the output voltage. The reference pixels are not bonded to a HgCdTe diode, and are not light sensitive. Smith et al. [2006] report exhaustive studies of both temporal and spatial noise for the SNAP R&D FPA #103. When carefully monitoring bias and temperature stability and applying reference pixel corrections, the spatial and temporal noise estimates are in excellent agreement. This demonstrates that external noise sources and long timescale bias drifts are properly accounted for and do not contaminate the detector noise measurement.

Figure 5.7 shows the total detector noise in 300 s as a function of number of Fowler samples. Fowler sampling is an attractive choice for SNAP due to the 30 s shutter closed time between exposures, which is needed to read the CCD detectors. The readout time for the NIR detectors is 1 to 2 s, depending on the number of outputs (16 for RVS and 32 for RSC) and the readout rate (nominally 100 kHz). These data rates allow up to 15 Fowler samples without extending the sampling into the exposure, which would reduce the effective exposure time. The loss of signal due to the reduced exposure time outweighs the small gain in noise performance from reading during the

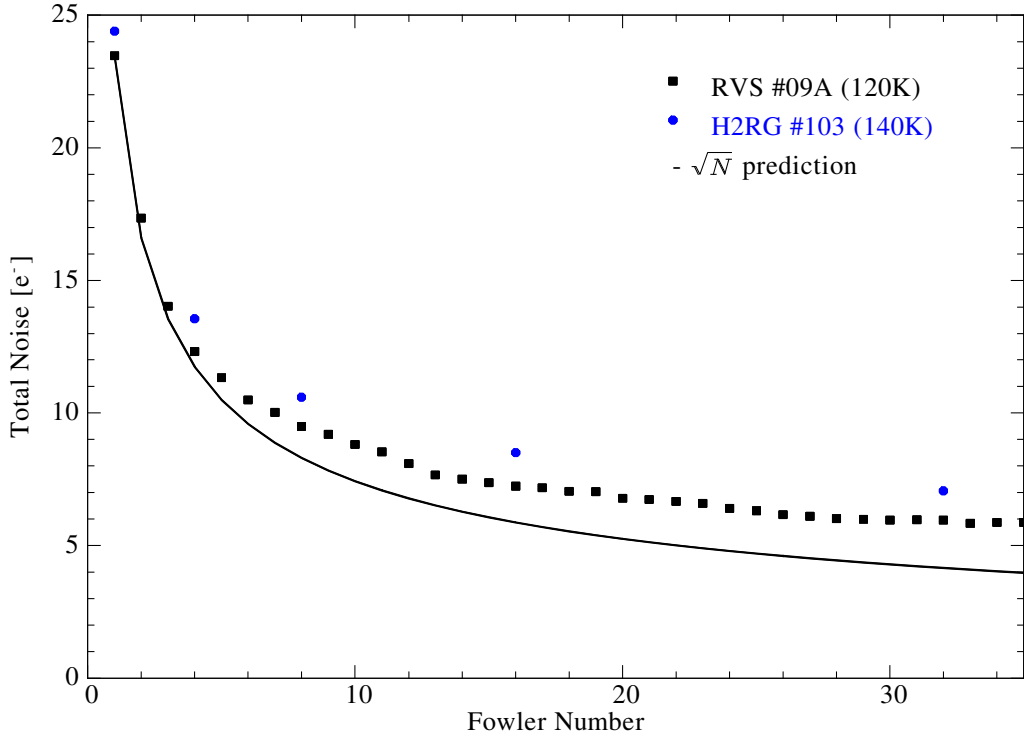


Figure 5.7. Fowler sampled noise data for two of the lowest noise detectors produced for SNAP, RVS #09A and H2RG #103. Both detectors achieve a Fowler-16 noise of less than $10 e^-$. H2RG #103 data provided by R. Smith.

exposure. The Fowler-16 noise⁴, which includes all noise sources in a 300 s exposure, is less than $8.5 e^-$ for both detectors shown. At this level, the total detector noise is far below the zodiacal background noise, consistent with the SNAP requirement.

The noise floor for Fowler sampling is determined by the dark current and $1/f$ noise in the multiplexer. The dark current is limited by cooling the detectors to 140 K (temperatures as low as 130 K are possible for the SNAP focal plane with passive cooling). $1/f$ noise in the multiplexer results from traps that produce a random telegraph signal (RTS). RTS is a discrete change in output voltage between two levels. Pixels where RTS is observed have one dominant trap that changes the resistance of the source follower FET as the trap empties and fills. The discrete changes in resistance appear as voltage swings on the output. The noise spectrum for

⁴Fowler-16 noise results are quoted here; the Fowler-15 noise is nearly identical, but is not always measured in laboratory tests.

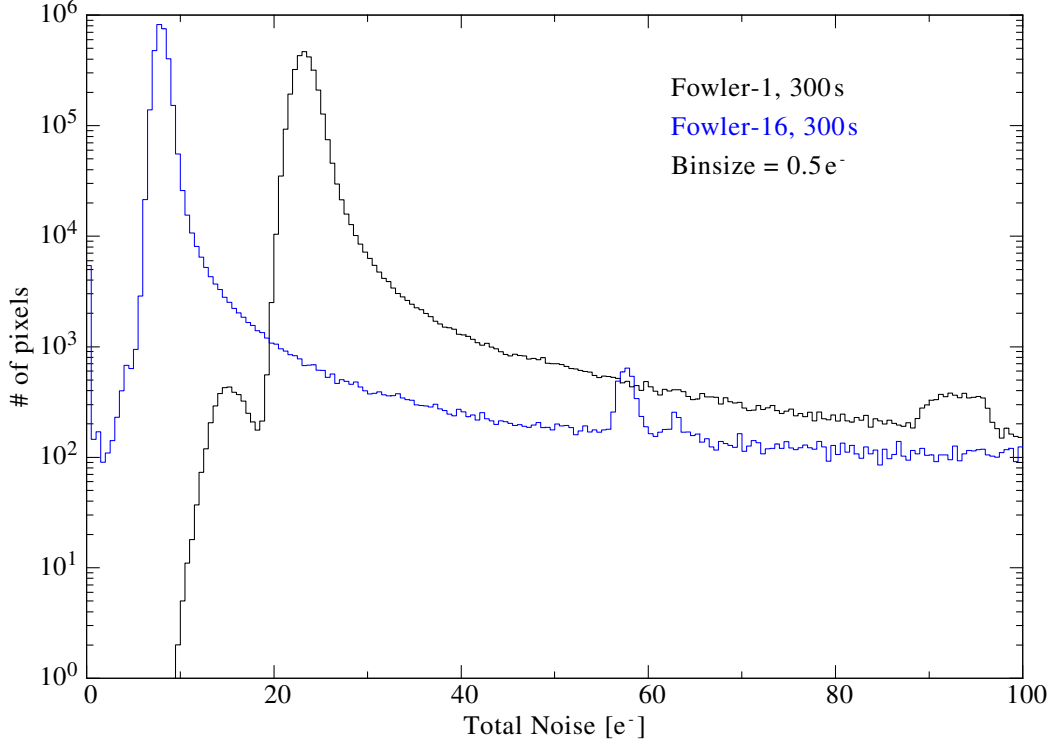


Figure 5.8. Fowler-1 and Fowler-16 noise histograms for H2RG #103. Reference pixels not included; the data are shown for area [540:2040, 4:2004].

a RTS signal is Lorentzian (proportional to $1/f^2$), where the frequency is determined by the time constants for the trap to fill and empty. Pixels that do not exhibit a strong RTS signal have many small traps. The combination of these traps produces a noise spectrum proportional to $1/f^n$ ($n \approx 1$). At long exposure times, the noise power from low frequencies dominates, and sets a minimum noise floor. Fowler sampling cannot be used to eliminate $1/f$ noise; only improvements in silicon processing to reduce the number of trapping centers can reduce this noise source.

Total Noise Distribution

Temporal noise measurements produce a histogram and map of the pixel noise across the detector, as shown in Fig. 5.8. High noise pixels identified in the histogram are studied to help understand the impact of different noise sources. For H2RG #103, 9% of the pixels have a noise more than 3σ above the modal value (for a Gaussian distribution only 0.15% of the data is greater than the mean plus 3σ). The main

sources of noise are high dark current, random telegraph signal in the multiplexer, and noise due to the HgCdTe diode. Process improvements to reduce the number of high dark current and noisy pixels that result from the HgCdTe growth and processing are being explored by Rockwell. The RTS noise results from discrete traps in the source follower FET of the multiplexer and is more difficult to eliminate.

Rockwell Status

Rockwell struggled to achieve low noise early in the SNAP program. The H2RG multiplexer shows a strong RTS signal in a small number of pixels, however the multiplexer is not the main noise source for most pixels. For the pixels which do not exhibit RTS noise, the HgCdTe diode is the dominant source of noise. The noise due to the multiplexer (measured by shorting the HgCdTe diode) is less than 1/4 of the total detector noise [<http://gargamel.physics.lsa.umich.edu>, Smith et al., 2006]. The evidence for noise originating in the HgCdTe diode is supported by results for 2.5 μm and 5 μm HgCdTe FPAs produced by Rockwell. The longer cutoff materials show consistently lower noise than the 1.7 μm HgCdTe. Process improvements at 1.7 μm implemented on FPAs #102 and #103 have succeeded in lowering the noise, and recent banded array results for WFC3 indicate that more improvement is possible. The Fowler-16 noise of 8.5 e^- for FPAs #102 and #103 is well below the zodiacal limit when combined with high quantum efficiency ($> 90\%$). The Fowler noise includes all dark current, glow, and other sources of random error for each 300 s exposure.

Raytheon Status

Raytheon did not have a history of producing 1.7 μm HgCdTe for astronomy before the SNAP program, so the noise expectations were unknown. The first lot of usable SNAP devices (lot #2), showed the best Fowler-1 read noise of any SNAP detector tested to date. RVS #598141 has a Fowler-1 noise of only 16 e^- . Unfortunately, the dark current is large in this device (20 $e^-/\text{pixel/s}$ at 140 K), and Fowler sampling does not reduce the noise at 140 K. This device does achieve less than 8 e^- (Fowler-16) total noise at 100 K, but the SNAP focal plane cannot be cooled to this temperature. RVS #09A also has good noise performance, and the lower dark current in this device leads to a Fowler-16 noise of 8 e^- at 130 K, within the operating range for the SNAP

focal plane. The R&D team is confident that Raytheon can meet the total noise requirements, if the dark current can be reduced to bulk levels at 140 K.

5.3.6 Quantum Efficiency

Optical calibration of NIR FPAs begins with measuring the quantum efficiency (QE). QE is the number of electrons counted in the detector divided by the number of incident photons. Improving the quantum efficiency was one of the challenges at the start of the infrared R&D program. Rockwell H2RG FPAs were near the QE specification at long wavelengths, but the QE fell at wavelengths below $1.2\ \mu\text{m}$. Raytheon had yet to produce a $1.7\ \mu\text{m}$ FPA, but claimed to be able to deliver high quantum efficiency across the entire NIR bandpass, from 0.9 to $1.7\ \mu\text{m}$. Achieving high QE improves statistical accuracy at the peak of the supernovae lightcurves, allows earlier detection, and eases the read noise requirement for background (zodiacal) limited performance [Brown et al., 2006b].

The system developed for measuring QE at UM is calibrated to 5% in absolute photon flux. A schematic of the quantum efficiency setup is shown in Fig. 5.9. This setup was designed at Indiana University and installed at Michigan in late 2003. It consists of a calibrated 200 W quartz-tungsten-halogen (QTH) lamp which illuminates a 6-inch integrating sphere through a series of narrow-band filters (FWHM ~ 10 nm). A 1 mm calibrated InGaAs photodiode sits in a dark enclosure between the light source and the FPA. The dewar and FPA are located on the opposite side of the dark enclosure. The absolute photon flux at the photodiode is transferred to a flux at the detector surface by $1/r^2$ scaling. A monochromator has been incorporated into the setup to provide continuous spectral coverage of $1.7\ \mu\text{m}$ NIR detectors.

The 5% uncertainty includes errors on the relative position of the calibrated photodiode and FPA, the dewar window transmission, and the calibration uncertainty in the photodiode (4%). The system is set for an upgrade in the winter of 2006 to incorporate a larger (3 mm) photodiode mounted in the same plane as the FPA and NIST calibrated at 140 K. The absolute calibration of the photon flux will be better than 2% with the new photodiode installed. The on orbit flux calibration for SNAP

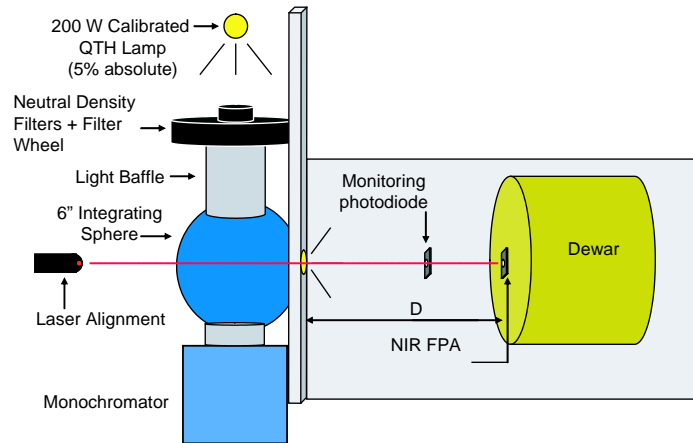


Figure 5.9. Schematic diagram of the optical components of the quantum efficiency setup.

must be better than 2%; the R&D program will demonstrate the same level of accuracy in laboratory measurements. This precision is also important for demonstrating the stability of our detectors by monitoring the QE over many months and years, as well as through temperature cycles and radiation exposure. Measurements of RVS #598141 at the University of Michigan indicate no noticeable change in QE over the course of more than a year and two processing steps (epoxy backfill and substrate thinning). This is the first SNAP HgCdTe detector that has undergone long term (> 1 year) QE testing, and all results indicate excellent stability, as shown in Fig. 5.11.

The measurement procedure begins with a dark, pedestal image, to measure the thermal background from the dark enclosure. The photon flux in each filter is calculated with the photodiode installed in the dark enclosure, then the diode is removed and the device is illuminated at each wavelength. The difference of the illuminated image and the pedestal determines the total signal in electrons (after applying the conversion gain). The QE at each wavelength is the total signal divided by the photon flux, after correcting for the distance from the photodiode to the FPA and the dewar window transmission. The illumination from the integrating sphere is uniform to better than 0.5% across the detector surface. The flat-field detector response highlights inter-pixel variations across the detector surface. Large sensitivity variations are observed near the long-wave cutoff in HgCdTe detectors from Rockwell, grown using MBE technology. The RVS detectors, grown by LPE, do not exhibit the same

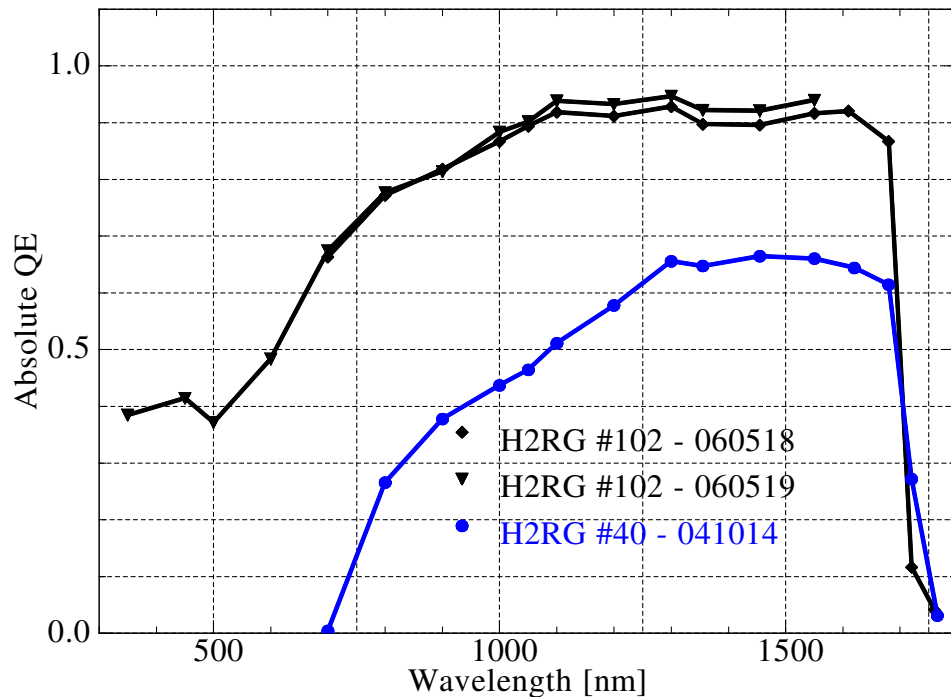


Figure 5.10. Quantum efficiency for RSC lot 1 FPA #40 and the more recent FPA # 102. The improved QE results from a combination of process improvements, substrate removal, and AR coating.

variation [Brown et al., 2005].

The system described above has been used to measure a number of SNAP $1.7 \mu\text{m}$ FPAs from both Rockwell and Raytheon. The results presented are representative of the current QE performance.

Rockwell Status

The internal quantum efficiency of HgCdTe should be close to 100%, but reflections at the surface lower the effective QE to $\sim 80\%$. An anti-reflective (AR) coating can reduce the reflection to 5%, and restore the QE to $\sim 95\%$. The QE in Rockwell FPAs was well below this limit early in the R&D program. RSC believed that part of the short wavelength ‘droop’ in QE (see Figure 5.10) was due to absorption in the substrate. High purity CdZnTe is completely transmitting above $0.85 \mu\text{m}$, but impurities in the substrate can absorb infrared light, especially at the short-wave end of the spectrum. To improve the short-wave QE Rockwell began to remove the CdZnTe

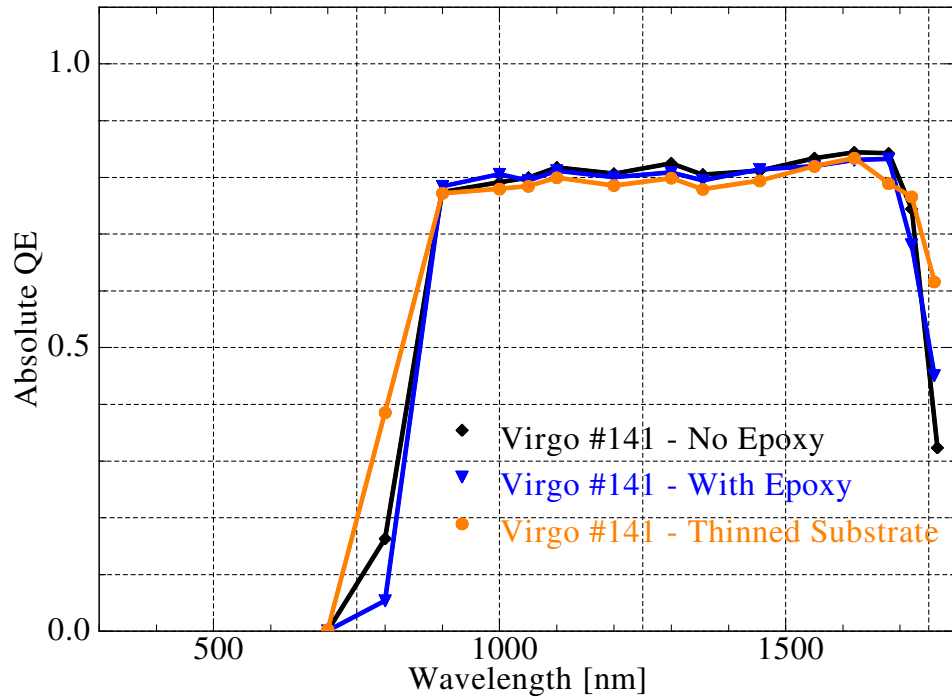


Figure 5.11. QE for RVS $1\text{k} \times 1\text{k}$ HgCdTe FPA #598141 after 3 different processing steps. No epoxy with substrate (black), with epoxy and substrate (blue), and with epoxy substrate thinned (orange). The QE in this device is remarkably stable over the course of a year and two major processing steps.

substrate (we later discovered that substrate removal was necessary to eliminate the impact of proton induced photoluminescence, see Sec. 5.3.10). This action did improve the QE in many detectors, but not up to 80%, as expected prior to AR coating. A problem with the collection of photo-generated charge within the HgCdTe diode existed. RSC solved this problem for FPAs #102 and #103. Figure 5.10 shows the QE of an early RSC device (FPA #40) along with the QE for FPA #102. There is drastic improvement in QE across the NIR bandpass, and response extending into the visible spectrum in the absence of the CdZnTe substrate. FPA #102 is substrate removed and AR coated; this FPA represents the best possible QE performance from 0.9 to 1.7 μm .

Raytheon Status

Most of the RVS detectors tested have flat, 80% QE from 0.9 to 1.7 μm . The RVS detectors are not AR coated and have an 800 μm thick CdZnTe substrate. One

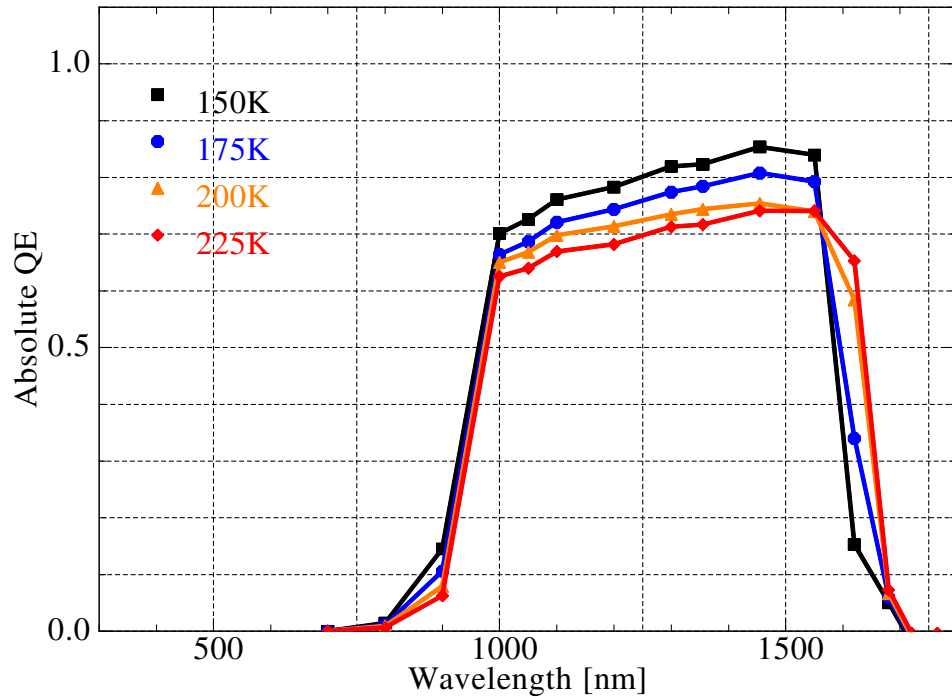


Figure 5.12. QE of an RVS InGaAs detector as a function of detector temperature. The InGaAs bandgap increases with decreasing temperature, shifting the cutoff wavelength towards the blue.

device, HgCdTe #7598141, was selected to develop substrate removal techniques at RVS. As noted above, substrate removal is now required to eliminate proton induced photoluminescence in the substrate. This device was originally tested at Michigan and has 80% QE and $16 e^-$ Fowler-1 read noise. The first step before removing the substrate is to backfill the indium bump-bond region between the HgCdTe diode and the multiplexer with epoxy. After this step, the FPA was returned to Michigan and retested. The QE remained stable despite slight changes in the conversion gain and read noise, due to increased capacitance in the presence of the epoxy. Next, the FPA was returned to RVS and the substrate was thinned to $\sim 10 \mu\text{m}$. The QE is also stable following this processing step. Quantum efficiency data for this RVS device are shown in Fig. 5.11.

The RVS InGaAs detector (ID R301IG) also exhibits high QE with no AR coating. The long-wave cutoff of InGaAs changes as a function of temperature. Many arsenides, such as InGaAs, have a strongly temperature dependent band gap. As

the temperature falls, the band gap increases and the high wavelength photons are no longer detected. This behavior is seen at 1620nm in Fig. 5.12. As the temperature drops, so does the long wavelength QE. Changes in the cutoff wavelength affect the depth of the SNAP survey. The limiting redshift for type Ia supernovae is approximately the cutoff wavelength in microns, about 1.57 for InGaAs at 140 K. The decreased survey depth, along with the lack of development resources for InGaAs and the maturity of the HgCdTe technology, led to the decision to use 1.7 μm HgCdTe for the SNAP NIR detectors.

Both manufacturers are capable of producing excellent QE, well in excess of the initial SNAP goals. This is a significant result in view of the importance of high QE, identified by the science simulations in Ch. 4. The improvement in QE is one of the major successes of the NIR program. With the QE over 90% and less than $10 e^-$ total noise, the detectors approach the ideal performance limit of a noiseless, 100% QE infrared detector.

5.3.7 Intra-pixel Variation

One of the major concerns for HgCdTe detectors is intra-pixel sensitivity variations. The SNAP pixel pitch is 18 – 20 μm , which results in a plate scale of 0.17 arcsec when combined with the SNAP optical assembly. This spacing undersamples the point spread function by a factor of 3 at 1 μm , and can degrade photometric accuracy. Early HgCdTe FPAs grown with PACE technology have large dips in sensitivity near the pixel boundaries [Finger et al., 1998]. Intra-pixel sensitivity variations of this nature can lead to large errors for undersampled photometry.

An important part of the infrared R&D program is to demonstrate accurate photometry with an undersampled point spread function (PSF). The University of Michigan took the lead on measuring intra-pixel variations and developed the ‘Spot-o-Matic,’ a tool to map out the intra-pixel structure of NIR FPAs [Barron et al., 2006]. The results measured with the Spot-o-Matic improved understanding of the detectors and uncovered a systematic substructure in one RSC device (FPA #40), which would have led to photometric errors greater than 5% for an undersampled in-

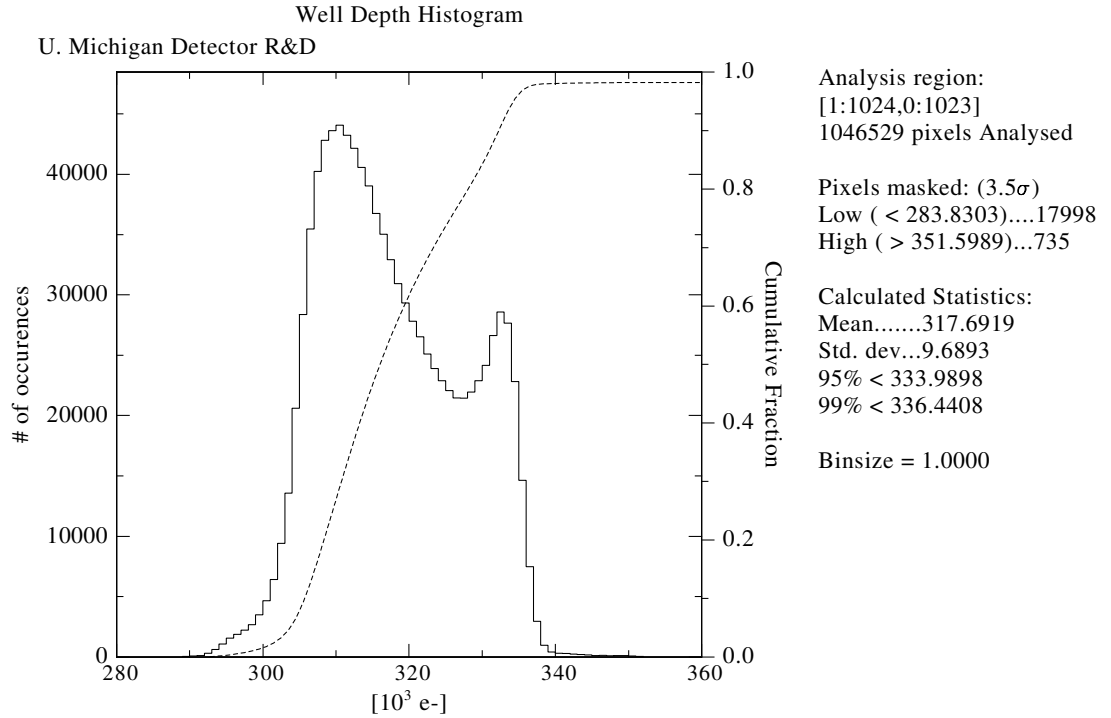


Figure 5.13. Sample well depth histogram for a RVS 1k device (ID RHG141).

strument such as SNAP. In-depth discussion of the Spot-o-Matic design, functionality and test results are presented in Sec. 5.6.

Both vendors have achieved the needed intra-pixel sensitivity for SNAP in high QE detectors. The uniformity of the intra-pixel response is highly correlated with the measured QE. Low QE devices exhibit periodic structure or large ($> 10\%$) random fluctuations, while results for detectors with near 100% internal QE show that 2% relative photometry can be restored with a simple sum over pixels, when illuminating with a spot size of only $1\ \mu\text{m}$ (FWHM). When a SNAP PSF is convolved with the measured response, the errors are much less than 1%. This is one of the outstanding issues for the SNAP NIR detectors that has been solved during the R&D program.

5.3.8 Well Depth

The well depth is the total amount of charge that is collected prior to saturation of the pixel output. As the pixel approaches saturation, the response becomes non-linear and additional charge does not change the output voltage. The well depth is deter-

mined by the pixel capacitance and the detector reverse bias. Increasing the reverse bias increases the well depth at the expense of slightly higher dark current (however, higher reverse bias actually lowers the read noise). The well depth specification for SNAP is not yet defined and will likely depend on the choice of sampling mode. If up the ramp sampling is used, the flux from bright objects can be measured even if the output saturates in less than 300 s. A well depth greater than $10^5 e^-$ provides sufficient coverage of all SNAP supernovae in the NIR filters. For ancillary science observations of bright sources, shorter exposure times can be used.

A sample well depth distribution is shown in Fig. 5.13 for RVS FPA #13A. The well depth of this device is $> 3 \times 10^5 e^-$. RVS detectors have a larger well depth than RSC due to the higher nodal capacitance (lower $\mu V/e^-$). Typical well depths for RSC H2RG FPAs are around $10^5 e^-$.

5.3.9 Persistence

Persistence is an effect related to the release of charge following exposure to light. Persistence was first observed in the HST NICMOS detectors [Daou and Skinner, 1997]. After a pixel is illuminated, the dark signal in the subsequent exposure increases above the normal dark current. This is thought to be due to the release of charge traps in the HgCdTe diode. Persistence is both time and flux dependent. Figure 5.14 shows the persistence signal after an illumination of $\sim 10^5 e^-$. For longer exposure times, the persistence signal increases, as more traps with longer time constants are filled.

Persistence is a serious issue when dealing with calibrated photometry, because it creates a systematic offset in the pixel output. The persistence signal depends on the detector characteristics and the distribution of objects in the sky. Average galaxies have a central surface brightness of 21.7 magnitudes/arcsec² in I (Freeman's law, see Binney and Merrifield [1998] pg. 221). The small pixel scale of the NIR detectors results in an integrated signal of $360 e^-$ per pixel for a typical galaxy in the SNAP field. For a persistence of 0.1 – 0.6% (see Smith et al. [2006]), the total persistence signal is only $.36 - 2.16 e^-$. Tests are ongoing to study the noise characteristics of

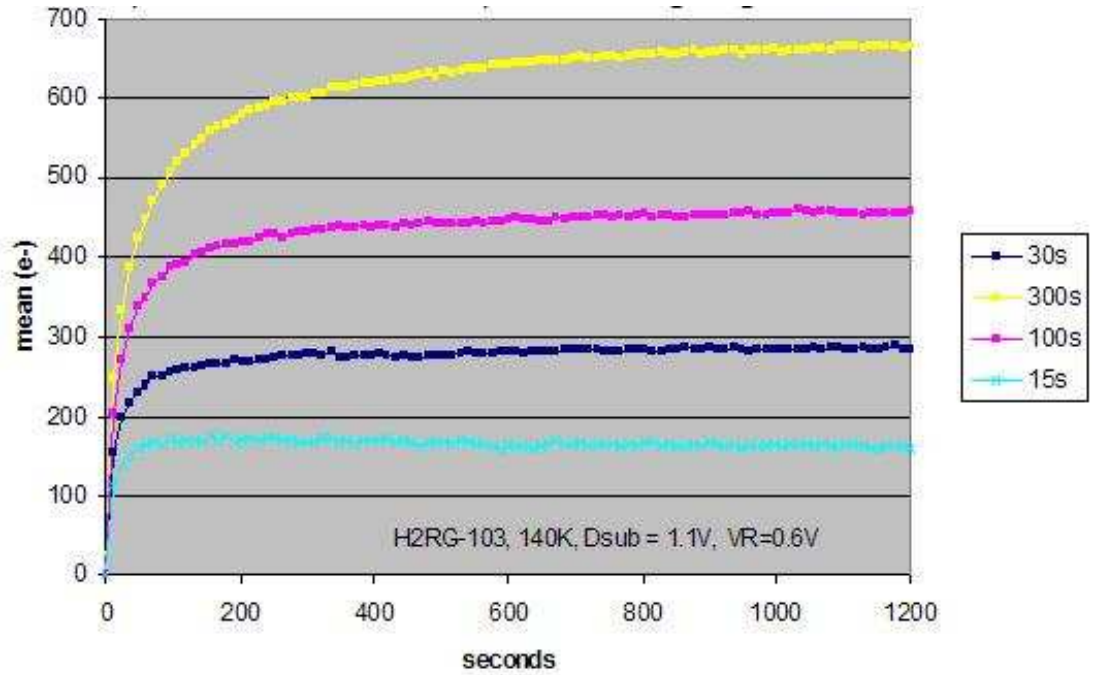


Figure 5.14. Persistence data for H2RG #103. A total signal of $10^5 e^-$ is delivered in 15, 30, 60, and 300 s. Data provided by R. Smith.

subtracting a persistence ‘map’ from each image based on the brightness distribution in the previous image. If the subtraction is successful, then only the shot noise on the persistence will exist, and this is a random noise source that is much lower than the total detector noise.

Eliminating any systematic offset that may result from persistence is one of the major concerns for both the NIR and calibration teams. The problem is being approached from the detector side by exploring readout and reset schemes to reduce or eliminate persistence. At the same time simulations of the brightness distribution for each SNAP field are being developed to simulate the number and range of impacted pixels. A preliminary look at the USNO-B fields [Monet et al., 2003] indicate that there are only approximately 70 point sources brighter than 21^{st} magnitude in the field of each SNAP NIR detector. A simple mask of all bright sources in the subsequent image can be used for these pixels with a minimal ($< 0.01\%$) loss of exposure efficiency.

5.3.10 Cosmic Rays and Luminescence

The noise and dark current performance of the NIR detectors are seriously compromised by both prompt and delayed optical emissions from the detector substrate due to cosmic rays. Figure 5.15 compares the cosmic ray events in long exposures for substrate-removed and substrate-intact devices. Both detectors experience single pixel events, where cosmic rays interact within the HgCdTe diode or the CMOS multiplexer. These events can be limited by shielding, but represent an unavoidable background that will contaminate a small percentage of the pixels in every exposure. The effect of single pixel cosmic ray events is to lower the operability and effective field of view. Diffuse cosmic ray events occur when a cosmic ray interacts in the detector substrate, and the subsequent decay deposits a small amount of charge into a large number of pixels. This is a potential source of systematic photometric uncertainty, but fortunately these events are eliminated by removing the CdZnTe substrate.

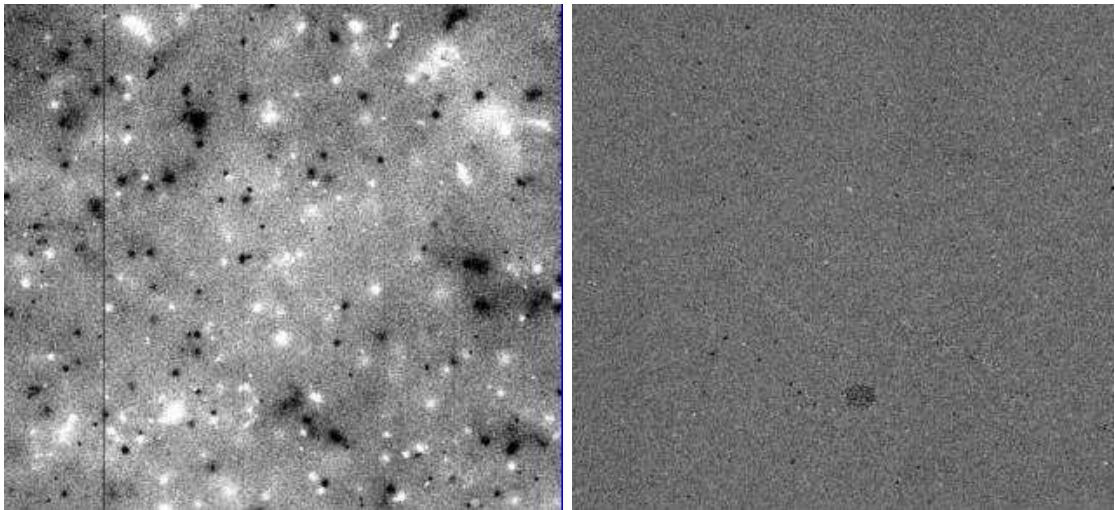


Figure 5.15. Cosmic ray events with and without CdZnTe substrate removed from H2RG detectors. Each image is the difference of consecutive dark frames to suppress dark current and hot pixels. Particle events in the first dark frame appear as negative (white) spots, and events from the second frame appear as positive (black) spots. Left: substrate intact, 3000s exposures, right: substrate removed, 3000s exposures.

Luminescence in the detector substrate is induced by energetic protons [Murakami et al., 2003]. Interactions in the substrate produce a prompt signal, due to dE/dX , and a delayed signal, due to nuclear excitation of Te, followed by positron decay.

The lifetime of the excited Te is approximately 1 week, and the resulting positron excites 850 nm photons which are detected by the HgCdTe diode. The cosmic ray rate at L2 and the cross section is such that the background due to delayed luminescence is nearly 1 photon/pixel/s, a factor of 10 times greater than the expected dark current. The detector substrate must be removed to eliminate this proton induced background. Figure 5.15 shows that removing the substrate does eliminate the diffuse photoluminescence. Rockwell has already developed complete substrate removal for 1.7 μm HgCdTe. RVS can thin the substrate to approximately 10 μm with diamond turning, but is yet to demonstrate complete substrate removal. Substrate removal is a manufacturing, not performance requirement, that has been identified and implemented by the HgCdTe vendors during the R&D program.

5.3.11 Other effects

In addition to all of the tests listed above, some secondary effects that could impact detector performance are being studied. These include flux dependent non-linearity and long term performance degradation, due to both aging and radiation damage. Flux dependent non-linearity has been observed in 1.7 μm HgCdTe detectors on the Hubble Space Telescope [Bolin et al., 2006]. Faint sources appear brighter when measured with the NIR detectors than when measured in the same bandpass using the CCD detectors. After applying a correction based on the CCD measurements, photometric errors less than 0.5% are achieved using the NIR detectors. SNAP has a similar overlap between the CCD and NIR detectors, and may be able to correct non-linearity if it is identified as an issue for SNAP. This is a potential systematic error that is being given serious consideration. It is difficult to quantify in laboratory measurements, because it requires a stable illumination of order 1 photon/pixel/s, measured with a linear reference in a low background environment. So far the only laboratory that can produce this is outer space, with white dwarfs as the illumination source and HST as the observing platform. The final stage of the R&D program will address non-linearity and determine its impact on SNAP NIR photometry.

Changes in performance as a result of aging or radiation damage are also be-

ing explored. Some degradation in dark current performance has been observed in HgCdTe detectors over the course of 2 to 3 years. The cause of the change is unknown at this time. Over the next few years, the best SNAP detectors will be repeatedly tested to look for changes in performance. Selected detectors will also be exposed to a radiation dose similar to what is expected for the SNAP mission. The results of these tests will uncover any changes in the NIR detector performance that may need to be monitored and calibrated during the course of the SNAP mission.

5.4 Detector Wrap Up

The NIR R&D program has made significant progress since its inception in 2003. Laboratory facilities and testing procedures have been established, and collaboration with Rockwell and Raytheon has produced high quality $1.7\ \mu\text{m}$ HgCdTe detectors that are near the ideal performance for the SNAP supernova survey. Sources of random error and photometric calibrations of quantum efficiency and intra-pixel variation have been studied in detail and will not limit the performance of the SNAP imager. Secondary effects of persistence and flux dependent non-linearity are now under study and do not appear to present any major problems. The R&D program is coming to an end and is ready to provide the HgCdTe vendors with NIR requirements and test procedures to qualify and select science grade FPAs for the SNAP program.

Some details on intra-pixel variations and capacitive coupling are given below. This work was conducted at the University of Michigan during the R&D program and represents two important steps in understanding FPA performance through innovative testing hardware and procedures. Parts of the text below are reproduced from papers accepted [Brown et al., 2006a] and submitted [Barron et al., 2006] to the Publications of the Astronomical Society of the Pacific (PASP).

5.5 Correlated Noise and Gain in Unfilled and Epoxy Underfilled Hybridized HgCdTe Detectors

Hybridized CMOS detectors are becoming increasingly popular in both the visible and infrared. For astronomical applications, low nodal capacitance is necessary to make precision observations over a large dynamic range of source intensities. As pixel sizes shrink to accommodate high resolution imaging, the effects of inter-pixel coupling become important [Kavadias et al., 1994]. A stochastic process such as diffusion can lead to charge transport between pixels but does not correlate the signal. Capacitive coupling is a deterministic process that shares charge after it is collected and correlates the pixel outputs.

Mutual capacitance between pixels attenuates the signal in a given pixel as the charge is deterministically shared with its neighbors. This attenuates the photon shot noise and leads to errors in standard variance estimators. Moore et al. [2006] shows that the strength of the coupling is related to the autocorrelation function. The autocorrelation can be estimated with a series of flat-field images, providing a straightforward test of the inter-pixel coupling strength. Finger et al. [2005] provide an alternate method which directly measures the pixel nodal capacitance by comparing the voltage change on an external calibrated capacitor with the voltage change on the pixel capacitors. Measurements of the nodal capacitance of epoxy backfilled Rockwell H2RG 2.5 μm cutoff HgCdTe using both methods yields the same results [Moore et al., 2006, 2003b,a, Finger et al., 2005]. Ignoring inter-pixel capacitance overestimates the pixel capacitance by up to 20%. Other coupling measurements include results from Figer et al. [2004] who use cosmic ray hits to estimate ‘crosstalk’ in a Rockwell H2RG 5 μm cutoff HgCdTe and a Raytheon SB-304 5 μm InSb FPA.

Most HgCdTe diodes are grown on a CdTe (or CdZnTe) substrate with a thickness of 200 – 800 μm . Shortwave HgCdTe is sensitive to wavelengths below 1700 nm, however for wavelengths shorter than 800 nm, the CdTe substrate absorbs the light before it reaches the active HgCdTe layer. Sensitivity at shorter, visible wavelengths is often desired, so the substrate is removed to increase the shortwave response. In

addition, substrate removal is necessary for low background space-based applications where proton induced luminescence in the substrate becomes important [Murakami et al., 2003]. With substrate removal in mind, and to improve mechanical stability, device manufacturers began to under-fill the gap between the HgCdTe diode and the multiplexer with epoxy. The epoxy is needed to prevent stress buildup in the very thin ($5 - 10 \mu\text{m}$) HgCdTe diode after the substrate is removed. The dielectric constant of the epoxy should increase the capacitive coupling between pixels following the under-fill.

The effect of correlated noise is immediately apparent when estimating the conversion gain using the photon transfer or noise squared vs. signal method [Mortara and Fowler, 1981, Janesick et al., 1985]. Gain, g , is defined in units of $\mu\text{V}/e^-$ and conversion gain, sometimes called inverse gain, g_c , in units of e^-/ADU . The pixel nodal capacitance (C_p) is then the electron charge divided by the gain

$$C_p = \frac{e}{g}. \quad (5.3)$$

The photon transfer method assumes a Poisson process; the mean is equal to the variance. A traditional variance estimator ignores correlated noise, which can underestimate the true variance. This overestimates the conversion gain (underestimates the gain) and leads to overestimates of the FPA read noise, dark current, and quantum efficiency. Apparent quantum efficiencies over 100% have been measured before correcting for inter-pixel capacitance. Accounting for the correlated noise from neighboring pixels corrects the conversion gain and quantum efficiency measurements.

Comparative measurements of the inter-pixel coupling in $1.7 \mu\text{m}$ cutoff HgCdTe FPAs from Rockwell Scientific and Raytheon Vision systems are presented below. Rockwell Scientific H2RG FPAs with epoxy under-fill exhibit correlations which result in a 16–20% systematic overestimation of the conversion gain. Results for a Raytheon Vision Systems $1.7 \mu\text{m}$ cutoff HgCdTe detector tested both before and after epoxy under-fill show increased coupling in the presence of the epoxy, and the coupling is not spatially symmetric.

5.5.1 Autocorrelation Procedure

A derivation of the relationship between the inter-pixel coupling and the measured autocorrelation is given by Moore et al. [2003b]. For the case of small coupling (ignoring terms of order the coupling squared), the autocorrelation coefficient is twice the coupling. The typical correlations measured in undepleted HgCdTe FPAs are a few percent. Detecting a correlation of this magnitude requires averaging more than 100000 pixels to reduce the noise to the fraction of a percent level.

To measure the autocorrelation function we take a series of Fowler-1 reads with approximately flat-field illumination. The illumination source is a 1300 nm LED reflected off a small light integrating cavity. All tests for 1.7 μm FPAs are conducted at 140 K inside an IR Labs ND-8 dewar. Different illumination levels are achieved by varying the LED current while keeping the FPA exposure time fixed. A maximum signal level of 40,000 photons/pixel is used. This is well below the full well (about 200,000 e^-) and avoids non-linear charge integration and pixel capacitance effects that occur near saturation. The autocorrelation tests are performed on engineering grade detectors that are part of a development effort; mis-connected and/or hot pixels often contaminate the images. Masks are applied to remove outlying pixels and results are checked against simulations to ensure accuracy. The autocorrelation is calculated from the difference of two Fowler-1 frames to minimize the effect of pixel to pixel variations. Simulations show that non-uniformity in the flat-field or detector response below the 5% level do not affect the measured correlation when using the difference method.

Data from the Rockwell H2RG FPA with epoxy under-fill shows 4% correlations to all neighboring pixels with a slight spatial asymmetry. The percent correlation is defined as the percentage of the total of the correlation matrix, in this case the normalized correlation matrix sums to one.⁵ There is no flux dependence observed in the range tested, however, tests did not include extremely low intensity levels where flux dependent gain has been observed in e.g. NICMOS detectors on Hubble [Bolin

⁵Some authors normalize the central value in the correlation matrix to one and define the percentage by dividing by all values by the central value.

et al., 2006]. The results presented are an average of many uniformly illuminated regions with defects and cosmic rays masked off. The slope of the variance vs. mean at different exposure levels provides an estimate of the conversion gain. The autocorrelation data for the unfilled (no epoxy) RVS FPA has much lower correlations, and the coupling is not spatially symmetric. Data analyzed for the same FPA with epoxy under-fill between the multiplexer and HgCdTe layers shows increased coupling.

5.5.2 Autocorrelation Results

The autocorrelation for a Rockwell H2RG $1.7\mu\text{m}$ HgCdTe with epoxy under-fill is shown in Table 5.2.

| | | | | | | |
|----|----|-----|------|-----|----|----|
| 13 | 7 | 7 | -3 | 1 | -3 | 11 |
| 0 | -9 | -1 | 22 | 7 | 14 | -8 |
| -4 | -5 | 34 | 210 | 37 | 9 | 22 |
| -3 | 12 | 265 | 5029 | 266 | 13 | -3 |
| 20 | 11 | 36 | 211 | 33 | -4 | -4 |
| -7 | 14 | 4 | 23 | -1 | -9 | -1 |
| 11 | -3 | 0 | -3 | 6 | 7 | 13 |

Table 5.2. Rockwell H2RG autocorrelation results. The noise on each coefficient is $8.6 ADU$ and the mean illumination is $6250 ADU$ ($1 ADU \equiv 5.75 \mu V$, measured at the pixel node).

The average correlation to neighboring pixels is 4.0% , near the limit where calculations for small coupling are valid. The slight asymmetry is likely due to asymmetric traces in the H2RG multiplexer and does not affect the coupling estimates. The capacitive model assumes equal coupling to each of the 4 neighbor pixels and negligible coupling to the corner pixels. Exactly calculating the coupling in this model results in a coupling strength of 2.17% . For this coupling strength, the observed correlation to the corner pixels should only be 0.09% . We observe an average correlation of 0.58% for the corner pixels, more than 3.5σ higher than the prediction in this simple model. This is strong evidence that there is a small amount of direct coupling to the corner pixels.

The central point in the correlation “matrix” of Table 1 is the autocorrelation of each pixel with itself, which is the standard moment analysis variance estimator for

data with zero mean

$$\sigma^2 = \frac{1}{2N} \sum_{i,j} D^2 [i, j]. \quad (5.4)$$

The factor of 2 results from taking the difference of two Fowler-1 frames, N is the total number of pixels and $D [i, j]$ is the magnitude of pixel i, j in the difference frame. For constant illumination the mean of $D [i, j]$ is zero. An estimate of the gain from data at a number of illumination levels using this standard variance estimator is $g = 4.15 \pm 0.01 \mu V/e^-$, or $C_p = 38.6$ fF. Adding the correlated noise from neighboring pixels yields the true gain for this Rockwell FPA: $g = 4.97 \pm 0.02 \mu V/e^-$, a nodal capacitance of only 32.2 fF. Finger et al. [2005] report a pixel capacitance of 40.9 fF using the standard variance method and 33.5 fF from direct capacitance measurements of $2.5 \mu m$ cutoff HgCdTe on the same multiplexer. The ratio of the two capacitance measurements are 1.20 and 1.22, respectively, good agreement for two different detector materials and methods.

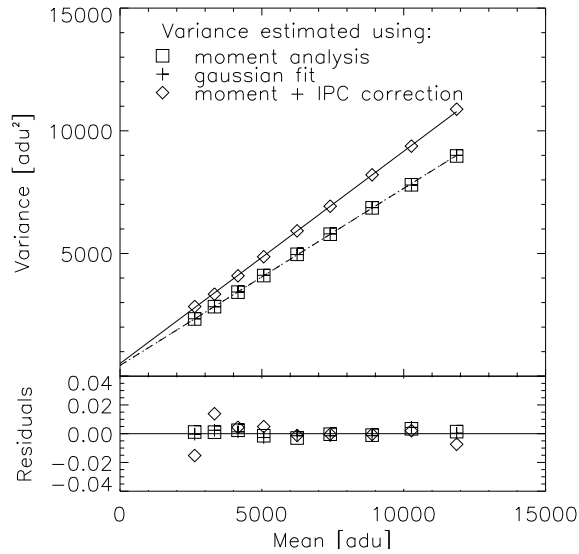


Figure 5.16. Conversion gain data for a H2RG $1.7 \mu m$ cutoff HgCdTe. Crosses represent the standard moment analysis, Gaussian fits are shown as open boxes and open diamonds are the moment analysis plus nearest neighbor correlations. There is no flux dependence in the range tested.

The variance vs. the mean for uniformly illuminated Fowler-1 frames is plotted in Figure 5.16. The curves represent three different variance estimators used to measure

the conversion gain: the standard variance estimator discussed above; a Gaussian fit to a histogram of the difference frame data; and the variance including correlations to neighboring pixels. The excellent agreement between the standard and Gaussian fit methods indicates that outliers and hot pixels have been properly masked. Unmasked outliers will cause the standard variance estimate to deviate from the Gaussian fit data. When this occurs, the errors due to bad pixels are magnified in the correlation calculation and the variance is incorrectly estimated.

The data from Rockwell H2RG arrays clearly shows the presence of correlated noise and its effect on the measured gain. To understand the cause of the correlations in these FPAs the tests were repeated for a HgCdTe device from Raytheon on a SB-301 multiplexer which has a different pixel size and multiplexer layout. This device was tested both before and after the epoxy under-fill was applied, which highlights the capacitive effects. The autocorrelation for the RVS device with no epoxy under-fill is shown in Table 5.3.

| | | | | | | |
|----|----|----|------|----|----|----|
| 5 | 5 | 6 | 7 | -4 | -6 | -1 |
| 9 | -6 | -2 | -3 | 3 | 2 | 14 |
| -1 | 7 | 3 | 20 | 0 | -4 | 0 |
| 6 | 2 | 50 | 4552 | 50 | 3 | 5 |
| 0 | -3 | -1 | 20 | 4 | 9 | 0 |
| 18 | 2 | 1 | -2 | -3 | -8 | 6 |
| 0 | -6 | -6 | 10 | 8 | 4 | 3 |

Table 5.3. Autocorrelation for and unfilled Raytheon HgCdTe FPA. The noise on each correlation coefficient is $7.5 ADU$ and the mean illumination level is $11500 ADU$ ($1 ADU \equiv 5.4 \mu V$, lower than the H2RG due to a higher multiplexer gain).

Note that the correlation matrix is highly asymmetric. The correlation is 2.5 times stronger across rows of the detector than down the readout columns. The detector junction is highly symmetric; coupling between the depletion regions of neighboring pixels through the bump bond region cannot cause the asymmetry. However, the metal lines in the SB-301 multiplexer readout unit cell are not symmetric. Coupling in the multiplexer itself must account for the asymmetry.

Since we are in the limit where correlations are small, the coupling to each neighbor is just half the correlation coefficient. The coupling across detector rows is 0.54%,

while up and down the columns it is 0.22%, compared to the noise of 0.08%. The total correlation to the four neighbor pixels is about 3%, which manifests itself as an error on the gain if correlations are ignored. This is in excellent agreement with M^cMurty et al. [2005], who independently measured a correction factor of 1.03 for a 2.5 μm cutoff HgCdTe on the same RVS SB-301 multiplexer for the VISTA project. Ignoring correlated noise, $g = 2.08 \pm 0.01 \mu\text{V}/e^-$. When using a variance estimator that includes correlations to neighboring pixels the gain is $g = 2.13 \pm 0.03 \mu\text{V}/e^-$. This corresponds to a pixel nodal capacitance of 75.1 fF, more than double that of the Rockwell FPA.

After an epoxy under-fill was added to this FPA the correlation coefficients increased, as shown in Table 5.4.

| | | | | | | |
|-----|-----|-----|------|-----|-----|-----|
| 0 | 5 | 0 | -5 | 0 | -3 | 7 |
| -13 | -7 | 4 | 9 | 5 | -12 | 12 |
| -4 | 2 | 16 | 42 | 28 | -1 | 2 |
| 10 | 13 | 113 | 4136 | 114 | 14 | 11 |
| 3 | -2 | 28 | 43 | 17 | 3 | -5 |
| 12 | -13 | 3 | 11 | 2 | -8 | -13 |
| 11 | -5 | -1 | -6 | 0 | 3 | -3 |

Table 5.4. Autocorrelation for an epoxy backfilled Raytheon HgCdTe FPA. The noise on each correlation coefficient is 9.6 *ADU* and the mean illumination level is 11350 *ADU* (1 *ADU* \equiv 5.4 μV).

The asymmetry between the columns and rows still exists at approximately the same magnitude. The correlation coefficients in both directions increased by a factor of 2.2 – 2.3; the coupling (correlation coefficient over 2) is now 1.25% across the rows and 0.48% up and down columns. A typical dielectric constant for an epoxy is 4.4; the observed increase in coupling is less than what is expected if all coupling is via the indium bumps. This fact, combined with the observed asymmetry, indicates that inter-pixel capacitive coupling occurs in the multiplexer as well as in the indium bump bond region.

With epoxy under-fill, the error on the standard variance estimator and gain increased to 9%. It is interesting to note that the pixel nodal capacitance increases slightly in the presence of the epoxy under-fill. The new gain is $g = 2.06 \pm 0.02 \mu\text{V}/e^-$,

or $C_p = 77.7$ fF.

5.5.3 Inter-pixel Capacitance Summary

Accurate determination of conversion gain with the photon transfer method is important for absolute calibration of quantum efficiency, read noise, and dark current measurements in the laboratory. Inter-pixel capacitance deterministically couples charge between pixels and attenuates the variance of the photon shot noise used to measure the conversion gain. Coupling also affects the signal to noise ratio for faint sources by spreading the signal over a larger number of pixels. For aperture photometry the additional noise added by these pixels degrades the overall photometric signal to noise ratio, leading to longer exposure times.

The pixel nodal capacitance can be estimated from the conversion gain using the autocorrelation function or measured directly with an external calibrated capacitor. For the autocorrelation method, adding the correlated noise from neighboring pixels accounts for the attenuation of the shot noise and corrects the conversion gain. Previous work has confirmed the agreement between these two methods using $2.5\mu\text{m}$ cutoff HgCdTe FPAs. The results presented here are consistent with these previous measurements for both Rockwell and Raytheon $1.7\mu\text{m}$ cutoff FPAs, indicating that the stoichiometry of the detector material has no effect on the coupling strength.

FPAs from two different vendors were tested to study the effects of inter-pixel capacitance. Rockwell Scientific and Raytheon Vision Systems $1.7\mu\text{m}$ HgCdTe with epoxy under-fill have different coupling strengths. The Rockwell H2RG multiplexer with an $18\mu\text{m}$ pixel pitch has 2 – 4 times the coupling of the RVS multiplexer with $20\mu\text{m}$ pixels. The smaller pixel spacing in the Rockwell FPA cannot account for the increased coupling. It appears that most of the difference is related to the lower nodal capacitance of Rockwell's FPAs. The Rockwell FPA capacitance is only 32.2 fF, less than half the Raytheon FPA's 77.7 fF capacitance. The same strength coupling capacitance between pixels will lead to more than twice the coupling in the Rockwell array, as observed.

Both vendors' detectors exhibit a spatial asymmetry in the correlation matrix,

with differences resulting from the multiplexer layout. The implant in the HgCdTe defines the depletion region and is highly symmetric to ensure uniform charge collection throughout the pixels. The small asymmetry in the autocorrelation for the Rockwell device suggests a fairly symmetric multiplexer layout as well. Known asymmetry in the Raytheon multiplexer leads to a 2.5 times smaller coupling down the readout columns than across the rows. As long as the asymmetry is known it can be compensated when reducing photometric data.

The same Raytheon FPA was also tested prior to epoxy under-fill. Testing the same device before and after epoxy backfill was a unique opportunity that came about as a result of the development of substrate removal techniques. The tests before the epoxy was added have about 2.2 times less coupling to the neighbors but show the same asymmetry observed after backfill. A standard epoxy has a dielectric constant of 4.4, twice the observed increase in coupling. This means only part of the capacitive coupling is occurring in the epoxy region between the indium bumps. The undepleted detector material is field free, so the additional coupling must occur in the multiplexer. Rockwell Scientific has reconsidered their multiplexer layout as a result of these discoveries. The new multiplexers are designed to minimize capacitive coupling between the traces; the studies of inter-pixel capacitive coupling during the SNAP R&D program helped bring about this change.

5.6 Spot-o-Matic Intra-pixel Response Measurements

Precise photometric observations require detailed understanding of the detector response. Large scale inter-pixel variations in detector response are characterized by a variety of well-established flat fielding methods. No such methods exist for the small scale intra-pixel sensitivity variations; the change in response within a pixel depending upon the location of the point-spread function (PSF). Small scale structure in the pixel response function (PRF) introduces uncertainty in the conversion between detected signal and incident light. This is particularly important for SNAP, which undersamples the PSF by up to a factor of 3.

5.6.1 Overview of Technique

An automated spot projection system has been developed to study the intra-pixel response in NIR sensors. The system, called the “Spot-o-Matic”, is part of the University of Michigan Near Infrared Detector Testing Facility. It is designed to measure one-dimensional and two-dimensional response profiles within pixels in large format NIR focal plane arrays (FPAs), developed for use in both ground and wide-field space surveys. The Spot-o-Matic scans a stable, micron sized spot across a small region of the detector and records the response at each spot position. A computer controlled $x-y-z$ stage allows large high resolution scans of 25 to 50 pixels with sub-micron motion control. Intra-pixel sensitivity variations were expected to be at the few percent level; therefore, the system was designed to achieve a relative accuracy of better than 1% within a small region of pixels. The Spot-o-Matic has been used to measure the PRF for a number of commercially produced large format NIR sensors, shown in Table 5.5.

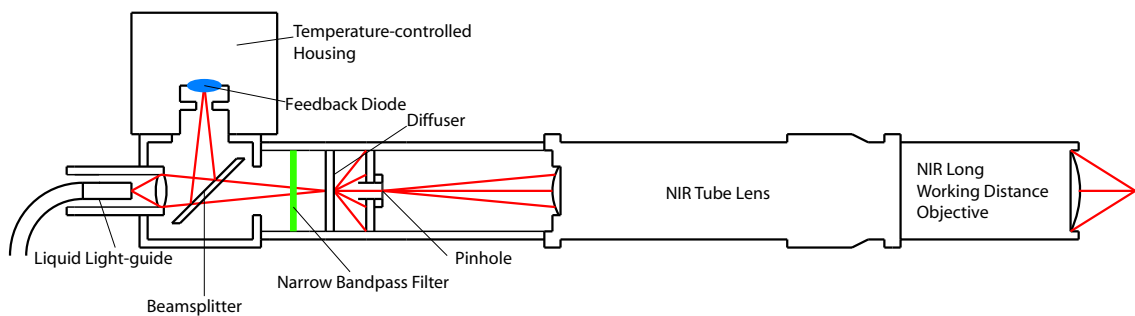


Figure 5.17. Schematic diagram of the optical components of the Spot-O-Matic.

The design for the Spot-o-Matic is based on a pinhole projector for visible light [Wagner, 2002], developed to measure diffusion in Charge Coupled Devices (CCDs), as shown in Fig. 5.17. A long working distance objective is used to project a spot onto a detector mounted inside a cold dewar. NIR detectors designed for low background applications must be cooled to limit the generation of thermal carriers (dark current) to acceptable values. The Spot-o-Matic instrument is described in Barron et al. [2006].

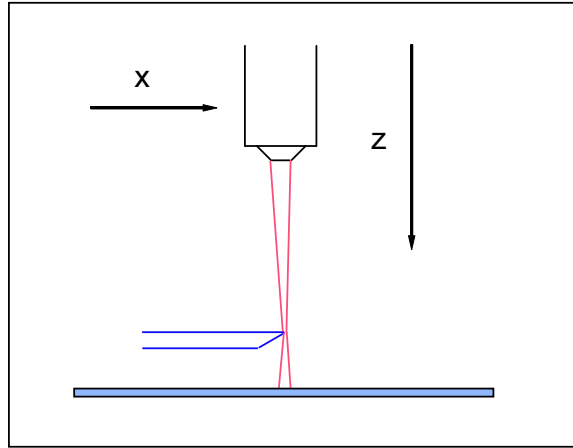


Figure 5.18. Schematic Diagram of the Foucault knife-edge scanning procedure. The point source image is scanned across a precision edge in the x -direction to determine the line-spread function. The image location is found by focusing in the z -direction to minimize the spot size.

5.6.2 Characterizing Beam Spots

To measure the intra-pixel response of individual pixels, the Spot-O-Matic is designed to produce spots much smaller than typical NIR pixels. Detectors are tested with 1050 nm and 1550 nm light. The two wavelengths are chosen to probe both the short and long wavelength response of 1.7 μm cutoff detectors. 1550 nm is chosen because the long wavelength cutoff InGaAs detectors, which is 1.7 μm at room temperature, drops to 1.57 μm at 140 K due an increased bandgap energy at lower temperature. 1050 nm is near the shortwave cutoff of 900 nm, but long enough to avoid absorption in the substrate above the active diode.

The beam spots are measured using the Foucault knife-edge technique, a procedure commonly used to determine the spatial profiles of images from point sources [Klimasewski, 1967]. The transmitted intensity is recorded as a spot is scanned across a mechanical obscuration (i.e. a razor blade) mounted about 2 mm above the detector surface, as shown in Fig. 5.18. The unobscured beam covers a few hundred pixels and is therefore insensitive to pixel sensitivity variations.

At a wavelength of 1050 nm, the beam has a Gaussian width of $\sigma = 0.95 \pm 0.03 \mu\text{m}$, while at 1550 nm $\sigma = 1.28 \pm 0.04 \mu\text{m}$. The measured beam includes contributions from the Airy disk and the demagnified geometric pinhole image. The full width at half

maximum (FWHM) of the Airy disk is related to the numerical aperture by

$$FWHM = 1.029\lambda \frac{\sqrt{1 - NA^2}}{2 NA}, \quad (5.5)$$

with $NA = 0.26$ for the Spot-o-Matic optics. The root mean squared (RMS) width of a circular spot is $\sigma = 0.816 d$ ($d = 0.5 \mu\text{m}$, the diameter of the demagnified pinhole image in the absence of diffraction). Adding the two components in quadrature, the expected spot size is $0.94 \mu\text{m}$ at a wavelength of 1050 nm and $1.32 \mu\text{m}$ at 1550 nm , in excellent agreement with the measured values.

5.6.3 Pixel Response Measurements

For pixel response measurements, a virtual knife-edge procedure is employed to focus the spot onto the detector surface. This procedure is similar to the Foucault knife-edge procedure, but instead of obstructing the light beam with a razor blade, a sub-pixel spot is scanned across the center of an individual pixel while recording the signal in that pixel. The edge of the pixel has the same function as the edge of the razor blade in the Foucault knife-edge scan. Diffusion between pixels widens the edge, but is constant and independent of the spot size. The best focus is reached when the edge width is minimized.

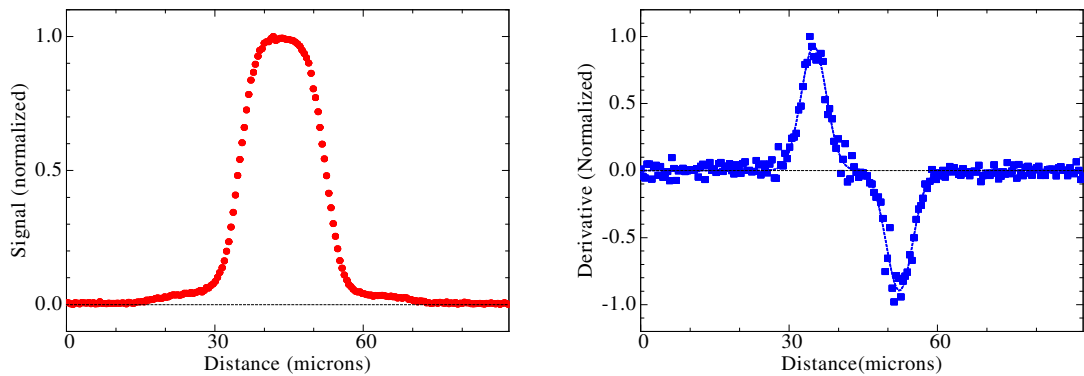


Figure 5.19. Top panel: One-dimensional scan of an arbitrary single pixel at a wavelength of 1050 nm . Bottom panel: Derivative of signal with best fit Gaussian functions over-plotted. The average width (σ) of the two Gaussians is $2.6 \mu\text{m}$.

Figure 5.19 shows the intensity profile of a single representative pixel and the

derivative at a wavelength of 1050 nm. The measured intensity profile shown in the upper panel is the result of the convolution of the Spot-o-Matic PSF and the pixel response function, which includes lateral charge diffusion and capacitive coupling between neighboring pixels. The edge transition's RMS width has increased from $\sigma = 0.95 \mu\text{m}$, obtained from the Foucault knife-edge scan, to $2.6 \mu\text{m}$. This indicates the presence of intra-pixel sensitivity variations due to lateral charge diffusion in the detector material.

Following the determination of the best focus with the virtual knife edge technique, a small region of pixels (approximately 6×6) is scanned in two dimensions to measure both the pixel response and the total integrated detector response as a function of spot position. A raster scan (scanning the spot repeatedly across the detector in x with incremental steps in y between scans) produces detailed two-dimensional pixel response profiles.

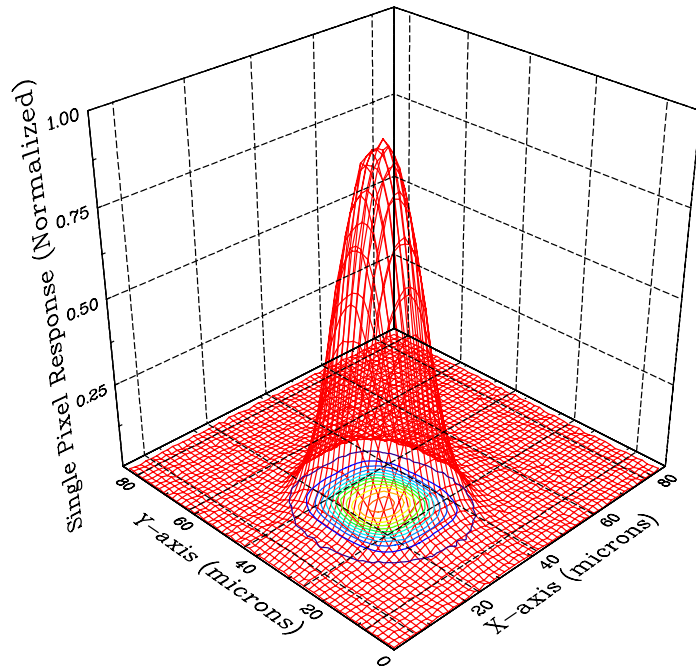


Figure 5.20. Two-dimensional scan of an arbitrary single pixel at a wavelength of 1050 nm. The grid on the bottom represents the physical size of the pixel ($18 \times 18 \mu\text{m}^2$).

The measured pixel response, shown in Fig. 5.20, is nearly symmetric with no apparent substructure. The observed sensitivity beyond the pixel boundary is due to

a combination of lateral charge diffusion, capacitive coupling and light from higher order rings of the Airy disk. When a spot (with wavelength 1050 nm) is centered in a pixel, approximately 2% of the light is diffracted onto the eight neighboring pixels. This light only accounts for a small fraction of the total signal measured in the eight neighboring pixels. The larger fraction is due to capacitive coupling between the pixels [Moore et al., 2003b]. This is a process that deterministically shares charge after the photons are collected, unlike diffusion which is random in nature and occurs prior to charge collection. The small pixel spacing of the measured sensors results in charge sharing between adjacent pixels, which widens the PRF and extends the sensitivity of each pixel far into the neighboring pixels. Extraction of the PRF requires a de-convolution of the measured pixel response and the measured point-spread function of the projected spot, as discussed in Sec. 5.6.4. The measured PRF is fit to extract a diffusion length and to determine the magnitude of the capacitive coupling. Previous estimates of capacitive coupling in hybridized HgCdTe detectors using the auto-correlation function [Moore et al., 2006] indicate a 1 to 2% coupling, depending on the pixel capacitance, which varies with manufacturer [Brown et al., 2006a].

5.6.4 Results and Analysis

The data obtained with the Spot-o-Matic undergo a number of different analyses. For one-dimensional scans, the data from rows of adjacent pixels is summed to identify dips in sensitivity between the pixels. Deconvolution techniques are used to remove the spot PSF and study diffusion and capacitive coupling which affect the intra-pixel structure. The two-dimensional scans are summed over an 8×8 region of pixels to probe the integrated response as a function of centroid position. Devices with a 100% fill factor should not have any dips at the pixel boundaries.

Table 5.5 lists the devices from two different vendors that have been tested using the Spot-o-Matic. The first three devices, which include HgCdTe and InGaAs, exhibit good intra-pixel response. Analysis of the two-dimensional summed response profiles shows that the integrated response is uniform to better than 2% in each of

| NIR sensor | Manufacturer | Device ID | Measured QE |
|------------|--------------|------------------|-------------|
| InGaAs | Raytheon | Virgo 1k | > 80% |
| HgCdTe | Raytheon | Virgo 598141 | > 80% |
| HgCdTe | Rockwell | H2RG #102 | > 80% |
| HgCdTe | Rockwell | H2RG #40 | 50 – 70% |
| HgCdTe | Rockwell | Banded Array #25 | 20 – 30% |

Table 5.5. The five $1.7\ \mu\text{m}$ HgCdTe FPAs that have been tested using the Spot-o-Matic. The top three sensors in the table have measured quantum efficiencies (QE) over 80%, equivalent to nearly 100% internal quantum efficiency. The two sensors below the line have lower quantum efficiency and non-uniform intra-pixel response.

these detectors. All three devices showing good uniformity have nearly 100% internal quantum efficiency, after correcting for reflections at the detector surface. The other two devices listed in the Table 5.5 have significantly lower quantum efficiency. These are experimental devices that were produced as part of an ongoing research and development program; the process was not optimized to produce high quantum efficiency. One of these devices (H2RG #40) exhibited a periodic structure in the pixel response, discussed in Sec. 5.6.5, while the other showed large random deviations (greater than 10%) in uniformity. Sections 5.6.4 and 5.6.4 present results for one HgCdTe device from the first three high quantum efficiency detectors that is typical of the response measured in all high quantum efficiency detectors. The periodic structure observed H2RG #40 is also presented, as this data is used in Sec. 5.6.6 to demonstrate the effects of abnormal pixel response on undersampled point source photometry.

Intra-Pixel Sensitivity Variations in One Dimension

Early HgCdTe devices showed reduced sensitivity near the pixel boundaries [Finger et al., 1998]. To test for sensitivity variations between pixels, several adjacent pixels are summed as displayed in Fig. 5.21. The integrated response is used to estimate the total variation in response as a function of PSF centroid position.

The summed data in Fig. 5.21 has an RMS fluctuation of 1.02%. At pixel boundaries the signal is shared equally between the two pixels, as is expected for pixels with a large fill factor. This result is typical of all high quantum efficiency HgCdTe and InGaAs detectors tested. The data suggests that photoelectrons are collected with close to uniform efficiency even if they are generated near pixel boundaries. It

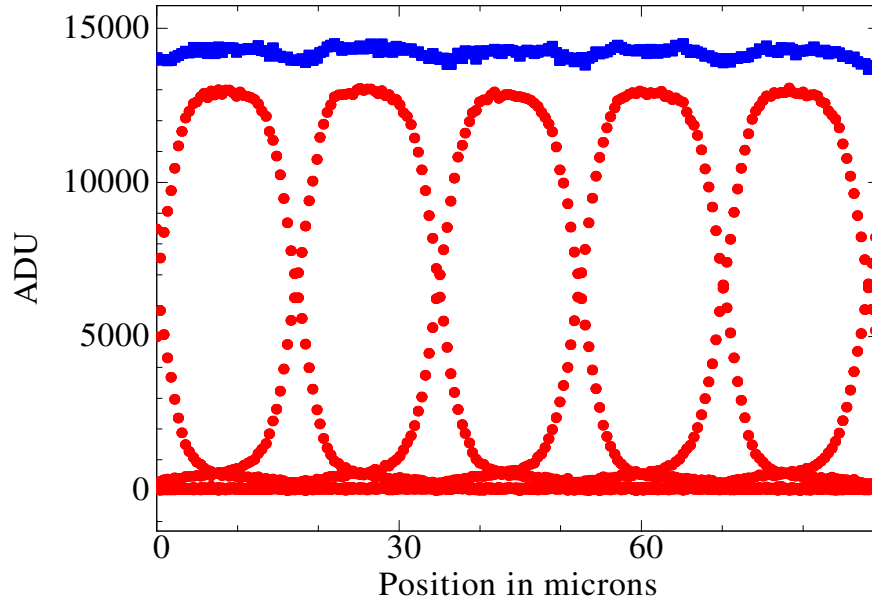


Figure 5.21. One-dimensional scan for 1050 nm light over 5 adjacent pixels located along the y -direction. The scan is performed through the center of the 5 pixels. The response of each individual pixel is displayed along with the summed response. The RMS fluctuation of the summed response from 20 to 70 μm is 1.02%.

confirms that lateral charge diffusion or capacitive coupling [Brown et al., 2006a, Moore et al., 2006], rather than inefficient charge collection, is the dominant source of the intra-pixel variation in this device. The tails in the PRF extend to the edge of the neighboring pixel; a clear sign of capacitive charge sharing between neighboring pixels.

Extracting the Pixel Response

To determine the true pixel response function, the PSF must be deconvolved from the raw data. The goal of the deconvolution procedure is to understand how charge collection varies within a pixel. The two main effects being studied are diffusion and capacitive coupling.

Deconvolution of discretely sampled data is often difficult due to the small magnitude of the high frequency Fourier components. One commonly used method that ameliorates this problem is Wiener deconvolution, which adds a small noise term to each Fourier term. Wiener deconvolution was attempted to remove the Spot-o-Matic

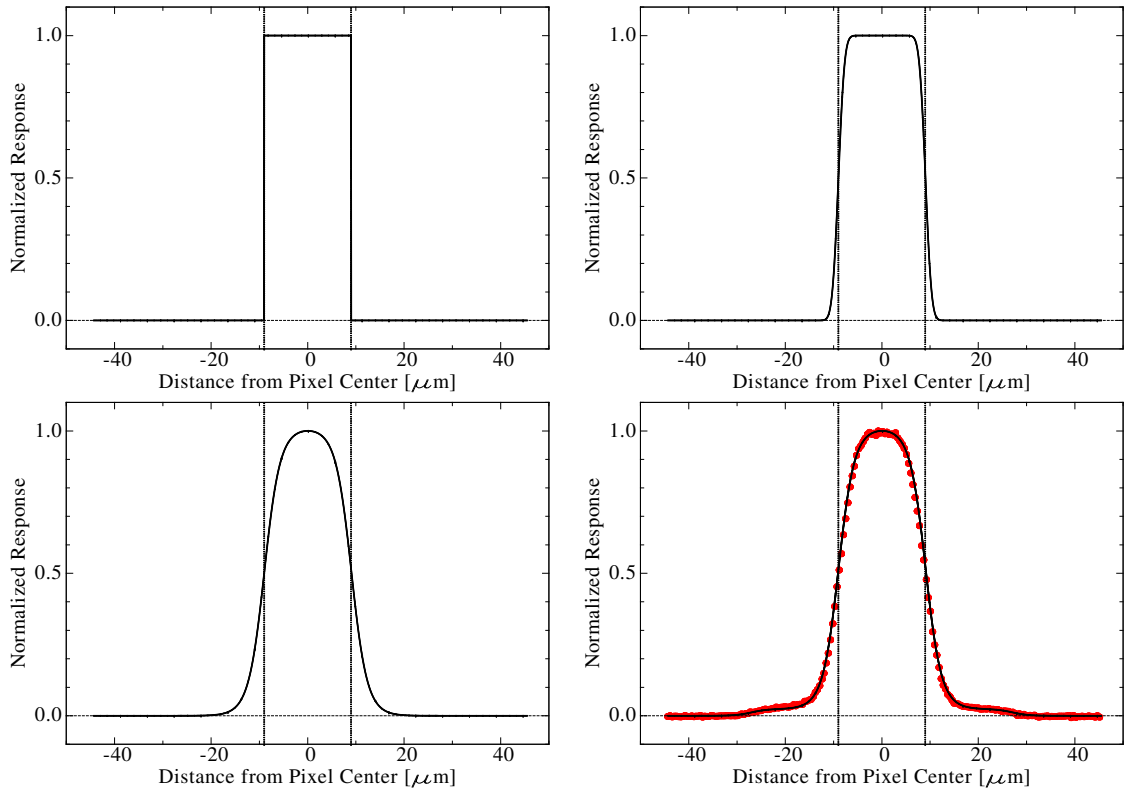


Figure 5.22. Convolution of one-dimensional pixel scan data. The procedure begins with a boxcar PRF (top left), then adds the Spot-o-Matic PSF (top right), lateral charge diffusion (bottom left) and finally capacitive coupling (bottom right). The dotted line represents the physical pixel boundary. The raw data is added in the bottom right panel.

PSF from the PRF data with limited success. A more effective solution to this problem is to approximate each component of the pixel response with a model response function then convolve the components and compare to the raw data. The detectors are modeled by convolving the measured Spot-o-Matic PSF with a boxcar response, diffusion, and capacitive coupling, then fitting for the magnitude of the diffusion and coupling with the raw data.

The fitting procedure begins with a two parameter (width and position) boxcar response function. The pixel pitch for the data presented is $18\ \mu\text{m}$; the width may be fixed at the known value or allowed to vary with little impact on the best fit diffusion and capacitive coupling. The boxcar is first convolved with the Spot-o-Matic PSF, a Gaussian with $\sigma = 0.95\ \mu\text{m}$ measured using the Foucault knife edge scanning procedure. The result is convolved with a diffusion term proportional to the hyperbolic secant, given as

$$I_D(\Delta x) \propto \text{sech}(\Delta x/l_d), \quad (5.6)$$

where l_d is the diffusion length and Δx is the distance from the location of the electron-hole pair. Finally, capacitive coupling is added by assuming a grid of identical pixels with a coupling coefficient α . Each pixel gains or loses a charge of α times the difference of the pixel value and each of its four neighbors. Figure 5.22 shows the progression from the initial boxcar response to the measured pixel response, using the best fit parameters.

The extracted pixel response is shown in Fig. 5.23. The pixel response includes only diffusion and capacitive coupling convolved with a boxcar response function. The best fit for to the raw one-dimensional scan data, which also includes the Spot-o-Matic PSF, is shown in the bottom right panel of Fig 5.22. The pixel response with and without the spot PSF included are nearly indistinguishable. The impact of the PSF is minimal when σ is much less than the diffusion length, l_d . For the pixel shown, best fit values for diffusion and capacitive coupling are $l_d = 1.87 \pm 0.02\ \mu\text{m}$ and $\alpha = 2.14 \pm 0.1\ \%$. Measurements of the coupling with the autocorrelation function give

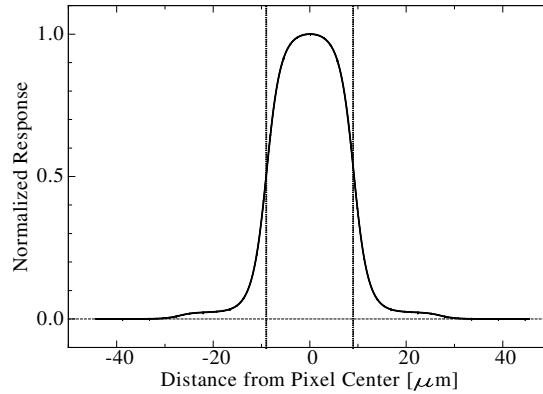


Figure 5.23. A boxcar response convolved with the best fit diffusion and capacitive coupling. This is the pixel response function with the effects of the Spot-o-Matic PSF removed.

$\alpha = 2.2 \pm 0.1\%$ [Brown et al., 2006a], in excellent agreement with the Spot-o-Matic results.

Intra-Pixel Sensitivity Variations in Two Dimensions

The two-dimensional Spot-o-Matic scans produce a wealth of information about the pixel structure and device performance. Figure 5.24 shows a two-dimensional scan extended over an array of 4×4 pixels. In order to include all the charge collected, an 8×8 array of pixels is summed to produce this spectrum. The fluctuations in the summed spectrum have an RMS deviation of 1.9%. Approximately 1% of the fluctuations are statistical, due to the large background from the warm optics blackbody radiating through the dewar window. Subtracting this noise in quadrature, the intra-pixel sensitivity variations measured for this device using a micron sized spot are 1.6%. When this detector response is convolved with a critically sampled PSF⁶, variations of this magnitude have no measurable effect on precision photometry (see Sec. 5.6.6).

One way to reduce the noise in the current setup is to take many exposures at each position and average the response. This has not been necessary for the measurements presented, which are intended to demonstrate the impact of intra-pixel variations on photometry. The statistical uncertainty limit of 1% is sufficient to achieve the goals

⁶Critical sampling is defined as a FWHM equal to 2 resolution elements.

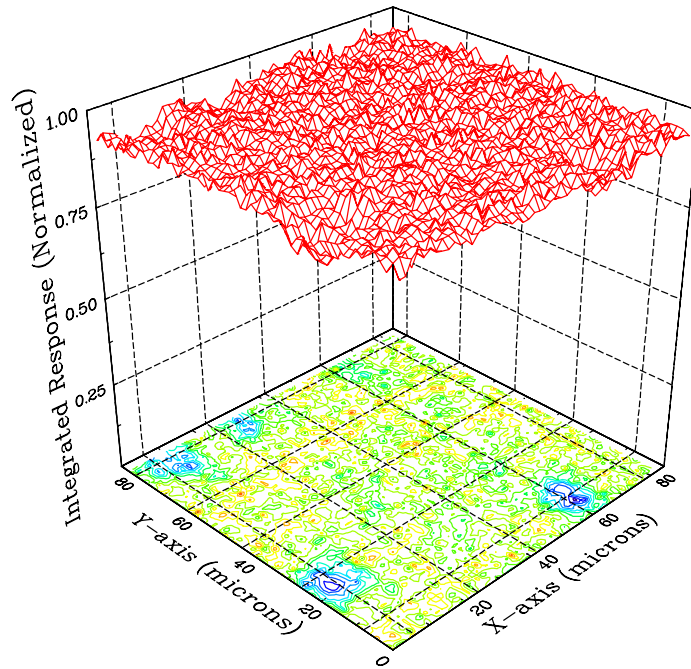


Figure 5.24. Two-dimensional scan for 1050 nm light, summed over an array of 8×8 adjacent pixels. Only the response of the inner 4×4 array is shown.

of the measurement. The statistical fluctuations quickly average out when convolving the measured two-dimensional response functions with larger point spread functions.

The four small dark patches in the contours in Fig. 5.24 are each a few microns wide and correspond to a drop in sensitivity of approximately 5%. These could be due to small dust particles on the detector surface, or defects in the HgCdTe which lead to traps or recombination. The same dips in sensitivity are reproduced in scans using 1550 nm light (not shown). These small dips are not apparent in flat-field images and do not impact photometry, however they show that the Spot-o-Matic can detect micron sized variations at the percent level. This measurement also demonstrates that a simple addition of adjacent pixels restores photometry to better than 2%, despite these dips in sensitivity.

5.6.5 A sensor with anomalous substructure - FPA #40

An anomalous intra-pixel structure was observed in one of the early engineering grade detectors tested at the University of Michigan. At the time it was delivered,

this detector was close to the best overall performance for $1.7\ \mu\text{m}$ HgCdTe at 140 K. The detector has 50 to 70% quantum efficiency, 35 electrons read noise (Fowler-1), and a dark current of $0.05\ \text{e}^-/\text{pixel}/\text{s}$, typical of the best performance achieved in developmental FPAs for the Hubble Space Telescope’s Wide Field Camera 3 upgrade. The current generation of detectors show improved quantum efficiency and lower read noise (the dark current was already near the theoretical limit at 140 K).

Spot-o-Matic measurements of this device uncovered an anomalous “chair-like” intra-pixel structure as shown in Fig. 5.25. The origin of this unusual intra-pixel sensitivity variation is not known, but is speculated to be caused by mask misalignment in the bonding process.

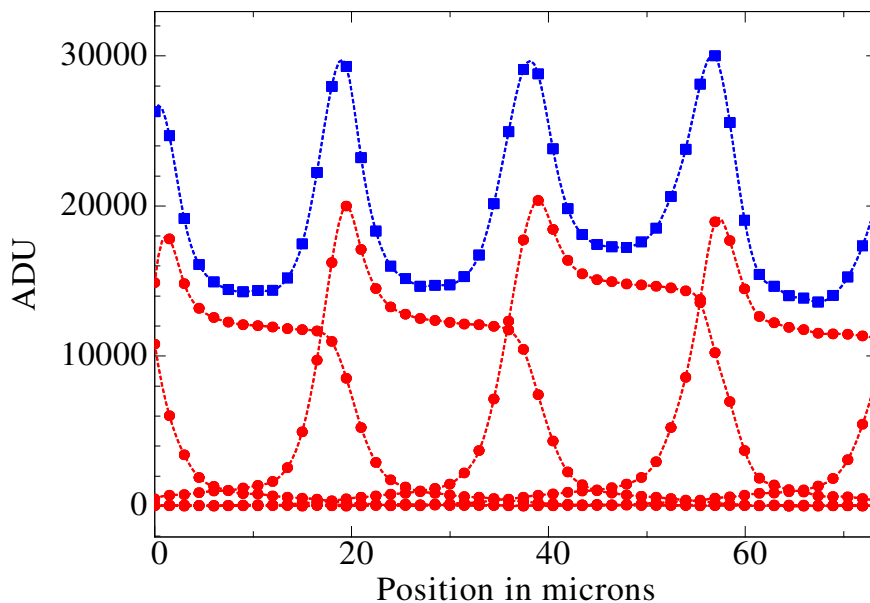


Figure 5.25. One-dimensional scan over four adjacent pixels located along the y -direction. The scan is performed through the center of the four pixels. The response of each individual pixel (filled circles) is displayed together with the summed response of the four pixels (filled squares).

The structure observed in this device is unlike anything that had been observed or even expected for a HgCdTe device. The pixel response was not symmetric; scans in the perpendicular direction do not show the same structure as Fig. 5.25. The two-dimensional profile of an individual pixel in Fig. 5.26 shows the asymmetry. The increased response near the edge of the pixel is especially puzzling. The same

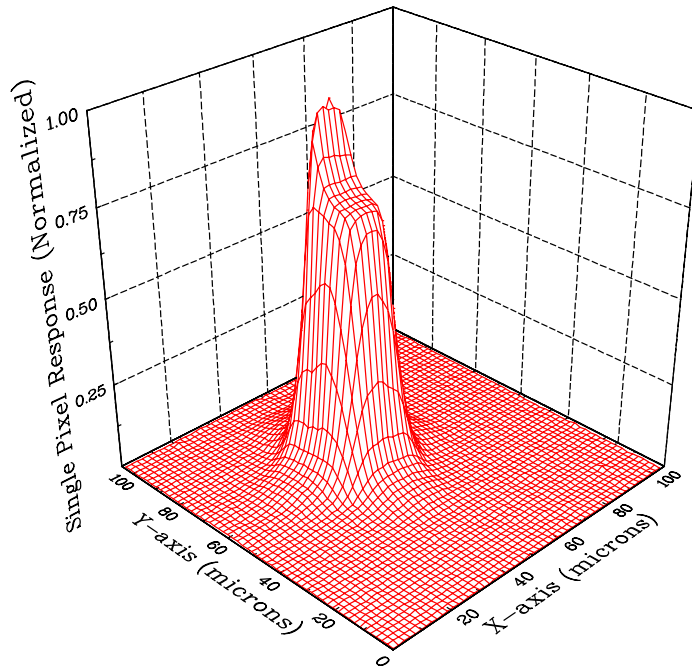


Figure 5.26. Two-dimensional scan of an arbitrary single pixel at a wavelength of 1300 nm.

structure is present in all the pixels tested on this detector. Three distinct regions, including near the edge and center of the detector, were sampled with the Spot-o-Matic and all exhibit similar intra-pixel response.

The summed response of this device exhibits periodic peaks and valleys, as shown in Fig. 5.27. The RMS variation in the summed spectrum is 18%. While this sensor appears to be an excellent device that passes all common tests (QE, noise, etc), the intra-pixel variations are averaged out in these tests and are therefore not observable. Such intra-pixel sensitivity variations can significantly degrade photometry in undersampled observations.

5.6.6 Photometry Simulations

The single pixel response functions and two-dimensional summed scans produced using the Spot-o-Matic can be used to simulate photometry errors for a range of different sampling frequencies. For critically or oversampled Gaussian point spread functions, the intra-pixel variations have little impact on photometry. However, when an instrument is undersampled, sensitivity variations (such as those observed in FPA

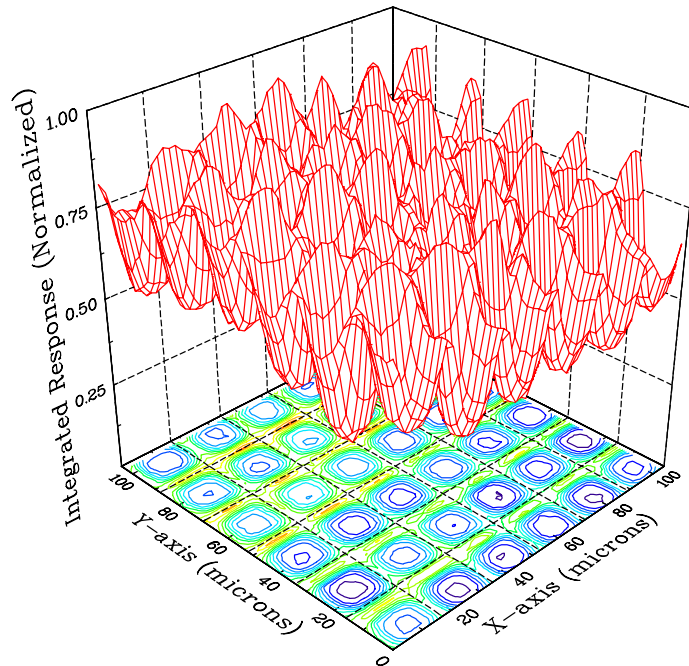


Figure 5.27. Two-dimensional scan summed over an array of 6×6 adjacent pixels.

40) can lead to RMS photometry errors larger than 5% for a modestly (factor of 3) undersampled instrument.

Figure 5.28 shows the fractional RMS error as a function of PSF size for the two detectors presented in Sec. 5.6.4. This plot assumes a grid of identical pixels with the two-dimensional response profiles shown in Figs. 5.20 and 5.26. The summed response spectrum of the pixel grid is convolved with a Gaussian PSF with FWHM ranging from a fraction of a pixel up to two pixels. For the three high quantum efficiency detectors tested, the photometric errors are less than 2% for any size PSF. If a detector has periodic structure in the summed spectrum, the photometric errors are well over 10% when the sampling is much less than critical. As the sampling frequency increases, the intra-pixel variations average out, and for a FWHM of more than two pixels the photometric errors are negligible.

5.6.7 Summary of Results

The Spot-o-Matic has been used to characterize the intra-pixel response of a number of $1.7 \mu\text{m}$ cutoff focal plane arrays from both Raytheon Vision Systems and Rockwell

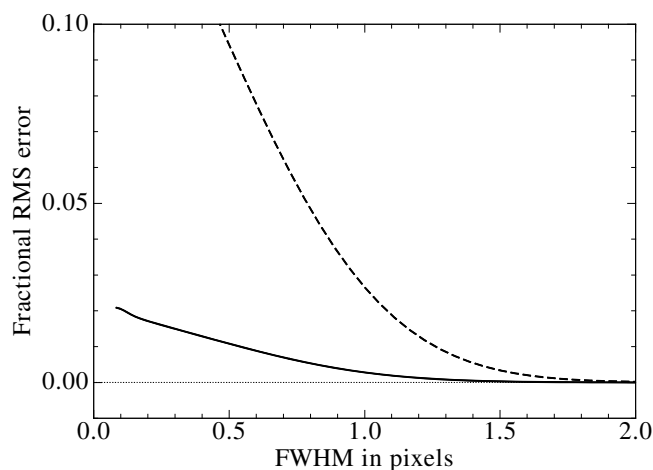


Figure 5.28. Fractional photometric error vs. sampling frequency for: a typical high quantum efficiency detector (solid curve); and FPA #40, with 50 to 70% quantum efficiency and an anomalous substructure in the pixel response (dashed curve).

Scientific. The results for devices with high quantum efficiency (near 100% internal quantum efficiency after accounting for reflections) indicate that the pixel response is uniform to better than 2% in all areas tested. This result is not surprising; high quantum efficiency detectors must count all of the incident photons. A surprising result came from a detector from an early research and development lot that had moderate quantum efficiency (50 to 70%) and reasonable noise and dark current. The intra-pixel structure in this device was highly asymmetric and had the greatest sensitivity near the edge of the pixels. Previous generations of HgCdTe devices had a low fill factor which lead to dips in sensitivity near the edges; increased sensitivity near the pixel boundary is an unexpected result that cannot be explained. This otherwise high quality detector would cause large photometric errors in an undersampled instrument. Spot-o-Matic measurements can find variations of this nature and help increase understanding of the intra-pixel structure of near infrared FPAs.

The Spot-o-Matic was developed as a tool to validate intra-pixel response in NIR FPAs for SNAP. The performance of the Spot-o-Matic allows for precision measurements of the intra-pixel structure of 1.7 μm cutoff NIR detectors. This unique instrument has ameliorated concerns about sensitivity variations and photometry errors

for NIR detectors. The results show that both vendors are capable of achieving the SNAP photometry requirements.

CHAPTER 6

Simulated Constraints on Dark Energy

The simulations used to define the detector requirements in Ch. 4 and the detector characterization results in Ch. 5 show that the best detectors from the NIR R&D program are approaching the performance of ideal NIR detectors. For observations of type Ia supernovae with the SNAP zodiacal background, the total detector noise is less than 25% of the total noise per 300 s exposure (assuming a 4 pixel aperture). A statistical accuracy of less than 2% is achieved up to a redshift of 1.7 when observing approximately 100 type Ia supernovae per $\Delta z = 0.1$ redshift bin. At this level of accuracy, systematic uncertainties begin to dominate the error budget for SNAP. The systematic uncertainty is difficult to quantify, so simple models that vary with redshift are used below to illustrate the impact of systematic uncertainties in the distance modulus measurements.

High signal to noise NIR observations of both low and high redshift supernovae limit the systematic uncertainty in a number of ways. For low z events, the NIR filters improve estimates of the dust extinction and provide increased spectroscopic coverage at long wavelengths. At high redshifts, the restframe B and V bands are observed exclusively with the NIR detectors. The filter design minimizes K-corrections, and the NIR arm of the spectrograph covers all of the key features in the supernova spectrum up to $z = 1.7$. Features in the supernova spectrum correlate with peak brightness and may uncover subclasses of type Ia supernovae within each sample. Part of the ‘intrinsic’ dispersion in type Ia events may be due to different metallicity or carbon/oxygen concentration that result from differences in the progenitor white dwarfs and the galactic environment where they reside. The unprecedented spectral and temporal coverage of supernova lightcurves that SNAP will attain is ideal for

identifying potential differences among type Ia explosions that are not apparent in existing observations. The SNAP NIR sub-systems are important for limiting systematic uncertainties and achieving the best possible constraints on dark energy.

This chapter begins with constraints on w_0 and w_a from type Ia supernovae. All of the data assume the default SNAP observing parameters: a 4 day cadence, 4 dithered 300 s exposures per pointing with a 2 m aperture¹, etc. The NIR detectors have QE = 90% and total noise = $10 e^-$, assuming all of the pixels are identical. To begin, the impact of statistical and systematic uncertainties are explored for two dark energy models. Next, results for simulations of 2000 supernovae, including fluctuations in the stretch, host galaxy dust extinction, and the distance modulus, are presented. These data assume a spatially flat cosmology and require prior knowledge of Ω_M to limit the uncertainty on the dark energy parameters. To address potential bias due to assumptions about the flatness and matter density, the supernova data are combined with CMB, weak lensing, and baryon acoustic oscillation data using a Fisher matrix analysis. The combination of these techniques results in uncertainties of $\sigma_{w_0} = 0.04$ and $\sigma_{w_a} = 0.12$ for a concordance Λ CDM cosmology. This uncertainty is consistent with the DETF goal for a stage IV² dedicated dark energy mission, such as SNAP.

6.1 Dark Energy constraints with Supernovae

The ability to constrain the dark energy equation of state with type Ia supernovae depends on the redshift range and accuracy of the distance modulus measurements. Space based measurements of high redshift supernovae are key to the SNAP science goals, as demonstrated by the improvement to existing dark energy constraints when including the small number of high redshift supernovae discovered with HST (Sec. 3.5). SNAP provides the field of view and accuracy needed to discover and follow up a large number of high redshift type Ia supernovae.

¹SNAP is considering a smaller, 1.8 m aperture. This is equivalent to reducing the QE by $\sim 20\%$.

²The DETF defines stage IV experiments as future missions currently being developed to study dark energy, such as a Square Kilometer Array (SKA) of radio telescopes, a Large Survey Telescope (LST), or the Joint Dark Energy Mission (JDEM). SNAP is a candidate mission for JDEM.

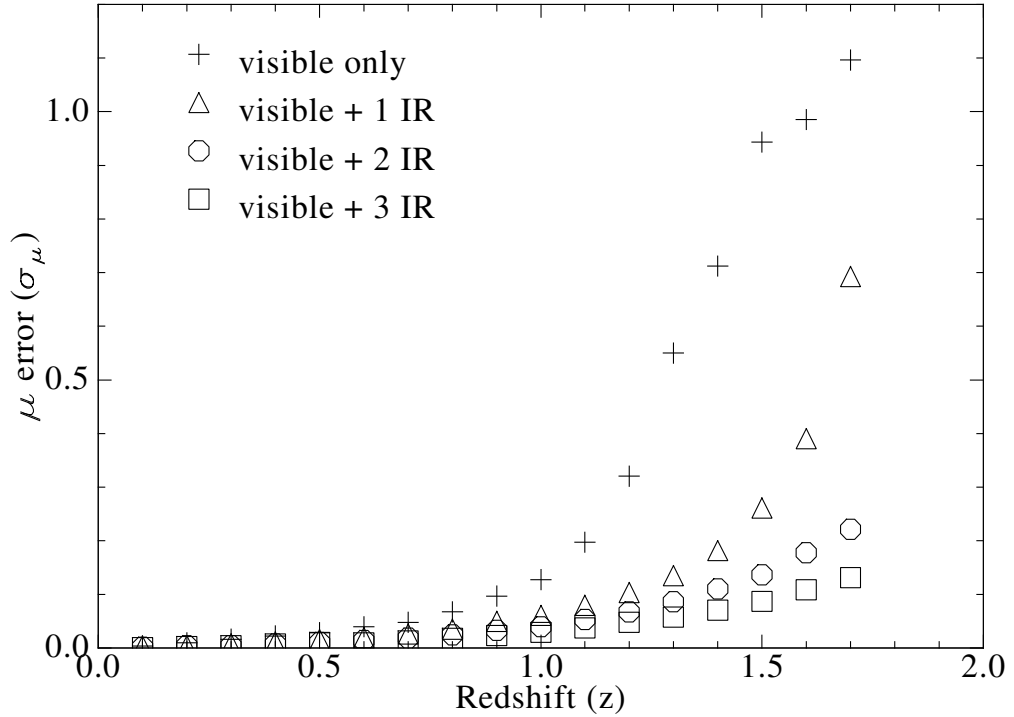


Figure 6.1. Distance modulus error vs. redshift for a SNAP supernova survey with 0, 1, 2, and all 3 NIR filters included.

The original SNAP design used a large, CCD only, focal plane, with a single NIR detector in a separate focal plane. Early in the program, the statistical power of high redshift supernovae for constraining dark energy was realized, and the need for NIR observations became clear. Linder and Huterer [2003] conclude that a systematic error limited supernova survey must extend to at least $z = 1.5$ to measure the time evolution of the dark energy equation of state. Based on such studies, the design was updated to include 36 CCDs and 36 NIR detectors in a shared focal plane. The addition of NIR observations improves the accuracy and redshift range of the supernova observations. Figure 6.1 shows the distance modulus error as a function of redshift for supernova surveys with varying degrees of NIR coverage. The choice of 3 NIR filters and 6 visible filters is based on signal to noise considerations and coverage of the supernova's restframe B band lightcurve. The SNAP filters are redshifted B band filters, log spaced to maintain approximately constant signal to noise with

redshift. The simulated data assume NIR detectors with a total noise of $10 e^-$ and $QE = 90\%$ from $0.9 - 1.7 \mu\text{m}$.

The NIR observations are most important above a redshift of 1. The results shown assume a space-based survey that is limited by the noise due to the zodiacal background photons. A visible imager in space could measure supernovae up to $z \approx 1.2$ with reasonable accuracy ($\sigma_{\text{stat}} < 0.5 \text{ mag}$); adding just 1 NIR filter covering the bandpass from $1.0 - 1.3 \mu\text{m}$ extends this to $z \approx 1.5$. For ground based observations, atmospheric absorption and sky brightness place a practical limit on the redshift range for type Ia supernovae at $z \approx 1$. Ground based observations above $z = 1$ with visible ($0.4 - 1.0 \mu\text{m}$) detectors are subject to Malmquist bias, preferentially discovering the brightest supernovae, which can systematically alter the dark energy constraints. In the NIR, the atmospheric effects for ground based observations are amplified, and the signal to noise needed to discover and follow high redshift supernovae cannot be achieved. A space-based NIR instrument is the only way to achieve accurate measurements of high redshift supernovae.

SNAP takes advantage of the unobscured observations available in space to extend the spectral coverage and redshift range of type Ia supernovae observations. SNAP will increase the number of well observed high redshift supernovae by an order of magnitude in just 16 months. The filters and observing strategy are designed to limit systematic uncertainties and provide high signal to noise observations to a redshift of 1.7 and beyond. Estimated constraints on the dark energy parameters w_0 and w_a are derived for SNAP assuming two different model cosmologies: a cosmological constant dark energy model ($w_0 = -1, w_a = 0$) and a brane world inspired model ($w_0 = -0.78, w_a = 0.32$, see Linder [2004]). Both models assume a spatially flat universe with $H_0 = 65 \text{ km s}^{-1} \text{ Mpc}^{-1}$ and $\Omega_M = 0.26$. SNAP is able to differentiate the similar expansion histories of these very different dark energy models with high confidence.

6.1.1 w_0 and w_a Constraints I

Constraints on the dark energy equation of state are estimated using the statistical uncertainties shown in Fig. 6.1 and a systematic error model discussed below. The dark energy constraints presented assume the default redshift distribution for type Ia supernovae in the SNAP deep survey with a bin size of $\Delta z = 0.1$ (see Fig. 4.8), plus 300 low redshift ($z \approx 0.01$) supernovae discovered by ground based instruments (e.g. Aldering et al. [2002]). To estimate constraints for a specific cosmology model, the distance modulus for each redshift bin is calculated using the cosmology model. The statistical variance in the i^{th} redshift bin is given as

$$\sigma_i^2 = \frac{\sigma_{\text{intrinsic}}^2 + \sigma_{\text{stat},i}^2}{N_i}, \quad (6.1)$$

where N_i is the number of supernovae in bin i , and $\sigma_{\text{intrinsic}} = 0.12^3$. The supernovae data are fit to estimate the covariance matrix for the fitting parameters. Using this method, the best fit parameter values are the ‘true’ values used to simulate the data, and the uncertainties are minimized. This is equivalent to using the Fisher matrix to estimate the parameter uncertainties; the covariance matrix is the inverse of the Fisher information matrix. The Fisher matrix is used below to combine supernova constraints with estimated constraints from weak lensing and baryon acoustic oscillation surveys.

The SNAP deep survey is designed to be systematic uncertainty limited for type Ia supernovae measurements. The statistical uncertainty on the distance modulus is minimized by observing more than 2000 type Ia supernovae. Systematic uncertainties are modeled as an irreducible redshift dependent error added to each redshift bin. The systematic uncertainty does not decrease when averaging supernova measurements, and can skew the best fit dark energy values away from the true value used to generate the supernova data. Two systematic error models have been proposed for the SNAP supernova survey: $\sigma_{\text{sys}} = 0.02 z/1.7$ [Kim et al., 2004] and $\sigma_{\text{sys}} = 0.02(1+z)/2.7$

³As mentioned earlier, this is a conservative estimate of the dispersion in the corrected distance modulus, considering the temporal and spectral coverage of the supernova lightcurves in the SNAP deep survey.

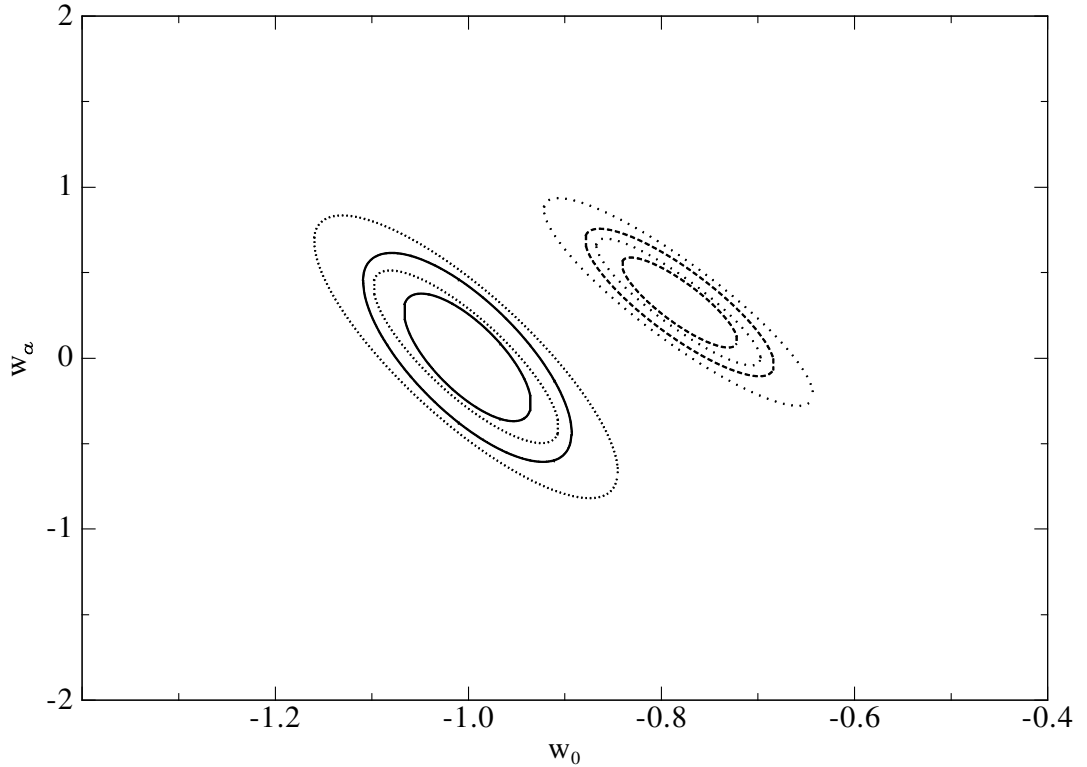


Figure 6.2. 68.3% and 95.4% confidence contours in the w_0 , w_a plane for a systematic uncertainty limited supernova survey. Two cosmology models are considered: a concordance, Λ CDM (solid and short dot), and a brane world model with $w_0 = -0.78$, $w_a = 0.32$ (dashed and long dot). The solid and dashed contours assume a systematic uncertainty of $\sigma_{\text{sys}} = 0.02(1+z)/2.7$; the two dotted contours add the statistical uncertainty in quadrature with σ_{sys} . All fits assume a spatially flat universe and a prior of $\Omega_m = 0.26 \pm 0.01$.

[Linder and Huterer, 2003, SNAP Collaboration: G. Aldering et al., 2004]. In both cases, the authors treat the systematic uncertainty as an irreducible random error. The latter model is more accurate at low redshifts and is used below. Random systematic errors increase the size of the confidence intervals, but do not (on average) change the best fit parameter values. Random systematic uncertainties give the limiting precision of the survey, assuming an infinite number of samples to reduce the statistical errors.

Figure 6.2 shows confidence intervals in the w_0 , w_a plane for a random systematic error of $0.02(1+z)/2.7$. Intervals are shown for a concordance Λ CDM cosmology ($w = -1$) and a brane world dark energy model, with $w_0 = -0.78$ and $w_a = 0.32$. Both models assume a spatially flat universe with $H_0 = 65 \text{ km s}^{-1} \text{ Mpc}^{-1}$, $\Omega_M =$

0.26, and $\Omega_X = 0.74$. Contours including the statistical uncertainty are also shown. Including the statistical error increases the uncertainty on w_a by approximately 40% for both models. The area of the 95% confidence contours (which is the DETF figure of merit) increases by a factor of 1.63 for the Λ CDM cosmology and 1.75 for the braneworld dark energy model. The statistical uncertainty does impact the dark energy constraints for the SNAP supernova program, but not as a result of the detector performance. NIR detectors with 90% QE and a total noise less than $10 e^-$ only increase the statistical error on each type Ia supernova by 0.01 mag compared to an ideal, noiseless detector. When averaging 80 to 100 supernovae per bin, the impact of the detector noise is negligible. In order to approach the systematic uncertainty limit, the aperture, exposure time, observing cadence or number of supernovae must increase. The NIR detectors have reached the level of accuracy where improvements in the detector performance have a minimal impact on the contours in Fig. 6.2.

The systematic uncertainty limit gives the best possible constraints on w_0 and w_a for a supernova survey extending out to $z = 1.7$. For the assumed systematic error model, the limiting precision is $\sigma_{w_0} = 0.04$ and $\sigma_{w_a} = 0.25$, when including a prior of $\Omega_M = 0.26 \pm 0.01$. For the brane world model, the constraints improve to $\sigma_{w_0} = 0.04$ and $\sigma_{w_a} = 0.17$. When prior knowledge of Ω_M is available, these two dark energy models are easily distinguished. If no prior information about the mass density is known, then distance modulus measurements from type Ia supernovae cannot distinguish these two forms of dark energy.

A more interesting and potentially dangerous systematic error model is one that systematically shifts the measured value of the distance modulus as a function of redshift. Evolution of the supernova peak magnitude with cosmic time is one possibility. Evolution could occur due to changes in the progenitor age or metallicity as a function of redshift. The magnitude of the evolution is difficult to predict, so the estimated uncertainty of $0.02(1+z)/2.7$ magnitudes [SNAP Collaboration: G. Aldering et al., 2004] is added to each redshift bin to illustrate the impact of a systematic error of this nature. When adding this systematic error, the best fit values for the dark energy parameters become $w_0 = -0.99 \pm 0.05$ and $w_a = -0.11 \pm 0.26$. Sub-

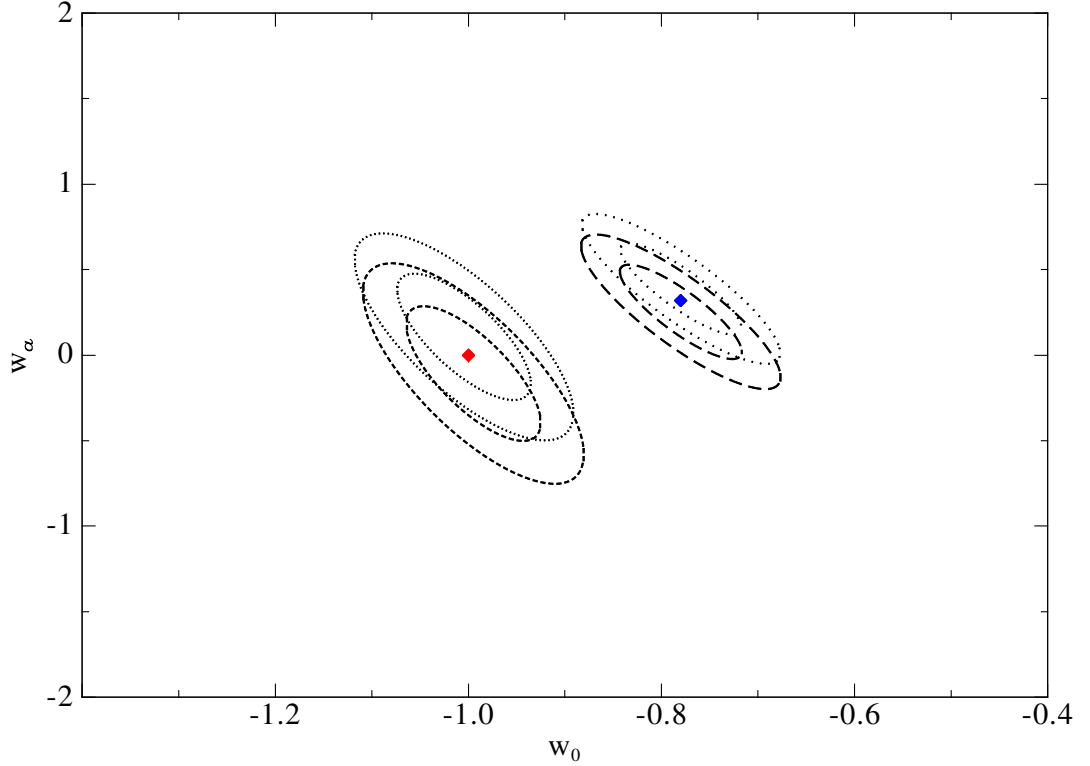


Figure 6.3. 68.3% and 95.4% confidence contours for w_0 and w_a when adding and subtracting a redshift dependent systematic error of $\sigma_{\text{sys}} = 0.02(1+z)/2.7$. Dashed contours add a systematic shift in distance modulus to each redshift bin, dotted contours subtract σ_{sys} from each redshift bin. Cosmological constant and braneworld dark energy models are shown. The diamonds represent the model cosmology parameters.

tracting the same systematic error from each redshift bin gives $w_0 = -1.01 \pm 0.05$ and $w_a = 0.11 \pm 0.24$. The resulting error contours for the cosmological constant and braneworld dark energy models are shown in Fig. 6.3. For a systematic uncertainty of this magnitude, the 68.3% error contours still include the true value of the dark energy equation of state. The prior constraint on the matter density is important for maintaining accuracy in the presence of systematic uncertainty. If the matter density is not constrained, the best fit dark energy parameters change more rapidly in the presence of systematic offsets in the distance modulus. Fortunately, the combination of existing CMB data and the SNAP gravitational weak lensing data provide the necessary constraint on Ω_M , as shown in Sec. 6.2.1.

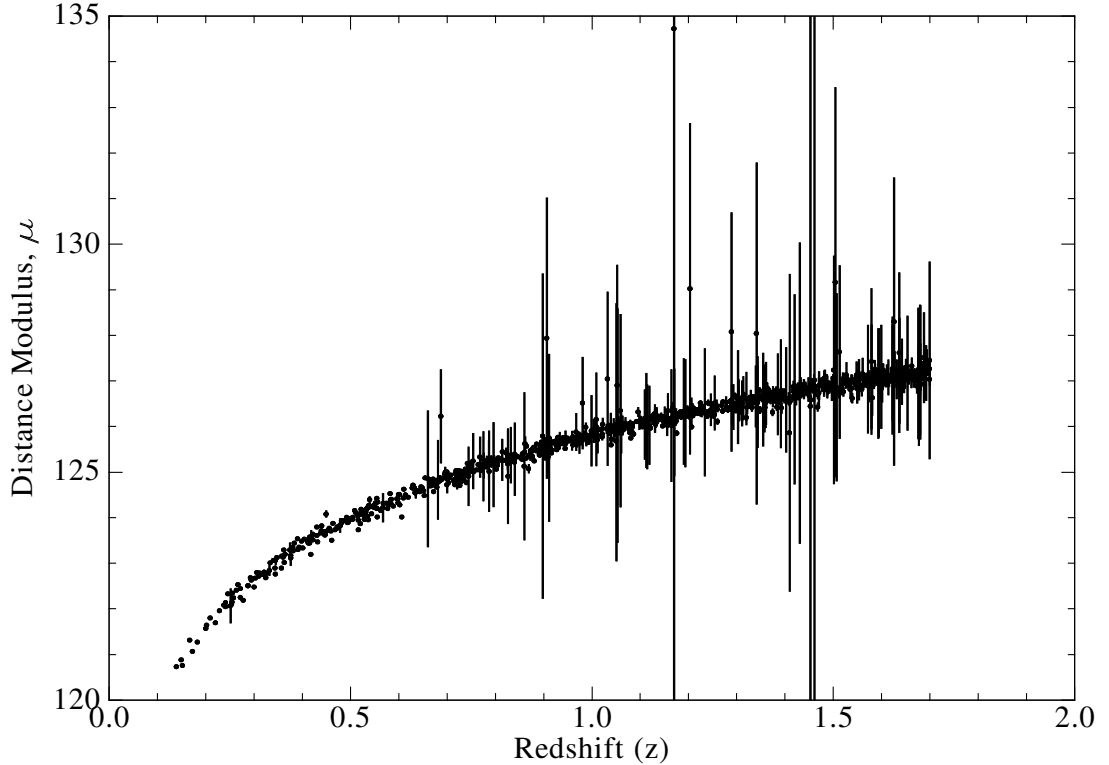


Figure 6.4. Simulated distance modulus data for 2000 type Ia supernova using the SNAPsim framework.

6.1.2 w_0 and w_a Constraints II

The data used to project constraints on w_0 and w_a in Sec. 6.1.1 use the known value of the distance modulus in each redshift bin. In order to simulate data for a survey like SNAP, statistical and systematic fluctuations must be added to the distance modulus data. This is accomplished in two ways. The simplest method is to sample the distance modulus in each redshift bin from a random Gaussian distribution with the mean given by the predicted distance modulus for the model cosmology (i.e. the true cosmology for the simulated data), and the variance given by Eq. (6.1) plus the systematic uncertainty. This method assumes all supernovae in each bin are (on average) identical. A more comprehensive method is to simulate complete lightcurves in the 9 SNAP filters and fit the distance modulus for 2000 supernovae individually. In this case each supernova has its own dust extinction, stretch, and statistical uncertainty extracted from the simulated data.

Figure 6.4 shows 2000 type Ia supernovae simulated using SNAPsim. Each supernova has a randomly generated explosion date and redshift, and is observed on a 4 day cadence in all 9 SNAP filters for 16 months. The points that deviate from the Hubble diagram and the data with large uncertainty are due to the nature of the lightcurve and distance modulus fitting used in SNAPsim. The simulation uses custom lightcurve and distance modulus fitting code, which is still in development [Kuznetsova et al., 2005]. The lightcurve fits fail to converge in some of the filters, even when signal to noise is high. When a lightcurve fit is unsuccessful, none of the information from the unsuccessful filter is used in the distance modulus estimate. The loss of information leads to large uncertainties in the distance modulus data. The distance modulus errors in Fig. 6.1 (and Sec. 4.4) are derived from data where the lightcurve fit is successful in at least 7 of the 9 filters. This approach utilizes all of the information and leads to uncertainties less than 0.13 mag up to $z = 1.7$. The current lightcurve fitting code also introduces a small bias in the fit value of the peak brightness, which results in a biased estimate of the distance modulus. As a result, the simulated data shown in Fig. 6.4 are not used to fit the dark energy equation of state at this time. The framework to simulate the type Ia supernova data and extract the cosmology parameters from distance modulus data are in place, and will be implemented once the lightcurve fitting issues are resolved.

The simulation software does provide an accurate estimate of the distance modulus uncertainty when the lightcurve fits are successful, as shown in Fig. 6.1. These data are used to quickly simulate distance modulus measurements for SNAP supernovae by sampling a Gaussian distribution in each redshift bin. Figure 6.5 shows the 68.3% and 95.4% confidence contours for simulated supernova data using this method, assuming no systematic uncertainties. For a Λ CDM cosmology, the best fit parameter values are $w_0 = -0.99 \pm 0.05$ and $w_a = 0.01 \pm 0.25$, assuming a prior on the mass density, $\Omega_M = 0.26 \pm 0.01$. For a braneworld inspired cosmology with an effective equation of state $w_0 = 0.78$, $w_a = -0.32$, the best fit values are $w_0 = -0.78 \pm 0.04$ and $w_a = 0.30 \pm 0.18$.

The best fit values vary around their true values for each realization of the simu-

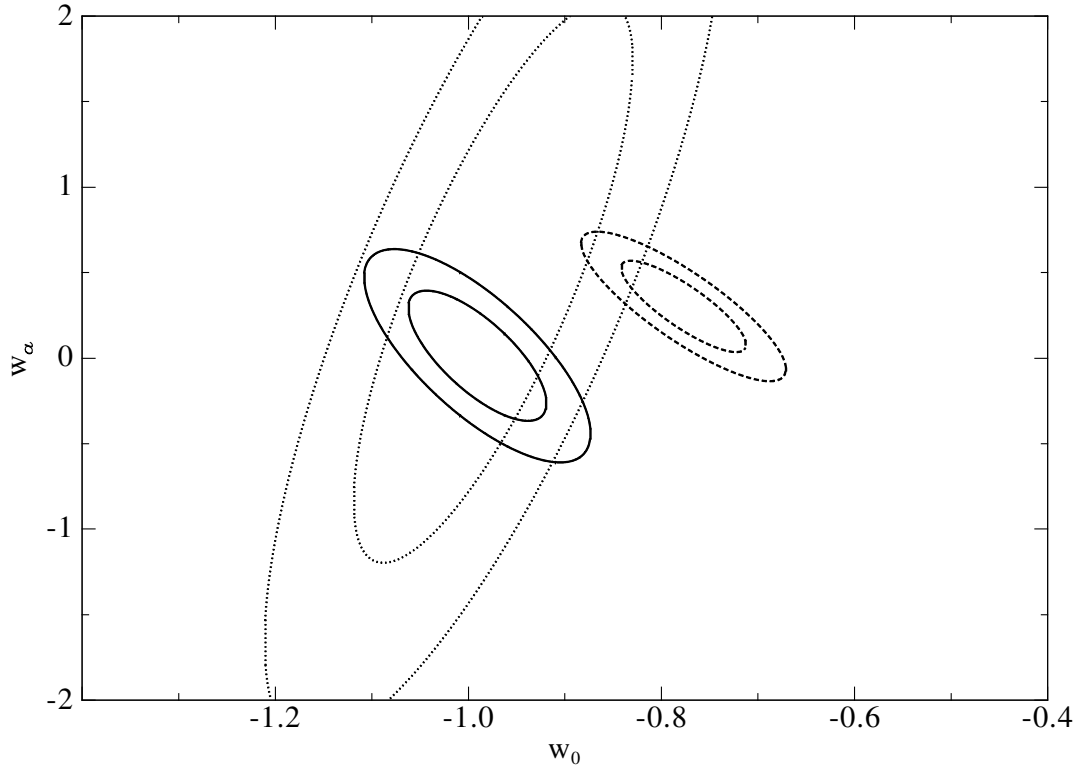


Figure 6.5. 68.3% and 95.4% confidence contours for w_0 and w_a from simulated SNAP supernova data. Two cosmology models are considered: a concordance, Λ CDM (solid and dotted), and a braneworld model with $w_0 = -0.78$, $w_a = 0.32$ (dashed). All the data assume a spatially flat universe. The dotted contours do not include any prior constraints. The solid and dashed contours include a prior on the mass density, $\Omega_M = 0.26 \pm 0.01$.

lated data. When fitting the Λ CDM case without a prior constraint on Ω_M , the best fit equation of state is $w_0 = -0.97 \pm 0.10$ and $w_a = 0.44 \pm 1.08$. In this case, the best fit value of Ω_M is 0.22 ± 0.13 ; the contours with the Ω_M prior in Fig. 6.5 extend beyond the contours with no prior because including the prior changes the best fit value to $\Omega_M = 0.26 \pm 0.01$. Adding a prior centered on the true value of Ω_M improves both the uncertainty and accuracy of the w_0 and w_a estimates. When working with real data, the true parameter values are unknown, and applying an incorrect prior can have the opposite effect, biasing the results away from the true values for w_0 and w_a . Replacing the simple prior on Ω_M with a combination of multiple data sets helps ensure that the results are not biased and incorporates additional information about the dark energy equation of state that is ignored by the simple prior model.

6.2 Constraining Cosmology with Multiple Techniques

The dark energy constraints in Sec. 6.1 rely on two key assumptions to accurately measure the dark energy equation of state: spatial flatness and independent knowledge of the matter density. The spatial flatness constraint is motivated by predictions from inflation [Guth, 1981] and supported by measurements of the CMB power spectrum [Spergel et al., 2003, 2006]. The constraint on the matter density is more difficult to attain. Future CMB experiments such as Planck [<http://www.rssd.esa.int/Planck/>] are expected to measure the matter density with an accuracy of 1%, however this depends sensitively on the dark energy equation of state. Many of the projections for Planck assume a constant dark energy equation of state (e.g. Balbi et al. [2003]). To avoid biasing the dark energy constraints, it is best to start with a general cosmology model with arbitrary curvature and no prior constraints on the density parameters. In a Fisher matrix approach, constraints are derived for each data set independently, then combined by summing the Fisher matrices. This eliminates any assumptions about the global curvature of the universe and incorporates knowledge of all parameters, not just Ω_M , from the experiments under consideration. This is also the approach used by the DETF [Albrecht et al., 2006].

The Fisher matrix for type Ia supernovae can be derived from the covariance matrix or by direct calculation of the derivatives of the distance modulus with respect to the fit parameters (see Sec. 3.4). Allowing for arbitrary curvature and removing the prior on Ω_M increases the uncertainty on the dark energy equation of state to $\sigma_{w_0} = 1.3$ and $\sigma_{w_a} = 4.0$, including both statistical and systematic uncertainties for SNAP type Ia supernovae. The uncertainties on the dark energy parameters and the contours in the w_0, w_a plane are consistent with the ‘optimistic’ DETF constraints for a space based survey of 2000 type Ia supernovae. Agreement with the results from an independent panel such as the DETF indicates that the systematic error model used to project dark energy constraints for SNAP is realistic and achievable.

To constrain dark energy, the Fisher matrix for type Ia supernovae is combined with a Fisher matrix derived from WMAP measurements of the CMB and an H_0

constraint from the Hubble Key project ($H_0 = 72 \pm 8 \text{ km s}^{-1} \text{ Mpc}^{-1}$ [Freedman et al., 2001]). The resulting confidence contours are similar to the constraints for supernovae alone assuming a spatially flat universe and no prior on Ω_M . The supernovae and CMB Fisher matrices are then added to weak lensing and baryon acoustic oscillation Fisher matrices provided by the DETF [<http://www.physics.ucdavis.edu/DETFast/>] (DETFast also provides the WMAP Fisher matrix) to estimate constraints on w_0 and w_a . Each of these measurements depends on the Hubble parameter, $H(z)$, in different ways (see Sec. 2.6), breaking degeneracies and improving constraints more than a simple prior model.

Most of the SNAP survey time is focused on type Ia supernova photometry and spectroscopy, however, the importance of the wide and panoramic surveys cannot be ignored. The 4 dithered exposures in the wide survey provide shape measurements of over 300 million galaxies that are used to measure weak gravitational lensing. In addition, baryon oscillation and cluster abundance data are contained in these surveys at no additional cost. The survey strategy and filters are not optimized for these measurements; a deep spectroscopic redshift survey is preferred for baryon oscillation measurements, and cluster surveys with only optical observations suffer from projection and selection effects. However, the photometric data from the wide and panoramic surveys does improve on existing baryon oscillation and cluster measurements, providing a cross check of the type Ia supernova and weak lensing results. Projected baryon oscillation data are shown below; the cluster abundances could also be used, but do not add to the dark energy constraints and are not considered at this time.

The DETF fiducial cosmology assumes a spatially flat universe with $\Omega_M = 0.27$, $w_0 = -1.0$, $w_a = 0$, and $H_0 = 72 \text{ km s}^{-1} \text{ Mpc}^{-1}$. The supernova data assume the same model cosmology. The increase in the matter density compared to the cosmology model in Sec. 6.1 leads to a minor change in the tilt of the error contours. The change in H_0 simply shifts the entire Hubble diagram and has no impact on the dark energy constraints.

6.2.1 Supernovae and Weak Lensing

The SNAP telescope and instrumentation provide high signal to noise wide field observing with excellent PSF stability. Both the supernova and weak lensing surveys provide an order of magnitude increase in the number of objects and improved accuracy compared to existing data sets. The combination of type Ia supernovae and weak lensing is particularly powerful due to the orthogonality of the confidence contours in the w_0, w_a plane. The degeneracy between the matter density and the dark energy equation of state that exists in luminosity distance measurements with supernova data is resolved in weak lensing surveys, which measure both the angular diameter distance and the linear growth factor. The geometric nature of the distance measurement, combined with the dependence of the growth of structure on $H(z)$, tightly constrains Ω_M and the dark energy parameters. The two methods also face different systematic uncertainties. Supernova measurements depend on well calibrated photometry, while shape measurements dominate the error budget for weak lensing. Agreement between these two methods is a clear sign that systematic errors are not dominating the measurement.

Figure 6.6 shows projected constraints for type Ia supernovae, weak lensing, and the combination of both datasets. The contours for the supernovae and weak lensing data both include constraints from WMAP measurements of the CMB and the HST key project. The CMB data is most useful for constraining the total density, favoring a spatially flat universe. The uncertainty for the supernovae data is $\sigma_{w_0} = 0.07$ and $\sigma_{w_a} = 0.69$, while weak lensing constrains $\sigma_{w_0} = 0.11$ and $\sigma_{w_a} = 0.27$. The combination of these methods gives $\sigma_{w_0} = 0.04$ and $\sigma_{w_a} = 0.14$, all assuming a cosmological constant form of dark energy.

The combination of supernovae and weak lensing leads to a smaller uncertainty on w_a compared to the data in Sec. 6.1, which assume spatial flatness and apply a prior constraint on the matter density. The general form of the model cosmology leads to degeneracies in the cosmological parameters for supernovae, CMB, and weak lensing data when each is considered alone. The measurements by themselves provide little information about the nature of dark energy. However, when considered simultane-

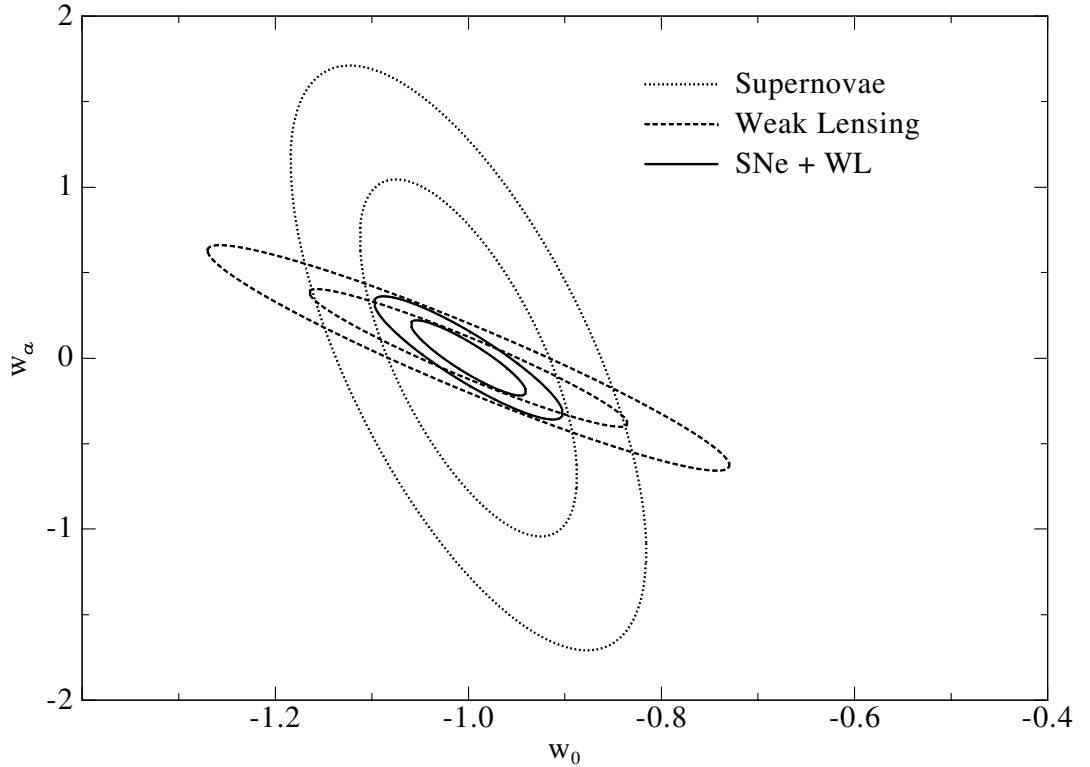


Figure 6.6. 68.3% and 95.4% confidence contours in the w_0 , w_a plane from SNAP supernova data plus WMAP CMB data and a 1000 deg² space based weak lensing survey. The weak lensing data are based on the ‘pessimistic’ systematic error model from the DETF.

ously, these three techniques are able to constrain the curvature and matter density, breaking the degeneracies and resulting in constraints on the dark energy equation of state consistent with the goals of the DETF for stage IV projects. The matter energy density is constrained to $\Omega_M = 0.27 \pm 0.005$ using all of the above data, a factor of 2 improvement over the assumed prior for Ω_M in Sec. 6.1. Better knowledge of Ω_M , which is affected most strongly by the weak lensing and CMB power spectra, improves the uncertainty on the time evolution of the dark energy equation of state.

The challenge with weak lensing is controlling systematic uncertainties in shape and redshift measurements. The final systematic error budget for the SNAP weak lensing survey is not yet known, so the DETF pessimistic systematic error model is used. The systematic errors include redshift dependent shear calibration bias, photo- z bias, intrinsic galaxy shape correlations, intrinsic shape density correlations and the shape of the theoretical power spectrum. The photo- z errors, in particular the catas-

trophic redshift errors, are reduced by NIR observations which break degeneracies with extended color information for all galaxies. The uncertainties related to shape measurements are all based on optical measurements at this time, since limited information is available on galaxy shapes in the infrared. The SNAP wide and panoramic surveys provide infrared shape measurements with the precision to characterize the evolution of galaxy shapes as a function of color and potentially improve shape and shear measurements for weak lensing.

6.2.2 Supernovae and Baryon Acoustic Oscillations

Baryon oscillation data are similar to weak lensing in that they provide an orthogonal measure of the dark energy equation of state due to a change in the dependence on $H(z)$. Baryon oscillations use features in the matter power spectrum to define an angular scale which is used to constrain the angular diameter distance. The shape of the power spectrum is sensitive to the Hubble constant and the matter and baryon densities, which are known from the ratio of the first and second acoustic peaks in the CMB power spectrum. The matter power spectrum is derived from the CMB power spectrum; combining the two does not lead to tight constraints on dark energy. To constrain dark energy with baryon oscillations, H_0 must be known to establish a scale for the angular diameter distance. The existing 10% measurement of H_0 is not sufficient for baryon oscillations alone to constrain the dark energy equation of state.

For a baryon oscillation survey covering 10000 square degrees (the SNAP panoramic survey covers 7000 – 10000 square degrees in all 9 bandpasses) with photometric redshifts measured to 0.01 the dark energy equation of state is constrained to $\sigma_{w_0} = 0.27$ and $\sigma_{w_a} = 0.79$. Despite the large errors on w_0 and w_a from baryon oscillation and WMAP CMB data, the combination with type Ia supernovae produces narrow constraints, as shown in Fig. 6.7. Using data from all three techniques lowers the dark energy uncertainty to $\sigma_{w_0} = 0.05$ and $\sigma_{w_a} = 0.31$. This uncertainty is comparable to the constraints in Sec. 6.1, which assume 2000 supernovae, a spatially flat universe, and a 1% measurement of the mass density. Baryon oscillations are still under development as a technique to constrain dark energy, and cannot match the performance

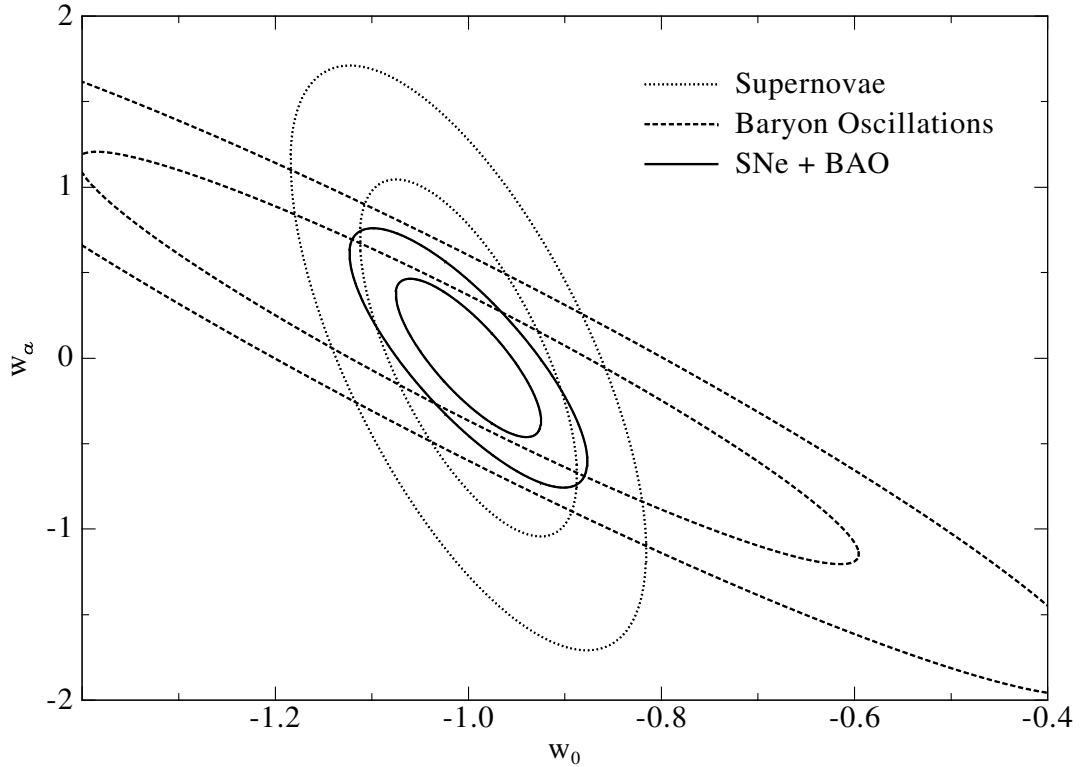


Figure 6.7. 68.3% and 95.4% confidence contours in the w_0 , w_a plane from SNAP supernova data plus WMAP CMB data and a baryon acoustic oscillation survey of 10^8 galaxies.

of weak lensing at this time.

6.2.3 All Techniques

Combining data from supernovae, the CMB, weak lensing, and baryon oscillations leads to the constraints in Fig. 6.8. The uncertainty on the dark energy equation of state is reduced to $\sigma_{w_0} = 0.04$ and $\sigma_{w_a} = 0.12$. The improvement over the dataset that excludes baryon oscillations is minor, due to the orientation of the baryon oscillation contours in the w_0 , w_a plane. The baryon oscillation data add little information that is not already present in the weak lensing measurements. Supernovae and weak lensing are complementary measurements that break parameter degeneracies, while baryon oscillations and weak lensing have the same dependence on the dark energy parameters and do not lead to substantial improvements when considered in concert. The baryon oscillation data will be most useful to check the supernova and weak lensing results to illuminate any systematic bias that may exist in these measurements.

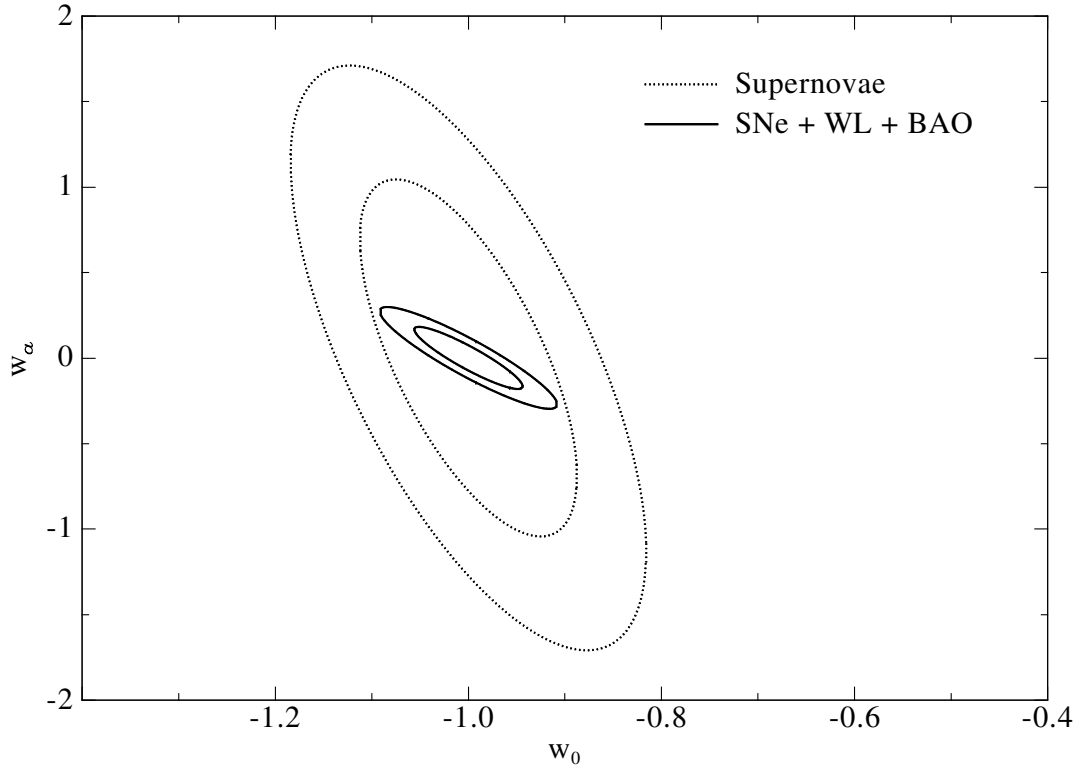


Figure 6.8. 68.3% and 95.4% confidence contours in the w_0 , w_a plane from SNAP supernova data plus WMAP CMB data, a 1000 deg² space based weak lensing survey, and a baryon acoustic oscillation survey of 10⁸ galaxies

While SNAP will measure baryon oscillations in the matter power spectrum through the wide and panoramic surveys, the instrumentation is optimized for supernovae and weak lensing. Baryon oscillation surveys do not require PSF stability for shape measurements or precision observations in the NIR bandpass, which are only available in space. A spectroscopic survey of galaxy redshifts is ideal for baryon oscillation measurements. Supernovae and weak lensing do require the PSF stability and low background NIR measurements that are accessible from a space based platform. Measurements of cluster abundances, discussed in Sec. 2.6, are similar to the baryon oscillation data at this point. They provide an intriguing and new way to attack the dark energy problem, but do not provide a compelling argument for a space based dark energy mission. Using the SNAP mission to constrain dark energy with type Ia supernovae and weak lensing while the baryon oscillation and cluster techniques continue to develop is the best approach at this time. The baryon acoustic oscil-

lation and cluster abundance data obtained during the SNAP wide and panoramic surveys provide a cross check of systematic errors. Future missions optimized to measure baryon oscillations and cluster abundances will provide an additional check of systematic errors and will help unravel the dark energy mystery.

6.3 Conclusions

The results in this chapter demonstrate the ability of the SNAP mission to constrain the dark energy equation of state and enlighten understanding of fundamental physics. The SNAP supernova survey, combined with the theoretical assumption of spatial flatness and prior knowledge of the mass density, can easily distinguish a cosmological constant from the brane world dark energy model considered above. Ignoring the prior assumptions about the curvature and matter density, the supernova and weak lensing surveys combine to produce even tighter constraints. A comparison of constraints for all of the different combinations of measurements and priors is given in Table 6.1.

All of the constraints shown assume a homogeneous and isotropic FRW cosmology. The energy components are perfect fluids and the evolution of the universe is determined by $H(z)$ and the Friedmann equation (see Sec. 2.3.4). There are many other theories describing the dynamics of the universe, which all predict different expansion histories. Even though the alternate cosmologies are not explored here, the data collected by the SNAP telescope are able to test and constrain the parameters of many models. Both the distance modulus errors from type Ia supernovae and the constraints on the dark energy equation of state demonstrate the accuracy of expected SNAP measurements. This accuracy is consistent with the DETF position that “exploration of the acceleration of the Universe’s expansion will profoundly change our understanding of the composition and nature of the Universe.” The parameterized equation of state serves as a way to quantify the measurements of the expansion and represent the observed data.

The accuracy of the supernova measurements relies on precision NIR photometry, especially at redshifts greater than 1. Linder and Huterer [2003] explored the constraints on the dark energy equation of state as a function of the uncertainty limit

| Data Sets | Assumptions | σ_{Ω_M} | σ_{w_0} | σ_{w_a} |
|-----------------------|---|---------------------|----------------|----------------|
| 2000 SNe (sys + stat) | flat Λ CDM | 0.130 | 0.10 | 1.08 |
| 2000 SNe (sys + stat) | flat Λ CDM, $\Omega_M \pm 0.01$ | 0.010 | 0.06 | 0.33 |
| 2000 SNe (sys only) | flat Λ CDM, $\Omega_M \pm 0.01$ | 0.010 | 0.04 | 0.25 |
| 2000 SNe (sys + stat) | flat Brane world, $\Omega_M \pm 0.01$ | 0.010 | 0.06 | 0.24 |
| 2000 SNe (sys only) | flat Brane world, $\Omega_M \pm 0.01$ | 0.010 | 0.04 | 0.17 |
| SNe + WMAP | Λ CDM | 0.025 | 0.07 | 0.69 |
| WL + WMAP | Λ CDM | 0.014 | 0.11 | 0.27 |
| SNe + WL + WMAP | Λ CDM | 0.005 | 0.04 | 0.14 |
| BAO + WMAP | Λ CDM | 0.031 | 0.27 | 0.79 |
| SNe + BAO + WMAP | Λ CDM | 0.017 | 0.05 | 0.31 |
| SNe + WL + BAO + WMAP | Λ CDM | 0.004 | 0.04 | 0.12 |

Table 6.1. Uncertainty on the dark energy equation of state for various combination of future dark energy measurements. All supernova data include statistical and systematic ($\sigma_{\text{sys}} = 0.02(1+z)/2.7$) errors unless otherwise noted. A prior of $H_0 = 72 \pm 8.0 \text{ km s}^{-1} \text{ Mpc}^{-1}$ is included for all data below the break-line.

and redshift, and found that a limiting error of 0.02 mag with a cutoff redshift of $z = 1.7$ gives equivalent results to a survey out to $z = 2.5$ with a limiting error of 0.03 mag. By pushing for the best possible performance from the NIR detectors, both statistical and systematic uncertainties are limited up to $z = 1.7$ for SNAP. A higher redshift mission that did not focus on controlling uncertainties would require higher cutoff detectors, external cooling of the detectors and telescope optics, and a longer mission lifetime due to spectroscopic constraints at high redshift. The SNAP infrared R&D program has succeeded in producing $1.7 \mu\text{m}$ cutoff HgCdTe detectors that exceed the initial specifications and deliver background (zodiacal) performance for type Ia supernova observations in the baseline mission design.

The detector testing and development is complemented by simulations of supernova lightcurves and distance modulus estimates as a function of the detector parameters. The simulation proceeds in steps from single observations in each filter, to complete multi-color lightcurves, to distance modulus estimates, and finally cosmological constraints using thousands of supernovae. The uncertainty on the distance modulus is an intermediate step between the detector requirements and science goals for constraining w_0 and w_a . Trade studies on the distance modulus error for high redshift type Ia supernovae as a function of the NIR detector read noise, dark current,

and quantum efficiency show that the achieved QE in the R&D detectors relaxes the noise requirement. The best R&D detectors deliver performance that exceeds the initial SNAP specifications and is zodiacal light limited for all of the SNAP surveys. These trade studies highlight the excellent performance of existing detectors and will define the final science grade requirements. In this chapter, estimates of the distance modulus errors for supernovae from $z = 0.1 - 1.7$ are used to project constraints on w_0 and w_a . Combining the supernova constraints with projected weak lensing and baryon acoustic oscillation data yields uncertainties of $\sigma_{w_0} = 0.04$ and $\sigma_{w_a} = 0.12$ on the dark energy equation of state from the SNAP mission. This represents a factor of 10 improvement compared to constraints from current missions, consistent with the goals of the DETF for a stage IV mission.

The nature of dark energy remains one of the fundamental mysteries in physics today. Understanding the mysterious energy component that is driving the acceleration of the universe requires multiple measurements with precise control of both statistical and systematic uncertainties. A number of tools exist to measure the properties of dark energy and the density of the fundamental energy components in the universe. Measurements of the CMB power spectrum, type Ia supernovae, weak lensing, baryon acoustic oscillations, and cluster abundances all play a role in our current understanding of the universe. The constraints from each of these techniques compliment the others in different ways. Data from the CMB are already available and is essential for measuring the curvature density and determining if the universe is spatially flat, as predicted by inflation. At the present, a space mission optimized for supernovae and lensing observations provides the best tool to measure the properties of dark energy. A wide field imaging instrument covering both the visible and NIR bandpasses provides the redshift range for type Ia supernovae and the excellent photo- z accuracy needed for weak lensing in a single mission dedicated to measuring dark energy. The infrared reach of the SNAP mission extends the redshift range used to study dark energy, providing insight into the time variation in the equation of state. SNAP takes advantage of the complementarity of multiple measurement techniques to uncover the nature of dark energy and improve understanding of fundamental physics.

BIBLIOGRAPHY

- U. Alam, V. Sahni, T. Deep Saini, and A. A. Starobinsky. Exploring the expanding Universe and dark energy using the statefinder diagnostic. *MNRAS*, 344:1057–1074, October 2003.
- A. Albrecht, G. Bernstein, R. Cahn, W. L. Freedman, J. Hewitt, W. Hu, J. Huth, M. Kamionkowski, E. W. Kolb, L. Knox, J. C. Mather, S. Staggs, and N. B. Suntzeff. Report of the Dark Energy Task Force. *ArXiv Astrophysics e-prints*, September 2006.
- G. Aldering. SNAP Sky Background at the North Ecliptic Pole. *SNAP Internal Document*, 2001.
- G. Aldering, G. Adam, P. Antilogus, P. Astier, R. Bacon, S. Bongard, C. Bonnaud, Y. Copin, D. Hardin, F. Henault, D. A. Howell, J.-P. Lemonnier, J.-M. Levy, S. C. Loken, P. E. Nugent, R. Pain, A. Pecontal, E. Pecontal, S. Perlmutter, R. M. Quimby, K. Schahmaneche, G. Smadja, and W. M. Wood-Vasey. Overview of the Nearby Supernova Factory. In J. A. Tyson and S. Wolff, editors, *Survey and Other Telescope Technologies and Discoveries. Edited by Tyson, J. Anthony; Wolff, Sidney. Proceedings of the SPIE, Volume 4836, pp. 61-72 (2002).*, pages 61–72, December 2002.
- L. H. Aller, I. Appenzeller, B. Baschek, H. W. Duerbeck, T. Herczeg, E. Lamla, E. Meyer-Hofmeister, T. Schmidt-Kaler, M. Scholz, W. Seggewiss, W. C. Seitter, and V. Weidemann. *Landolt-Börnstein: Numerical Data and Functional Relationships in Science and Technology - New Series " Gruppe/Group 6 Astronomy and Astrophysics " Volume 2 Schaifers/Voigt: Astronomy and Astrophysics / Astronomie und Astrophysik " Stars and Star Clusters / Sterne und Sternhaufen.*

- Landolt-Bornstein: Numerical Data and Functional Relationships in Science and Technology, 1982.
- R. A. Alpher, H. Bethe, and G. Gamow. The Origin of Chemical Elements. *Physical Review*, 73:803–804, April 1948.
- G. W. Angus, B. Famaey, and H. S. Zhao. Can MOND take a bullet? Analytical comparisons of three versions of MOND beyond spherical symmetry. *MNRAS*, 371:138–146, September 2006.
- N. A. Bahcall, F. Dong, P. Bode, R. Kim, J. Annis, T. A. McKay, S. Hansen, J. Schroeder, J. Gunn, J. P. Ostriker, M. Postman, R. C. Nichol, C. Miller, T. Goto, J. Brinkmann, G. R. Knapp, D. O. Lamb, D. P. Schneider, M. S. Vogeley, and D. G. York. The Cluster Mass Function from Early Sloan Digital Sky Survey Data: Cosmological Implications. *ApJ*, 585:182–190, March 2003.
- A. Balbi, C. Baccigalupi, F. Perrotta, S. Matarrese, and N. Vittorio. Probing Dark Energy with the Cosmic Microwave Background: Projected Constraints from the Wilkinson Microwave Anisotropy Probe and Planck. *ApJ*, 588:L5–L8, May 2003.
- T. Barreiro, E. J. Copeland, and N. J. Nunes. Quintessence arising from exponential potentials. *Phys. Rev. D*, 61(12):127301–+, June 2000.
- N. Barron, M. Borysow, K. Beyerlein, M. Brown, C. Weaverdyck, W. Lorenzon, M. Schubnell, G. Tarlé, and A. Tomasch. Sub-pixel response measurement of near-infrared sensors. *Submitted to PASP, October 2006*, 2006.
- G. Bernstein and B. Jain. Dark Energy Constraints from Weak-Lensing Cross-Correlation Cosmography. *ApJ*, 600:17–25, January 2004.
- G. M. Bernstein and M. Jarvis. Shapes and Shears, Stars and Smears: Optimal Measurements for Weak Lensing. *AJ*, 123:583–618, February 2002.
- M. S. Bessell. UBVRI passbands. *PASP*, 102:1181–1199, October 1990.

- P. R. Bevington and D. K. Robinson. *Data reduction and error analysis for the physical sciences*. Data reduction and error analysis for the physical sciences, 3rd ed., by Philip R. Bevington, and Keith D. Robinson. Boston, MA: McGraw-Hill, ISBN 0-07-247227-8, 2003., 2003.
- N. Bilić, G. B. Tupper, and R. D. Viollier. Unification of dark matter and dark energy: the inhomogeneous Chaplygin gas. *Physics Letters B*, 535:17–21, May 2002.
- J. Binney and M. Merrifield. *Galactic astronomy*. Galactic astronomy / James Binney and Michael Merrifield. Princeton, NJ : Princeton University Press, 1998. (Princeton series in astrophysics) QB857 .B522 1998 (\$35.00), 1998.
- T. Boker et al. NICMOS Dark Current Anomaly: Test Results. *NICMOS Instrument Science Report*, 00-002, 2000.
- R. Bolin, A. Riess, and R. de Jong. NICMOS count-rate dependent non-linearity tests using flatfield lamps. *NICMOS Instrument Science Report*, 001, 2006.
- M. Brown, M. Schubnell, and G. Tarlé. Correlated Noise and Gain in Unfilled and Epoxy-Underfilled Hybridized HgCdTe Detectors. *PASP*, 118:1443–1447, October 2006a.
- M. G. Brown et al. Development of NIR Detectors and Science Driven Requirements for SNAP. In *Proceedings of the SPIE, Volume 6265, pp. (2006)*., July 2006b.
- M. G. Brown, M. Schubnell, G. Tarle, R. Smith, M. Bonati, D. Guzman, D. Figer, N. Mostek, S. Mufson, D. Cole, S. Seshardi, SNAP Collaboration, and SNAP Simulation Team. Development of NIR Detectors and Science Driven Requirements for SNAP. *Bulletin of the American Astronomical Society*, 37:1282–+, December 2005.
- M.G. Brown. Raytheon sb-301 ingaas - dark signal test report_v1.1. [http://snap.lbl.gov/bscw/bscw.cgi/d121201/Raytheon SB-301 InGaAs - Dark Signal Test Report_v1.1.ppt](http://snap.lbl.gov/bscw/bscw.cgi/d121201/Raytheon%20SB-301%20InGaAs%20-%20Dark%20Signal%20Test%20Report_v1.1.ppt), 2005.

- E. M. Burbidge, G. R. Burbidge, W. A. Fowler, and F. Hoyle. Synthesis of the Elements in Stars. *Reviews of Modern Physics*, 29:547–650, 1957.
- S. Burles, K. M. Nollett, and M. S. Turner. What is the big-bang-nucleosynthesis prediction for the baryon density and how reliable is it? *Phys. Rev. D*, 63(6):063512–+, March 2001.
- J. A. Cardelli, G. C. Clayton, and J. S. Mathis. The relationship between infrared, optical, and ultraviolet extinction. *ApJ*, 345:245–256, October 1989.
- M. Chevallier and D. Polarski. *Int. J. Mod. Phys.*, D10(213), 2001.
- D. J. H. Chung and K. Freese. Cosmological challenges in theories with extra dimensions and remarks on the horizon problem. *Phys. Rev. D*, 61(2):023511–+, January 2000.
- D. D. Clayton. *Principles of stellar evolution and nucleosynthesis*. Chicago: University of Chicago Press, 1983, 1983.
- D. Clowe, M. Bradač, A. H. Gonzalez, M. Markevitch, S. W. Randall, C. Jones, and D. Zaritsky. A Direct Empirical Proof of the Existence of Dark Matter. *ApJ*, 648:L109–L113, September 2006.
- S. Cole, W. J. Percival, J. A. Peacock, P. Norberg, C. M. Baugh, C. S. Frenk, I. Baldry, J. Bland-Hawthorn, T. Bridges, R. Cannon, M. Colless, C. Collins, W. Couch, N. J. G. Cross, G. Dalton, V. R. Eke, R. De Propris, S. P. Driver, G. Efstathiou, R. S. Ellis, K. Glazebrook, C. Jackson, A. Jenkins, O. Lahav, I. Lewis, S. Lumsden, S. Maddox, D. Madgwick, B. A. Peterson, W. Sutherland, and K. Taylor. The 2dF Galaxy Redshift Survey: power-spectrum analysis of the final data set and cosmological implications. *MNRAS*, 362:505–534, September 2005.
- R. Colistete, Jr., J. C. Fabris, S. V. B. Goncalves, and P. E. de Souza. Dark energy, dark matter and the Chaplygin gas. *ArXiv General Relativity and Quantum Cosmology e-prints*, October 2002.

- M. Colless. First results from the 2dF Galaxy Redshift Survey. *Royal Society of London Philosophical Transactions Series A*, 357:105–+, January 1999.
- A. Conley, G. Goldhaber, L. Wang, G. Aldering, R. Amanullah, E. D. Commins, V. Fadeyev, G. Folatelli, G. Garavini, R. Gibbons, A. Goobar, D. E. Groom, I. Hook, D. A. Howell, A. G. Kim, R. A. Knop, M. Kowalski, N. Kuznetsova, C. Lidman, S. Nobili, P. E. Nugent, R. Pain, S. Perlmutter, E. Smith, A. L. Spadafora, V. Stanishev, M. Strovink, R. C. Thomas, and W. M. Wood-Vasey. Measurement of Ω_m , Ω_Λ from a Blind Analysis of Type Ia Supernovae with CMAGIC: Using Color Information to Verify the Acceleration of the Universe. *ApJ*, 644:1–20, June 2006.
- A. R. Cooray and D. Huterer. Gravitational Lensing as a Probe of Quintessence. *ApJ*, 513:L95–L98, March 1999.
- P. S. Corasaniti and E. J. Copeland. Constraining the quintessence equation of state with SnIa data and CMB peaks. *Phys. Rev. D*, 65(4):043004–+, February 2002.
- A. W. J. Cousins. Revised zero points and UBV photometry of stars in the Harvard E and F regions. *MNRAS*, 166:711–+, March 1974a.
- A. W. J. Cousins. Standard Stars for VRI Photometry with S25 Response Photocathodes [Errata: 1974MNSSA..33....1C]. *Monthly Notes of the Astronomical Society of South Africa*, 33:149–+, 1974b.
- D. Daou and C. Skinner. Persistence in NICMOS : Results from Thermal Vacuum Data D. *NICMOS Instrument Science Report*, 97-023, 1997.
- C. Deffayet, G. Dvali, and G. Gabadadze. Accelerated universe from gravity leaking to extra dimensions. *Phys. Rev. D*, 65(4):044023–+, February 2002.
- S. Eidelman et al. WIMPs and Other Particle Searches. *Phys. Lett. B*, 592:1, 2004.
- A. Einstein. Besprechung von "A. Einstein: Die Grundlage der allgemeinen Relativitätstheorie". *Naturwissenschaften*, 4:481, 1916.

- A. Einstein. Lens-Like Action of a Star by the Deviation of Light in the Gravitational Field. *Science*, 84:506–507, December 1936.
- D. J. Eisenstein, I. Zehavi, D. W. Hogg, R. Scoccimarro, M. R. Blanton, R. C. Nichol, R. Scranton, H.-J. Seo, M. Tegmark, Z. Zheng, S. F. Anderson, J. Annis, N. Bahcall, J. Brinkmann, S. Burles, F. J. Castander, A. Connolly, I. Csabai, M. Doi, M. Fukugita, J. A. Frieman, K. Glazebrook, J. E. Gunn, J. S. Hendry, G. Hennesy, Z. Ivezić, S. Kent, G. R. Knapp, H. Lin, Y.-S. Loh, R. H. Lupton, B. Margon, T. A. McKay, A. Meiksin, J. A. Munn, A. Pope, M. W. Richmond, D. Schlegel, D. P. Schneider, K. Shimasaku, C. Stoughton, M. A. Strauss, M. SubbaRao, A. S. Szalay, I. Szapudi, D. L. Tucker, B. Yanny, and D. G. York. Detection of the Baryon Acoustic Peak in the Large-Scale Correlation Function of SDSS Luminous Red Galaxies. *ApJ*, 633:560–574, November 2005.
- P. G. Ferreira and M. Joyce. Cosmology with a primordial scaling field. *Phys. Rev. D*, 58(2):023503–+, July 1998.
- D. F. Figer, B. J. Rauscher, M. W. Regan, J. C. Balleza, R. H. Barkhouser, L. E. Bergeron, G. R. Greene, S. Kim, S. R. McCandliss, E. Morse, R. Pelton, T. Reeves, U. Sharma, P. Stelmanski, H. S. Stockman, and M. Telewicz. Independent detector testing laboratory and the NGST detector characterization project. In J. C. Mather, editor, *IR Space Telescopes and Instruments. Edited by John C. Mather . Proceedings of the SPIE, Volume 4850, pp. 981-1000 (2003).*, pages 981–1000, March 2003.
- D. F. Figer, B. J. Rausher, M. W. Regan, E. Morse, J. Balleza, L. Bergeron, and H. S. Stockman. volume 5167, pages 270–301. Proc. SPIE, 2004.
- G. Finger, P. Biereichel, H. Mehrgan, M. Meyer, A. F. Moorwood, G. Nicolini, and J. Stegmeier. Infrared detector development programs for the VLT instruments at the European Southern Observatory. In A. M. Fowler, editor, *Proc. SPIE Vol. 3354, p. 87-98, Infrared Astronomical Instrumentation, Albert M. Fowler; Ed.*, pages 87–98, August 1998.

- G. Finger et al. *Workshop on Scientific Detectors for Astronomy*, Springer-Verlag, 2005.
- W. L. Freedman, B. F. Madore, B. K. Gibson, L. Ferrarese, D. D. Kelson, S. Sakai, J. R. Mould, R. C. Kennicutt, H. C. Ford, J. A. Graham, J. P. Huchra, S. M. G. Hughes, G. D. Illingworth, L. M. Macri, and P. B. Stetson. Final Results from the Hubble Space Telescope Key Project to Measure the Hubble Constant. *ApJ*, 553: 47–72, May 2001.
- K. Freese and M. Lewis. Cardassian expansion: a model in which the universe is flat, matter dominated, and accelerating. *Physics Letters B*, 540:1–2, July 2002.
- A. Friedmann. *Zs. f. Phys.*, 10, 1922.
- G. Gamow. Expanding Universe and the Origin of Elements. *Physical Review*, 70: 572–573, October 1946.
- M. Geddo, V. Bellani, and G. Guizzetti. Optical study of the strain effect in pseudomorphic $\text{In}_{1-x}\text{Ga}_x\text{As-InP}$ heterostructures. *Phys. Rev. B*, 50:5456–5461, August 1994.
- L. M. Germany. *Ph.D. Thesis*. PhD thesis, Australian National Univ., 2001.
- K. M. Gorski, A. J. Banday, C. L. Bennett, G. Hinshaw, A. Kogut, G. F. Smoot, and E. L. Wright. Power Spectrum of Primordial Inhomogeneity Determined from the Four-Year COBE DMR Sky Maps. *ApJ*, 464:L11+, June 1996.
- A. H. Guth. Inflationary universe: A possible solution to the horizon and flatness problems. *Phys. Rev. D*, 23:347–356, January 1981.
- M. Hamuy, M. M. Phillips, J. Maza, N. B. Suntzeff, R. A. Schommer, and R. Aviles. A Hubble diagram of distant type IA supernovae. *AJ*, 109:1–13, January 1995.
- M. Hamuy, M. M. Phillips, N. B. Suntzeff, R. A. Schommer, J. Maza, and R. Aviles. The Absolute Luminosities of the Calan/Tololo Type IA Supernovae. *AJ*, 1996a.

- M. Hamuy, M. M. Phillips, N. B. Suntzeff, R. A. Schommer, J. Maza, R. C. Smith, P. Lira, and R. Aviles. The Morphology of Type IA Supernovae Light Curves. *AJ*, 1996b.
- C. M. Hirata and U. Seljak. Can superhorizon cosmological perturbations explain the acceleration of the universe? *Phys. Rev. D*, 72(8):083501–+, October 2005.
- H. Hoekstra, H. K. C. Yee, and M. D. Gladders. Current status of weak gravitational lensing. *New Astronomy Review*, 46:767–781, November 2002.
- F. Hoyle, W. A. Fowler, G. R. Burbidge, and E. M. Burbidge. Origin of the Elements in Stars. *Science*, 124:611–614, October 1956.
- <http://cminuit.sourceforge.net/>. Minuit.
- <http://gargamel.physics.lsa.umich.edu>. University of michigan fpa test results.
- <http://map.gsfc.nasa.gov/>. Wmap.
- <http://www.jwst.nasa.gov/>. James webb space telescope.
- <http://www.physics.ucdavis.edu/DETFast/>. Detfast.
- <http://www.rssd.esa.int/Planck/>. Planck.
- E. Hubble. A Relation between Distance and Radial Velocity among Extra-Galactic Nebulae. *Proceedings of the National Academy of Science*, 15:168–173, March 1929.
- L. Hui. Weighing the Cosmological Energy Contents with Weak Gravitational Lensing. *ApJ*, 519:L9–L12, July 1999.
- M. L. Humason, N. U. Mayall, and A. R. Sandage. Redshifts and magnitudes of extragalactic nebulae. *AJ*, 61:97–162, April 1956.
- B. Jain, U. Seljak, and S. White. Ray-tracing Simulations of Weak Lensing by Large-Scale Structure. *ApJ*, 530:547–577, February 2000.
- J. Janesick, K. Kalassen, and T. Elliott. volume 570, pages 7–19. Proc. SPIE, 1985.

- J. R. Janesick. *Scientific charge-coupled devices*. Scientific charge-coupled devices, Bellingham, WA: SPIE Optical Engineering Press, 2001, xvi, 906 p. SPIE Press monograph, PM 83. ISBN 0819436984, 2001.
- S. Jha. *Exploding stars, near and far, Ph.D. Thesis*. PhD thesis, Harvard Univ., October 2002.
- H. L. Johnson and W. W. Morgan. Fundamental stellar photometry for standards of spectral type on the revised system of the Yerkes spectral atlas. *ApJ*, 117:313–+, May 1953.
- J. B. Johnson. Thermal agitation of electricity in conductors. *Phys. Rev.*, 32(1):97, Jul 1928.
- N. Kaiser, G. Squires, and T. Broadhurst. A Method for Weak Lensing Observations. *ApJ*, 449:460–+, August 1995.
- A. Kamenshchik, U. Moschella, and V. Pasquier. An alternative to quintessence. *Physics Letters B*, 511:265–268, July 2001.
- S. Kavadias, K. Misiakos, and D. Loukas. *IEEE Transactions on Nuclear Science*, 40 (2):397–401, 1994.
- A. Kim, A. Goobar, and S. Perlmutter. A Generalized K Correction for Type IA Supernovae: Comparing R-band Photometry beyond $z=0.2$ with B, V, and R-band Nearby Photometry. *PASP*, 108:190–+, February 1996.
- A. G. Kim, E. V. Linder, R. Miquel, and N. Mostek. Effects of systematic uncertainties on the supernova determination of cosmological parameters. *MNRAS*, 347: 909–920, January 2004.
- R. Klimasewski. *Ph.D. Thesis*, 1967.
- B. Koester et al. *Submitted to ApJ*, 2006.

- E. W. Kolb, S. Matarrese, A. Notari, and A. Riotto. Effect of inhomogeneities on the expansion rate of the universe. *Phys. Rev. D*, 71(2):023524–+, January 2005a.
- E. W. Kolb, S. Matarrese, and A. Riotto. On cosmic acceleration without dark energy. *ArXiv Astrophysics e-prints*, June 2005b.
- E. W. Kolb and M. S. Turner. *The early universe*. Frontiers in Physics, Reading, MA: Addison-Wesley, 1988, 1990, 1990.
- N. V. Kuznetsova, A. Bonissent, and A. G. Kim. A Study of SNAP Simulation Lightcurve Fitter Parameters. *Bulletin of the American Astronomical Society*, 207:–+, December 2005.
- Robert W. Leach and Frank J. Low. volume 4008, pages 337–343. *Proc. SPIE*, 2000.
- G. Lemaître. *Ann. Soc. Sci. Bruxelles*, 47, 1927.
- G. Lemaître. Expansion of the universe, A homogeneous universe of constant mass and increasing radius accounting for the radial velocity of extra-galactic nebulæ. *MNRAS*, 91:483–490, March 1931.
- E. V. Linder. Exploring the Expansion History of the Universe. *Physical Review Letters*, 90(9):091301–+, March 2003.
- E. V. Linder. Probing gravitation, dark energy, and acceleration. *Phys. Rev. D*, 70(2):023511–+, July 2004.
- E. V. Linder and D. Huterer. Importance of supernovae at $z > 1.5$ to probe dark energy. *Phys. Rev. D*, 67(8):081303–+, April 2003.
- C. H. Lineweaver and T. M. Davis. Misconceptions about the Big Bang. *Scientific American*, 292:36–45, 2005.
- P. Lira. *MA Thesis*. PhD thesis, University of Chile, 1995.
- R. Lupton. *Statistics in theory and practice*. Princeton, N.J.: Princeton University Press, —c1993, 1993.

- P. A. Mazzali, E. Cappellaro, I. J. Danziger, M. Turatto, and S. Benetti. Nebular Velocities in Type IA Supernovae and Their Relationship to Light Curves. *ApJ*, 499:L49+, May 1998.
- I. S. McLean, editor. *Electronic imaging in astronomy. Detectors and instrumentation*, 1997.
- C. W. McMurtry, T. S. Allen, A. C. Moore, W. J. Forrest, and J. L. Pipher. Characterization of 2.5 micron HgCdTe VIRGO/VISTA detector array. In T. J. Grycewicz and C. J. Marshall, editors, *Focal Plane Arrays for Space Telescopes II. Edited by Grycewicz, Thomas J.; Marshall, Cheryl J. Proceedings of the SPIE, Volume 5902, pp. 152-160 (2005).*, pages 152–160, August 2005.
- C. W. McMurtry, T. S. Allen, A. C. Moore, W. J. Forrest, and J. L. Pipher. volume 5902, page 590208. Proc. SPIE, 2005.
- M. Milgrom. A modification of the Newtonian dynamics as a possible alternative to the hidden mass hypothesis. *ApJ*, 270:365–370, July 1983.
- R. Miquel. Optimizing the Redshift Distribution of the SNAP SN Survey. *Bulletin of the American Astronomical Society*, 207:–+, December 2005.
- D. G. Monet, S. E. Levine, B. Canzian, H. D. Ables, A. R. Bird, C. C. Dahn, H. H. Guetter, H. C. Harris, A. A. Henden, S. K. Leggett, H. F. Levison, C. B. Luginbuhl, J. Martini, A. K. B. Monet, J. A. Munn, J. R. Pier, A. R. Rhodes, B. Riepe, S. Sell, R. C. Stone, F. J. Vrba, R. L. Walker, G. Westerhout, R. J. Brucato, I. N. Reid, W. Schoening, M. Hartley, M. A. Read, and S. B. Tritton. The USNO-B Catalog. *AJ*, 125:984–993, February 2003.
- A. Moore et al. volume 5017, pages 240–253. Proc. SPIE, 2003a.
- A. Moore et al. *Opt. Eng.*, 45:076402, 2006.
- A. Moore, Z. Ninkov, and W. Forrest. volume 5167, pages 204–215. Proc. SPIE, 2003b.

- L. Mortara and A. Fowler. volume 290, pages 28–33. Proc. SPIE, 1981.
- M. M. Murakami et al. *IEEE Transactions on Nuclear Science*, 50(4):1013, 2003.
- P. Nugent, A. Kim, and S. Perlmutter. K-Corrections and Extinction Corrections for Type Ia Supernovae. *PASP*, 114:803–819, August 2002.
- P. Nugent, M. Phillips, E. Baron, D. Branch, and P. Hauschildt. Evidence for a Spectroscopic Sequence among Type Ia Supernovae. *ApJ*, 455:L147+, December 1995.
- H. Nyquist. Thermal agitation of electric charge in conductors. *Phys. Rev.*, 32(1): 110–113, Jul 1928.
- J. B. Oke and A. Sandage. Energy Distributions, K Corrections, and the Stebbins-Whitford Effect for Giant Elliptical Galaxies. *ApJ*, 154:21–+, October 1968.
- T. Padmanabhan. *Structure Formation in the Universe*. Structure Formation in the Universe, by T. Padmanabhan, pp. 499. ISBN 0521424860. Cambridge, UK: Cambridge University Press, June 1993., June 1993.
- T. Padmanabhan. Dark Energy: Mystery of the Millennium. *ArXiv Astrophysics e-prints*, March 2006.
- J. A. Peacock. *Cosmological Physics*. Cosmological Physics, by John A. Peacock, pp. 704. ISBN 052141072X. Cambridge, UK: Cambridge University Press, January 1999., January 1999.
- P. J. E. Peebles. *The large-scale structure of the universe*. Research supported by the National Science Foundation. Princeton, N.J., Princeton University Press, 1980. 435 p., 1980.
- P. J. E. Peebles. *Principles of physical cosmology*. Princeton Series in Physics, Princeton, NJ: Princeton University Press, —c1993, 1993.

- P. J. E. Peebles and B. Ratra. Cosmology with a time-variable cosmological 'constant'. *ApJ*, 325:L17–L20, February 1988.
- A. A. Penzias and R. W. Wilson. A Measurement of Excess Antenna Temperature at 4080 Mc/s. *ApJ*, 142:419–421, July 1965.
- S. Perlmutter, G. Aldering, G. Goldhaber, R. A. Knop, P. Nugent, P. G. Castro, S. Deustua, S. Fabbro, A. Goobar, D. E. Groom, I. M. Hook, A. G. Kim, M. Y. Kim, J. C. Lee, N. J. Nunes, R. Pain, C. R. Pennypacker, R. Quimby, C. Lidman, R. S. Ellis, M. Irwin, R. G. McMahon, P. Ruiz-Lapuente, N. Walton, B. Schaefer, B. J. Boyle, A. V. Filippenko, T. Matheson, A. S. Fruchter, N. Panagia, H. J. M. Newberg, W. J. Couch, and The Supernova Cosmology Project. Measurements of Omega and Lambda from 42 High-Redshift Supernovae. *ApJ*, 517:565–586, June 1999.
- S. Perlmutter, S. Gabi, G. Goldhaber, A. Goobar, D. E. Groom, I. M. Hook, A. G. Kim, M. Y. Kim, J. C. Lee, R. Pain, C. R. Pennypacker, I. A. Small, R. S. Ellis, R. G. McMahon, B. J. Boyle, P. S. Bunclark, D. Carter, M. J. Irwin, K. Glazebrook, H. J. M. Newberg, A. V. Filippenko, T. Matheson, M. Dopita, W. J. Couch, and The Supernova Cosmology Project. Measurements of the Cosmological Parameters Omega and Lambda from the First Seven Supernovae at $Z \geq 0.35$. *ApJ*, 483:565–+, July 1997.
- M. M. Phillips. The absolute magnitudes of Type IA supernovae. *ApJ*, 413:L105–L108, August 1993.
- M. M. Phillips, P. Lira, N. B. Suntzeff, R. A. Schommer, M. Hamuy, and J. Maza. The Reddening-Free Decline Rate Versus Luminosity Relationship for Type IA Supernovae. *AJ*, 118:1766–1776, October 1999.
- N. Pogson. Magnitudes of Forty Minor Planets for the first day of each Month in 1858. *MNRAS*, 18:47–+, December 1857.

- W. H. Press and P. Schechter. Formation of Galaxies and Clusters of Galaxies by Self-Similar Gravitational Condensation. *ApJ*, 187:425–438, February 1974.
- A. Refregier. Weak Gravitational Lensing by Large-Scale Structure. *Annual Review of Astronomy and Astrophysics*, 41:645–668, 2003.
- A. Refregier and D. Bacon. Shapelets - II. A method for weak lensing measurements. *MNRAS*, 338:48–56, January 2003.
- A. Refregier, R. Massey, J. Rhodes, R. Ellis, J. Albert, D. Bacon, G. Bernstein, T. McKay, and S. Perlmutter. Weak Lensing from Space. III. Cosmological Parameters. *AJ*, 127:3102–3114, June 2004.
- A. G. Riess, A. V. Filippenko, P. Challis, A. Clocchiatti, A. Diercks, P. M. Garnavich, R. L. Gilliland, C. J. Hogan, S. Jha, R. P. Kirshner, B. Leibundgut, M. M. Phillips, D. Reiss, B. P. Schmidt, R. A. Schommer, R. C. Smith, J. Spyromilio, C. Stubbs, N. B. Suntzeff, and J. Tonry. Observational Evidence from Supernovae for an Accelerating Universe and a Cosmological Constant. *AJ*, 116:1009–1038, September 1998.
- A. G. Riess, W. H. Press, and R. P. Kirshner. Using Type IA supernova light curve shapes to measure the Hubble constant. *ApJ*, 438:L17–L20, January 1995.
- A. G. Riess, W. H. Press, and R. P. Kirshner. A Precise Distance Indicator: Type IA Supernova Multicolor Light-Curve Shapes. *ApJ*, 473:88–+, December 1996.
- A. G. Riess, L.-G. Strolger, J. Tonry, S. Casertano, H. C. Ferguson, B. Mobasher, P. Challis, A. V. Filippenko, S. Jha, W. Li, R. Chornock, R. P. Kirshner, B. Leibundgut, M. Dickinson, M. Livio, M. Giavalisco, C. C. Steidel, T. Benítez, and Z. Tsvetanov. Type Ia Supernova Discoveries at $z > 1$ from the Hubble Space Telescope: Evidence for Past Deceleration and Constraints on Dark Energy Evolution. *ApJ*, 607:665–687, June 2004.
- Rockwell. *HAWAII-2RG Technical Documentation, Version 1.1b*, 2004.

- E. Rozo et al. *in preperation*, 2006.
- B. Ryden. *Introduction to cosmology*. Introduction to cosmology / Barbara Ryden. San Francisco, CA, USA: Addison Wesley, ISBN 0-8053-8912-1, 2003, IX + 244 pp., 2003.
- V. Sahni and Y. Shtanov. Braneworld models of dark energy. *Journal of Cosmology and Astro-Particle Physics*, 11:14–+, November 2003.
- A. D. Sakharov. Violation of CP Invariance, C Asymmetry, and Baryon Asymmetry of the Universe. *Journal of Experimental and Theoretical Physics Letteres*, 5:24–+, January 1967.
- H. B. Sandvik, M. Tegmark, M. Zaldarriaga, and I. Waga. The end of unified dark matter? *Phys. Rev. D*, 69(12):123524–+, June 2004.
- P. Schneider, J. Ehlers, and E. E. Falco. *Gravitational Lenses*. Gravitational Lenses, XIV, 560 pp. 112 figs.. Springer-Verlag Berlin Heidelberg New York. Also Astronomy and Astrophysics Library, 1992.
- B. F. Schutz. *A First Course in General Relativity*. A First Course in General Relativity, by Bernard F. Schutz, pp. 392. ISBN 0521277035. Cambridge, UK: Cambridge University Press, February 1985., February 1985.
- A. Sen. Rolling Tachyon. *Journal of High Energy Physics*, 4:48–+, April 2002.
- H.-J. Seo and D. J. Eisenstein. Baryonic Acoustic Oscillations in Simulated Galaxy Redshift Surveys. *ApJ*, 633:575–588, November 2005.
- R. Smith, C. Bebek, M. Bonati, M. G. Brown, D. Cole, G. Rahmer, M. Schubnell, S. Seshadri, and G. Tarle. Noise and zero point drift in $1.7\mu\text{m}$ cutoff detectors for SNAP. In *High Energy, Optical, and Infrared Detectors for Astronomy II*. Edited by Dorn, David A.; Holland, Andrew D.. *Proceedings of the SPIE, Volume 6276*, pp. (2006)., July 2006.

- R. Smith et al. 2005-02-16 bias optimization. [http://snap.lbl.gov/bscw/bscw.cgi/d121212/2005-02-16 Bias optimization.ppt](http://snap.lbl.gov/bscw/bscw.cgi/d121212/2005-02-16%20Bias%20optimization.ppt), 2005.
- R. Smith et al. 2006-06-01 collab mtg r.smith persistence. [http://snap.lbl.gov/bscw/bscw.cgi/d200855/2006-06-01 Collab Mtg R.Smith Persistence.ppt](http://snap.lbl.gov/bscw/bscw.cgi/d200855/2006-06-01%20Collab%20Mtg%20R.Smith%20Persistence.ppt), 2006.
- R. M. Smith, M. Bonati, and D. Guzman. VIRGO-2K 2.25- μ m HgCdTe dark current. In J. D. Garnett and J. W. Beletic, editors, *Optical and Infrared Detectors for Astronomy. Edited by James D. Garnett and James W. Beletic. Proceedings of the SPIE, Volume 5499, pp. 119-130 (2004).*, pages 119–130, September 2004.
- SNAP Collaboration: G. Aldering, W. Althouse, R. Amanullah, J. Annis, P. Astier, C. Baltay, E. Barrelet, S. Basa, C. Bebek, L. Bergstrom, G. Bernstein, M. Bester, B. Bigelow, R. Blandford, R. Bohlin, A. Bonissent, C. Bower, M. Brown, M. Campbell, W. Carithers, E. Commins, W. Craig, C. Day, F. DeJongh, S. Deustua, T. Diehl, S. Dodelson, A. Ealet, R. Ellis, W. Emmet, D. Fouchez, J. Frieman, A. Fruchter, D. Gerdes, L. Gladney, G. Goldhaber, A. Goobar, D. Groom, H. Heetderks, M. Hoff, S. Holland, M. Huffer, L. Hui, D. Huterer, B. Jain, P. Jelsky, A. Karcher, S. Kent, S. Kahn, A. Kim, W. Kolbe, B. Krieger, G. Kushner, N. Kuznetsova, R. Lafever, J. Lamoureux, M. Lampton, O. Le Fevre, M. Levi, P. Limon, H. Lin, E. Linder, S. Loken, W. Lorenzon, R. Malina, J. Marriner, P. Marshall, R. Massey, A. Mazure, T. McKay, S. McKee, R. Miquel, N. Morgan, E. Mortsell, N. Mostek, S. Mufson, J. Musser, P. Nugent, H. Oluseyi, R. Pain, N. Palaio, D. Pankow, J. Peoples, S. Perlmutter, E. Prieto, D. Rubinowitz, A. Refregier, J. Rhodes, N. Roe, D. Rusin, V. Scarpine, M. Schubnell, M. Sholl, G. Smadja, R. M. Smith, G. Smoot, J. Snyder, A. Spadafora, A. Stebbins, C. Stoughton, A. Szymkowiak, G. Tarle, K. Taylor, A. Tilquin, A. Tomasch, D. Tucker, D. Vincent, H. von der Lippe, J. Walder, G. Wang, and W. Wester. Supernova / Acceleration Probe: A Satellite Experiment to Study the Nature of the Dark Energy. *ArXiv Astrophysics e-prints*, May 2004.
- D. N. Spergel, R. Bean, O. Dore', M. R. Nolta, C. L. Bennett, G. Hinshaw, N. Jarosik,

- E. Komatsu, L. Page, H. V. Peiris, L. Verde, C. Barnes, M. Halpern, R. S. Hill, A. Kogut, M. Limon, S. S. Meyer, N. Odegard, G. S. Tucker, J. L. Weiland, E. Wollack, and E. L. Wright. Wilkinson Microwave Anisotropy Probe (WMAP) Three Year Results: Implications for Cosmology. *ArXiv Astrophysics e-prints*, March 2006.
- D. N. Spergel, L. Verde, H. V. Peiris, E. Komatsu, M. R.olta, C. L. Bennett, M. Halpern, G. Hinshaw, N. Jarosik, A. Kogut, M. Limon, S. S. Meyer, L. Page, G. S. Tucker, J. L. Weiland, E. Wollack, and E. L. Wright. First-Year Wilkinson Microwave Anisotropy Probe (WMAP) Observations: Determination of Cosmological Parameters. *ApJS*, 148:175–194, September 2003.
- P. J. Steinhardt, L. Wang, and I. Zlatev. Cosmological tracking solutions. *Phys. Rev. D*, 59(12):123504–+, June 1999.
- J. L. Tonry, B. P. Schmidt, B. Barris, P. Candia, P. Challis, A. Clocchiatti, A. L. Coil, A. V. Filippenko, P. Garnavich, C. Hogan, S. T. Holland, S. Jha, R. P. Kirshner, K. Krisciunas, B. Leibundgut, W. Li, T. Matheson, M. M. Phillips, A. G. Riess, R. Schommer, R. C. Smith, J. Sollerman, J. Spyromilio, C. W. Stubbs, and N. B. Suntzeff. Cosmological Results from High-z Supernovae. *ApJ*, 594:1–24, September 2003.
- M. S. Turner. Dark Energy and the New Cosmology. *ArXiv Astrophysics e-prints*, August 2001.
- D. Tytler, J. M. O’Meara, N. Suzuki, and D. Lubin. Review of Big Bang Nucleosynthesis and Primordial Abundances. *Physica Scripta Volume T*, 85:12–+, 2000.
- L. A. Ureña-López and T. Matos. New cosmological tracker solution for quintessence. *Phys. Rev. D*, 62(8):081302–+, October 2000.
- M. Wagner. *Ph.D. Thesis*, 2002.

- L. Wang, G. Goldhaber, G. Aldering, and S. Perlmutter. Multicolor Light Curves of Type Ia Supernovae on the Color-Magnitude Diagram: A Novel Step toward More Precise Distance and Extinction Estimates. *ApJ*, 590:944–970, June 2003.
- Y. Wang, V. Kostov, K. Freese, J. A. Frieman, and P. Gondolo. Probing the evolution of the dark energy density with future supernova surveys. *Journal of Cosmology and Astro-Particle Physics*, 12:3–+, December 2004.
- Y. Wang and M. Tegmark. Uncorrelated measurements of the cosmic expansion history and dark energy from supernovae. *Phys. Rev. D*, 71(10):103513–+, May 2005.
- S. Weinberg. *Gravitation and Cosmology: Principles and Applications of the General Theory of Relativity*. Gravitation and Cosmology: Principles and Applications of the General Theory of Relativity, by Steven Weinberg, pp. 688. ISBN 0-471-92567-5. Wiley-VCH , July 1972., July 1972.
- S. Weinberg. The cosmological constant problem. *Reviews of Modern Physics*, 61: 1–23, January 1989.
- O. C. Wilson. Possible Applications of Supernovae to the Study of the Nebular Red Shifts. *ApJ*, 90:634–+, November 1939.
- S. E. Woosley and T. A. Weaver. The physics of supernova explosions. *ARA&A*, 24: 205–253, 1986.
- I. Zlatev, L. Wang, and P. J. Steinhardt. Quintessence, Cosmic Coincidence, and the Cosmological Constant. *Physical Review Letters*, 82:896–899, February 1999.
- F. Zwicky. Die Rotverschiebung von extragalaktischen Nebeln. *Helvetica Physica Acta*, 6:110–127, 1933.